INTERACTIONS OF FERRIPROTOPORPHYRIN IX *WITH NEUTRAL LIPIDS AND DETERGENTS:*

INSIGHTS INTO THEIR ROLE IN β-HAEMATIN FORMATION

by

Aneesa Omar

Thesis presented for the degree of

Doctor of Philosophy (Ph.D.)

In the Department of Chemistry

University of Cape Town

May 2015

Supervisor: Professor Timothy J Egan

Declaration

Interactions of ferriprotoporphyrin IX with neutral lipids and detergents:

Insights into their role in β-haematin formation

I, Aneesa Omar, hereby declare the following:

(1) The above-titled thesis is my own original work, from concept to execution with the recommended guidance from my supervisor, Professor Timothy J Egan.

(2) In cases where the work of others has been discussed, it has been cited and referenced accordingly.

(3) No part of this thesis has been, is being or will be submitted for another degree at this or any other university.

(4) I grant the University of Cape Town free license to reproduce this work in its entirety or in part for the purposes of research.

Having declared this, I hereby present this thesis for examination for the degree of Doctor of Philosophy (PhD) in Chemistry.

Signed at the UNIVERSITY OF CAPE TOWN

Aneesa Omar Signed by candidate

Date 08/05/2015

Abstract

The malaria parasite ingests between 80-100% of the host red blood cell's iron in the form of haemoglobin, which is catabolised to amino acids and ferriprotoporphyrin (Fe(III)PPIX), that it subsequently detoxifies to form the biocrystal, haemozoin. Neutral lipids have been implicated as the biological molecules responsible for the nucleation of haemozoin *in vivo,* though their exact role is unclear. This thesis has investigated the interaction between these lipids and Fe(III)PPIX. By exploiting the fluorescence quenching ability of Fe(III)PPIX, Stern-Volmer plots were generated to estimate the concentration of Fe(III)PPIX partitioned into Nile red stained neutral lipid droplets (NLBDs) over a pH range. The pH dependence was found to correlate with the charge of the Fe(III)PPIX molecule and the largest amount of Fe(III)PPIX partitioning was observed under the acidic pH conditions of the parasite digestive vacuole (pH 4.80), where haemozoin is formed. From the fluorescence maximum of Nile red, the relative polarity inside the lipid droplets was shown to lie between that of acetone and octanol with a Dimroth-Reichart $E_T(30)$ parameter of 45 kcal/mol. The lipophilicity of Fe(III)PPIX was validated by measuring the octanol-water partition coefficient, log D_{OW}, as 1.8 for the ionised form at pH 7.5 and a log *P* of 2.8 for the neutral form. 4-aminoquinoline drugs, chloroquine and amodiaquine, decreased the partitioning of Fe(III)PPIX into NLBDs at low pH owing to the consistently charged nature of the drug-Fe(III)PPIX complex. In contrast, the quinoline methanols, quinidine and quinine, strongly increased the observed lipophilicity of Fe(III)PPIX in a pH dependent manner. Quinidine was found to effect the largest increase on Fe(III)PPIX partitioning into NLBDs which was proposed to be due to a previously established inherent increased lipophilicity of the quinidine-Fe(III)PPIX complex.

Neutral detergents have been used to mimic lipids to initiate β-haematin (synthetic haemozoin) formation in high-throughput screening. The speciation profile of Fe(III)PPIX in detergent solution was investigated using UV-vis spectroscopy and magnetic susceptibility measurements. The π-π dimer to μ-oxo dimer equilibrium constant, log *K*, was evaluated in different detergents so the percentage μ-oxo dimer could be predicted at any pH and Fe(III)PPIX concentration. The predominance of the π-π dimer species of Fe(III)PPIX in both neutral detergent monomeric and micellar solution at pH 4.80 was shown to correlate with the detergents ability to form β-haematin. Charged detergents, SDS and CTAB, that were found not to favor the π-π dimer, failed to promote β-haematin formation. ^{1}H NMR and Stern-Volmer quenching experiments of a hydrophobic NR fluorescence signal inside neutral detergent micelles by Fe(III)PPIX revealed interaction with the hydrophobic fatty acid moiety

of the detergent suggesting that it is buried within the micelle. Despite neutral detergents ability to stabilise the π-π dimer in acidic solution, measurement of the association constants of quinoline antimalarials and Fe(III)PPIX in detergent showed no change from the pre-established complexation between these drugs and the monomeric or μ-oxo dimer Fe(III)PPIX species in aqueous solution. Detergents were however, shown to decrease the surface tension of aqueous solution, facilitating the crystallisation process.

To investigate how closely these neutral detergents mimic lipids in haemozoin formation, a comparison between the reported kinetic profile of β-haematin formation at a lipid-aqueous interface and that obtained in the neutral detergent, NP-40, was conducted. The kinetics of NP-40 mediated β-haematin formation were found to conform to the Avrami model with n=1, exhibiting a half-life of 19 min to form a maximum yield of 56% at a markedly slower rate than in the lipid. Chloroquine and quinidine were found to decrease the rate of β-haematin formation in NP-40 in a reversible manner, to achieve a consistent yield of 52-55%. A crystal adsorption model based on the Langmuir isotherm was employed to explain the observed decrease in rate constant such that an adsorption equilibrium constant (log K_{ads}) for each drug was determined from the kinetic data. Quinidine was found to adsorb more strongly than chloroquine, in contrast to the previously reported findings in the lipid system, where a combination of drug adsorption and precipitation of a drug-Fe(III)PPIX complex was proposed to explain the decrease in yield at high drug concentration. In the absence of any evidence of precipitation of a drug-Fe(III)PPIX complex in NP-40 solution, the reversible adsorption of drug to the fastest growing face of the β-haematin crystal was proposed to be solely responsible for the observed decrease in rate constant. An independent measurement of this adsorption was provided by UV-vis spectroscopy of these drugs with preformed β-haematin, confirming that quinidine strongly adsorbs onto β-haematin in NP-40 solution. This work provides the first description of the aggregation state of Fe(III)PPIX and the first detailed kinetic investigation of β-haematin inhibition by antimalarials in neutral detergent solution. The ability of neutral detergents to promote β-haematin formation has been attractive for providing a fast cheap means of assaying haemozoin inhibition activity; however, a crucial finding is that there remain fundamental differences between the detergent system and the biological lipid environment that prevails inside the parasite digestive vacuole. When interpreting results from detergent-mediated high throughput screening assays cognisance of these differences is needed.

Publications and Conference Proceedings

Publications:

Parts of this thesis have been published in the following references

Chapter 4: Ferriprotoporphyrin IX (Fe(III)PPIX) partitioning into synthetic neutral lipid droplets

(1) A. N. Hoang, R. D. Sandlin, A. Omar, T. J. Egan, and D. W. Wright, *Biochemistry*, 2010, **49**, 10107–16.

Chapter 6: Preparation of β-haematin at the pentanol/aqueous interface

(2) Y. Corbett, S. Parapini, S. D'Alessandro, D. Scaccabarozzi, B. C. Rocha, T. J. Egan, A. Omar, L. Galastri, K. a Fitzgerald, D. T. Golenbock, D. Taramelli, and N. Basilico, *Microbes Infect.*, 2015, **17**, 184–194.

Conference Proceedings:

2011: 16–21st January, 40th Convention of the South African Chemical Institute(SACI), Johannesburg, South Africa. (**Won poster prize**)

Poster: "Investigating the role of neutral lipid droplets in haemozoin formation"

2011: 7–12th August, 15th International Conference on Biological Inorganic Chemistry, Vancouver, Canada.

Poster: "Understanding the role of lipids in haemozoin formation with detergent models"

2013: 22–26th July, 16th International Conference on Biological Inorganic Chemistry,

Grenoble, France.

Poster: "The effects of quinolone antimalarials on the kinetics of detergent-mediated

β-haematin formation".

2013: 10 October, Research Day, University of Cape Town, South Africa

Poster: "Investigating the role of lipids in haemozoin formation" (**Won poster prize**)

Acknowledgements

I would like to thank my supervisor **Professor Timothy John Egan** for teaching me how to ask the right questions and then go and find something, even if they were not the answers you were looking for.

Dr David Kuter- You are the Action Hero of Haem! And You've saved me from speciation disaster! Thank you, You will be a great Super-Visor one day.

The Haem Team (Past and Present): Thank you for the group meetings, the lab clean-ups and the chats: **Dr Kanyile Ncokazi**, **Dr Melvin Ambele** (Magic Chemistry), **Dr Tameryn Stringer**, **Jill**, **John O**, **Khwezi**, **Nikki**, **Roxanne O**, **Stefan**, **Fabrizio** and **Kathryn** and to my partners in crime: **John Woodland** and **Roxanne Mohunlul** – Try!- For everything else, there's Nitric acid!

Dr Katherine de Villiers and **Dr Johandie (Kaliefie) Gildenhuys** for helpful group meeting discussions, the drug-haem crystal structures, and the Kinetic Model.

Neil Ravenscroft – Thank you for the opportunity to learn from you – be it NMR or Coffee.

I am grateful to the following people for the part they played in helping me acquire and analyse data as well as teaching me several useful skills; **Professor DW Wright** and **The Wright lab** at Vanderbilt University for my sabbatical in high-throughput screening especially to **Kim** and **Becca** for teaching me to culture parasites. **Professor Jackson**, **Ahmed** and **Faten** for M.P, potentiometry and NMR help. **Pete Roberts** for NMR, **The Electron Microscopy Unit**, **Miranda** and **Mohammed** for helping me sort fact from fiction in fluorescence and TEM microscopy. **Susan** and **Dirk** at the **Confocal Microscope** at UCT Medical School. **Susanna Vasic** and **Helen Divey** at UCT Chemical Engineering for allowing me to use their Zetasizer and **Dr Belinda McFadzean** for kindly assisting me with the surface tension measurements.

To our Admin Magicians, **Deirdre**, **Saroja**, **Pauline**, **Leeta** and **Shenaaz**- Thank you for all your help over the years.

To **Arthur, Yaasien, Pieter**, **Monica**, **Sammy**, **Thabisa**, **Ma Adelaide**, **Carol**, **Kenneth**, **Goodman** and **Fred** for taking care of the basics without which there is no research.

To my Lunchtime Professors **Luigi Nassimbeni**, **Allen Rodgers**, **Susan Bourne**, **David Gammon**, **Neil Ravenscroft**, **Graham Jackson** and **Karin Badenhorst** -Thank You for expanding my education.

To all my friends especially **Ailyssa, Nicole, Zerene, Madoda, Runil, Anthea, Vaughan, Preshendren, Allenda, Wade, Nakeeta** and many others who have supported and encouraged me to complete this mission.

To my Family, **Laurell, Natasha, Rhoda, Khala, James and Jackli** and all the rest for the love, support and pride you have given me since I began my long career as a student.

To **Kyle**, I have too many things to thank you for, most of which involve your endless support and taking care of the big and little things without which I would never have got here.

A large final Thank You to the **NIH grant number R01AI083145** for all running expenses and scholarship support**, NRF grant number 79585** and the **University of Cape Town** for personal funding.

Glossary of Terms, Abbreviations and Definitions

Iron species

βH, (β-haematin) – synthetic haemozoin. Also called haematin anhydride, referring to the propionate linked dimer of reciprocal haematin molecules that are hydrogen bonded to adjacent dimers.

Fe(III)PPIX – Ferriprotoporphyrin IX referred to as ferrihaem, haem or haematin, where the axial ligand is either ^{-}OH/ H_2O

haem – prosthetic group composed of Fe (iron) and porphyrin ring. In this thesis, monomeric form of haem is **Fe(III)PPIX**, also referred to as **ferrihaem**

haematin – ferrihaem with and a fifth axial ligand, in this case $^{-}OH/H_2O$, porcine source.

haemin – ferrihaem with Cl^{-} axial ligand

Hb – Haemoglobin

Hz (haemozoin) – malaria pigment produced by blood-feeding parasites, microcrystalline form of reciprocal Fe(III)PPIX dimers linked by hydrogen bonds.

PPIX, protoporphyrin IX – a porphyrin consisting of a tetrapyrrole containing methyl, vinyl and propionic acid side chains

π-π dimer – co-facial association dimer of Fe(III)PPIX molecules

μ-oxo dimer – covalent dimer of Fe(III)PPIX with bridging oxide ligand.

μ-propionato dimer – 'haematin anyhydride' dimer with the propionate of one Fe(III)PPIX molecule coordinated to the Fe^{3+} metal centre of an opposite faced Fe(III)PPIX molecule which in turn is coordinated via its propionate group to that Fe^{3+} centre.

Lipid solutions

Ace:MeOH – acetone: methanol solution, 1:9 volume/ volume, lipid solvent

MSG – *rac*- 1- monostearoylglycerol

MPG – *rac*- 1-monopalmitoylglycerol

DOG – *rac*-1,3-dioleoylglycerol

DLG – *rac*-1,3-dilinoleoylglycerol

DPG – *rac*-1,3-dipalmitoylglycerol

NLB – Neutral Lipid Blend, biologically relevant mixture of acylglycerols (MSG: MPG: DOG: DLG: DPG) in mole ratio 4:2:1:1:1.

NLD/s – Neutral lipid droplet/s

SNLDs – synthetic neutral lipid droplets

SNLBDs – synthetic neutral lipid blend droplets

detergents

CHAPS – 3-[(3-Cholamidopropyl)dimethylammonio]-1-propanesulfonate

SDS – Sodium dodecyl sulfate

CTAB – hexadecyl-trimethyl-ammonium bromide

NP-40 – octylphenoxypolyethoxyethanol, Nonident P40

Tween 20 – Polyoxyethylene (20) sorbitan monolaurate

CMC – Critical micellar concentration, stable detergent aggregates in solution with defined properties

buffers

MES – (2-(*N*-morpholino)ethanesulfonic acid; buffer range pH 5.5 - 6.7)

HEPES – (4-(2-hydroxyethyl)-1-piperazineethanesulfonic acid; buffer range pH 6.6 – 8.0)

CHES – (2-(Cyclohexylamino)ethanesulfonic acid; buffer range pH 8.5 – 10.00)

parasite terminology

DV – Digestive/ food vacuole of parasite

P*f* – *Plasmodium falciparum,* malaria parasite of the genus *Plasmodium*

Pv – *Plasmodium vivax*, species of the genus, *Plasmodium* (malaria parasite)

trophs – trophozoites, metabolically active developmental stage of parasite life-cycle

VAR – Vacuolar accumulation ratio of drug concentrations inside and outside digestive vacuole ($log\ D_{pH5.2}$ / $log\ D_{pH7.4}$)

Antimalarial drugs

AQ – Amodiaquine, 4-[(7-chloroquinolin-4-yl)amino]-2-[(diethylamino)methyl]phenol

ART – Artemisinin

CQ – Chloroquine, (*RS*)-*N'*-(7-chloroquinolin-4-yl)-*N*,*N*-diethyl-pentane-1,4-diamine

DHA – Dihydroartemisinin

eQD – 9-Epiquinidine, (8R,9R)-6'-Methoxycinchonan-9-ol, quinidine enantiomer

eQN – 9-Epiquinine, (8S,9S)-6'-Methoxycinchonan-9-ol, quinine enantiomer

Hf – Halofantrine

IC_{50} – 50% inhibitory concentration

MF – Mefloquine

PYR – Pyrimethamine

QD – (8R,9S)-Quinidine, (1S)-[(2R,4S,5R)-5-ethenyl-1-azabicyclo[2.2.2]octan-2-yl]-(6-methoxyquinolin-4-yl)methanol

QN – (8S,9R)-Quinine, (1R)-[(2S,4S,5R)-5-ethenyl-1-azabicyclo[2.2.2]octan-2-yl]-(6-methoxyquinolin-4-yl)methanol

SP – Sulphadoxine

General

% – Percentage

Ace – Acetone

AFM – Atomic force microscopy

CBSO – citric acid buffer saturated octanol

CSD – Cambridge Structural Database

cryo-TEM – cryogenic transmission electron microscopy

cryo-XT – cryogenic soft X-ray tomography

DMF – N, N-dimethylformamide,$(CH_3)_2NCHO$, solvent, 99.8% assay grade, Sigma Aldrich®

Em – Emission

ES – Excited state

Ex – Excitation

F – Fluorophore in its ground state

F* – Excited state fluorophore

FQ – Ground state fluorophore-quencher complex

F*Q – Excited state fluorophore complexed with quencher

Fl. Int. – Fluorescence intensity, measured in arbitrary units (arb. units) based on PMT (photo-multiplier tube) voltage setting

GS – Ground state

HDP – haem detoxification protein

HOMO – Highest occupied molecular orbital

HPLC – High performance liquid chromatography

HRP II, III – Histidine-rich proteins II and III

IFE – Inner Filter Effect

IR – Infrared

k_q – Bimolecular quenching constant, obtained for Stern Volmer collisonal quenching

K_p – partition constant between two non-miscible phases

K_{SV} – Stern-Volmer quenching constant, product of $k_q.\tau$

LCAO – Linear combination of atomic orbitals

log D_{ow} – logarithm of distribution coeffiecient in octanol and aqueous solution

log P_{ow} – logarithm of partition coefficient of unionised form between octanol and aqueous solution

LUMO – Lowest unoccupied molecular orbital

Maldi-Tof – Matrix-assisted laser desorption ionisation time of flight mass spectrometry

max – Maximum

MD – Molecular dynamics (*in silico* simulation techniques)

MeOH – Methanol

min – Minimum

M_L – Angular momentum quantum number

MO – Molecular orbital

NMR – Nuclear magnetic Resonance

NR – Nile red fluorescent dye, (9-diethylamino-5H-benzo[α]phenoxazine-5-one)

Oct – Octanol

pD – pH of a deuterated sample

PIFE – Primary Inner Filter Effect

pK_a – log of an ionisation constant usually acid dissociation

Q – Quencher

SAMs – Self-assembled functionalized alkanethiol monolayers

SIFE – Secondary Inner Filter Effect

SV – Stern- Volmer (fluorescence quenching)

τ – Fluorescence lifetime of a fluorophore

T_m – gel-to-fluid transition temperature of lipids

TICT – Twisted intramolecular charge transfer

TLC – Thin Layer Chromatography

μ – Average magnetic moment

UV-vis – Ultraviolet/visible

WHO – World health organization

Table of Contents

Chapter 1: Introduction and Literature Review

(1.1) The global burden of malaria

Arguably, the most devastating infectious disease in history, malaria is thought to be responsible for exacting the largest toll on human and economic resources around the world since it was first recorded in 1600.[1] In fact, the true burden of this disease will never be properly quantified as infection may occur asymptomatically and often cases are not reported in rural settings. Today, malaria is incident in ninety-seven countries encompassing six WHO geographical regions, placing an estimated 3.2 billion people at risk of infection (Fig.1.1).[2] The bulk of this infection occurs in developing regions, particularly Africa, where approximately 90% of all malaria fatalities occurred in 2013.[2] This prevalence in mainly Sub-Saharan Africa is compounded by the tropical climates, scarce resources and poor health infrastructure.[3]

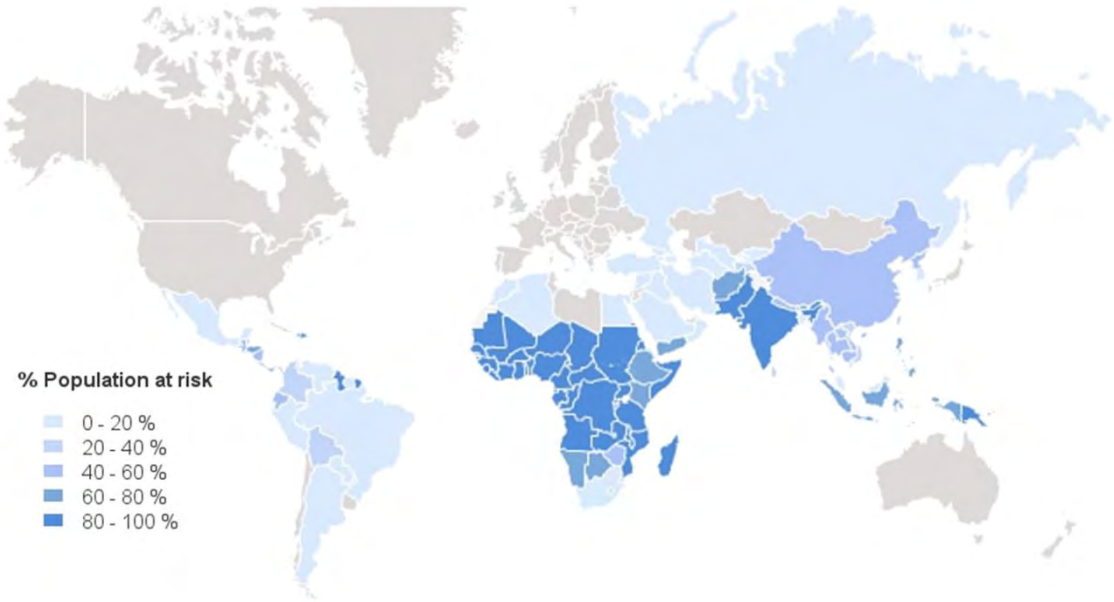

Figure 1.1. Global percentage of population risk for malaria infection shown by blue shading, the grey areas represent regions of no risk as reported by world malaria report 2013. Map created using the Global Malaria Mapper (©Medicines for Malaria initiative).[4]

Malaria features as number six of the Millennium Development Goals, which aimed to halt the spread and lower the incidence of this disease by 2015. To achieve this aim, great strides have been made by the eradication campaign in distribution and use of bed nets, increased global funding for existing treatments and the development of novel drugs, successfully reporting that the number of deaths decreased by forty-seven percent worldwide in 2013.[2] Malaria control follows an integrated strategy of "universal coverage", applying the prevention and treatment techniques that are central to the "Roll back Malaria" initiative.[3] However, despite these efforts, malaria incidence is still endemic and the complications of treating children under the age of five, pregnant women and patients with HIV and other infectious diseases like tuberculosis and Ebola, severely hamper any progress toward relieving the burden of this disease, especially on the African continent.[5] Added to this, resistance to current antimalarial therapies, poses a great challenge to achieving malaria eradication.[6] In the fight against this global issue, an understanding and study of the agent of this disease has made a substantial impact toward eliminating malaria.

(1.2) The malaria parasite

Malaria is transmitted through the saliva of the infected female *Anopheles* mosquito, carrying a protozoan parasite of the genus, *Plasmodium*. Five species have been reported to affect humans; *P. malariae*, *P.ovale* and *P. knowlesi* occur with low incidence and fatality rates. While, *P. vivax (Pv)* and *P. falciparum (Pf)* are the most prevalent, with the latter being responsible for the majority of malaria associated deaths.[1,7] The life cycle of the malaria parasite consists of two distinct parts, each occurring in the mosquito vector and human host, offering a complicated sequence of parasite stages that have proven difficult to target at once, this is illustrated in Fig. 1.2.[8] The cycle begins as a mosquito (primary host) feeds on infected blood from a secondary human host, ingesting parasite gametocytes that travel to the midgut of a carrier mosquito.[9] Thereafter undergoing sexual reproduction to form male and female gametes that fuse and undergo several stages of maturation to form complete oocysts that rupture releasing sporozoites into the salivary glands in a process called the sporogonic cycle. The unaffected mosquito vector then transmits the infection to another human host where the parasites are circulated in the bloodstream until they reach the liver to infect a hepatocyte commencing the liver stage of their life-cycle.[10] At this stage, the liver schizonts can either lie dormant (in *P.malariae* and *P. vivax*) in a period associated with

asymptomatic malaria or after 4-5 days of growth and multiplication, the schizont can burst to release merozoites that invade the red blood cells (RBCs) to begin the metabolically active, blood stage.

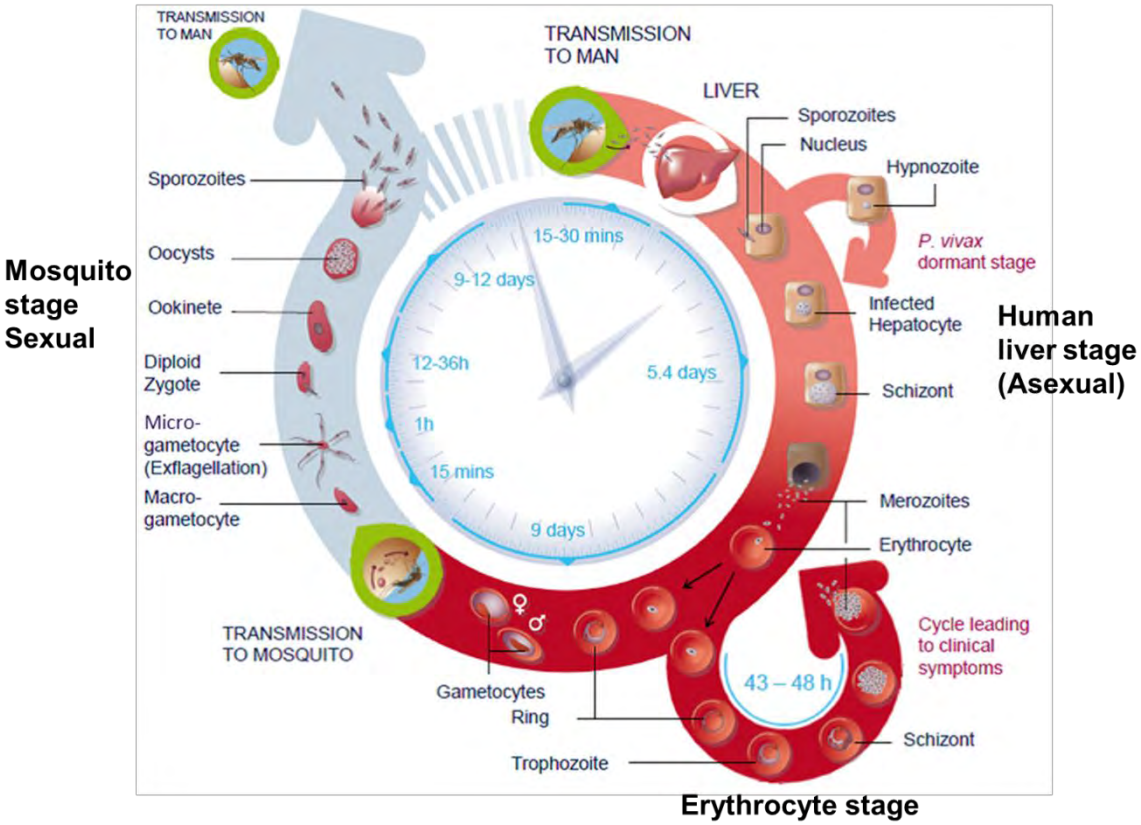

Figure 1.2 The life cycle of the malaria parasite encompassing the mosquito stage to human transmission followed by the human liver and blood cell stages with illustrated corresponding time periods. Reproduced and edited from Delves et al., (2012) in open access journal, Plos one.[8]

The blood stage of the malaria parasite's life cycle consists of asexual reproduction of the merozoites and involves ingestion of the host's erythrocyte haemoglobin (Hb) as a source of amino acids. The development starts with formation of a ring that grows rapidly to develop the pre-digestive food compartments that fuse to form the digestive vacuole (DV) in the trophozoite (troph) , eventually maturing into a schizont again, before rupturing to release an increased number of merozoites to continue the blood stage infecting a new RBC.[11] The released parasites and debris stimulate host production of pro-inflammatory cytokines, interleukins I and 6 (IL-1, IL-6) and tumor necrosis factor α (TNF-α) in an innate immune

response triggering the onset of the pathogenic symptoms of the disease.[12,13] This release of a new batch of merozoites every 48 h is responsible for the fevers, chills, nausea and body-aches that are symptomatic of *P. falciparum* and *P.vivax* infection.[1] Several merozoites continue to mature into gametocytes in the blood stream ensuring the passage into another mosquito vector upon feeding to complete the entire life-cycle. Several parasites evade human immune responses by entering host cells, amongst them, the malaria parasite is among the most successful, as the bulk of its life-cycle is spent in the human RBC.[14] It is during this erythrocyte stage that the parasite is most virulent, ingesting and degrading between 60-80% of the host's RBC Hb. This process occurs from the ring to the troph stage inside the acidic DV, in a mechanism that is thought to provide a food source from the breakdown of the protein, globin, into amino acids as well as to make space for the growing parasite.[15–17]

(1.3) Haemoglobin degradation pathway

The ingestion, catabolism and fate of Hb in the malaria parasite is referred to as the Hb degradation pathway and is the primary target of past and present antimalarial drugs.[18] Illustrated by the schematic in figure 1.3, the various processes to achieve the final product are discussed throughout section 1.3.

(1.3.1) Haemoglobin catabolism

Briefly, the pathway is initiated by invagination of the parasitic plasma membrane to form transport vesicles (TV) that transfer Hb from the host RBC to the interior of the DV of the parasite. Process (A) of Fig.1.3 then commences, Hb is quickly cleaved proteolytically into iron (II) protoporphyrin IX (Fe(II)PPIX) or 'haem' and globin, the protein component which is broken down by a series of aspartic (plasmepsins I, II, IV and histoaspartic protease) and cystic proteases (falcipains 1, 2 and 3) as well as being digested into smaller fragments by the zinc metalloprotease (falcilysin) and dipeptidylaminopeptidase (PfDPAP1).[19–22] The resultant peptides are transported out of the DV where they undergo further cleavage to afford the amino acids that serve as a nutrient source for parasite protein synthesis elsewhere in the cell.[23,24] The four Fe(II)PPIX units that are released upon Hb degradation are

rapidly auto-oxidised by to the ferric form of iron protoporphyrin IX, Fe(III)PPIX or what is called, haematin (Fig. 1.4).[25]

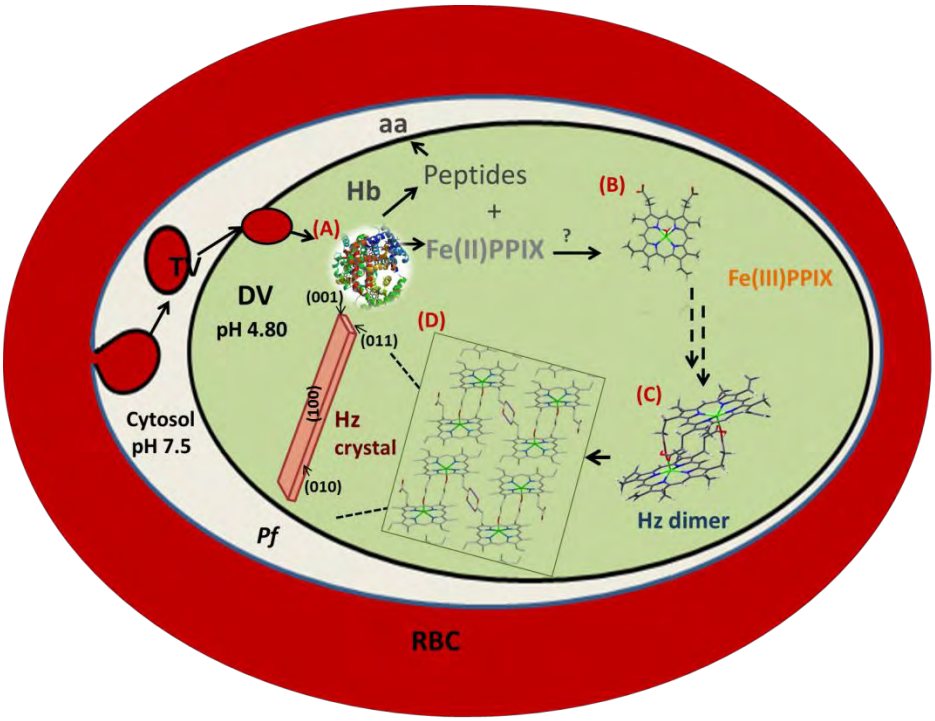

Figure 1.3. Schematic representation of the Hb degradation pathway in an infected RBC. Process **(A)** is the proteolytic digestion of Hb to peptides (that are further broken down outside the DV) and Fe(II)PPIX which is oxidised to yield, **(B)** Fe(III)PPIX. Free Fe(III)PPIX is converted to a unit of reciprocal cyclic dimers **(C)** in a unknown mechanism that involves the formation of an Fe-carboxylate linkage between Fe(III)PPIX molecules, which are further hydrogen bonded to each other to form a Hz crystal **(D)**. The crystal morphology is illustrated with each face annotated. **Hb** image from RCSB PDB (www.rcsb.org) PDB ID 1GZX, reprinted from Paoli et al.[26–29]

Fe(III)PPIX (product B in Fig. 1.3) is a five co-ordinate protoporphyrin molecule consisting of a tetrapyrrole macrocycle with two vinyl and four methyl as well as two propionic acid group side chains attached to a Fe(III) metal centre and an axial ligand, that is pH dependent being either hydroxide ($^{-}$OH) or water (H_2O).[30] The pH of this acidic digestive compartment has been measured and reported to vary between pH 4.5 - 5.5 from fluorescence probe experiments, however, Haywood et al. have recently reported an estimate of pH 4.8 -5.2 in early trophs.[31,32] The accumulation of Fe(III)PPIX or Fe(III)PPIX-drug adducts in the parasite

DV has been correlated with the development of oxidative reactive species which have been shown to cause the lipid peroxidation that is thought to be responsible for parasite death.[33–35] It is capable of disrupting parasite homeostasis by competitively binding key enzymes such as those involved in Hb degradation or catalysing the formation of small peptide fragments from proteins.[36,37] It has also been shown free Fe(III)PPIX has a role in parasite metabolism where addition of free Fe(III)PPIX was observed to cause an initial decrease in the activity of PfGAPDH (regulatory enzyme in glycolytic pathway).[38] PfGAPDH is implicated in other essential parasite processes for example nuclear RNA transport, DNA replication and membrane fusion, rendering the parasite vulnerable to a build-up of free Fe(III)PPIX.[39]

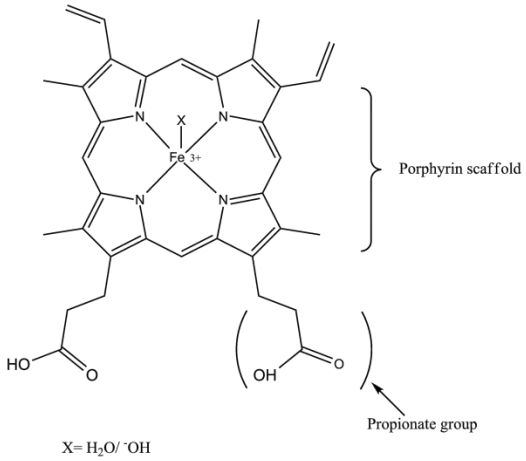

Figure 1.4 Structure of Fe(III)PPIX with the porphyrin scaffold and propionate side chains highlighted. The pH dependent axial ligand, X is H_2O at the prevailing pH of the acidic digestive vacuole.

More destructive, is the oxidative stress effects upon the release of free Fe(III) which is capable of interaction with parasite glutathione (GSH) causing lipid peroxidation through what is believed to be an intercalation mechanism due to its lipophilic nature.[34,36] To circumvent this, the parasite employs a Fe(III)PPIX detoxification mechanism that sequesters the potentially harmful Fe(III)PPIX as an inert bio-crystal called haemozoin (Hz) (process C and product D in Fig. 1.3).[40] By contrast, in mammals, Fe(III)PPIX is catabolised by the microsomal heme oxygenase enzyme, a key point of difference that makes this haem detoxification a unique parasite specific drug target.[41] The drugs used to target this pathway and inhibit Hz formation will be discussed later on.

(1.3.2) Haemozoin

(1.3.2.1) Evolution of the understanding of haemozoin

The process of Hz formation is not well understood. Since its first discovery in the eighteenth century, prior to identification of the disease, the exact mechanism of formation of these crystals appearing as a black pigment (malaria pigment) remains to be elucidated. From the nineteenth century until 1911, it was thought that this discolouration, found in the liver and brain of malaria victims, was the skin pigment, melanin, however, Carbone and Brown independently proved that the substance was in fact composed of haem or Fe(III)PPIX (Fig. 1.4).[42,43] A time-line of each discovery that contributed to the current understanding of Hz is summarised in Fig. 1.5. For many years, the exact nature of this pigment was misunderstood encumbering investigations into its chemical structure, however, in 1991, Slater and colleagues found that a synthetic form of a microcrystalline Fe(III)PPIX called β-haematin (βH) was identical in nature and composition to isolated *P. falciparum* Hz.[42] This confirmed a study from a few years before by Fitch and Kanjananggulpan which had shown Hz from malaria parasites to be composed only of Fe(III)PPIX.[30]

Using UV-visible (UV-vis) absorbance and infrared (IR) spectroscopy and X-ray techniques, including extended x-ray absorption fine structure (EXAFS) spectroscopy and powder diffraction, the authors were able to demonstrate unequivocally that their synthetic haematin derivative, β-haematin (βH) was chemically the same as the biological extracts. They proposed that βH was formed by the formation of a Fe–O bond between the oxygen of a propionate group of one Fe(III)PPIX to the Fe(III) centre of an adjacent Fe(III)PPIX molecule allowing polymerisation to form the crystal.[44] By comparison of IR spectra of the Fe(III)PPIX starting material and those of Hz and βH, the diagnostic stretching frequencies of the coordinated C=O and the C–O bonds were first identified. The belief that this insoluble form of Fe(III)PPIX was an anhydride polymer was widely held during this time and propagated until the structure was elucidated.

(1.3.2.2) Structure and crystal morphology of synthetic haemozoin, β-haematin

In 1997 Bohle and colleagues, obtained the X-ray powder diffraction (PXRD) pattern of both Hz isolated from late troph extracts and βH.[45] They correctly identified the centrosymmetric

space group corresponding to the triclinic unit cell P-1, leading to a proposed structure composed of antiparallel polymer chains. However, in 2000, the same group elucidated the structure of βH by Rietveld refinement, dispelling the polymer theory and showing that the asymmetric unit was composed of reciprocal cyclic dimers of Fe(III)PPIX in which the propionate group of one porphyrin was coordinated to the Fe(III) centre of the adjacent porphyrin.[27]

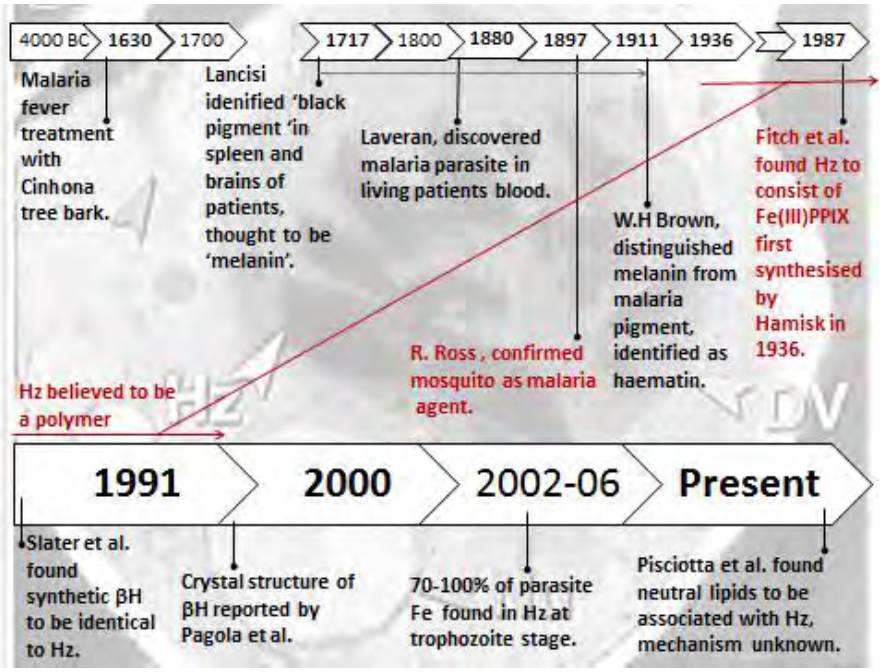

Figure 1.5 A timeline of the impactful discoveries in the history of haemozoin (Hz) investigations. The background picture depicts a TEM of Hz crystals seen in the DV of an infected RBC was reproduced with permission from figure 2, in S. Kapishnikov et al., PNAS, (2012) ©The National Academy of Sciences, USA.[46]

The dimers were hydrogen bonded to each other via the other propionic acid group of each porphyrin to form the crystal structure pictured in Fig. 1.6. Subsequently, since, this first report of the crystal structure, many studies have been conducted toward understanding the mechanism of its formation both *in vitro* and *in vivo,* all contributing to the bulk of available knowledge on this pigment today. Spectroscopic studies have shown that Hz triclinic crystals are entirely composed of five-coordinate Fe(III)PPIX of high-spin state, $S = {}^{5}/_{2,}$ and is isostructural to its synthetic counterpart, βH. [47–49]

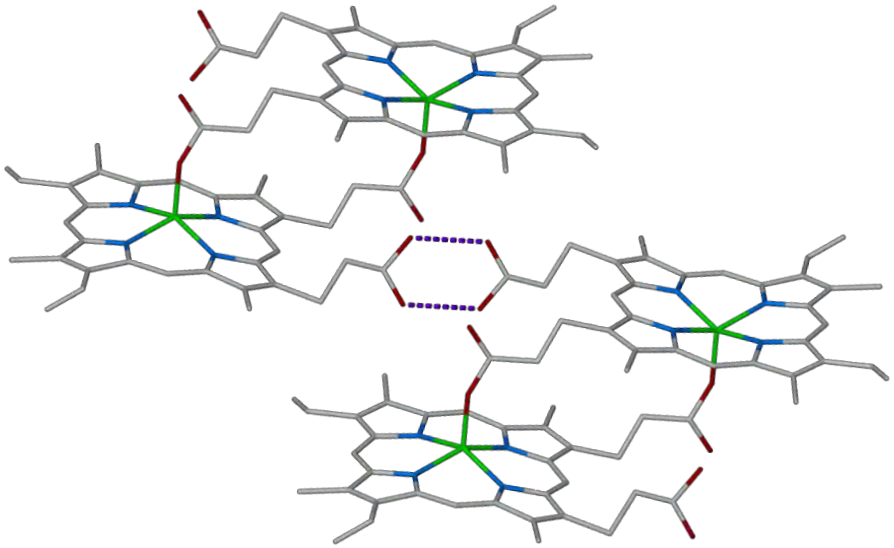

Figure 1.6 Molecular structure of Hz or βH. The Fe(III)PPIX dimeric unit with Fe–O bond between the Fe(III) centre of one Fe(III)PPIX molecule coordinated to the O–C=O (propionate) group of another Fe(III)PPIX molecule in a reciprocal fashion, this dimer is hydrogen bonded to another dimer via an O---OH interaction of the second propionic acid group to form the crystal packing observed for βH.[50]

Exploiting the published structure of βH, Buller et al. investigated the theoretical growth form of the crystal and its isostructural natural counterpart, Hz.[28] The Hartman-Perdok theory that the slowest growing faces are expressed in the crystal morphology which is dependent on the layer energy released when a new layer is formed, E_1 and the inverse of the energies of attachment per molecule when a new layer is deposited onto the crystal surface, E_{att}, was employed to explain the observed crystal face expression.[51] Computed values for E_{att} and E_1 allowed for the proposed needle-like crystal morphology along the c-axis with dominant (100) and (010) faces expressed as well as the less developed (011) and minor 001 faces. The authors compared this theoretical morphology to isolated Hz crystals from different species which matched their model closely; this is illustrated in Fig. 1.7. The (001) face which is not expressed as a major face in the crystal habit was proposed to be the fastest growing face of βH, characterised by its highly negative attachment energy and corrugated surface.[28]

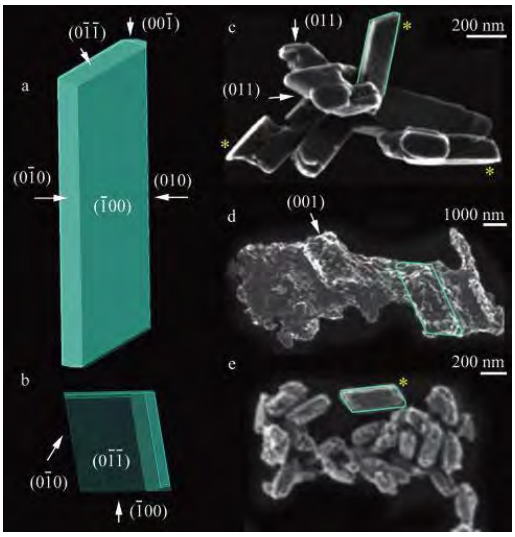

Figure 1.7 (a-b) Theoretical βH crystal morphology viewed along the a and c axis with the miller indices of the expressed faces indicated. **(c-e)** Superimposed images of theoretical morphology with SEM micrographs of Hz crystals isolated from P. *falciparum* and other blood-feeding organisms, S. *mansoni* and H. *columbiae*, respectively, indicating similar crystal habit. Image reproduced with permission from Buller et al., (2002), ©American Chemical Society.[28]

(1.3.2.3) Stereoisomers of β-haematin

It was later proposed that four stereoisomers of βH are theoretically possible in solution, based on the enantio-facial symmetry of Fe(III)PPIX that results in four different possible occupational arrangements of the vinyl groups on the periphery of the porphyrin ring. [52] The authors claimed that the original structure was reported to only contain the designated centrosymmetric isomer, *cd*$\bar{1}_1$. [27,52] Another centrosymmetric isomer, *cd*$\bar{1}_2$ and two chiral structures, *cd2(+)* and *cd2(-)* were proposed to exist (Fig. 1.8). Initially, only the centrosymmetric units were thought to be incorporated into the growing βH crystal in large amounts, forming two distinct major and minor phases, as the presence of the chiral structures were shown to retard crystal growth in a capping mechanism that was suggested to account for the microcrystalline size of βH crystals. Later studies by the same group, using powder X-ray diffraction (PXRD) techniques and computational density functional theory (DFT) modelling, showed the powder diffraction data was consistent with two occupancy models, the major phase consisted of a mixture of the achiral isomer, *cd*$\bar{1}_1$ and the chiral isomer, *cd2(+*) with a 50:50 occupancy.[53] A minor phase consisting of *cd*$\bar{1}_1$ with

small amounts of each chiral isomer was also proposed and it was suggested that the crystal consisted of all four phases, *cd*$\bar{1}_1$, *cd2(+)* *cd*$\bar{1}_2$, and *cd2(-)* with occupancies of 58:17:17:8.[53]

The initial proposal was met with a degree of skeptism from Bohle et al., where the authors re-examined the PXRD patterns of other βH data sets in an attempt to resolve the presence of three extra *Bragg* reflections noted by Strassø et al. [52,54] The authors stated that although the observed vinyl disorder is consistent with the presence of the chiral isomers, the available PXRD data alone is insufficient to distinguish a biphasic model from a situation where the interference of these isomers is tolerated and merely manifests as vinyl disorder.[54] This issue remains unresolved.

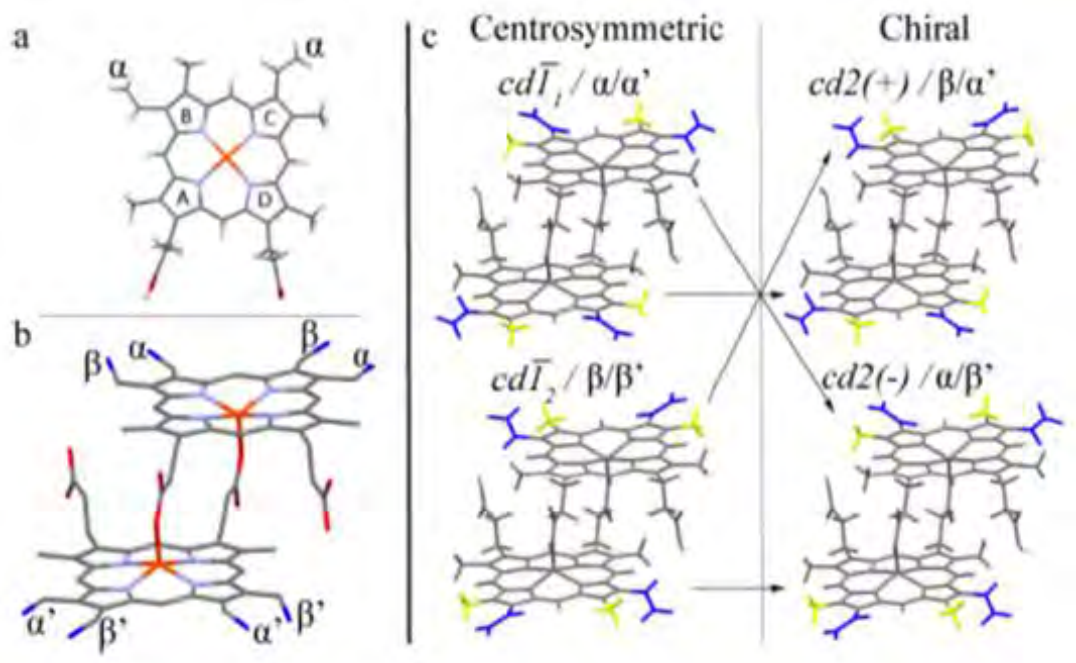

Figure 1.8: Molecular structure of **(a)** Fe(III)PPIX to indicate the α, positions of the vinyl groups with all the possible positions in a βH dimer are shown in **(b)**. **(c)** The four stereoisomers of βH, differing in the vinyl group positions, as indicated, are categorised according to their symmetry, the two centrosymmetric cyclic dimers, *cd*$\bar{1}_1$, and *cd*$\bar{1}_2$ and the chiral dimers, *cd2(+)* and *cd2(-)* with pseudo-2-fold symmetry. Image is reproduced with permission from Strassø et al. (2014)© American Chemical Society.[53]

(1.3.2.4) Single crystal X-ray diffraction of β-haematin

Despite there being several reports of its synthesis using a variety of reproducible methods and the structure having been reported from solving the PXRD pattern in 2000, the formation of a robust βH crystals large enough for a single crystal X-ray diffraction collection has proved elusive.[27] In an attempt to further understand βH formation and crystal composition, Klonis et al. reported a reanalysis of the crystal structure data for βH and compared it with synchrotron PXRD data of Hz crystals isolated from *P.falciparum.*[55] Although analysed differently, the original structure of βH was confirmed with Hz and found to be similar in structure, albeit with a greater amount of disorder in the Fe(III)–O bond. This was rationalised by the resultant homogeneity of the synthesised βH compared with the natural product, Hz and an earlier observation of Walczak and co-workers where they used EXAFS to examine the iron environment in βH and Hz, showing that differences in the Fe(III)–O bond length in Hz compared to βH results in a variable occupancy of the axial oxygen atom.[56] Klonis et al. also controversially proposed that crystal nucleation is initiated by formation of non-covalent π-π type dimers of Fe(III)PPIX that align (with their axial ligands directed outward) in columns via P-type anti-parallel polymer interactions, which are stabilised by and coordinated to adjacent columns via interaction with the μ-propionato dimer (μ-Pr).[56] This was in contrast with the prevailing theory that the βH crystal was formed from cyclic μ-propionato dimers linked via π-π interactions and hydrogen bonds.[57] The structures of these proposed units and this suggested mode of crystal initiation are pictured in Fig. 1.9. These structures of Fe(III)PPIX will be discussed in detail over the following pages.

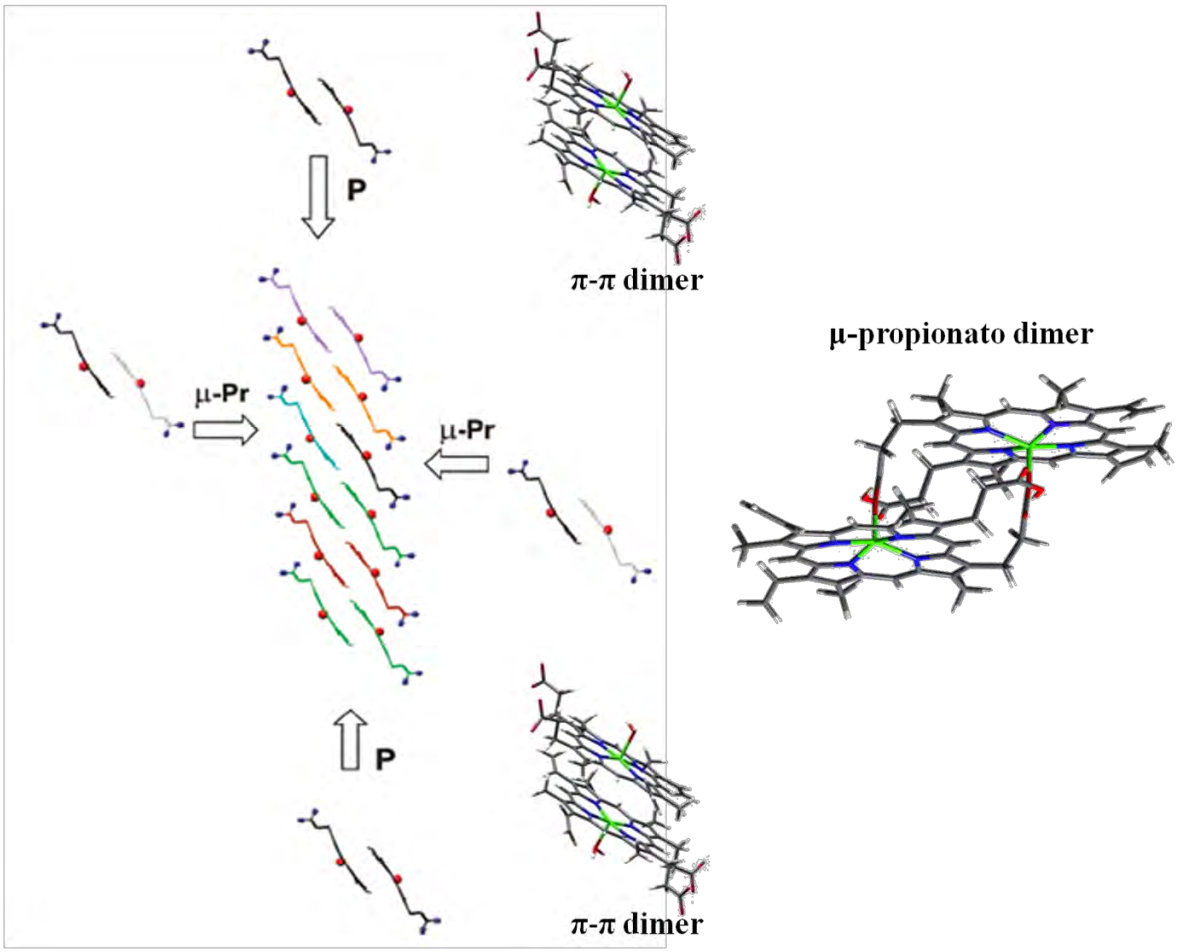

Figure 1.9 The proposed model of Hz formation from the μ-propionato (μ-Pr) and π- π dimers of Fe(III)PPIX via P-type interactions. The π- π dimer columns are proposed to extend into 2D sheets via μ-propionato linkages. Molecular structures of these dimers are provided to show their structure, with the axial ligands of the π- π dimer being either aqua or $^{-}$OH in aqueous (aq) solution. Figure reproduced and adapted with permission from Klonis et al., (2010)© American Chemical Society.[55]

Hz has been shown to be morphologically different but structurally and chemically identical to a pigment isolated from other blood-feeding organisms, *Schistosoma mansoni* and *Rhodinus Prolixus*.[58] The structure of Hz isolated from these species using synchrotron radiation PXRD was shown to match that of the reported structure of βH with the characteristic Fe(III)PPIX dimers linked via reciprocal Fe-carboxylate bonds, identified.

The structure of an Fe(III)mesoporphyrin IX compound, called mesohaematin anhydride which contained ethyl groups in the usual vinyl group positions of the protoporphyrin, was shown to be isostructural to βH, forming propionate linked cyclic dimers (μ-Pr dimers) which were hydrogen bonded to DMSO (dimethyl sulfoxide) solvent molecules instead of each

other as in the case of haematin anhydride.[56,59] However, the similarity between this analogue and βH was found to be greater than that for Fe(III)PPIX and βH using EXAFS, leading the authors to conclude that the haematin anhydride consisted of μ-propionato dimers and not haematin monomers.[60]

Bohle and colleagues recently proposed that Ga(III)PPIX was a good model of Fe(III)PPIX due to their similarity in charge, coordination number preferences and ionic radii.[61,62] They successfully obtained a single crystal structure of this Gallium analogue of βH, which was characterised by the propionate bridged dimeric Ga(III)PPIX units, however, these were linked through intradimer hydrogen bonding of free propionic acid groups and the central metal, Ga(III) in this case was found to be six co-ordinate, with a pyridine ligand bound *trans* to the coordinated propionate.[62] Nevertheless, this single crystal structure provided several insights into the crystal state of such molecules providing information that is lost in PXRD refinement.

Recently, a closer analogue was fortuitously obtained when the first single crystal structure of a βH DMSO solvate was reported.[63] The single crystal was grown in the presence of free base chloroquine (CQ), which the authors rationalised to have acted like the base, 2,6-lutidine, originally used to crystallise βH in the first report of its structure. [63,64] The repeating centrosymmetric unit matched that of a proposed μ-propionato dimer consisting of two pentacordinate iron (III) porphyrins shifted laterally in the plane so that the two porphyrins are orientated with the opposite faces aligned parallel to each other and linked via a reciprocal propionate oxygen-Fe bond (Fig. 1.10).[55] The crystal data used to solve the structure of the repeating unit and the external crystal morphology also matched that of the reported structures for Hz and βH solved by PXRD, however, a difference in crystal packing was observed.[27,55] The presence of three DMSO solvent molecules with one hydrogen bonded to the free propionate group of both Fe(III)PPIX molecules was suggested to confer a significant amount of lateral overlap of the porphyrin cores.[63]

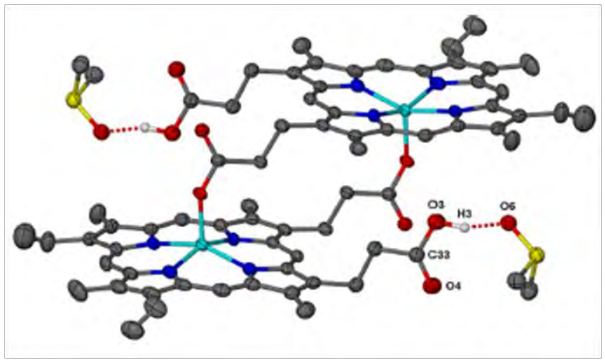

Figure 1.10 The μ-propionato dimer reported by Gildenhuys et al. as the symmetrical repeating unit of β-haematin grown as a DMSO solvate. The hydrogen bonds between the DMSO solvent and a free propionic acid group on both porphyrin rings are indicated by a dashed red line. Non-relevant solvent molecules and hydrogens were omitted for clarity with the ellipsoids drawn at 50% probability for each atom. Image was reprinted with permission from Gildenhuys et al. (2013), © American Chemical Society [63]

(1.3.3) State of Fe(III)PPIX in solution

In order to understand the process of crystal formation, several studies on the Fe(III)PPIX starting material have been performed.[65–69] Fe(III)PPIX behaviour in solution has been studied in great detail, however, the presence of a variety of species and aggregation states have complicated the evolution of the understanding this molecule and its interactions.[70–72] Fe(III)PPIX has a vast and complicated speciation in different solutions.[73] The existence of several different aggregation states reported in the earlier literature led to many contrasting accounts of this speciation in solution. [74–80] The UV-vis changes in the absorbance spectrum upon dimerisation were often analysed and characterised as polymerisation, coupled to this, the low solubility of Fe(III)PPIX in aq solution at certain pH values, initially hampered investigation into its speciation at low pH.[81,82] Two landmark studies by Brown and colleagues, suggested that Fe(III)PPIX existed as a dimeric species in alkaline pH solution characterised by marked changes in the most intense band in the UV-vis spectrum, that were inconsistent with Beers' law behaviour.[76] The dimerisation of monomeric Fe(III)PPIX, *M*, to form the dimer, *D*, was found to fit a simple linearised equilibrium describing the dimerisation constant, *K*, and number of protons exchanged in the process, *n* (Eqn. 1.1.1 - 1.1.3). Where K_{obs} is the pH dependent dimerisation constant at a particular H^+ concentration.

$$2M \overset{K}{\Leftrightarrow} D + n[H^+] \quad (1.1.1)$$

$$K = \frac{[D][H^+]^n}{[M]^2} \quad (1.1.2)$$

$$\log K_{obs} = \log K + n[H^+] \quad (1.1.3)$$

Analysis of the extinction coefficients of each species allowed for the calculation of log K_{obs} and *n,* which was reported to be one for both the monomer and dimer species enabling the calculation of a pK_a (dimer) as 7.5.[76] A structural model of this dimer was proposed through identification of a characteristic Fe-O-Fe stretching frequency at 900 cm^{-1} in the IR spectrum of a solid sample precipitated from DMSO in the presence of NaOH, which was shown to be a μ-oxo bridged Fe(III) dimer characterised by an oxide ligand coordinated to the Fe(III) centres of both Fe(III)PPIX molecules (Fig. 1.11). [83] The structure proposed was thought to consist of two antiferromagnetically coupled Fe(III) centres which deviated 0.5 Angstroms (Å) out of the porphyrin plane toward the oxide ligand, a Fe-O bond length of 1.8 Å and a Fe-O-Fe bond angle that was found to be between 165-180°, based on previously reported crystal structures of other metalloporphyrins.[74,84–86]

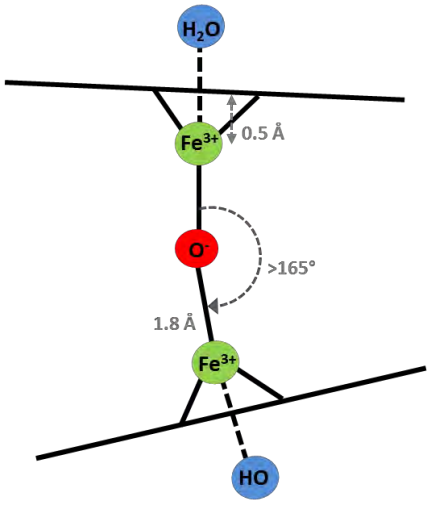

Figure 1.11 Early molecular model of the μ-oxo dimer form of Fe(III)PPIX as proposed by Brown et al. The angles and bond lengths were subsequently supported by X-ray crystal structure of the dimethyl ester derivative, however, the sixth coordinated H_2O or ^-OH ligand is not present in the structure.[76,87]

However, the published structure of μ-oxo-bis[(protoporphyrin IX dimethyl ester)iron(III)], a close analogue of Fe(III)PPIX, was subsequently shown to be five co-ordinate lacking the sixth water or hydroxide ligand proposed.[87] A later study to probe the magnetic and spectroscopic properties of the Fe-O-Fe linkage by O'Keefe et al., confirmed the existence of these antiferromagnetically coupled μ-oxo dimers by temperature dependent magnetic susceptibility measurements, however, they were not found to form spontaneously in aq solution and instead required the presence of a weak organic base (10% pyridine) in solution.[88] Despite this observation, and several reports of different types of aggregation states for Fe(III) and other metalloporphyrins in the literature, the belief that the μ-oxo dimer species was the predominant form of Fe(III)PPIX in solution persisted.[74,89–93] It was not until recently, in 2007, that de Villiers et al. showed conclusively through UV-vis spectroscopy and magnetic susceptibility measurements, that the dominant species of Fe(III)PPIX in aq solution was in fact a non-covalently associated π-π dimer. [66] This species was characterised by two Fe(III) porphyrins linked through π-stacking with their axial ligands facing outward from each other (pictured in Fig. 1.9). [66] The key distinguishable differences between these two dimeric forms of Fe(III)PPIX were the magnetic coupling of the antiferromagnetic μ-oxo dimer species yielding a magnetic moment, μ, of about 2.0 μ_B and the diagnostic absorption bands present in the charge-transfer (CT) region of the UV-vis spectrum between 550-650 nm for the μ-oxo dimer initially highlighted by O'Keefe and colleagues. [66,88] These were found to absent in the π-π dimer spectrum, with an observed μ of 4.6 μ_B, corresponding to an ad-mixed spin state, S= $^3/_2$, $^5/_2$. [66]

Subsequently, a comprehensive study by Asher et al. characterised the solvent effects on Fe(III)PPIX speciation.[72] The speciation of Fe(III)PPIX was investigated in mixed aqueous solutions (high and low salt) over a pH range and in the presence of a variety of aprotic (eg. DMSO) and protic (eg. methanol) solvents using UV-vis and ^{1}H NMR spectroscopy, magnetic susceptibility and diffusion measurements. The authors showed that water and polar protic solvent solutions, as measured by their Dimroth-Reichardt hydrophobicity parameter, $E_T(30)$, > 48.4 kcal.mol^{-1}, were found to induce the π-π dimer form of Fe(III)PPIX.[72] On the other hand, at low to neutral pH, in aprotic solvent mixtures, the monomeric species of Fe(III)PPIX was prevalent. However, as the pH of the solution was increased, the μ-oxo dimer species was favoured in mixed aq aprotic solvents (water-miscible) of low polarity. An investigation

of the temperature dependence of this μ-oxo dimer equilibrium in 40% aq DMSO showed its formation to be endothermic, indicating that this process was entropy driven under the conditions tested. The entropically favoured formation of the μ-oxo dimer species was proposed to be a solvation effect around the axial $^{-}OH/H_2O$ ligand under the pH conditions of interest. Aprotic solvents are only capable of acting as hydrogen bond acceptors and therefore at alkaline pH, offer reduced solvation potential around the ^{-}OH axial ligand, requiring an increase in the water concentration around this ligand, relative to the bulk solvent. This process presumably results in the observed entropy decrease, favouring the release of one H_2O ad two H^+ ions to form the μ-oxo dimer species. Conversely, in polar protic solvent mixtures capable of acting as both hydrogen bond donors and acceptors at high pH, can replace the solvating water molecules around the axial ^{-}OH ligand. This concept was explored by the solvent system choices by Asher et al., where it was found that the degree of π-π dimer species domination in solution, was correlated to the polarity of the solvent medium.[72]

This suggestion recently gained support from a molecular dynamics (MD) simulation study that provided evidence of these solvation shells around each species, showing that the monomeric and π-π dimer species displayed prominent solvation shells around their axial ligands, and although solvated, the oxide bridge of the μ-oxo dimer, represented a drastic reduction in solvation, considering it was shared between the two porphyrins.[69] The formation of higher aggregates of π-stacked μ-oxo dimers in concentrated salt solutions was suggested to occur as a result of competition for the hydration sphere around the axial ligand, lowering the stability of the hydrophilic face of the porphyrin (ligated face) relative to the μ-oxo dimer. The polar protic environment would still however favour the observed formation of π-stacked aggregates.[72] A summary of their findings and the different conditions required for each Fe(III)PPIX species is presented in Scheme 1.1. This capacity for varied Fe(III)PPIX speciation in solution is often overlooked in the literature and needs to be considered when investigating βH formation and Fe(III)PPIX-drug interactions.[94]

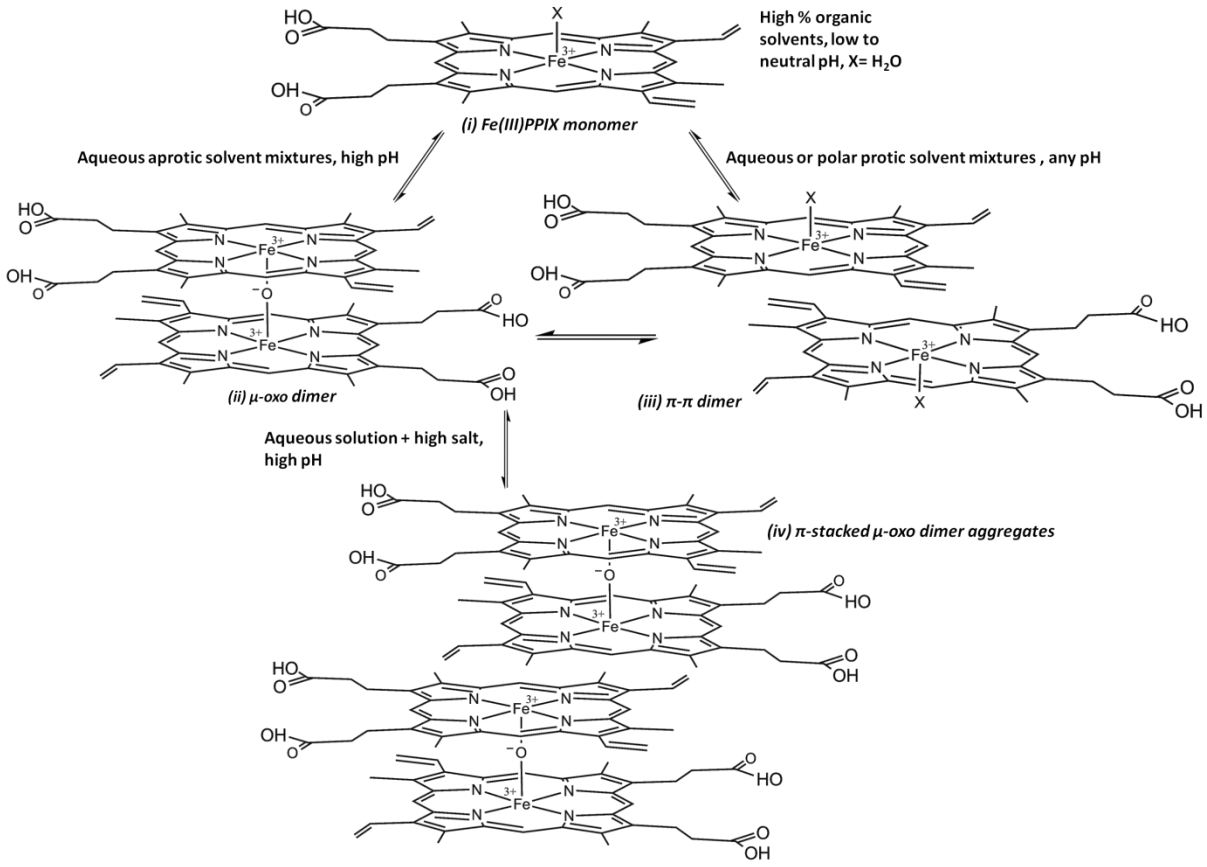

Scheme 1.1 Representations of predominant species of Fe(III)PPIX in aq, mixed-aq and high concentration solvent or salt solutions under variable conditions as characterised by UV-vis spectroscopy , magnetic susceptibility and diffusion measurements.[72]

(1.3.4) Theories of haemozoin formation in vivo

To date the mechanism of Hz formation *in vivo* is yet unelucidated, however, several investigations into this process have been reported.[29] Widely held theories include auto-catalysis, spontaneous formation, enzyme-catalysed detoxification mechanisms, and facilitation by histidine-rich proteins or lipid mediated biocrystallisation and even a combination of these processes. While multiple reports have provided evidence for each of these mechanisms, their exact roles are unclear and further investigation is required. A few of the most pertinent advances in the field are discussed here.

(1.3.4.1) Protein catalysed formation of haemozoin

In biology, a wide variety of detoxification processes are catalysed by enzymes or specific protein systems, efficiently compartmentalising each step in a series of specific interactions that are capable of completing structural transformations.[95] Theories of enzyme catalysed Hz formation were first postulated in 1991 by Slater and Cerami, who showed lysed troph extracts, containing what was believed to be the active enzyme, haem polymerase, were capable of converting Fe(III)PPIX into Hz.[96] Studies were able to show "inhibition of this enzyme" upon addition of quinoline antimalarials.[97,98] However, this notion was dispelled upon publication of a study conducted by Dorn et al. which showed that heating of extracts, addition of "polymerases" or additional product, had no effect on the observed ability to mediate synthetic Hz formation and thus concluded that no such enzyme was present in the extracts. [99] The authors went on to propose that Hz formation may in fact be as a result of an auto-catalytic process based on their observations that an increased amount of product formed in the presence of either Hz or βH. [99] This theory however, offered no explanation as to how the initial nucleation step occurred.

Later, Sullivan et al. proposed that histidine-rich proteins (HRP II and III) were involved in this process.[100] This idea was perpetuated [101,102] until it was later shown that these HRP proteins were not as efficient at producing Hz as initially thought and was found to be mainly located in the cytosol of the red blood cell rather than at the site of Hz formation, inside the DV. [103–105] It was thus proposed that Hz formation is a coordinated two-step process involving lipids and *Pf*HRP II.[104] Finally, the involvement of these histidine-rich proteins in Hz formation was disproved when studies found that in mutated species which lack the genes for the formation of these proteins, Hz was still detected.[106,107] The presence or absence of *Pf*HRP II or III was also found to have no effect on βH crystal morphology.[108]

The hypothesis of protein catalysed Hz formation was recently rekindled when another protein called, haem detoxification protein (HDP), was proposed by Jani et al. and shown to bind Fe(III)PPIX strongly (-log K_d = 7.1) at an average of 2.7 binding sites per protein molecule.[109] Recombinant HDP was found to effect a 50% conversion to βH within 20 min, however, HDP was found to lack the N-terminal sequence required for protein transport

signalling in order for it to be shuttled from accumulation in the parasite cytoplasm to the site of Hz formation in the DV. [109–111]

The most recent proposal involving proteins implicated in haemoglobin degradation and Hz formation, was a 200 kDa protein assembly of falcipain 2/2′, plasmepsin II, plasmepsin IV, HAP, falcilysin and HDP, introduced by Chugh et al. in 2012.[112] The authors proposed from *in vitro* co-immunoprecipitation and MALDI-TOF mass spectrometry results, that HDP and falcipain 2 interact strongly, in the form of a Hz formation complex (HFC), to directly associate with the growing Hz crystal. Interestingly, a recent study on identification of the proteins associated with and embedded within isolated Hz crystals from *P.falciparum* extracts in the Egan laboratory using proteomics techniques found no evidence of the proteins belonging to the proposed complex.[113] On the other hand, lipoproteins were identified, with known functions in lipid transport and biosynthesis, as were neutral and phospholipids, which lent further credence to an alternative hypothesis that lipids and not proteins are the biomolecules responsible for Hz formation *in vivo*. *Plasmodium* parasites are incapable of *de novo* biosynthesis of cholesterol and fatty acids, however, to develop its membranes, a significant amount of host lipid appropriation occurs throughout development.[114] The complete lipid profile of the malaria parasite through all its stages of development is yet unelucidated but those that have been identified, have been shown to play a role in Hz formation.[115]

(1.3.4.2) Lipid mediated haemozoin formation

The possible involvement of biomolecules other than enzymes or individual proteins in Hz formation was explored in 1995 when Bendrat et al. controversially suggested that lipids may be responsible for mediating Hz formation *in vivo* and were likely the source of the observed auto-catalytic behaviour of Hz extracts.[116,117] Through high-performance liquid chromatography (HPLC) analysis the authors were able to identify methyl esters of oleic, palmitic and stearic acids associated with the parasite lysates active in Hz formation. In a reply to this work, Ridley et al. showed that acetonitrile extracts from troph infected and uninfected erythrocytes were capable of initiating *in vitro* βH formation, leading the authors to propose that it was the acidic pH of the parasite lysate that was responsible for the observed Hz specificity.[99,117] Later work by Fitch et al. on chloroform extracts of *P. berghei*

infected erythrocyte lysates showed that at least 70% of the proposed "haem polymerase" activity could be attributed to the cholesterol, phospholipids and acylglycerols found by TLC analysis of the extracts.[118] Fitch and co-workers suggested that the lipids act by solubilising Fe(III)PPIX to facilitate Hz formation. The authors showed that mono and dioleoyacylglycerols as well as the detergent sodium dodecyl sulphate (SDS) were capable of mediating βH formation *in vitro*.[118] The phospholipids, phosphatidylinositol, phosphatidylserine, sphingomyelin and phosphatidylcholine were also found to initiate βH formation.[119] In support of lipid involvement, Jackson et al. showed that the lipophilic fluorescent probe Nile Red (NR) stained neutral lipid droplets of about 100 nm in size composed of di and triacylgylcerols associated with the parasite DV of infected erythrocytes.[120] Fluorescence and confocal microscopy images of lipid bodies stained with NR obtained from the various stages of *Plasmodium* infection, are shown in Fig. 1.12. Further imaging evidence was provided in a review by Coppens and Vielemeyer, where Hz crystals were shown to be enveloped by neutral lipid bodies inside the parasite DV, also shown in Fig. 1.12.[121]

Tripathi and co-workers in 2002, and later, as mentioned, Pandey et al., had postulated that lipids were involved in the biocrystallisation of Hz from studies showing that linoleic acid and the addition of mono-1-rac-oleoyl glycerol were capable of initiating βH formation.[122,123] In 2007, in a landmark study by Tripathi, along with Pisciotta and other authors showed by subcellular fractionation of parasite extracted Hz through a concentrated sucrose solution with malachite green staining, that mono and diacylgylcerols as well as polar lipids were in close association with Hz within the parasite DV (Fig. 1.13).[124] A unique blend of neutral mono and diacylgycerol lipids were proposed to be the main components of the lipids found associated with Hz *in vivo*. The neutral lipid blend (NLB) includes, *rac*-1-monostearoylglycerol (MSG), *rac*-1-monopalmitoylglycerol (MPG), *rac*-1,3-dioleoylglycerol lipid (DOG), *rac*-1,3-dilinoleoylglycerol (DLG) and *rac*-1,3-dipalmitoylglycerol (DPG), identified to be present in the volume ratio 4:2:1:1:1 from TLC and electron-spray ionisation mass spectrometry lipid analysis on saponin-purified trophs. Lipid extracts from purified digestive vacuoles, whole trophs, uninfected erythrocytes, the neutral lipid blend and a series of lipid standards were tested for Fe(III)PPIX crystallisation ability *in vitro* at pH 4.80, 37 °C where it was shown that the monoacylglycerols were the most efficient at producing βH.[124] The authors offered

several suggestions as to the role of these lipids in Hz formation, expanding on earlier theories initially proposed by Fitch et al.[118] and Jackson et al.[120] postulating that the neutral lipid bodies offer a non-aqueous environment that excludes water, allowing for facile transformation of Hz dimers from the π-π dimer form of Fe(III)PPIX by release of axial water ligands under the acidic conditions of the DV. [124]

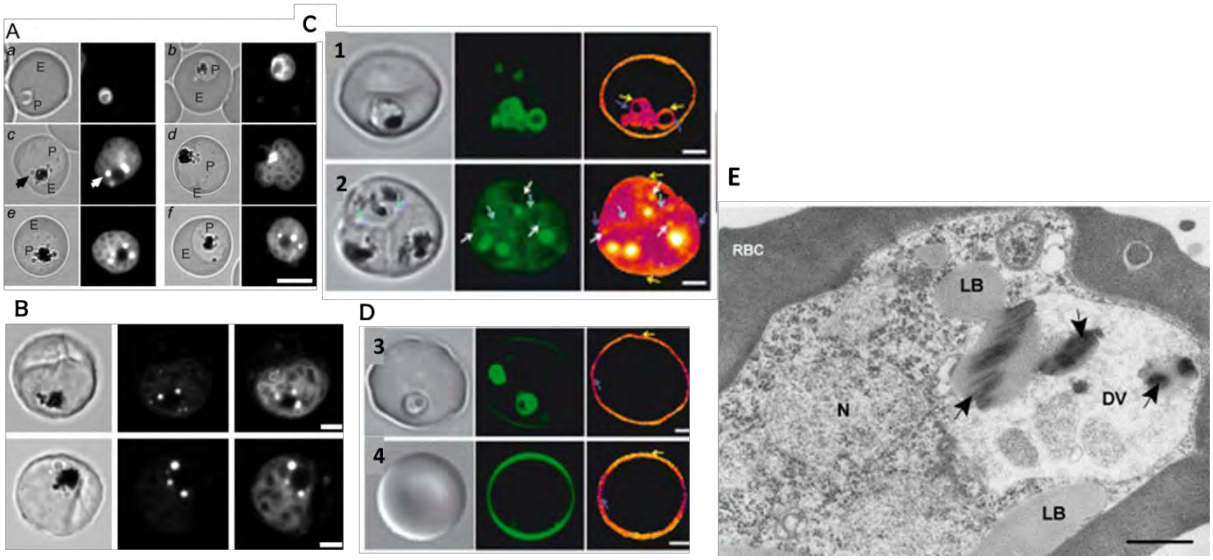

Figure 1.12 Identification of lipid bodies (LB) associated with Hz in *Pf*. infected erythrocytes shown in panels **A-B** taken with brightfield (left) and fluorescence (right) microscopy images of NR labelled lipids in malaria parasite at the (**a**) ring, (**b**) young troph, (**c-f**) mature tropozoite to schizont stages of its life-cycle. NR staining of a parasite with young troph infection in brightfield and under fluorescence (green) shown in panel **(C)** (**1**). A comparison of the signal obtained with multiple troph infection of one erythrocyte is offered by panel (**2**). Panels **(D)** (**3**) and (**4**) compare the staining pattern obtained in an infected erythrocyte with an un-infected one (only the erythrocyte membrane is stained), respectively. Furthermore, the LBs identified within *Plasmodium* were shown to be associated with Hz within the DV of the malaria parasite as highlighted by the arrow in panel **(E)**. Scale bars represent 5 and 2 μM in **A** & **B**. Images **A-D** reproduced with permission from Jackson et al. (2004) © John Wiley and Sons.[120] Image **E** copied with permission from Coppens and Vielemeyer, (2005), ©Australian Society for Parasitology Inc, Published by Elsevier Ltd.[121]

As mentioned, the malaria parasite is not the only blood-feeding organism to detoxify Fe(III)PPIX as Hz crystals. While it is unknown if their mechanism of formation is exactly the same due to the extracellular formation of Hz in these organisms compared to the

intracellular process by *P. falciparum*, the identification of Hz inside lipid droplets or membrane bound vesicles from the midgut of *S. mansoni* and *R. prolixus* offers considerable support to the theory that this process is a lipid-mediated one.[58]

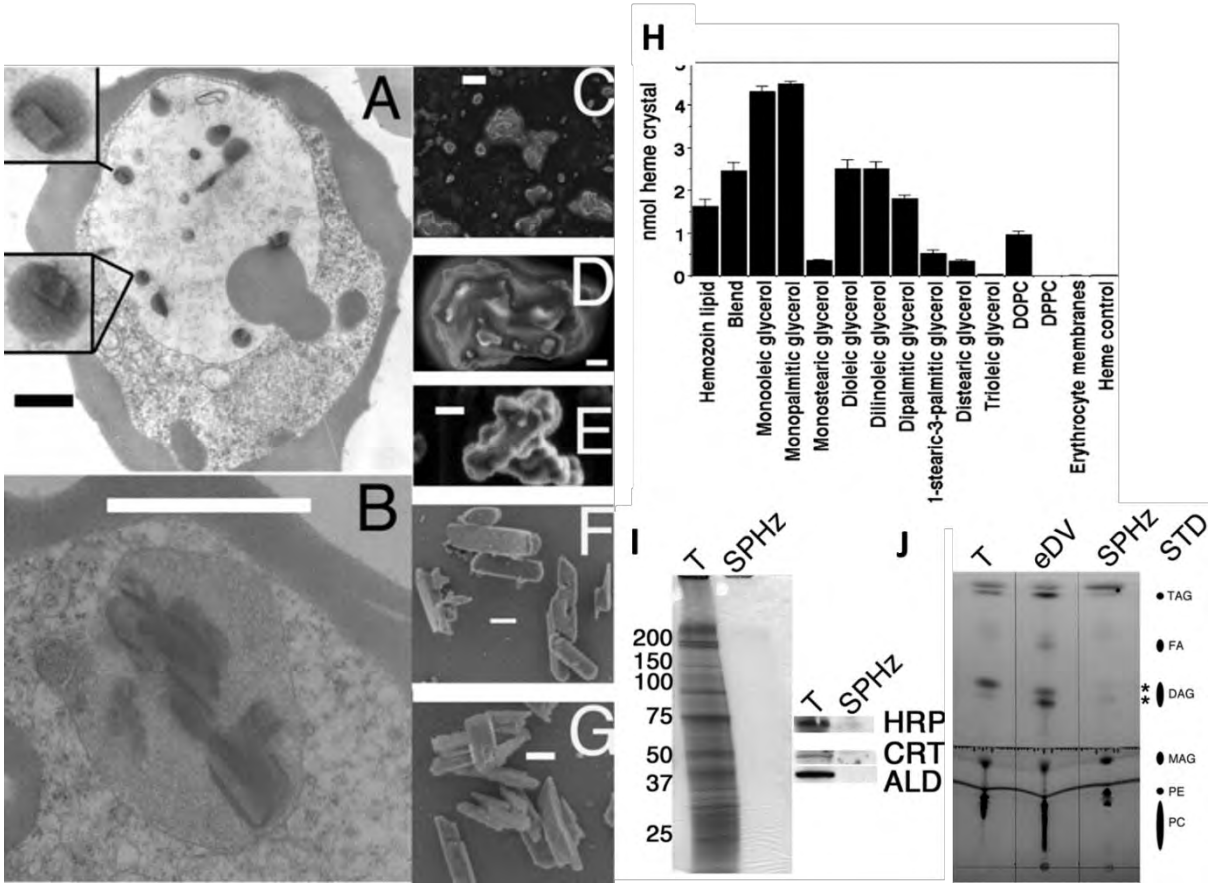

Figure 1.13 TEM images of (**A and B**) malachite green stained LBs in parasite infected erythrocytes, a scanning electron micrograph of Hz inside the parasite DV which is shown to be enveloped by lipids. Panels (**C-G**) show Hz after successive stages of wash, where images **C-E** depict lipid deposits around the crystals, while (**F-G**) show TEM images of delipidated Hz crystals. Scale bar represents 1 µm. (**H**) shows the yields of βH formed by extracted lipid and each acylglycerol lipid component as identified by TLC. (**I**) SDS-Page gel electrophoresis showing minimal protein content in the right lane compared to the whole troph (left lane). No evidence of HRP, PfCRT or cytosolic Pf-aldolase (ALD) was identified in saponin-purified trophs (T) or Hz (SPHz) by Western blot analysis. The lipids found were identified by TLC against lipid standards (**J**) showing a dominance of acylglycerols in isolated T, enriched digestive vacuoles (eDV) and SPHz. Reprinted with permission from Pisciotta et al. (2007), ©The Biochemical Society.[124]

(1.4) Studies on the mechanism of haemozoin formation

Several *in vitro* studies between Fe(III)PPIX and these neutral lipids as well as with solvents and lipid-like molecules to form βH have been performed, the most relevant of which will be discussed over the following pages.

(1.4.1) Conversion of Fe(III)PPIX to β-haematin, in vitro

To shed light on the possible role of lipids in the process of Hz formation, An earlier study by Egan et al. investigated the formation of βH at model organic / aq interfaces based on insights obtained from MD simulations showing that the π-π dimer Fe(III)PPIX species spontaneously arranges its conformation to that of a βH crystal unit precursor (μ-propionato dimer) *in vacuo*, suggesting that crystallisation is facilitated by the absence of competing water molecules for hydrogen bonding (Fig. 1.14).[57] Simulations in aq solution did not result in the spontaneous formation of the μ-propionato dimer precursor since the propionate groups were observed to move away from the Fe(III) centers to interact with the bulk water molecules. This led the authors to conclude that the non-aq environment offered by lipids was required for crystallisation.[57]

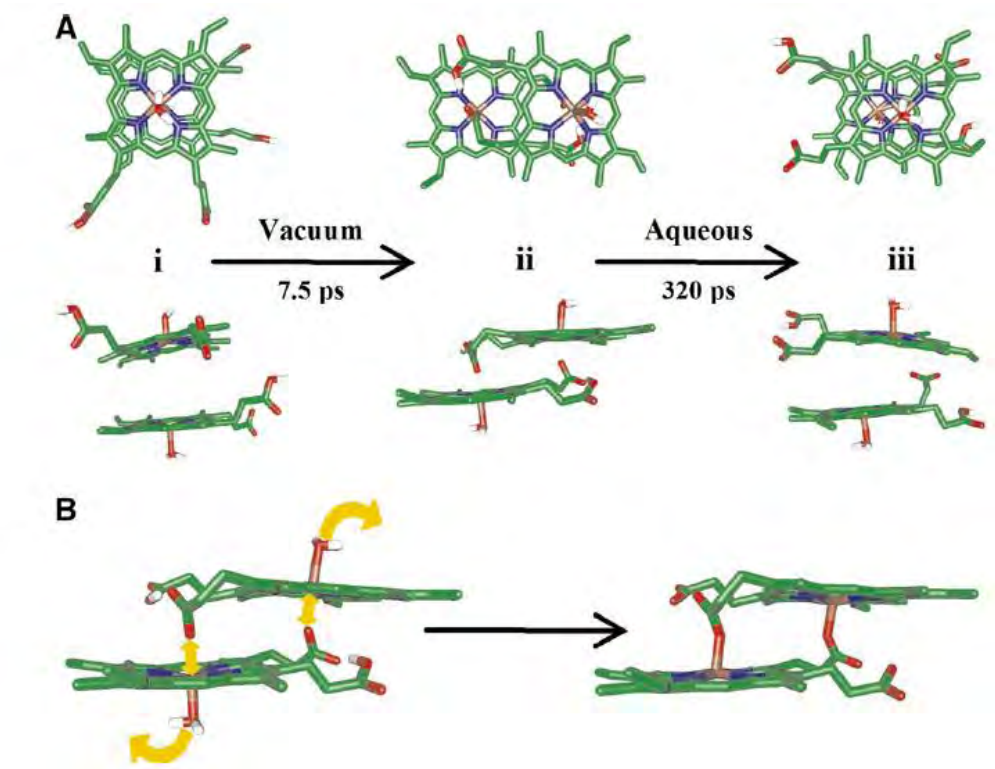

Figure 1.14 (A) Results of an MD simulation conducted on (**i**) Fe(III)PPIX π-π dimers in the absence (**ii**) and presence of water. (**iii**) In vacuum, the conversion to a structural βH precursor is spontaneous, but it is not formed in aq solution. **(B)** shows the proposed conversion step of this precursor to the μ-propionato dimer present in the βH crystal unit in the absence of water. Image reproduced with permission from Egan et al. (2006),© Elsevier.[57]

Further studies by de Villiers et al. using grazing incidence synchrotron X-ray diffraction (GXID) and X-ray reflectivity techniques on a premixed solution of Fe(III)PPIX at the model lipid, 1-myristoyl-glycerol (MMG)/air interface showed the formation of βH crystals oriented with their {100} faces parallel to the water surface.[125] This was interpreted by proposing a stereospecific interaction between the exposed OH groups of MMG clusters and Fe(III)PPIX molecules to nucleate orientated crystallisation (Fig. 1.15a), suggesting that it was evidence of the effect of the favorable stereochemical interactions between the surface polar lipid head groups and the exposed -CO_2H group via the oxygen lone pair on the {100} face of Fe(III)PPIX. By analogy, the orientation of βH crystals was investigated at the surface of self-assembled functionalized alkalanethiol monolayers (SAMs) with either OH or CH_3 groups or a mixture of the two. Comparable to the lipid, OH functionalized SAMs were found to induce

βH nucleation primarily at its {100} face, whereas the alkyl functionalized SAMs induced nucleation preferentially via the {010} face as well as the {100} face.[125] The {010} face is shown to expose the porphyrin ring CH groups (vinyl and methyl moieties) and was proposed to be likely to enjoy favourable interactions with the CH_3-functionalised SAMs.

In support of this theory, a recent publication showed that lipid droplets of the proposed neutral lipid blend nucleate βH at the {100} and {$\bar{1}$00} faces.[126] A comparison of these crystals with Hz isolated from parasite extracts and βH formed at the pentanol/ aq interface using transmission electron microscopy (TEM) appeared to indicate that the size distribution of the neutral lipid droplets (NLDs) which were found to be in contact with the βH crystals formed, determined their sizes (Fig. 1.15 d). Crystals formed at the pentanol/aq interface appeared to be longer than those nucleated by NLDs, possibly due to the flat surface of the interface, as opposed to the curved lipid surface. Furthermore, βH crystals were found to lie on the surface of NLDs rather than inside as previously proposed.[127] The larger Hz crystals from *Pf* DV extracts, were suggested to have formed aligned to the parasite DV membrane rather than smaller NLDs inside the DV.[126] This hypothesis was consistent with evidence that DV inner membrane phospholipids or neutral lipid rafts rather than NLDs are responsible for Hz nucleation *in vivo*.[46]

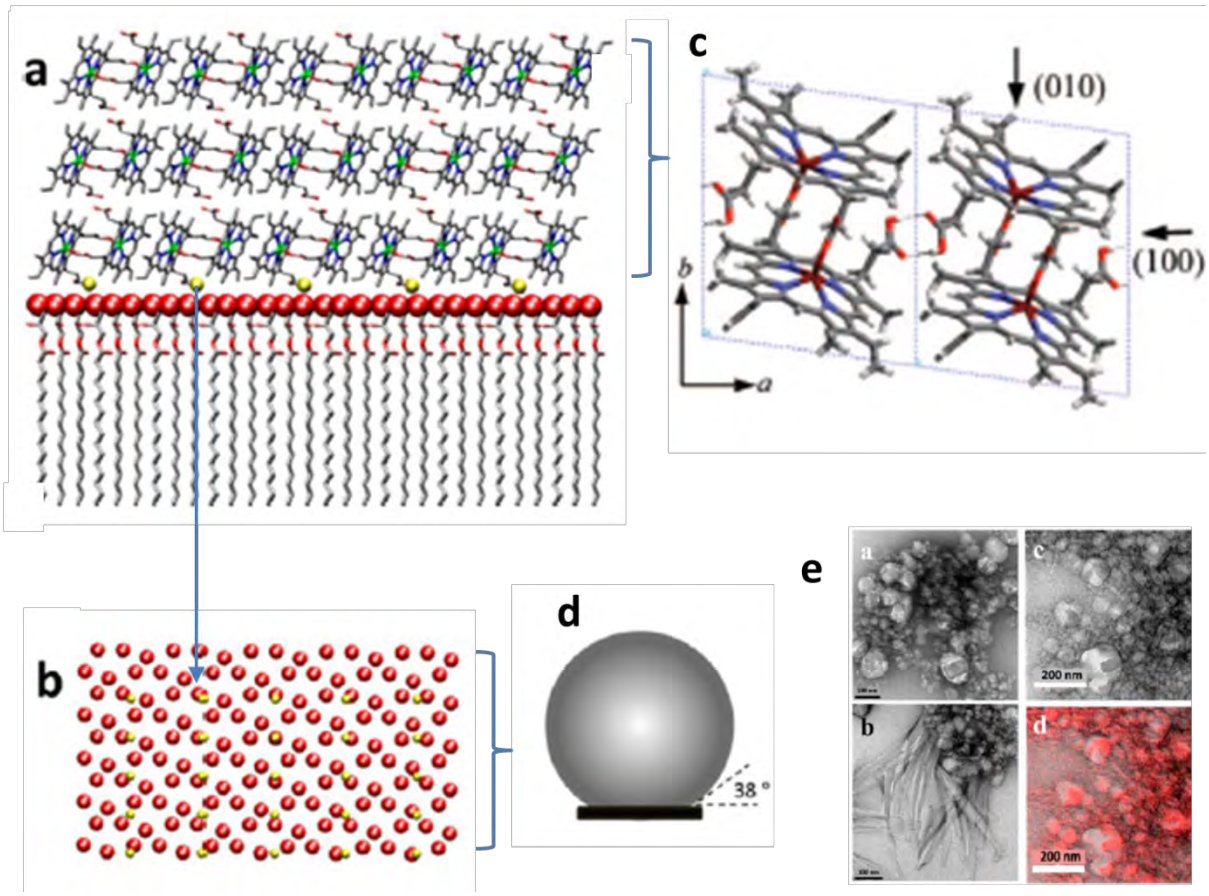

Figure 1.15 (a) An illustration of the stereochemical contacts between βH and MPG lipid surface showing the proposed model for templated crystal growth, the near match between the positions of the βH propionic acid groups (yellow) at the {100} face and every third glycerol OH group (red) of the lipid is highlighted in **(b)**. The packing arrangement of βH along the c axis with {100} and {010} faces, illustrated by arrows is shown in **(c)**. The image in **(d)** depicts the angle of contact between βH and the surface of the NLD (assuming a spherical NLD), as observed from **(e)** TEM (a-c) and EELS (d) of βH crystals associated with the surface of NLDs. Image **(c)** reproduced with permission from de Villiers et al., (2009),©American Chemical Society[125] and Images **(a, b, d&e)** reproduced with permission from Ambele et al., (2013),©American Chemical Society.[126]

(1.4.2) Location of and type of lipid involved in haemozoin formation

A percentage of the literature on lipid mediated Hz formation is polarised, with a considerable number of studies indicating that the phospholipids that comprise the DV or transport vesicle (TV) membranes rather than the proposed neutral acylglycerol lipid droplets, are the site of Hz formation *in vivo*.[46,119,128–131] Kapishnikov and co-workers have investigated this extensively using cryogenic soft X-ray tomography (cryo-XT) and 3D electron microscopy to show Hz clearly visible inside the parasite DV, inside infected erythrocytes.[46,128] The Hz crystals of early trophs were shown to be aligned side by side along the needle crystal *c* axis parallel to the inner leaflet of a somewhat flattened DV membrane as seen by 3D rendering of the serial surface view microscopy images (Fig. 1.16). This was suggested to be the site of nucleation of Hz crystals. Later stage trophs and schizonts, were found to have larger Hz crystals toward the center of a more spherical DV, with all crystals orientated toward their $\{100\}$ faces. The Hz crystals were never observed to be on the surface of or surrounded by acylglycerol lipids in contrast to earlier studies, nor was any Hz detected in Hb transport lipid vesicles.[129] The authors proposed that heterogeneous nucleation of Hz crystals occurs at the inner DV membrane, which after crystal growth and maturation, break away from the membrane presumably because of the observed change in DV membrane curvature. The inner leaflet of the DV membrane has been shown to be much more fluid than the outer leaflet due to the presence of phospholipids such as phosphatidylethanolamine, phosphatidylserine, and phosphatidylinositol and a high proportion of saturated fatty acids.[114]

It was acknowledged that phospholipid head groups were unlikely to induce the observed orientated nucleation and an acylglycerol lipid film adsorbed to or a part of the inner leaflet of the DV membrane was proposed as the nucleating lipid. They also suggested that Hz crystals grew in the aq phase, despite the thinking that a hydrophobic environment is required for loss of the axial H_2O ligand to form the precursor to βH, the μ-Propionato dimer.[125,132] A later publication by the same authors illustrated the DV membrane thickness between 4-5 nm, of which, roughly 86% comprises a lipid bilayer approximately 4.2 nm thick, with the remainder taking the form of isolated double layer patches of 8 nm thickness. [130] This thickness was proposed to arise from a mixture of phospholipids, cholesterol and

acylgylcerols, the latter of which, make up the inner lipid leaflet that is suggested to nucleate Hz formation.

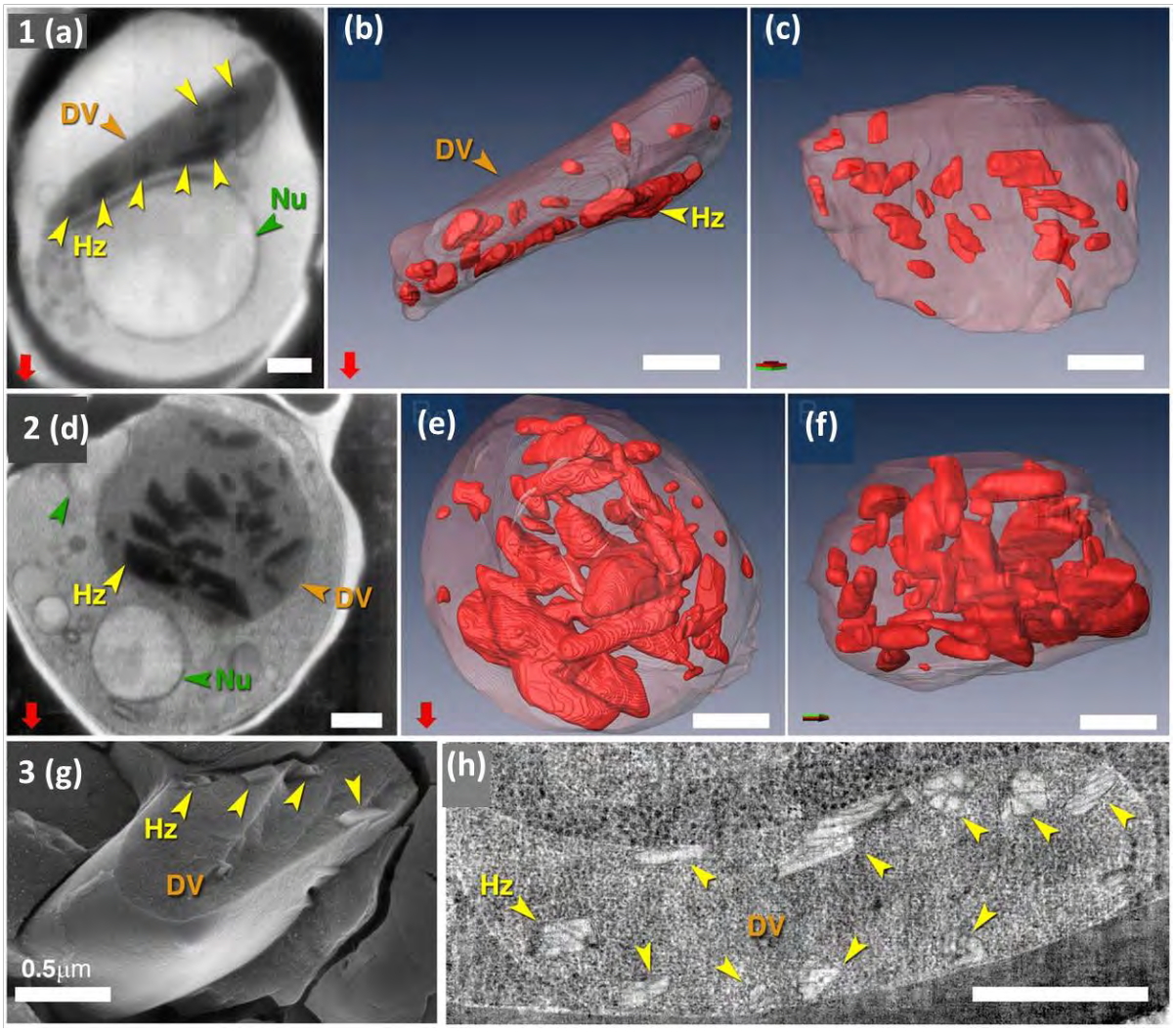

Figure 1.16 TEM and cryo-XT images of different stage parasites with Hz crystals highlighted by yellow arrows. **(1)** Panel **(a)** depicts a TEM of an early stage troph with smaller crystals aligned along the inner DV membrane, **(b-c)** surface rendered in 3D, with orthogonal views to show the alignment of Hz crystals along the flattened DV membrane **(2d)** TEM images of a later schizont stage **(e-f)** the larger Hz crystals in the center of a spherical DV can be clearly seen. **(3g-h)** The alignment and orientation of the Hz crystals parallel to the DV membrane is shown. Images reproduced with permission from Kapishnikov et al. (2012),©National Academy of Sciences.[46]

An early report published by Ginsberg and Demel demonstrated the ability of Fe(III)PPIX to intercalate into phospholipid monolayers effecting a measurable increase in the surface pressure.[133] The authors showed that the degree of Fe(III)PPIX incorporation into the

phospholipid membrane was determined by the speciation of Fe(III)PPIX, either as a monomer or dimer in which the former exhibited a greater amount of intercalation. Other than size, no reasons for this preference were offered and very little literature has explored the speciation effect on lipid permeation any further.

In support of the DV membrane being the site of Hz nucleation, *in vitro* studies on the ability of phospholipids to nucleate βH formation have been published.[119,131,134] These works found that selected phospholipids and were efficiently and rapidly able to catalyse the crystallisation of Fe(III)PPIX to βH. The ability of selected phospholipids to induce βH formation at 37 °C was found to be inversely correlated to their gel-to-fluid transition temperature (T_m), which the authors suggested was due to the required membrane fluidity for Fe(III)PPIX insertion into acyl chains of phospholipids.[131] This was observed in differential scanning calorimetry studies of the proposed neutral lipid blend which was found to have unique melting properties compared to its saturated and unsaturated lipid components, which were found to have higher and lower T_m values, respectively.[135] The blend was proposed to possess greater fluidity with less orientated packing, than its individual components. To explain these observations and offer suggestions as to the possible role of either neutral lipids or the DV membrane in Hz formation, some understanding of crystal nucleation and growth together with the role of stereochemical interactions is required.

(1.4.3) Crystal nucleation and growth in the context of lipid and solvent mediated β-Haematin formation

The transformation of Fe(III)PPIX into Hz *in vivo* or βH *in vitro* is the conversion of an amorphous solid into a crystalline solid material. Classical nucleation theory describes the aggregation of dissolved molecules in a supersaturated solution into organised nuclei of radius, r. The free energy of the surface of this new phase is positive and proportional to the square of the radius of the nucleus, however, the energy driving aggregation to form the nucleus is negative and proportional to the volume of the nucleus or r^3.[136] Once the nucleus has grown past a critical threshold size, r*, in a metastable phase, the total free energy of

the system begins to decrease as continued growth stabilises the transformation of the metastable phase to the new thermodynamically stable phase.[137] Crystallisation processes are said to follow Ostwalds rule of stages or step-rule where the process of transformation occurs first by nucleation of new crystal nuclei either spontaneously or by the introduction of a heterogeneous stimulus.[138] The Avrami equation models the complicated processes of nucleation and growth in the solid to solid state transformation with the following assumptions; (1) Nucleation occurs randomly and homogeneously over the entire untransformed portion of the material, (2) The growth rate is independent of the extent of transformation and (3) the growth rate is uniform in all directions.[139,140] It has been shown to provide an approximate description of the kinetics of crystallisation of Fe(III)PPIX.[63,67,141]

The Avrami constant, *n*, describes both the seed-formation dynamics or type of nucleation and the dimensionality of growth of the crystal at a constant temperature. *n* is usually an integer between 1-4, reflecting the nature of the nucleation , either instantaneous or sporadic and the shape of the particles formed, either in 1, 2 or 3-dimensions to give rods, discs or spherical crystals, respectively. The rate constant, *z*, is a function of the nucleation rate (N) of new particles and growth rate (G), dependent on the volume and thus densities of the reactant (ρ_r) and product (ρ_p) as described in equation (Eqn) 1.2.1. The overall transformation kinetics are given by Eqn. 1.2.2., where m_0 is the initial mass of Fe(III)PPIX and m_R, is the mass of Fe(III)PPIX after the crystallisation reaction has occurred at time t. The kinetics of transformation typically follow a sigmoidal profile allowing for a period of slow initial and end transformation with rapid crystallisation in between.[138]

$$z = 4\pi N G^3 . \rho_p / 3\rho_r \qquad (1.2.1)$$

$$\frac{m_R}{m_0} = e^{-(zt)^n} \qquad (1.2.2)$$

Egan et al. reported the kinetics of βH formation from 4.5 M acetate buffer at 60 °C to be sigmoidal with *n* = 4, indicating an initial slow phase to allow for sporadic nucleation (continuous and random) and crystal growth in 3-dimensions to form spherical crystals which terminate upon full conversion of Fe(III)PPIX into βH.[67] The rate constant was

reported to be dependent on temperature, stirring rate, acetate concentration and pH. Another solvent, benzoic acid, was also found to initiate βH formation at a much lower concentration than acetate solution.[141] The kinetics of this process were similarly found to be sigmoidal and fitted the Avrami equation, with *n* = 4. The authors explained the increased activity of benzoic acid by observing the kinetics of βH formation in a series of substituted benzoic acids and monitoring the temperature dependence of the acetate and benzoic acid reactions. The activity of the benzoic acids was proposed to be as a result of their propensity to form hydrogen bonds in solution whereby the carboxylic acid groups were suggested to disrupt any hydrogen bonds between Fe(III)PPIX propionate groups and axial H_2O ligands, a process required for facilitation of βH formation. The benzene group in benzoic acid was suggested to allow for further π-π interactions with Fe(III)PPIX to discourage the observed π-stacking of Fe(III)PPIX in solution causing the increased activity observed compared to acetate solution.[141] The kinetics of βH formation in phospholipid and neutral lipid solution have subsequently been investigated, offering biologically relevant rates of crystallisation to account for the estimated concentrations of free Fe(III)PPIX in the DV.[16,57,142,143] Initial studies found that individual neutral lipids and the blend of neutral lipids induced rapid formation of βH under biomimetic conditions with half-lives ranging between 1 and 4 min (Fig. 1.17).[57,127] Confocal microscopy was employed to show that βH formation occurs in close association with neutral lipids, however, the Avrami equation was not applied to these data. [143]

A recent comprehensive study on the kinetics of βH formation was reported at a model lipid/aq interface.[63] The observed exponential kinetics were modelled using the Avrami equation, with a reported *n* = 1 and a rate constant of 0.19 ± 0.02 min^{-1} corresponding to instantaneous nucleation and growth to form linear crystals. The lipid was found to promote βH formation from a fixed number of preformed nuclei with crystal growth in 1-dimension which was reported to be consistent with the observed morphology of long needle-shaped βH crystals.[144]

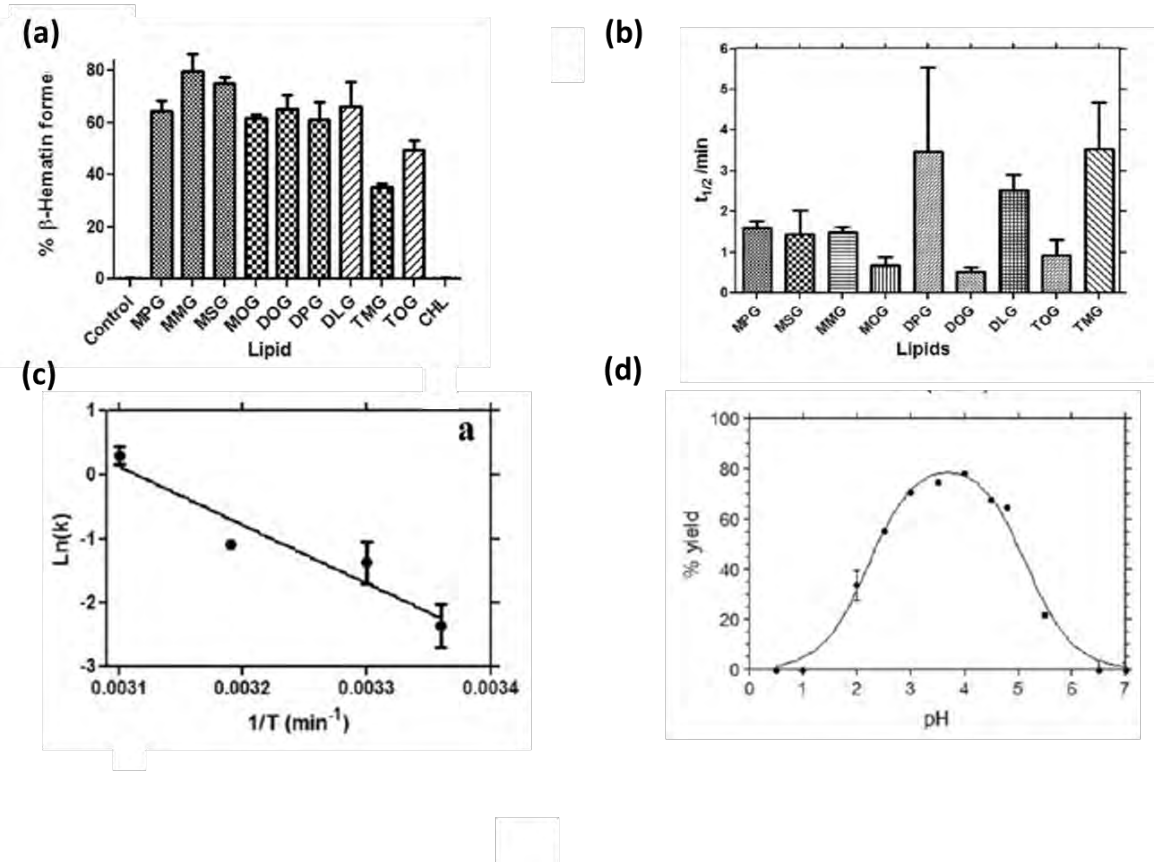

Figure 1.17 Multiple *in vitro* studies of neutral lipid mediated βH formation. **(a)** The βH yields obtained with different lipids. Monoacylglycerides: MPG, MSG and MOG; diacylglycerides: DOG, DPG, DLG, triglycerides: TOG and TMG and cholesterol (CHL). **(b)** The time taken (min) to form 50% βH ($t_{1/2}$) for each lipid with the smallest observed half-life obtained for MOG and DOG. **(c)** The Arrhenius behaviour for MSG at pH 4.8 constructed from rate constants with slope (activation energy) of 76 KJ.mol^{-1}. **(d)** The effect of pH on the yield of βH obtained with MSG at 37 °C. Figures reproduced with permission from Hoang et al. (2009),©Royal Chemical Society.[127]

The exact site of Hz formation in the malaria parasite DV is still unconfirmed and the specific type of lipid molecule responsible for its crystallisation may be neutral acyl glycerols or charged phospholipids as the discussed works have postulated. Regardless of the nature of the lipid associated with Hz formation, the chemical relevance of a lipid mediated biocrysatllisation of Fe(III)PPIX is also unknown, to further the understanding of these interactions, the neutral acylglycerol lipids identified from TLC samples on parasite DV extracts by Pisciotta et al. were chosen to probe this and are the focus of this project.[124]

(1.4.4) Lipid mimics and other inducers of β-Haematin formation

Lipid solutions and interfaces are dynamic and often difficult to study due to particle flux from coalescence and viscosity effects that result in light scattering and poor reproducibility.[145–147] Coupled to this issue, commercially available purified lipids are expensive compared to common organic solvents. To circumvent these complications, several studies on the conversion of Fe(III)PPIX to βH have been conducted in solvent systems that serve as lipid mimics. As mentioned, octanol, pentanol and other alcohols have been shown to effectively induce βH formation in the literature.[57,148] This ability has been linked to their degree of hydrophobicity and inherent ability to solubilise Fe(III)PPIX in acidic solution.[148] Huy et al. also proposed that the lower surface tension of these solutions serves to decrease the energy required for forming βH nuclei.[149] This phenomenon has also been reported for the ability of polyethylene glycols (PEGS) to induce βH formation in acidic solution.[150]

Recently, research on the formation of βH from citrate buffer-saturated octanol solutions (CBSO) have shown that Fe(III)PPIX is four orders of magnitude more soluble in this solution than in aqueous solution at pH 4.8.[151] The surface morphology of crystals prepared from this octanol solution was compared with those grown in 0.1 M acetate solution, of which the latter was found to exhibit unusual macro- and mesoscopic features not observed for the former or Hz crystals. The authors concluded that the organic lipid environment is essential for βH crystal formation. Following this, the same researchers published a biomimetic method of growing large 50 μm βH crystals from CBSO solution upon which they very recently proposed, using *in situ* atomic force microscopy (AFM), that crystallisation follows a strictly classical mechanism where two-dimensional nucleation occurs from solute molecules followed by epitaxial growth.[152,153]

Neutral mono and diacylglycerol lipids are amphiphilic molecules that are believed to act by templated nucleation through their exposed polar OH groups.[125] Due to the difficulty of studying lipid systems and their high cost, several groups have explored the ability of amphiphilic detergents to mimic lipids in the βH formation process.[118,154,155] Specifically two sets of researchers have shown that neutral detergents, Tween-20 and NP-40, are capable of effectively initiating βH formation in moderate to high yields over approximately four to six

hours.[150,151] Detergents are structurally unique molecules as they enable both hydrophobic interactions through their hydrocarbon chain portion and hydrophilic interactions through some polar headgroup with other substances contributing to a host of physical and chemical properties in solution.[156,157] Mostly employed for the solubilisation and crystallisation of membrane proteins, detergents are defined by their ability to self-assemble and interact with hydrophobic surfaces in a concentration-dependent manner.[158]

Increasing concentrations of detergent molecules in solution are known to form noncovalent aggregated structures called micelles (Fig. 1.18).[159] The spontaneous association of amphiphilic molecules into thermodynamically stable micellar aggregates in aq solution leads to a reduction of the energetically unfavourable contact between polar water and the non-polar hydrocarbon chain parts of the detergent, while still maintaining the favourable polar contacts with the hydrophilic bulk solution. This unique structure enables detergents to solubilise nonpolar or organic materials in the hydrophobic regions of the micelle which enables detergent properties that differ from pure detergent monomer solution. The concentration at which detergent monomers begin to form these aggregated structures is referred to as the Critical Micellar Concentration (CMC) and is dependent on buffer or salt concentrations in solution as well as the pH and temperature of the solution.[160]

There are multiple techniques to determine the CMC of a particular detergent, one method in particular exploits the solvatochroism of the hydrophobic dye, Nile Red (9-diethylamino-5H-benzo[α]phenoxazine-5-one).[161,162] NR is an intensively fluorescent dye in hydrophobic solvents or environments. It has been shown to emit the maximum fluorescence intensity with increasing hydrophobicity and thus it is highly selective for lipid or micelle environments. [163,164] NR is classified as a twisted intramolecular charge transfer (TICT) fluorescent probe.[165] Generally, this class of probe responds to photoexcitation by twisting toward an ideal perpendicular excited state. The rate of formation of this TICT excited state decreases with increasing polarity (measured as $E_T(30)$) of the solvent environment, decreasing the fluorescence intensity of the emitted signal. Hence, this extrinsic dye is used as a sensitive biological marker of micropolarity.[166] In hydrophobic environments, excited state-fluorophore molecules experience an intramolecular electron transfer from the dialkylamino donor moiety to an adjacent acceptor (aromatic system) by twisting about the bond between them such that they are perpendicular, forming a highly polar TICT state that

is accompanied by an increase in fluorescence intensity and decrease in emission wavelength.[166] Determination of detergent CMC is possible by measuring the increase in NR fluorescence emission as the regions of hydrophobicity increase upon micellisation (Fig. 1.18).[161]

At concentrations well-below to the optimum detergent concentration at which micelles form in solution, several reports of interactions of detergent monomers to form premicellar aggregates have been made.[167–171] The smaller metastable aggregates of detergent dimers, trimers and higher aggregates have also been shown to exhibit increased hydrophobic regions and to lower the surface tension of aq solution like their more concentrated counterparts.[172]

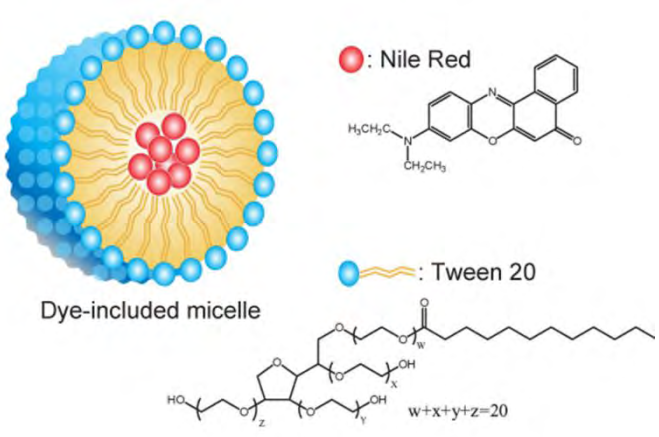

Figure 1.18 A schematic representation of the hydrophobic dye, Nile red, encapsulated to interact with the non-polar hydrocarbon chain region inside a neutral TWEEN-20 detergent micelle with polar ethoxylate headgroups directed outward. Image reproduced with permission from Takai et al., (2013), ©iop.org.[162]

Both the neutral detergents mentioned above were utilised at concentrations well below their reported CMCs in the βH formation experiments and while no mechanistic studies have been reported about the role of detergents in Fe(III)PPIX crystallisation, these neutral amphiphiles and all the lipophilic systems discussed, have successfully been utilised as lipid 'mimics' in colorimetric assays to screen for potential βH inhibitors.[155,173–176] The drugs that target the Hz formation pathway are historically the most successful antimalarials, however, their mechanisms of action are not fully understood.[177]

(1.5) Targeting haemozoin formation for drug treatment

(1.5.1) Quinoline antimalarials

Natural treatments have been used to treat malaria for over thousands of years, with the earliest stemming from the Qinghao plant (*Artemisia annua*) in China[178,179] and later quinoline based antimalarials, isolated from *Peruvian or Jesuit's bark* (later called Cinchona bark) in Peru, used as a natural fever remedy and spread to other parts of the world by the Jesuit priests.[180] This powdered bark was utilised across the world until eventually the active alkaloid compounds, QN and Cinchonidine, were identified in 1820.[181] Limited supply and widespread demand led to the attempted synthesis of quinine, however, this was not accomplished until 1944, by which time the Bayer synthetic antimalarial, Chloroquine (CQ), was already the front-line antimalarial drug.[177,181] CQ was successfully used to treat infection until the emergence of chloroquine-resistant parasites initially in isolated regions and later, spreading throughout the world until its use was eventually phased out. The current treatment for uncomplicated *P.falciparum* malaria infection varies throughout each WHO region and includes artemisinin combination therapy (ACT) of two different drugs with varied modes of action, usually artemether and lumefantrine.[8,182] Although the mechanism of action of artemisinin and its derivatives is highly controversial, it is known that the presence of the endoperoxide bridge is essential for their antimalarial activity[183] and they are responsible for significant oxidative stress within the parasite[184–186], however, this has not been shown to affect Hz formation despite earlier assertions to this.[187] The structures of these drugs, other quinoline based antimalarials as well as selected non-quinoline drugs and are shown in Figure 1.19.

Despite widespread resistance to CQ and its analogues, quinoline-based antimalarials represent a powerful class of antimalarials that remain attractive due to their cheap easy synthesis and the low toxicity and safety of use during pregnancy of some of the compounds. Thus a greater understanding their mode of action offers the potential to design better targeted antimalarials with increased efficacy.[177] Many studies have reported these drugs to accumulate inside the parasite DV and act against the intraerythrocytic stage of the parasite life-cycle.[31,188,189]

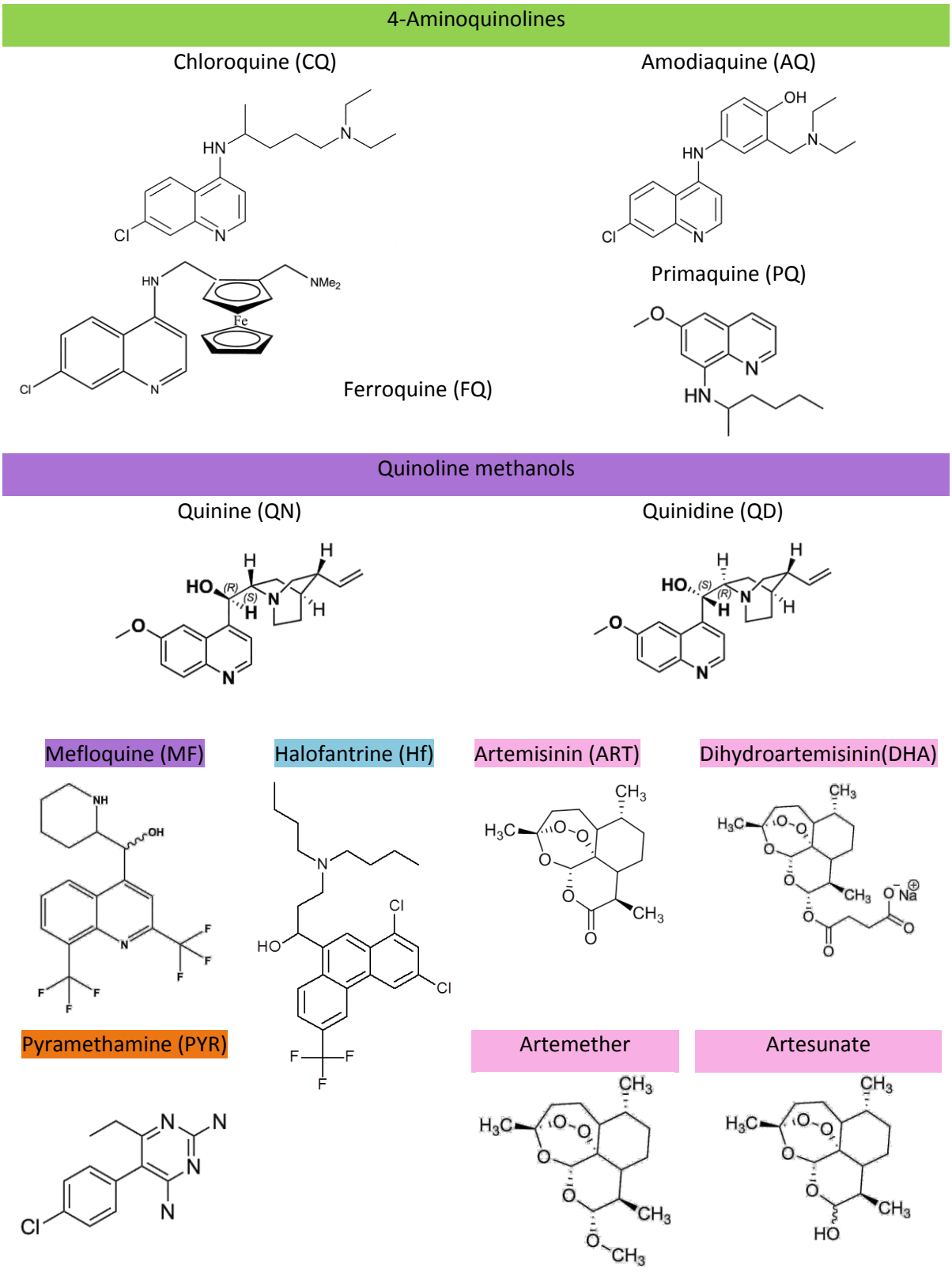

Figure 1.19 The molecular structures of selected quinoline and related antimalarial drugs including the 4-aminoquinolines (green) and quinoline (purple) and aryl methanols (blue) which comprise the Hz inhibitors, as well as important non-quinoline related antimalarials including the anti-folate pyrimethamine (orange) and the artemisinin derivatives (pink).

While the relative effect may vary between the different structural families within this class of antimalarials the most notable effects of quinoline drug treatment include swelling of the DV,[190] inference with Hb ingestion,[191,192] morphological deficiencies of Hz crystals,[193–195] slower parasite growth and eventual death so that the leading hypothesis on their mechanism of action is their ability to inhibit normal Hz formation.[195,196] Other mechanisms of action have been proposed such as DNA intercalation[197,198] or inhibition of enzymes and proteins involved in the Hb degradation pathway including vacuolar phospholipases[199], Hb proteases[200] and even glutathione in the cytosol.[201] However, a recent study by Combrink et al. reported, by using a cell fractionation assay, that a dose-dependent increase in Fe(III)PPIX concentration was measurable upon CQ treatment which was found to correlate with a decrease in the parasite growth curve.[195] In fact, the percentage free Fe(III)PPIX curve was found to cross the parasite survivial curve at approximately the IC_{50} of the drug as seen in Fig. 1.20. A key result was that single-dose treatment with drugs, artesunate and lumefantrine as well as other quinoline antimalarials, amodiaquine, mefloquine and quinine above their IC_{50} concentrations, were all shown to correspond to an increase in percentage free Fe(III)PPIX and a decrease in the amount of Hz formed. This was shown not to be the case for drugs pyrimethamine and sulphadoxine (SP), known to be antifolates rather than targeting the Hz pathway.

In support of this mechanism, *in vitro* studies have shown that these quinoline drugs are capable of inhibiting βH formation[96,202] in ways that have been linked to their lipophilicity [203–205], their pH trapping ability of passive diffusion of charged drugs into the acidic DV [206] and their affinity for binding Fe(III)PPIX in solution.[207] Very early on Macomber et al. noticed the accumulation of CQ in the parasite DV suggesting that this and the effect of CQ on the morphology of Hz was integral to its mechanism of action.[194] Chou and co-workers first identified that CQ strongly binds Fe(III)PPIX from parasite lysates and subsequent research has explored the formation of drug-Fe(III)PPIX complexes in solution that are thought to prevent Fe(III)PPIX from being incorporated into the growing Hz crystal and increase the solubility over Fe(III)PPIX acting as inhibitors of the biomineralisation process.[208,209]

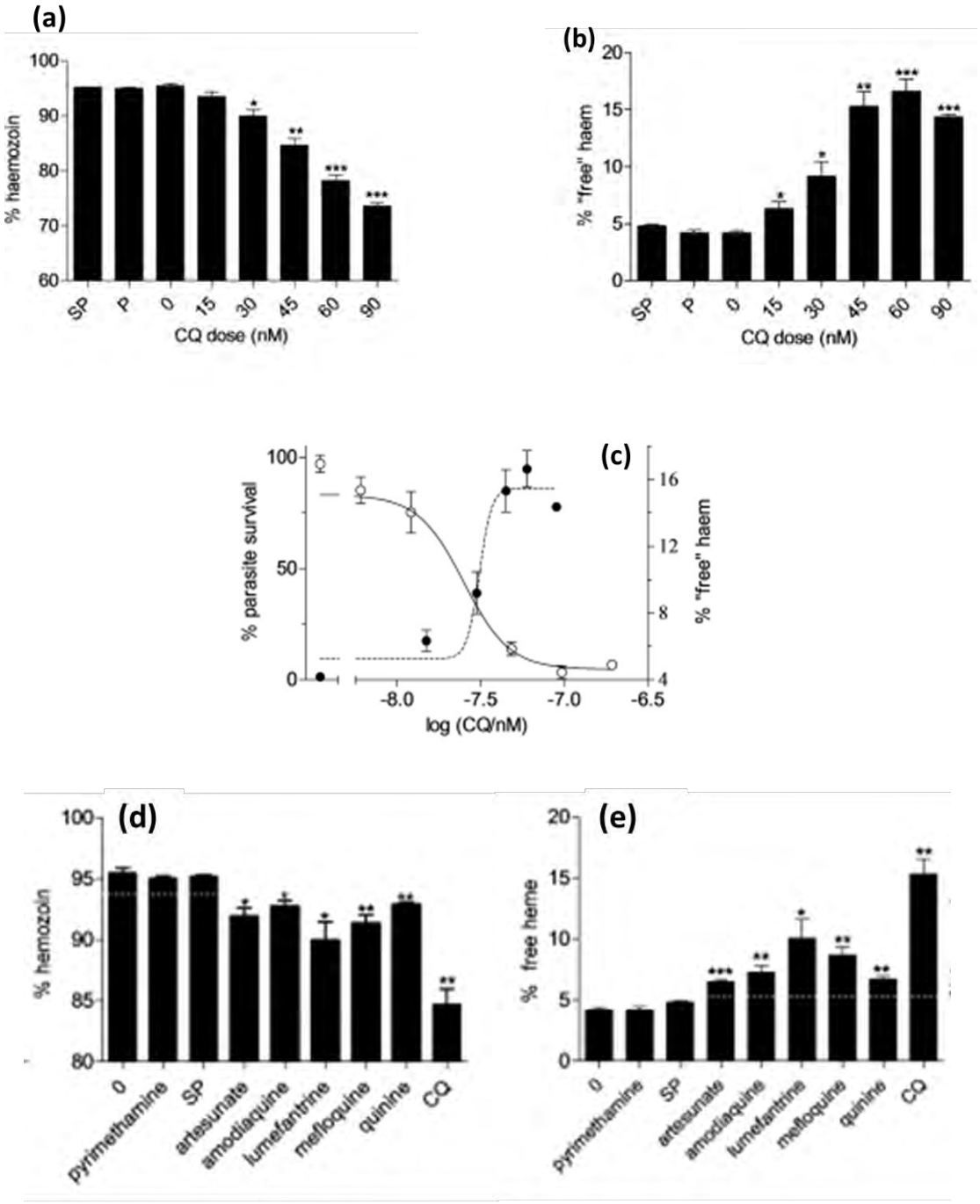

Figure 1.20 Decrease in Hz formation (a&d) and increase in Fe(III)PPIX (b&e) upon CQ (Dose-dependent) and other antimalarial drug treatment of troph stage parasites. Panel (c) shows the correlation between this increase in Fe(III)PPIX and decreasing parasite survival where the curves intersect at the IC_{50} of CQ. Reproduced with permission from Combrink et al. (2013)©American Chemical Society.[195]

(1.5.2) Interaction of quinoline antimalarials and Fe(III)PPIX in solution

Initial reports of studies with nitrogen-containing compounds such as pyridine and cyanide, which showed the ability to bind to and effect changes in the UV-vis spectrum of Fe(III)PPIX in solution led to further studies to measure the ability of quinoline antimalarials (all bearing N-donor atoms) to bind Fe(III)PPIX in solution.[207,210] A variety of spectroscopic and other analytical techniques were employed by various groups from the reports by Chou and Fitch using equilibrium dialysis[208] to Mössbauer characterisation of drug-Fe(III)PPIX complexes[70] , and binding constant values reported by Dorn et al. using isothermal titration calorimetry (ITC) at pH 6.5 and 37°C.[211] This paper proposed that CQ interacts with μ-oxo dimer form of Fe(III)PPIX thereby decreasing the amount of monomeric Fe(III)PPIX available for crystallisation after an earlier report by Moreau et al. suggested CQ interacts with two Fe(III)PPIX μ-oxo dimers in a sandwich type complex via a hydrophobic interaction upon analysis of ^{1}H NMR shifts of CQ in the presence of Fe(III)PPIX.[212] Subsequent ITC measurements by Vippagunta et al. investigated the thermodynamics of association between CQ and its analogues with Fe(III)PPIX reporting multiple CQ molecules to interact with Fe(III)PPIX to form a drug-Fe(III)PPIX complex.[213,214] Bacchawat et al. expanded upon this thermodynamic study of the complexes of CQ and its analogues with Fe(III)PPIX by performing ITC measurements in detergent solution which apparently ensured monomeric Fe(III)PPIX interaction.[215] The authors of these works, however, were unaware of the tendency of Fe(III)PPIX to form two different types of dimers in solution and the assumption that inclusion of triton-X-100 detergent would ensure monomeric Fe(III)PPIX without any spectroscopic confirmation of the fact is questionable.[66]

Thus later studies measured the strength of association between Fe(III)PPIX and several antimalarials in aq DMSO solution so that a correlation between the log *K* of binding and in vitro antimalarial efficacy was made. Aqueous DMSO has been shown to induce the monomeric form of Fe(III)PPIX as described above (section 1.3.3) and therefore the authors were able to monitor changes in the intense Soret band at 405 nm upon association.[216,217] Though these studies were performed in completely different solvent systems and direct comparison is not strictly correct, the values reported by Egan et al. in a two separate reports and the results obtained by Dorn et al. using ITC for the most relevant quinoline drugs are presented in Table 1.1.[211,218]

Table 1.1 Association constants for selected quinoline antimalarial-Fe(III)PPIX complexes determined by UV-vis spectroscopy and ITC experiments.

Drug:Fe(III)PPIX (1:1) association	log *K* (25°C, 40% Aq DMSO, HEPES 20 mM, pH 7.5)[a]	log *K* (aq buffer 250 mM,pH 6.5)[b] stoichiometry (drug:Fe(III)PPIX)
Chloroquine (CQ)	5.52 ± 0.03	5.60 ± 0.19 (1:2)
Amodiaquine (AQ)	5.39 ± 0.04	4.97 ± 0.14 (1:2)
Quinidine (QD)	5.02 ± 0.03*	–
Quinine (QN)	4.10 ± 0.02	4.32 ± 0.04 (1:2.5)
Mefloquine (MF)	3.90 ± 0.08	4.1 ± 0.2 (1:1.5)
Halofantrine (Hf)	5.29 ± 0.01*	4.66 ± 0.07 (1:1)

[a,]*Reported by Egan et al. [218,219] [b]log *K* calculated from *K* values reported by Dorn et al.[211]

The shortcomings of these studies were that low drug aqueous solubility meant that most binding studies were performed in mixed aq systems and at pH values greater than the pH of the parasite DV. The complicated aggregation of Fe(III)PPIX in solution also led to varied binding stoichiometries being proposed for the different drugs especially for QN and MF which were proposed by Dorn et al. to interact with an unusual number of Fe(III)PPIX molecules (Table 1.1). High field NMR spectroscopy was used to evaluate the formation of drug-Fe(III)PPIX complexes for several antimalarials in solution with the authors initially reporting that all the quinoline drugs interact with Fe(III)PPIX μ-oxo dimers.[220,221] However, later studies by this group used magnetic susceptibility studies to show that QN and CQ differentially perturb the monomer- μ-oxo dimer equilibrium with the former favouring monomeric Fe(III)PPIX and the latter proposed to interact with the μ-oxo dimer form of Fe(III)PPIX in aq DMSO and also in cationic and neutral detergent micelles.[222,223] Following on from this observation, Crespo et al. reported a detailed pH investigation of the binding constant of CQ and Fe(III)PPIX in aq methanol solution in which Fe(III)PPIX was reported to be a π-π dimer species, however CQ was found to bind Fe(III)PPIX in a 2:1 stoichiometry, with the authors suggesting that the drug was likely to interact with an unligated face of Fe(III)PPIX and was therefore not the π-π dimer but the μ-oxo dimer with which CQ was proposed to interact.[68]

A very recent comprehensive study using multiple spectroscopic techniques showed the complex that forms between Fe(III)PPIX and CQ in solution was a μ-oxo-dimer and determined by Job Plot that CQ binds Fe(III)PPIX with a 1:2 stoichiometry and an aq association constant, log K_{obs} of 6.5 ± 0.2.[224]

Several works have proposed that rather than interacting through π-π stacking exclusively, quinoline methanol antimalarials form covalent or coordination complexes with Fe(III)PPIX.[225,226] Warhurst conducted a spectrophotometric study of the Fe(III)PPIX complexes formed with QN, QD and MF in benzene where he reported direct coordination of the Fe(III) metal centre in Fe(III)PPIX to the quinuclidine nitrogen (QD and QN) and the piperidine nitrogen (MF).[225] It was later demonstrated using spectroscopic and magnetic studies by Behere and Goff that in non-aq media, an alkoxide-Fe(III) linkage between the hydroxyl of quinine and metal centre of Fe(III)PPIX exists to form a QN-Fe(III)PPIX coordination complex.[226] Later in 2011, Alumasa et al. performed several NMR and binding studies on QN analogues with variation at key functionalities.[227] After evaluation of their βH inhibition and anti-parasite activities, it was proposed that the QN-Fe(III)PPIX structure was formed upon alkoxide coordination and furthermore the formation of a salt-bridge between the quinuclidyl nitrogen and the QN hydroxy proton involved in coordination.

(1.5.3) Fe(III)PPIX-quinoline antimalarial drug complexes

While NMR spectroscopy, Mössbauer studies and various computational methods have been used to propose models for the structure of these antimalarial drug-Fe(III)PPIX complexes, the first crystal structure of an antimalarial-Fe(III)PPIX compound was published as recently as 2008, for the aryl-methanol drug, Hf (Fig. 1.21).[228] Single crystal X-ray diffraction confirmed that monomeric Fe(III)PPIX interacted with Hf through alkoxide coordination of the deprotonated drug hydroxyl group to the Fe(III) centre of Fe(III)PPIX in addition to π-stacking of the phenanthrene ring over the porphyrin and formation of an intermolecular hydrogen bond between the protonated alkyl nitrogen of Hf and the propionate oxygen of a neighbouring Fe(III)PPIX, as predicted through earlier studies.[226,229] The authors proposed that this mode of binding was likely for the structurally similar quinoline methanol drugs, QN and QD, which was confirmed recently when the crystal structures of their Fe(III)PPIX

complexes were published (Fig 1.21).[230] Both quinoline methanol drugs, QN and QD, were found to complex Fe(III)PPIX through formation of an alkoxide bond to the Fe(III) centre via their benzylic alcohol functional group as well as π-stacking between the porphyrin and aromatic ring systems and finally the formation of an intramolecular hydrogen bond between the protonated amine of the quinuclidine ring and the propionate oxygen of Fe(III)PPIX. Previously performed molecular modelling calculations on the strain energy required to form this intramolecular hydrogen bond showed that the ease in which it was formed correlated with the observed biological activity of these drugs and their inactive enantiomers, epiquinine (eQN) and epiquinidine (eQD).[228] It was suggested that QD, the most active of the quinolone methanol drugs, exhibited the lowest energy penality associated with formation of this hydrogen bond,[228] an observation that was confirmed by the crystal formation with this hydrogen bond present despite being crystallised from an environment rich with hydrogen bond partners (3:7 DMSO: methanol).[230] These coordination complexes were all obtained from organic solvents that may allow for specific interactions that are either absent or exclude those that only relevant in aq solution therefore the question whether these complexes exist in aq or lipophilic solution, remains relevant.

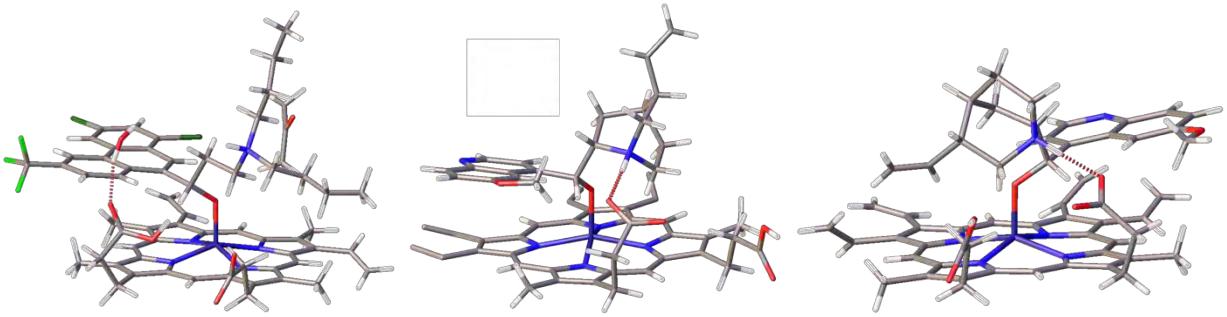

Figure 1.21 Crystal structures of aryl methanol (Hf) and quinoline methanol (QN and QD) drugs and Fe(III)PPIX. All the structures possess the proposed three-point binding mode of (1) the alkoxide bond from each drug hydroxyl group to the Fe(III) centre of Fe(III)PPIX. (2) The π-stacking between the ring systems and (3) formation of a hydrogen bond between the propionate of Fe(III)PPIX and the protonated quinuclidine or aliphatic nitrogen on each drug (for adjacent Fe(III)PPIX molecules in Hf, not shown here). Structures reproduced from Cambridge Structural Database (CSD) reference codes: BOCGEG (Hf), CETTOM (QN) and CETTUS (QD).[231]

To date, no crystal structures of a 4-amino quinoline drug-Fe(III)PPIX complex have been published. Solid state characterisation of the precipitated CQ-Fe(III)PPIX complex from acidic aq solution has yielded conflicting reports of Fe(III)PPIX speciation with solid-state NMR studies leading to a proposed covalent CQ-Fe(III)PPIX complex.[232] In contrast, Dascombe et al. performed mass spectrometry on an isolated Fe(III)PPIX adduct with a CQ analogue, metaquine with a molecular ion peak that correspond to a 1:1 complex for this drug.[233] These results contrast with those obtained from Mössbauer measurements of isolated CQ-Fe(III)PPIX and QN-Fe(III)PPIX complexes where the former produced a distinctly different spectrum which was suggested to correspond to the μ-oxo dimer compared to the latter, which was subsequently proven to correspond to a 1:1 complex.[70,230] In light of an alternative proposed mechanisms of action for this class of antimalarial, the possibility of this drug not exerting its influence through Fe(III)PPIX complexation has recently been explored.

(1.5.4) Interaction of quinoline antimalarials with haemozoin/ β-Haematin

Not all compounds that exhibit Fe(III)PPIX binding abilities are capable of inhibiting Hz formation *in vitro*.[203,234,235] Neither have all Hz inhibitors been shown to associate with Fe(III)PPIX in solution, thus an alternative mechanism of action has been proposed and explored.[28,63,236] Early work by Sullivan et al. using TEM detected that CQ was in close association with Hz crystals and later upon discovery of CQ's ability to complex Fe(III)PPIX, suggested that the drug-Fe(III)PPIX complex could be incorporated into the growing crystal thereby preventing any further Fe(III)PPIX deposition and effectively inhibiting crystal growth.[236] This mechanism was thought to be responsible for the exaggerated accumulation of all quinoline drugs in the DV.[237] Later, when it was established that Hz was not a coordination polymer and could not be inhibited by coordination at a single site, it was suggested that the quinoline antimalarials themselves act by adsorbing to the smallest and fastest growing (001) and $(00\bar{1})$ crystal faces of Hz capping further crystal growth.[27]

Pagola et al. suggested this based on the amount of erythrocyte Hb, the surface area of Hz crystals and the proportion of CQ measured to be accumulated in the DV and the surface area of Hz crystals. The (001) and $(00\bar{1})$ Hz crystal faces are highly corrugated with grooves between the exposed vinyl and methyl groups of the porphyrins, as well as the flexible

propionic acid groups allowing for stereospecific contact with Hz inhibitors.[28] A model of the proposed drug-Hz adsorption was published by Buller et al. using molecular modelling to identify four stereospecific molecular interactions between the exposed unligated porphyrin faces and propionic acid side chains of the crystal and monoprotic CQ (Fig. 1.22). [28] Specifically, (i) the formation of a salt bridge between the protonated nitrogen in the CQ side chain and an exposed COO^- of a Fe(III)PPIX propionic acid (2.7 Å). (ii) An interaction between the quinoline N of CQ and the proton of a vinyl group on the porphyrin (2.4 Å), (iii) an interaction between the 7-chloro substituent on the quinoline ring of CQ and the methyl group on a Fe(III)PPIX (3.0 Å) and finally (iv) a contact between the NH of the CQ 4-amino side chain and the π electron cloud of a C=C group on a neighbouring porphyrin (2.7 Å).

The use of exclusively protonated CQ in this model poses a question as to the charge of the drug inside the parasite DV which pK_a measurements have shown to be unlikely to be monoprotonated under acidic conditions.[238] The first experimental evidence for this mechanism was offered by a study using GIXD techniques on the effect of 10% CQ and QN on βH crystal growth.[144] Solomonov and co-workers reported that the rate of βH crystal formation was decreased in the presence of these drugs and the crystal morphology was affected. βH crystals grown in chloroform medium containing these drugs was found to have tapered ends (Fig. 1.23) which was suggested to be as a result of quinoline drug adsorption to exposed (001) and (011) crystal ledges. The authors rationalised that the adsorption of a quinoline additive to the crystal on a particular face would manifest by as a reduction in crystal coherence on the perpendicular face which could be observed as a broadening of the *Bragg* reflection along that length. Synchrotron PXRD measurements were able to show a lack of symmetry and elongated diffraction pattern of weak intensity that was suggestive of a reduced crystal domain along the c-axis.[144]

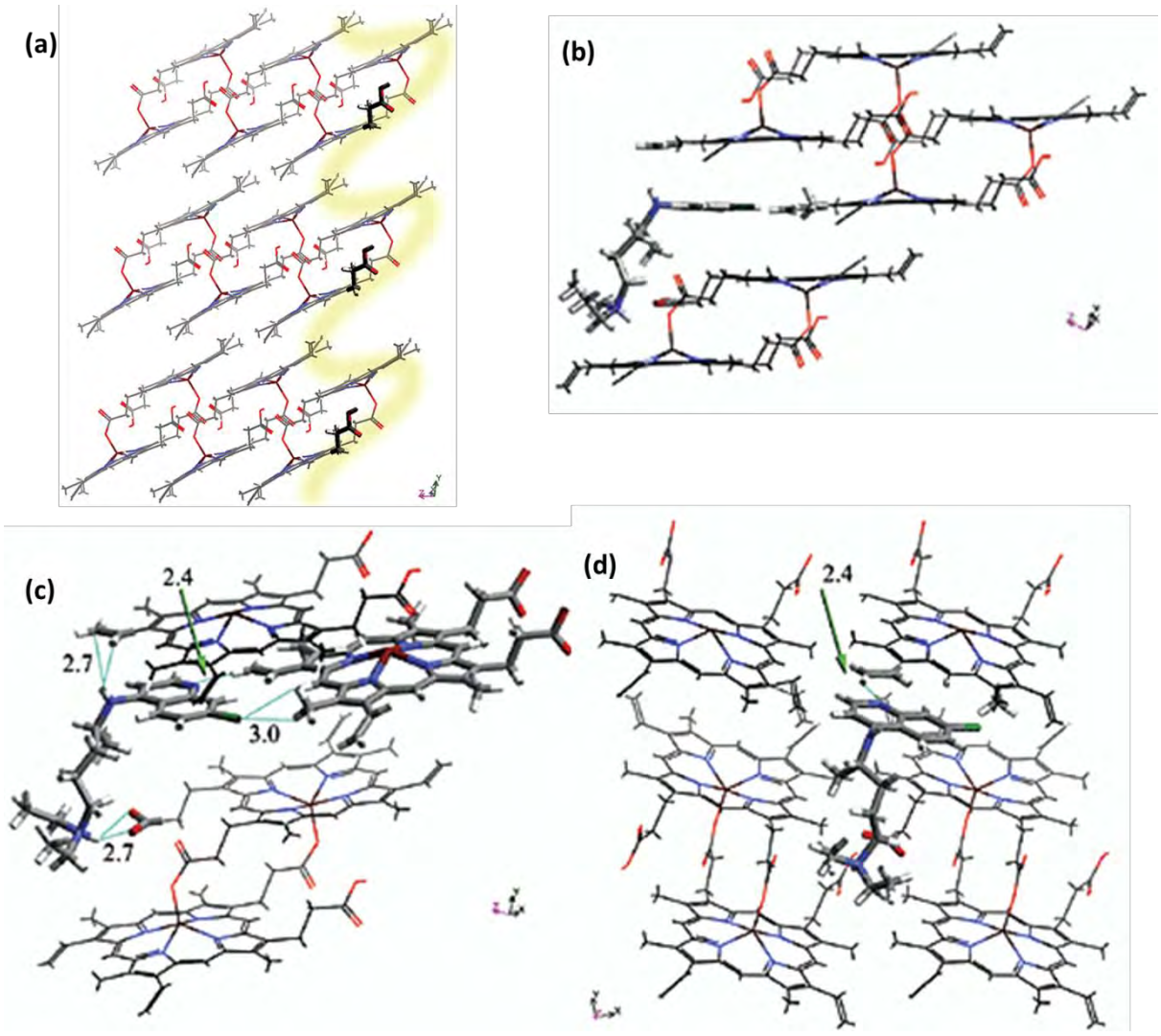

Figure 1.22(a) View along the a-axis of βH to show corrugated surface of the (001) face with 'grooves' highlighted in yellow for the proposed quinoline antimalarial interaction which is shown in **(b)**. The interactions proposed for CQ include **N**···**H**CC (2.4 Å), **Cl**···**H**$_3$C (3.0 Å), **N**H···**O**$_2$C (2.7 Å), N**H**···**CC**(π-cloud) (2.7 Å) as seen in **(c)** and shown perpendicular to the (001) face in **(d)**. Images reproduced with permission from Buller et al. (2012) © American Chemical Society.[28]

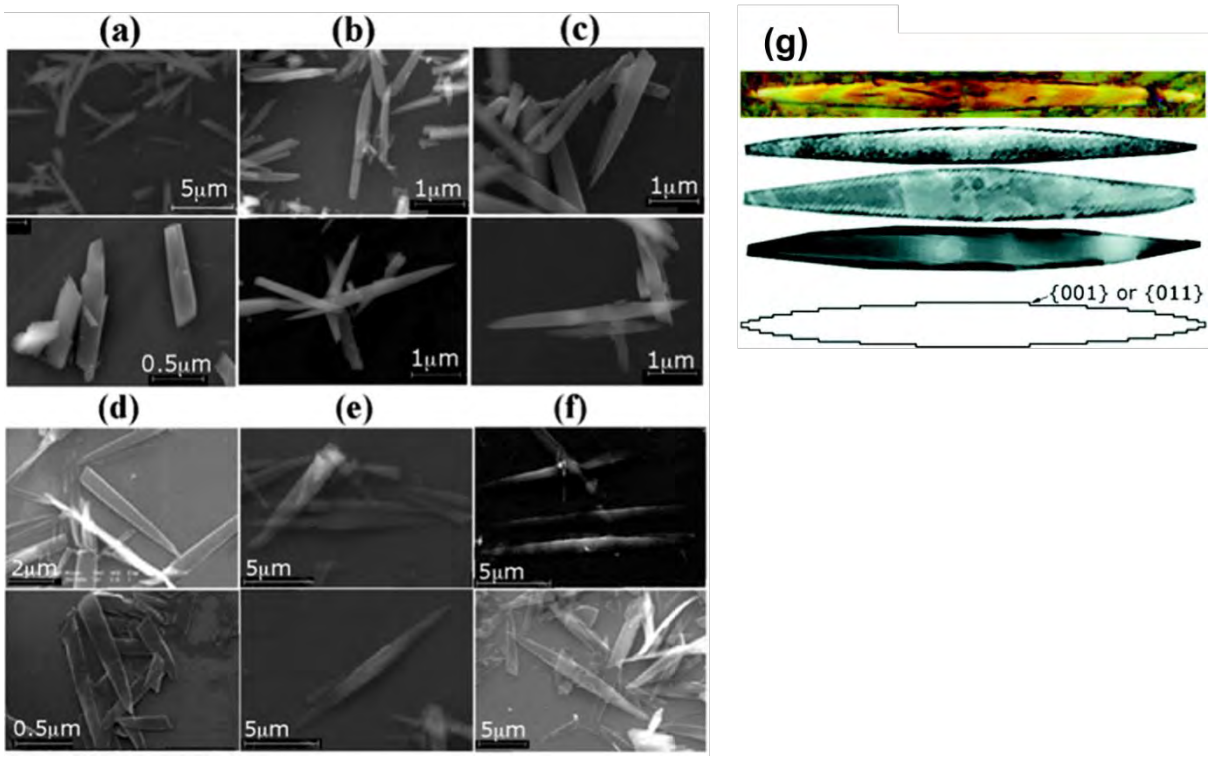

Figure 1.23 SEM-micrographs of βH crystals grown from DMSO-MeOH in **(a)** the absence of antimalarials and **(b&c)** in the presence of 10% QN and CQ, respectively. Images **(d-f)** were of crystals grown from chloroform in the absence of drug **(d)** and with 10% QN and CQ, respectively. **(e&f)** to illustrate the symmetrical tapered ends induced by the proposed drug adsorption. **(g)** Images of the symmetrical βH crystal grown in 10% drug solution in colour from an optical microscope and in blue from TEM. The 'ledges' for quinoline adsorption are indicated on the (001) and (011) faces. Images are reproduced with permission from Solomonov et al., (2007),©American Chemical Society.[144]

Alternative support for this adsorption model was recently obtained from a kinetic study of βH formation mediated by a model lipid, MPG, in the presence of quinoline antimalarials CQ and QD.[63]

(1.5.5) Kinetic model of β-Haematin inhibition in neutral lipid solution

A recent investigation into the effect of two quinoline antimalarials on the rates of lipid-mediated βH formation reported a decrease in rates observed in the presence of drug at low concentration leading to an eventual decrease in the yield of βH formed at higher drug concentrations.[63] At no point over the drug range tested was complete inhibition of βH

formation observed. In order to explain this, the authors proposed a kinetic model that combined two proposed modes of inhibition to compete with the crystallisation of Fe(III)PPIX as illustrated in Scheme 1.2.

To account for the initial decrease in rates of βH formation in the presence of low drug concentrations, the authors proposed that the quinoline antimalarials adsorbed to available sites on the growing βH crystal face to impede crystal growth. This process alone was insufficient to account for the eventual decrease in yield at high drug concentrations and so the ability of these drugs to complex Fe(III)PPIX was also considered. As the concentration of drug was increased, this complex was proposed to precipitate out of solution depleting the amount of Fe(III)PPIX available for crystallisation.

The observed initial decrease in rate of crystallisation and exponential kinetic profile was modelled with the Avrami equation (1.2.2) and using the Langmuir isotherm to account for the adsorption of the drug to crystal surface sites. The experimental data was found to fit this adsorption model such that the strength of drug adsorption to the crystal face, $K_{ads,}$ was computed for CQ and QD with log K_{ads} of 5.55 ± 0.03 and 4.92 ± 0.01 for each drug, respectively.[63] Interestingly the strength of this adsorption was found to correlate with reported biological activity of these drugs.[239] This observation was also in agreement with the suggestion by Buller et al. that there exists shorter porphyrin-drug contact distances between the (001) face of βH and CQ compared to QD.[28] To account for the observed decrease in the yield of βH at high drug concentrations, the solution state interaction of these drugs with Fe(III)PPIX to form solid drug-Fe(III)PPIX complexes with a rate constant of k_2 that was also incorporated into the kinetic model which is described by equation 1.3.

$$\%\ \beta\mathrm{H} = \frac{100\mathrm{Yz}}{(\mathrm{z} + k_2[D]^2 + k_2 K_{ads}[\mathrm{D}]^3)}\left(1 - \mathrm{e}^{-\left(\frac{\mathrm{z}+k_2[D]^2+k_2K_{ads}[\mathrm{D}]^3}{1+K_{ads}[D]}\right)\mathrm{t}}\right) \qquad (1.3)$$

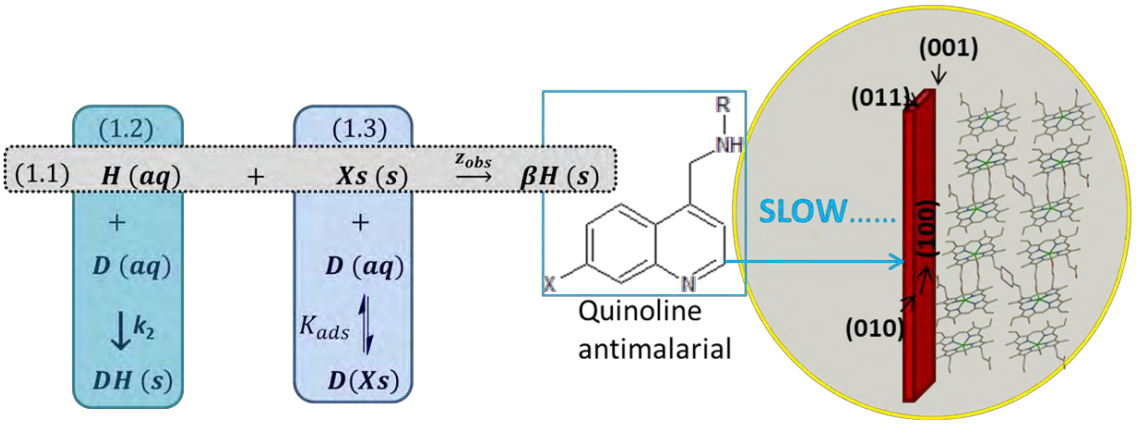

Scheme 1.2 Proposed kinetic model for (1.1) βH formation with rate constant, z_{obs} , in the presence of quinoline antimalarial drugs, D, in a lipid system. (1.2) The Fe(III)PPIX starting material, H, is thought to form a solid drug-Fe(III)PPIX complex, DH, with rate constant, k_2, in a competing process (1.3) with the adsorption of the drug onto the βH crystal surface, Xs, with adsorption constant, K_{ads}, as illustrated by the graphic. Scheme adapted with permission from Gildenhuys et al., (2013)©American Chemical Society.[63]

Subsequently, independent validation of the quinoline drug adsorption to preformed βH crystals was provided by measuring the depletion of drug concentration in solution after 48 hr incubation with the crystals in aq solution.[240] This report showed that both CQ and QD adsorbed to βH crystals, however, quantitation of this adsorption was not provided. Regardless of their exact mechanism of action, quinoline antimalarials affect a known target that remains attractive for parasite specific inhibitors.

A very recent paper by Olafson et al. utilised time-resolved AFM to show that CQ adsorbs to the (001) face of βH between Fe(III)PPIX growth steps thereby affecting 2-D nucleation leading to slower step-growth and at higher concentrations ([CQ] = 2 μM), complete inhibition of crystal layer generation.[153] This adsorption of CQ to particular sites that result in hindered step propagation of the crystal was proposed to be the mechanism of action of CQ. The authors, however, assume that CQ forms a 1:1 complex with Fe(III)PPIX in solution despite the evidence of alternative speciation mentioned and thus dismiss this complexation as insufficient to account for the reduced growth rates measured by AFM.[153] Many insights on the mechanism of action of active pharmaceuticals have come from study of their *in vitro* properties.[122,202] To reconcile the mechanisms of action of these drugs, several approaches

have been taken, and integral to them was evaluation of the βH inhibition activities of known quinoline antimalarials. Traditionally this class of antimalarials have been very successful and thus efforts to design novel analogues that circumvent resistance pathways are ongoing.[176,241–243] With reports of artemisinin resistance emerging in different regions,[244] large scale *in vitro* drug screening against this target has been employed to characterise known and unknown inhibitors with novel pharmacophores.[175,176,245]

(1.5.6) Lipophilic assays for screening β-haematin inhibitors

The ability of various compounds to inhibit βH formation has been investigated using a variety of methods including UV-vis spectrophotometry, fluorometric and radiometric assays.[96,123,202,245–250] Initial screening for βH inhibitors employed actual troph lysate, Hz extracts and seed βH crystals to induce crystallisation and measure antimalarial effect[246,251], however, these assays were subsequently replaced by cheaper less time-consuming colorimetric tests that used acetate buffer or fatty acids to initiate βH formation under acidic pH conditions and physiological and non-physiological temperatures.[119,252–254]

Each assay has a βH initiator and a detection method for quantifying the amount of βH formed either directly or by measurement of the Fe(III)PPIX starting material post incubation with a number of different pH, temperature and incubation times used.[119,255] The most commonly used methods of detection include the pyridine hemichrome inhibition of β-haematin (Phiβ) assay developed by Ncokazi and Egan which exploits the ability of 5% aqueous pyridine solution to bind unreacted Fe(III)PPIX to form the easily quantified six-coordinate bis-pyridyl complex that exhibits the characteristic sharp Soret band at 405 nm present in a typical absorbance spectrum of monomeric Fe(III)PPIX.[253] Other methods exploit the differential solubility of the starting material, Fe(III)PPIX, and the βH product in solutions of 0.15 M sodium bicarbonate and 2% SDS solution or DMSO followed by base treatment to isolate each fraction for quantification.[118,119,250] IR spectrophotometry and PXRD techniques are used to confirm the presence of βH. The IC_{50} (50% inhibitory concentration) of each drug is reported as either the concentration at which only 50% βH is formed or at which 50% unconverted Fe(III)PPIX remains in solution. This value for a particular drug can vary from assay to assay but these assays usually serve to provide an indication of potential Hz inhibition in the parasite and are a first indication of lead properties.[255]

Recently, these assays aimed to be more biologically relevant while maintaining the advantage of short incubation times and cheap materials for high-throughput screening. Thus the use of neutral detergents as lipid 'mimics' to mediate βH formation for assaying potential inhibition activity has become standard.[255] As mentioned, the first application of these amphiphilic solutions as initiators for βH formation was by Fitch et al. where the authors showed that SDS and TWEEN-80 were capable of effectively forming βH,[118] later Huy et al. applied this in a TWEEN-20 mediated colorimetric assay to evaluate inhibition activity under biomimetic conditions.[250] Currently another neutral detergent NP-40 has primarily been used in a multiwell plate assay to identify potential novel βH inhibiting compounds.[155,175,256] The activity trends obtained with these lipophilic *in vitro* assays compare well with other assays and the biological activities of established Hz inhibiting antimalarials drugs so that they have been used to train *in silico* prediction models of potential drug activity.[239,241,257]

Table 1.2 lists the IC_{50} values obtained using the NP-40 detergent and other initiator assays as well as those obtained in an *in vitro* parasite assay against the chloroquine sensitive *P. falciparum* strain, 3D7, published by Hawley et al. for each drug.[239] While these values all differ, the observed biological trend in activity is maintained, with the 4-amino quinolines, CQ and AQ, showing increased activity over the quinoline methanols, QD and QN. This differential activity is thought to arise from a difference in their mechanism of action via differential interaction with Fe(III)PPIX or the crystal product itself.[191,258] However, the use of different types of inducers that all mediate βH crystallisation has not been probed to offer a mechanistic understanding of their role in this process. While attempts to rationalise the mechanisms of lipid-mediated Hz formation and quinoline drug inhibition over the course of this work were unrealistic, further understanding of the processes that comprise Fe(III)PPIX crystallisation in the acidic environment of the parasite DV is clearly necessary.

Table 1.2 Efficacy (IC_{50}) of drugs from two types of quinoline antimalarial families, the 4-aminoquinolines (CQ and AQ) and the quinoline methanols (QD and QN) for *in vitro* activity against Haemozoin formation (nM) and strength of β-Haematin inhibition (μM).

DRUG	Biological IC_{50} (nM) CQ-sensitive (D6)[a]	βH inhibition Assay type (βHIA) (μM)					
		Phiβ equivalents (12.9 M acetate)[b]	NP-40[c]	TWEEN-20[d]	Hz extract[e]	neutral lipid [f]	BHIA[g] in equivalents (acetic acid)
CQ	14	1.19 ± 0.03	53	59 ± 6.8	45 ± 9	16.4 ± 0.5	1.63 ± 0.64
AQ	7.8	1.45 ± 0.08	21	45.3 ± 1.2	60 ± 1	9.0 ± 0.4	0.85 ± 0.25
QD	21.5	1.5 ± 0.1	24.7 ± 1.4*	-	-	51.1 ± 5.8	-
QN	34.2	3.5 ± 0.2	52.3 ± 1.7*	170 ± 12.3	160 ± 10	73.9 ± 12.8	5.48 ± 1.31

[a]Biological IC_{50} values obtained from Hawley et al. [259]

[b] Phiβ values reported by Ncokazi et al.[253]

[c] NP-40 assay values reported by Carter et al.[155]

[d] TWEEN-20 initiator IC_{50} obtained from Huy et al.[173]

[e]Purified Hz initiator assay reported by Dorn et al.[119]

[f] IC_{50} obtained from MPG/aq interface (Gildenhuys, 2013).[240]

[g] BHIA from Parapini et al.[255] ,

*Unpublished results, (Egan Laboratory, 2014).

(1.6) Aims and Objectives

(1.6.1) Aims

This work aimed to probe the nature of the interaction between Fe(III)PPIX and the proposed biological neutral lipid blend by establishing the lipophilicity of Fe(III)PPIX, to investigate of the effect of known quinoline antimalarials on this lipid partitioning and to use detergents as lipid 'mimics' to evaluate their ability to mediate β-Haematin formation through stabilisation of a particular Fe(III)PPIX species so that insights into the behaviour of Fe(III)PPIX in a lipophilic environment may be made. Lastly, to investigate the kinetics of β-Haematin formation in this detergent environment in the absence and presence of quinoline antimalarials to determine its suitability as a lipid 'mimic' in drug screening. To achieve these aims the following objectives were proposed:

(1.6.2) Objectives

(1) Evaluate the lipophilicity of Fe(III)PPIX and measure its partitioning profile into neutral lipid droplets over a pH range using fluorescence quenching.

(2) To determine the effect of quinoline antimalarials on this partitioning profile over the same pH range.

(3) To use UV-visible spectrophotometry and magnetic susceptibility to analyse the speciation of Fe(III)PPIX in neutral, zwitterionic, cationic and anionic detergent solutions as a function of pH at concentrations above and below their critical micellar concentration.

(4) To evaluate the ability of each detergent to promote β-Haematin formation under physiological pH and temperature conditions with regards to their established speciation of Fe(III)PPIX.

(5) To determine the association constants and stoichiometry of interaction between quinoline drugs and Fe(III)PPIX in detergent solution and their effect on speciation.

(6) To probe the nature of detergent-Fe(III)PPIX interaction using ^{1}H NMR spectroscopy.

(7) To measure the kinetics of detergent mediated βH formation in the presence of quinoline drugs using a proposed kinetic model to compare the effect of a neutral detergent with that of the neutral lipid in this process.

Chapter 2:
Theoretical background to techniques employed

(2.1) Introduction

Several classical physical and analytical chemistry techniques were employed throughout this project to study the behaviour of ferriprotoporphyrin IX (Fe(III)PPIX) in amphiphilic solution. The primary technique used throughout this work to characterise the speciation of Fe(III)PPIX and to probe its drug association properties was ultraviolet visible (UV-vis) spectroscopy (see 2.2). Solution state magnetic susceptibility measurements, specifically Evans method nuclear magnetic resonance (NMR) spectroscopy (see 2.3) experiments were also used to confirm the prevalent Fe(III)PPIX species. Infrared (IR) spectroscopy (see 2.4) and powder X-ray diffraction (see Chapter 6) were used to confirm the presence of β-haematin (βH) products. Fluorescence spectroscopy (see 2.5) was conducted in order to monitor the partitioning of Fe(III)PPIX into lipid droplets by Nile Red quenching experiments. This chapter outlines the fundaments of each technique and highlights key understandings in the study of metalloporphyrin chemistry and interactions with relevance to this work.

(2.2) UV-visible spectroscopy

(2.2.1) General theory

UV-vis spectroscopy is a well-established versatile, sensitive and cost-effective technique for analytical chemistry enabling the use of dilute samples and eliminating the need for specialised solvents.[260] This technique provides insight into the electron distribution within a molecule by measuring its interaction with light in the UV (wavelength (λ) = 10 - 380 nm) and visible (λ = 380-750 nm) portion of the electromagnetic spectrum.[261] The absorbance of photons by molecules can result in an electronic transition from their lowest energy ground state configuration to a higher energy excited state.[261] The types of allowed electron transitions upon UV-vis excitation from filled σ or π molecular orbitals (MO's) to empty σ^* or π^* MO's (Figure 2.1) give rise to the intense spectroscopic features associated with the distinctive electronic distribution of a certain molecular species. $\sigma \rightarrow \sigma^*$ transitions require the largest amount of energy and appear at low absorption wavelengths (< 200 nm) while

$n \rightarrow \sigma^*$ transitions associated with non-bonding lone pairs on saturated compounds display absorption peaks in the region of 150 -250 nm. Most UV-vis absorption peaks (200 - 750 nm) arise from lower energy transitions from $n \rightarrow \pi^*$ and $\pi \rightarrow \pi^*$ excited states.[262] Many inorganic compounds also show charge transfer (CT) absorption bands where radiation absorption involves the transfer of electrons (e^-) from a donor component to an orbital associated with the acceptor component. Transitions that are observed for a particular molecule is dependent on the molecular structure and symmetry of that molecule.[263]

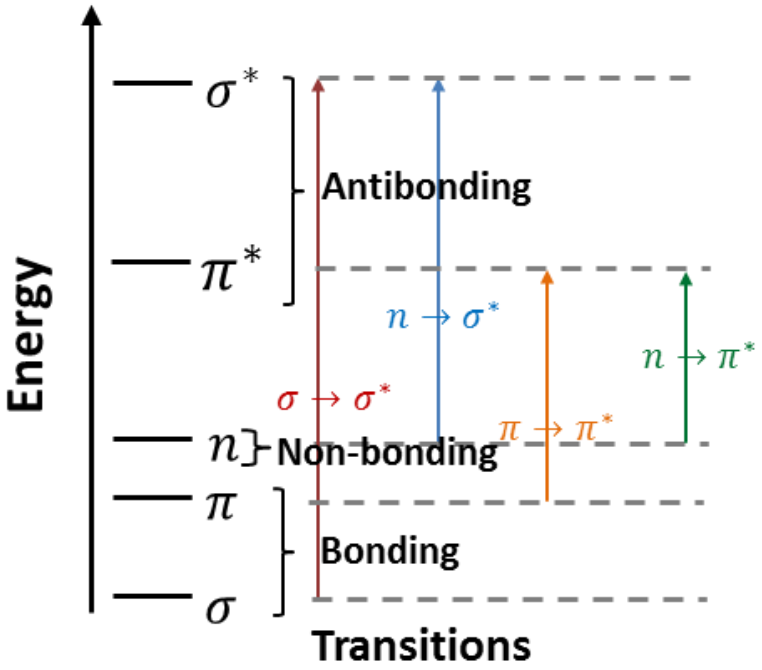

Figure 2.1 Electron transitions as a result of excitation in the ultraviolet-visible region.

As shown in Figure 2.2, a lamp source provides light which is passed through a diffraction grating that splits it up into its components. A monochromator (**M**) isolates each component wavelength of light which is then passed through the sample where it is either transmitted (allowed passage through) or adsorbed by the molecules in the sample.

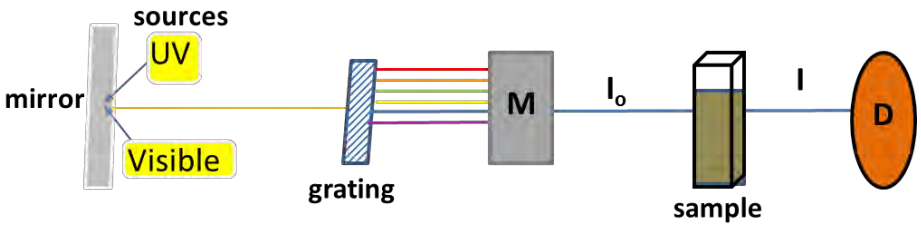

Figure 2.2. A schematic diagram of basic UV-vis spectrophotometer

The amount of light allowed through the sample, the percentage transmittance ($I/I_0 \times 100$) is measured by an electronic detector depicted as **D**. The resulting absorbed light is the ratio of the incident light, $\mathbf{I_o}$ and the intensity of radiation measured by the detector, **I.**[264] Typical UV-vis output is an absorbance (- log T) as this function can be linearly related to the concentration of the sample using the Beer- Lambert Law (Eqn. 2.1). [265]

$$\boldsymbol{A}\ (unitless) = \log\left(\frac{I}{I_0}\right) = \varepsilon_\lambda\ \boldsymbol{c}\ l \qquad (2.1)$$

Absorbance (**A**) or log of the ratio of detected light, *I* to incident light, I_0 (Transmission) is related to the distance the incident light must travel through the sample (pathlength of the cuvette), ***l*** (in cm) and the concentration, **c** of the sample (mol.dm^{-3}) and the molar absorptivity at a particular wavelength (nm), referred to as the extinction coefficient, $\boldsymbol{\varepsilon_\lambda}$ is a measure of the probability that a photon of that energy will be absorbed by the sample.[266] This linear relationship between concentration of solute and absorbance at a particular wavelength is widely used to quantify molecules in solution after accounting for any reflection of light, light scattering by aggregating solutes or excitation of any samples susceptible to fluorescence emission.

(2.2.2) The electronic spectrum of Fe(III)PPIX

Porphyrins and their metallated derivatives exhibit a unique electronic signature in the UV - vis spectrum.[267] Fe(III)PPIX is a metalloporphyrin with characteristic features arising from its 22 conjugated π electrons in the porphyrin macrocycle, approximate four-fold D_{4h} symmetry, d^5 valence electron count and in this case, high-spin Fe^{3+} centre. These porphine properties along with any ligand to metal charge transfer electronic transitions contribute to its

chromophore and determine the prominent features of its UV-vis spectrum shown in Figure 2.3a. [74]

Gouterman's four orbital model is the foremost theory for the interpretation of the UV-vis spectrum of Fe(III)PPIX resulting from transitions between the two highest occupied molecular orbitals (HOMOs) to the two lowest unoccupied molecular orbitals (LUMOs) of the porphine moiety predicted from a linear combination of atomic orbital (LCAO) calculation using an extended Hückel treatment for conjugation.[268] The model proposes that excitation of ground state electrons from occupied π MO's (symmetry labels $\mathbf{a}_{2u}$ and $\mathbf{a}_{1u}$) to unoccupied π^* MO's (labelled $\boldsymbol{e}_{xg}$ *and* e_{yg}) account for the UV-vis pattern observed. Transitions between these orbitals produce two excited states, both of $^1\mathrm{E}_\mathrm{u}$ character which are split by strong orbital mixing with varied energy and intensity. [269] The most intense band, the Soret or B band is observed in the 400 nm region with Ɛ ≃10^5 $M^{-1}.cm^{-1}$ (shown in blue, Fig.2.3a) originates from $\pi \rightarrow \pi^*$ transitions from the nearly degenerate $\mathbf{a}_u$ HOMOs to the doubly degenerate ***e**** LUMOs. The weaker Q-bands with Ɛ ≃10^4 $M^{-1}.cm^{-1}$ (shown in green, 470-550 nm) originate from another transition from the symmetrical $\mathbf{a}_{2u}$ HOMO orbital to the $\boldsymbol{e}_g^*$ LUMOs (Figure 2.3b). [270]

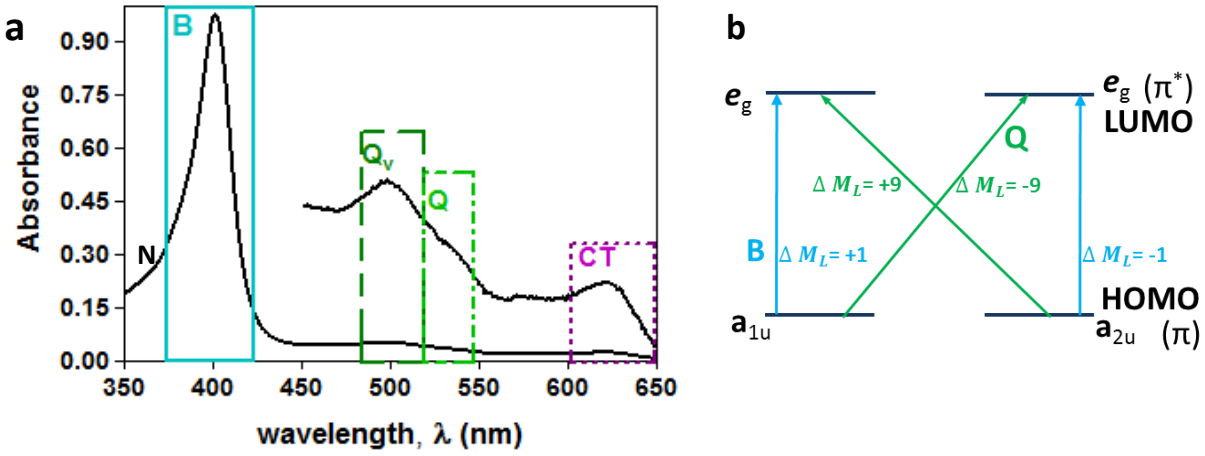

Figure 2.3 (a) UV-vis spectrum of Fe(III)PPIX obtained from 40% (v/v) aq DMSO, pH 7.5 with the main bands highlighted, B (λ=375-425 nm) and Q (λ = 475–550 nm) bands arise from π HOMO → π * LUMO transitions highlighted by the Gouterman four orbital model, the CT (λ= 600-650 nm) band explained by the CT transitions of the LCAO model as well as higher excited state, N (λ = 350nm) band are depicted. **(b)** Highlight of MO transitions that result in B and Q bands, the ΔM_L values accounting for the band intensity difference are given for each transition.

The transitions leading to the B band are accompanied by quantum mechanically allowed changes in the angular momentum quantum number ($\Delta M_L = \pm 1$), the ground state electron and excited state electron circulate in opposite direction resulting in increased electron-electron collisions (Hund's rule) and therefore displaying a higher energy absorption. [269] Upon excitation, Q band transitions have $\Delta M_L \neq \pm 1$ with their electrons circulating in the same direction, effectively resulting in partial cancellation of dipole moments and lower energy bands (Figure 2.3b). [271] The difference in intensity observed between the B and Q bands can be explained by their difference in ΔM_L. The selection rule (Laporte orbital rule) states that electronic transitions with $\Delta M_L = \pm 1$ are allowed accounting for an intense band for a higher energy excited state manifested as the B band. Lower energy state Q band transitions accompanied by $\Delta M_L = \pm 9$ are forbidden and exhibit lower oscillator strength.[271] The electrons in the $e_g(\pi^*)$ MOs can be promoted to a vibrationally excited state causing further splitting of the B and Q bands into $B_{x,y}$ and $Q_{x,y}$ bands respectively (Figure 2.4).

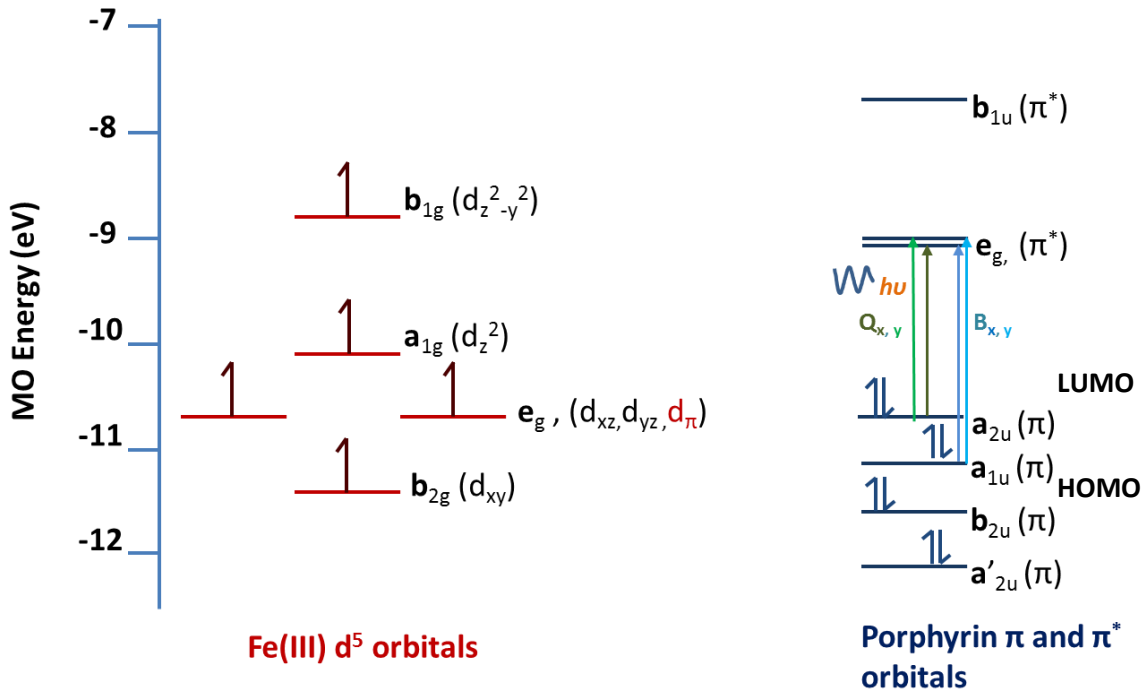

Figure 2.4 Molecular orbital diagram for Fe(III)PPIX, Fe(III) and porphyrin orbitals calculated using LCAO theory. When irradiated ($h\upsilon$), $\pi \rightarrow \pi^*$ transitions from the porphyrin a_{1u}, a_{2u} HOMO orbitals to the e_g LUMO orbitals produce intense B (Soret) and weak Q-bands, characteristic of haem UV-vis spectrum.

The degree, position and nature of substitution on the porphyrin affect the symmetry which results in variation in the vibronic splitting of the Q band. [267,272] Transition moments to the higher excited states from the lower occupied MO's $\mathbf{a}'_{2u,}\ \mathbf{b}_{2u} \rightarrow\ \boldsymbol{e}_g(\pi^*)$ can give rise to other minor bands, such as the **N**-band appearing as a shoulder to the intense Soret band.[267]

Although sufficient to account for the $\pi \rightarrow \pi^*$ transitions responsible for the most intense bands observed in the UV-vis spectrum of haem, the Gouterman four orbital model fails to account for all the unique features of the spectrum that arise from the nature of the metal, its axial ligand and the peripheral groups on the porphyrin.[273] Fe(III)PPIX in pH neutral aqueous solution is a five-coordinate, high spin (S = $^5/_2$) with H_2O as the axial ligand leading to d^5 occupancy of the metal atomic orbitals. The Hückel LCAO method applied by Makinen and Churg to determine the MO diagram of iron porphyrins as demonstrated for H_2O-metmyoglobin is depicted in Figure 2.4.[274] The peaks arising from the porphyrin transitions identified using LCAO theory are consistent with those identified by Gouterman's four orbital model. Additional charge transfer bands visible in the 600-650 nm region of the UV-vis spectrum (Fig. 2.3a) of haem correspond to $\mathbf{a}_{1u}$ /$\mathbf{a}_{2u} \rightarrow\ \boldsymbol{d}_\pi$ transitions from the ligand to the metal d_{xz} /d_{yz} orbitals which have been shown to be dependent on the electronic nature of the axial ligand.[273]

(2.2.3) The electronic spectra of dimeric Fe(III)PPIX

UV-vis spectroscopic changes have long been used to confirm the presence of and distinguish between porphyrin aggregates.[275] While the potential speciation of Fe(III)PPIX is vast and complicated, it has been reported to exist in aqueous solution as two distinct dimeric species. The dominant species in aqueous solution has been identified as a π-π dimer with a characteristic UV-vis signature (Figure 2.5b).[66]

(2.2.3.1) π-π dimer species of Fe(III)PPIX

π-π Dimers are non-covalently associated five-coordinate Fe(III)PPIX molecules with axial ligands ($^-$OH/H_2O at a particular pH) aligned on opposite faces of interacting monomeric ferriprotoporphyrin units as depicted in Figure 2.5a. The main spectroscopic change highlighted in Figure 2.5b upon formation of a π-π dimer is a hypochromic effect including broadening and splitting of the B (Soret) band from a sharp single peak at 400 nm to a two-

humped peak from 350-400 nm with ε_{max} at 396 nm. [66] A small bathochromic shift of the Q bands is also observed.

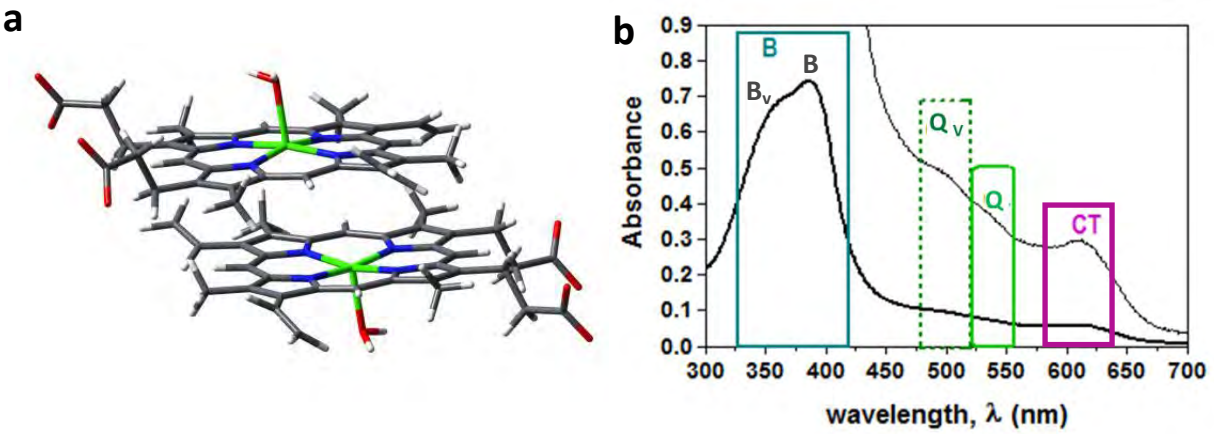

Figure 2.5 (a) Molecular structure of π-π dimer species of Fe(III)PPIX, **(b)** UV-vis spectrum of π-π dimer obtained in aqueous solution pH 7.50 HEPES 20 mM with B_v, B, Q_v, Q and charge transfer (CT) bands highlighted.

There are four possible transitions for the dimer of which none are degenerate with the monomer accounting for the different appearance of their UV-vis spectra. The selection rules can be determined from a semi-classical electrostatic vector model. The spectroscopic bands observed are a function of the oscillator strength of the electronic transition in each Fe(III)PPIX molecule, the inverse of the distance between the central metal atoms in the dimer and the alignment of transition dipoles in each unit.[276] Kasha's molecular exciton model details the treatment of excited states of weakly interacting aggregates and can account for the changes in UV spectra observed.[276] The molecular exciton is the delocalised electronic excitation where the whole molecule is comprised of identical sub-units which are separated by a short distance (a few Å) compared to the wavelength of the incident photon (≈ hundreds of nm) and therefore are both interacting with the oscillating electric field.[277] Weak coupling is described as a situation where no band shape change is observed, instead hypo or hyperchromism upon dimerisation is noted.[277]

Traditionally, three general dimer models can exist; where the transition dipole moments of individual units are orientated in a parallel, in-line or co-planar fashion, these are depicted in Figure 2.6. The ovals correspond to individual molecules and the arrows represent transition dipole moments, orientated in either direction.

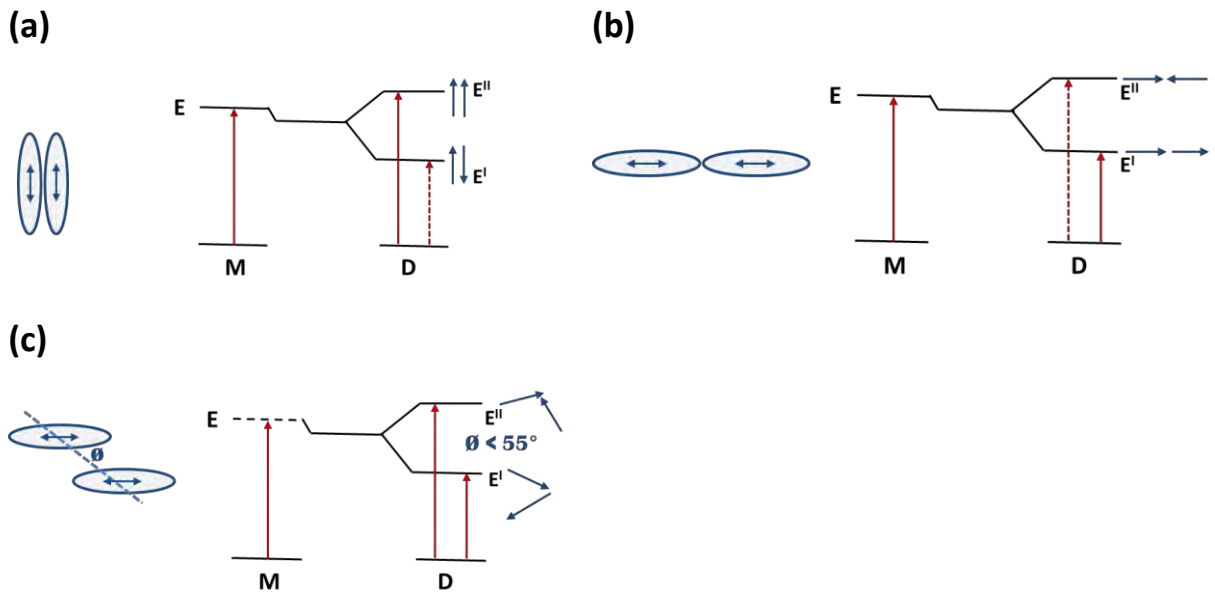

Figure 2.6 Schematic representation of exciton band energy resulting from transition dipole moments orientated in a **(a)** parallel, **(b)** in-line and **(c)** co-planar fashion. Solid arrows represent allowed transitions and dashed lines correspond to forbidden transitions. **M** and **D** are descriptors for the monomer and dimer respectively. ^{I}**E** and ^{II}**E** describe the exciton energy states. In **(a)** and **(b)** arrows show in phase or out-of-phase alignment of transition dipole moments. **ø** is the angle between polarisation axes and the line between the centre of each molecular unit.

The molecular transition moment is given by the vector sum of the individual transition dipole moments of each unit. In phase orientated transition dipole moments result in an allowed, higher energy excited state, ^{II}**E** due to increased dipole-dipole repulsion. Transitions from the ground state to an out of phase excited state, ^{I}**E** are lower in energy and are forbidden. The angle, **ø** between interacting porphyrins determines the dimer type with **ø** = **0**° and **ø** = **90**° corresponding to parallel and in-line situations respectively (see Fig. 2.6a). The parallel dimer therefore exhibits a blue shifted UV peak relative to the monomer as a consequence of this. For the in line dimer (b), the opposite case exists where a transition from monomer to dimer is accompanied by a red shifted UV peak (longer wavelength) for the allowed 'in phase' transition moment dipoles corresponding to the lower energy excited state, ^{II}**E**. [276]

The co-planar or obliquely head-to-tail orientated transition moment dipoles (see Fig. 2.6c) with in phase arrangement of transition moment dipoles being attractive lead to a lowering

of exciton energy, ^{I}E corresponding to a bathochromic shift. The out of phase arrangement is repulsive and is consistent with an increase in energy of the excited state, ^{II}E which is accompanied by a hypsochromic shift. The transition moments for electron dipole transitions from the ground state to the exciton state for this arrangement are both allowed. In a situation where $\phi \approx 55°$, the exciton splitting is zero, irrespective of intermolecular distance. The π-π Dimer species of Fe(III)PPIX displays the blue shifted B band outlined in situation (a), parallel dimers, and (c), co-planar oblique dimers, with the latter likely to be present in aqueous solution.[92,278] The split soret band, B and B_v is further broadened into to a lower energy band with its transition moment dipole along the *z* axis and a higher energy band with its transition moment dipole along the *x* or *y* axis.[279] Further broadening and splitting of the B band has been attributed to the loss of D_{4h} symmetry upon dimerisation.[280]

(2.2.3.1) μ-oxo dimer species of Fe(III)PPIX

The μ-oxo dimer is depicted in Figure 2.7.The two porphyrins are covalently linked via a μ-oxo bridge between the central Fe(III) ions. This species of Fe(III)PPIX has strikingly different UV-vis features, including a split and broadened B band (320 – 410 nm) as compared to the monomer and the appearance of a single broad envelope encompassing the Q and CT region (around 600 nm).

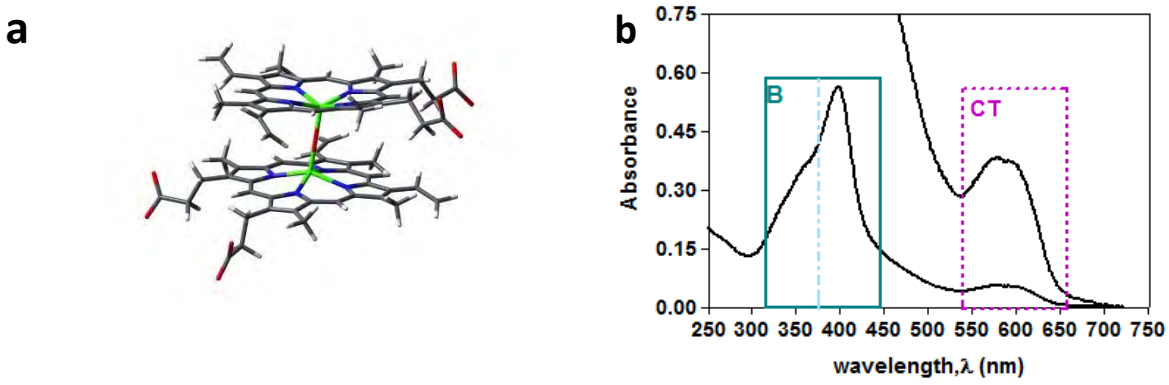

Figure 2.7 (a) Molecular structure of μ-oxo dimer form of Fe(III)PPIX monomers covalently linked through an oxo bridge, **(b)** UV-vis spectrum of μ-oxo dimer obtained in aq 40% (v/v) DMSO, CHES 20 mM, pH 10 with B band and charge transfer (CT) bands highlighted.

The presence of two ring systems invites the possibility of increased delocalisation and a greater number of one-electron transitions contributing to excited states.[281] The loss of the

H_2O axial ligand to form the oxide bridge can be held accountable for the changes in the low energy portion of the spectrum and it can be postulated that molecular exciton theory can explain the splitting and broadening of the Soret band.[277] Density-functional theory (DFT) based UV-vis spectroscopic modelling of different species of Fe(III)PPIX recently identified the theoretical origin of the spectroscopic differences in the μ-oxo dimer species.[282] The moderate field H_2O axial ligand is replaced by a weak field O^{2-} ligand allowing for better overlap of the porphyrin π^*orbitals with metal d orbitals, thus increasing the energy of the Fe^{3+} $\boldsymbol{d}_{\pi}$ and $\boldsymbol{d}_{z}{}^{2}$ orbitals. The spectroscopic changes observed, are attributed to the key changes in MO energies of the filled π MOs and the metal d-orbitals which result in a decreased energy gap between the π and π^* orbitals. In addition, some CT excitations ($\pi \rightarrow \boldsymbol{d}_{\pi}$) appear to contribute to the low energy broadening of the Soret peak.[282]

A larger proportion of CT transitions were identified when compared to monomeric Fe(III)PPIX involving $\pi \rightarrow \boldsymbol{d}_{\pi}$ and $\pi \rightarrow \boldsymbol{d}_{z}{}^{2}$ excitations. The broad envelope appearing at 550 – 650 nm originates from excitations that consist of transitions of admixed $\pi \rightarrow \pi^*$ and $\pi \rightarrow \boldsymbol{d}_{\pi}$ character resulting in the shift of traditional Q bands to a lower energy and charge transfer bands to a new higher energy peak where the subsequent broad overlapped absorption peak has a shared classification of Q and CT bands.

Deviations from Beer-Lambert law behaviour by a sample is a general indication of aggregation of chromophores. Absorbance spectra can be used to probe the formation and subsequent equilibrium of dimers or higher aggregates by observed spectroscopic shifts. A wavelength where two components or more exist in solution and appear to have the same molar absorptivity, $\boldsymbol{\varepsilon_{\lambda}}$ is known as an isosbestic point, often used as a reference absorbance in equilibrium species calculation since the absorbance at such a point adheres to the Beer-Lambert law regardless of species.[283,284] The observed UV-vis spectroscopic differences can thus be attributed to a specific species of Fe(III)PPIX with unique electronic transitions which can be used as a tool for species identification.

(2.3.1) Magnetic susceptibility measurements

The study of how substances respond when placed in a magnetic field is well established.[285] Substances experience a magnetic flux when exposed to a magnetic field of a certain strength, this magnetic moment, μ is dependent on the mass susceptibility, χ_g ($cm^3.g^{-1}$) of a molecule.[285]

$$\mu_B = 2.84\sqrt{\chi_g.Mw_{sample.}T} = 2.84\sqrt{\chi_m.T} \qquad (2.3.1)$$

Experimentally, the value of μ can be determined from molar magnetic susceptibility, χ_m, measurements. χ_g is a measure of a sample's susceptibility to being magnetised per unit field applied. The average magnetic moment, μ (μ_B) of a sample can be calculated by multiplying χ_g by the molecular weight of the substance and the temperature at which the experiment is performed, the product of χ_g and M_w yields, χ_m ($cm^3.mol^{-1}$), the molar susceptibility. A theoretical μ can also be calculated from the spin state of the molecule in Eqn. 2.3.2.

$$\mu = 2 \times\sqrt{S(S+1)}\ where\ S = no.\ unpaired\ electrons \times \frac{1}{2} \qquad (2.3.2)$$

Paramagnetism is derived from the spin and angular momentum of molecules.[285] χ_g can be either negative or positive, where $\chi_g < 0$ corresponds to diamagnetic substances and $\chi_g > 0$ corresponds to paramagnetic substances, which have permanent magnetic moments, even in the absence of magnetic fields.[286]

Diamagnetic samples have all their electron spins paired with zero net magnetic moment resulting in a weakly repelled sample in a magnetic field which is temperature independent. Diamagnetism is inherent in all samples due to paired inner shell electrons hence the "diamagnetic" contribution to a paramagnetic compound's magnetic susceptibility must be accounted for by use of Pascal's constants.[287] Paramagnetic samples have some electron spins unpaired, resulting in a stronger attraction to a magnet. Interacting paramagnets within a sample via the "exchange mechanism" can have three displacements; termed ferromagnetism and antiferromagnetism and ferrimagnetism. The orientations of magnetic

moments in a sample in the absence of a magnetic field of a **(a)** paramagnet, **(b)** antiferromagnet, **(c)** ferromagnet and **(d)** ferrimagnet are shown in Figure 2.8.

Paramagnets **(a)** have randomly aligned moments of the same magnitude; antiferromagnets **(b)** have their unpaired electrons aligned in opposite directions with no net magnetic moment, while ferromagnets **(c)** have aligned electron spins and an overall magnetic moment and ferrimagnets **(d)**, have electron spins aligned opposite to each other with an unequal no. of spins in each orientation leading to a net magnetic moment.[285] These forms of paramagnetism display characteristic magnetic susceptibilities, χ and temperature dependencies. [288] The varying temperature dependence of each form of paramagnetism can be used to distinguish between the different types.

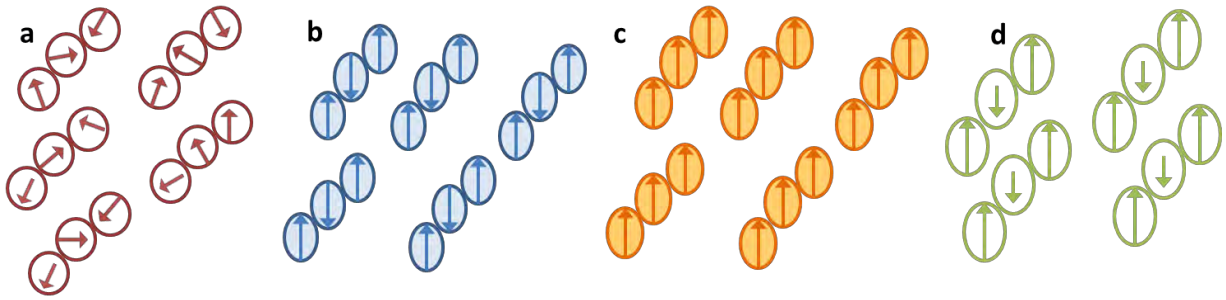

Figure 2.8 Alignment of magnetic moment dipoles within a sample in the absence of a magnetic field at zero temperature in the absence of a magnetic field. **(a)** Paramagnetism, **(b)** antiferromagnetism, **(c)** ferromagnetism and **(d)** ferrimagnetism.

Monomeric Fe(III)PPIX with axial ligand = H_2O is high spin with spin quantum number, S = $^5/_2$ and a spin- only theoretical magnetic moment, μ = 5.9 μ_B calculated from equation 2.3.2.[72] For paramagnetic five-coordinate ferrihaems, theoretical magnetic moments, μ = 1.7, 3.9, and 5.9 correspond to low spin (S= $^1/_2$), intermediate spin (S= $^3/_2$) and high spin (S= $^5/_2$) complexes respectively. In μ-oxo dimer type Fe(III)PPIX, $\mu \approx 2\ \mu_B$ [224] which temperature dependence studies have shown is a result of antiferromagnetic coupling (see Fig. 2.8 b) between each iron centre,[282] and not a low spin, S= $^1/_2$ species, with its magnetic susceptibility increasing with increasing temperature.[289] The π-π dimer species of ferrihaem that dominates in aqueous solution has recently been shown to yield a magnetic moment of $\mu \approx 4.8$ corresponding to a mixed intermediate and high-spin spin quantum number, S=$^3/_2$, $^5/_2$. [224]

(2.3.2) Evans NMR Method - Solution-phase Fe(III)PPIX magnetic susceptibility measurements

Evans noted that the chemical shift of a peak in the proton resonance spectrum of a molecule is dependent on the bulk susceptibility of the solvent medium.[290] The shifts caused by the presence of a paramagnetic substance in the bulk medium can be measured relative to a reference sample in the absence of any paramagnetism, the difference in peak position of these samples allows for measurement of the paramagnetic susceptibility of substances in dilute solution.

The difference in chemical shift, Δf (Hz) of a solvent (H_2O) peak in a ^1H NMR spectrum is measured for both the inner paramagnetic sample and the outer reference sample in a co-axial tube. The H_2O signal present in small amounts in D_2O in both samples is measured. The H_2O signal frequency from the paramagnetic species, (eg. Fe(III)PPIX) present is shifted relatively downfield compared to the H_2O peak in the reference sample. Thus Δf is negative (f_{ref} - $f_{paramagnetic\ sample}$) which can be related to μ of the Fe(III)PPIX sample via the calculation of the mass susceptibility, χ_g $(cm^3.g^{-1})$ in equation 2.3.3, where m is the molality of the sample ($g.cm^{-3}$) and χ_0 is the diamagnetic contribution of Fe(III)PPIX (approximated from Pascal's constants) for Fe(III) and H_2O/O^{2-} and an experimental value for PPIX contribution .[282] f is the frequency of the NMR instrument used in Hz. Eqn. 2.3.4 can be used to calculate χ_g, the paramagnetic contribution of Fe(III)PPIX as outlined in Eqn. 2.3.1 which yields a measured value for the μ of a specific ferrihaem species.

$$\chi_g = \frac{-3\,\Delta\,\mathrm{f}}{4\,\pi\,\mathrm{f}.m} - \chi_0 \qquad (2.3.3)$$

$$\chi_g = \chi - \chi_D \qquad (2.3.4)$$

$$\mu_B = 2.84\sqrt{\chi_g.MW_{sample.}T} = 2.84\sqrt{\chi_m.T} \qquad (2.3.1)$$

(2.4) Infrared (IR) spectroscopy

IR spectroscopy is a valuable analytical tool which provides information about the identity of functional groups present in a sample and their connectivity in all three states of matter. Molecules that show infrared absorption have a net change in their electric dipole moment during vibration; the intensity of the band is proportional to the magnitude of the change. IR peaks occur when the frequency of infra-red radiation absorbed is of a resonant frequency with a vibrating dipole in the molecule. Simply, a molecule can be thought of as separate masses connected by bonds which are treated as springs where resonant frequencies are related to the masses of the atoms and the strength of the bond. The bond stretching, contracting or bending in phase (symmetric) or out of phase (asymmetric) refer to the 3N-6 normal modes of vibration for a non-linear molecule with N atoms. Asymmetric stretches produce the most intense bands. Lower energy modes include band wagging, scissoring, rocking or twisting. [291] The number of normal modes of vibration per molecule is related to the difference between the degrees of translational freedom per atom and the degrees of rotational freedom in the x, y, z plane. A linear molecule can only move in two dimensions and thus has 3N-5 normal modes. An Infrared spectrum plots the intensity of infrared radiation (transmittance) against the wavenumber, $\bar{\upsilon}$ (cm^{-1}) or frequency of a band. Characteristic functional groups in a molecule are associated with IR peaks with specific wavenumbers.[291]

(2.4.1) Fourier Transform-IR Spectroscopy (FT-IR)

Fourier Transform IR spectroscopy is based on one fundamental technique; interferometry which is the interference of radiation between two beams to produce a signal that is a function of the change of pathlength between the two beams. A Michelson interferometer (Figure 2.9) analyses the frequencies present in that composite signal by dividing the incident beam into two beams with a path difference dependant on the location of the moving mirror, M_1.[291] Another stationary mirror, M_2 is located perpendicularly to the plane of the translational mirror and the broadband incident beam from an infrared source. A beam-splitter component is made of a semi-reflecting film and bisects the plane of these

two mirrors. When the two spilt beams recombine, there is constructive or destructive interference between the two phase shifted beams depending on the extra pathlength one beam has taken as a result of the translating mirror. About 50% of the beam reflected from the stationary mirror is transmitted through the beam splitter and detected through the sample while 50% of the beam is reflected back to the source. The detected signal varies with the distance the beams travel, d or $d+x$ (Fig. 2.9) as the two beams alternate between being in and out of phase and is associated with radiation ($\bar{\upsilon}$) of the wavelength of the beam. The mathematical conversion of this variation in radiation with pathlength to a variation in intensity with wavenumber is performed by the Fourier-transformation of the electric signal in the detector to an IR spectrum.[292]

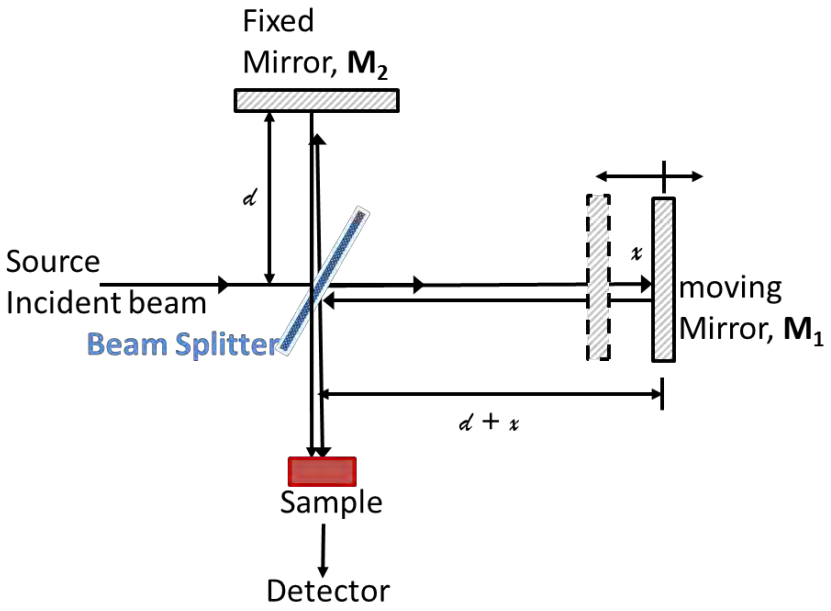

Figure 2.9 A schematic depicting the components of a Michelson interferometer in a FT-IR spectrophotometer. The amount of transmittance of IR radiation is measured as a function of the path, d that the beams travel after being split into two different components.

(2.4.2) Attenuated-Total Reflectance FT-IR Spectroscopy (ATR-FTIR)

Reflectance techniques to measure the total amount of light reflected as opposed to absorbed by a sample, provide a convenient means of measuring the IR spectrum of a sample with low preparation time and cost due to direct sample measurement. This technique operates on the phenomenon of total internal reflection.[293] A radiation beam

enters a less dense medium from one of greater refractive index and density and is internally reflected provided the angle of incidence,θ, is greater than the critical angle between the two mediums, illustrated in Figure 2.10. A crystal with a high refractive index and ideal transmission properties serves as an internal reflection element and is designed to be in contact with the sample. Total internal reflection of radiation at the interface between the two media of varied refractive index, *n*, creates an *evanescent wave* that penetrates into the media with the lower refractive index. In the regions of the infrared spectrum where the sample absorbs energy, the *evanescent wave* is attenuated or altered; this energy is then transferred back to the reflected IR beam in the crystal and is eventually passed onto the detector as the reflected beam. A spectrum is obtained by measuring the interaction of the *evanescent wave* with the sample.[291]

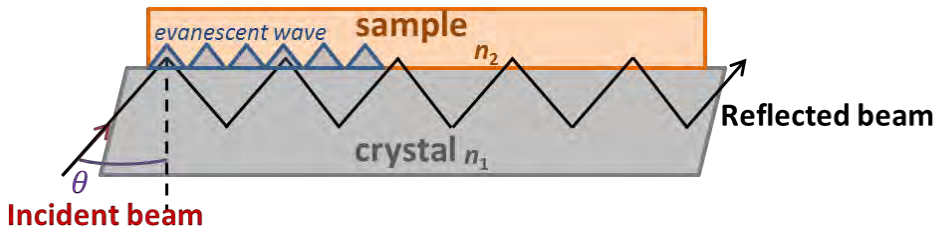

Figure 2.10 Schematic of an attenuated total reflectance cell, with incident beam reflectance at the crystal-air interface creating an evanescent wave through crystal and sample with refractive indexes, n_1 and n_2 respectively.

The types of crystal most commonly used to ensure good internal reflection are zinc selenide or germanium, however, the use of costly diamond has been shown to be the most robust and durable with an optimally high refractive index and low solubility.[293]

(2.4.3) ATR-FTIR of β-haematin for characterisation

Formation of β-haematin, the synthetic analogue of haemozoin from Fe(III)PPIX using a variety of mediators is characterised by the coordination of a propionic acid side chain of one Fe(III)PPIX monomer to the Fe(III) centre of another.[44] The β-haematin crystal is composed of these dimers hydrogen bonded to each other in a bicyclic fashion.[27] Diagnostic shifts in the IR stretching frequencies observed for the carboxylate groups (R-CH_2-CH_2-COO^-)

upon dimerisation from 1720 and 1650 cm^{-1} to 1664 and 1211 cm^{-1} corresponding to the C=O and C-O stretches of the coordinated propionate moiety can be used to confirm the presence of β-haematin in a sample. [44]

(2.5) Fluorescence Spectroscopy

When a photon of light is absorbed by a sample its interaction with this radiation is characterised by several transitions. Those of interest to fluorescence spectroscopy are associated with the vibrational and electronic energy levels.[294] At any finite temperature, T, a molecules' electrons are distributed among the energy levels available to it through thermal effects. The ratio of electrons in the upper and lower energy levels is given by the Boltzmann distribution calculated in equation 2.5.1 where the energy difference between the HOMO and LUMO states is ΔE and kT is the thermal energy with Boltzmann constant= 1.3 X 10^{-23} $J.K^{-1}$.

$$\frac{n_{upper}}{n_{lower}} = exp^{\left(\frac{-\Delta E}{kT}\right)} \qquad (2.5.1)$$

The possibility of transitions occurring from $n_{upper} \rightarrow n_{lower}$ is as likely as those from $n_{lower} \rightarrow n_{upper}$ such that a transition or absorption to a higher energy level can only occur if the difference between populations of the energy levels is significant, with the lower energy level having greater occupancy. At room temperature, vibrational energy level spacings result in a ratio of $(\frac{n_{upper}}{n_{lower}})$ = $\sim 10^{-3}$, whereas for electronic energy levels where the spacings are greater the ratio is $\sim 10^{-21}$. Each electronic transition has many broad normal vibrations from collisions and electrostatic interactions with surrounding solvent molecules. The vibrational sub-levels also possesses a ladder of rotational states that are significantly broadened due to hindered rotation upon solvent molecule collision.[266]

At ambient temperature, the outer electrons of most molecules' occupy the lowest vibrational level of the ground electronic state (GS) .[295] Upon absorption of a photon of light, electrons can be promoted to an excited state (ES). Decay of an electron from an ES results in emission of light which is termed photoluminescence, of which there are two types namely fluorescence (Fig. 2.11a) or phosphorescence (Fig. 2.11b) which arise from decay originating from a different ES as seen in Figure 2.11.[295] The former (a) occurs when the

electron excited to the higher energy MO has the opposite spin to the remaining unpaired electron in the lower MO. This electronic configuration is said to be "spin-paired" and is called a singlet state, since the total spin quantum number, $\sum S_i$, with $S_i = \pm\frac{1}{2}$ is zero and the multiplicities, $M = (2S + 1)$ of both the ground, S_0 and excited states, S_n are equal to 1.

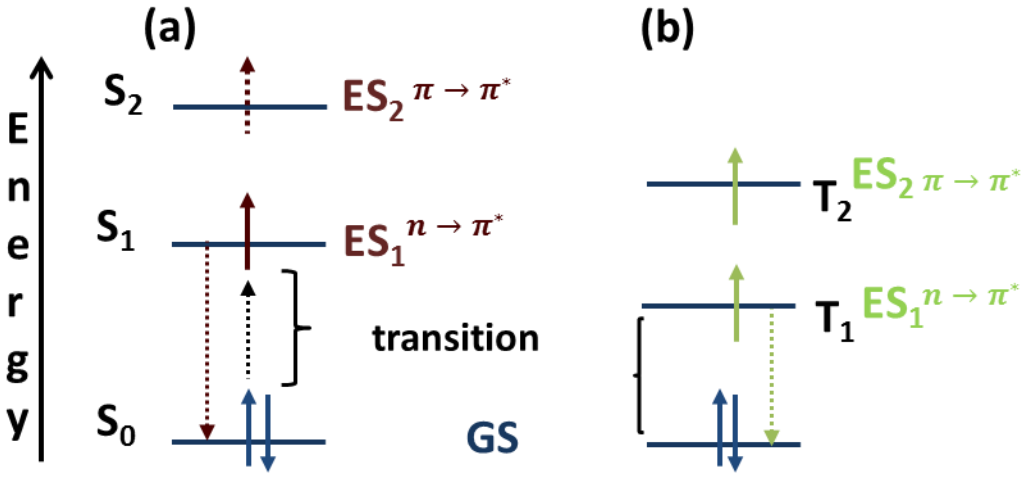

Figure 2.11 Schematic to show the distinction between two types of photoluminescence;**(a)** Fluorescence occurs with decay from spin-paired Singlet excited states (ES) and **(b)** Phosphorescence occurs with decay from spin- parallel triplet ES' to the ground state (GS).

Phosphorescence (b) occurs when the excited electron has the same spin as the unpaired electron in the GS. It is termed a triplet state, characterised by a set of spin parallel electrons with $\sum S_i = 1$ and $M = 3$.[295]

A chromophore that emits a photon is called a fluorophore.[266] The Jablonksi energy diagram in Figure 2.12 illustrates some of the electronic processes that can occur upon excitation of a fluorophore. [296]

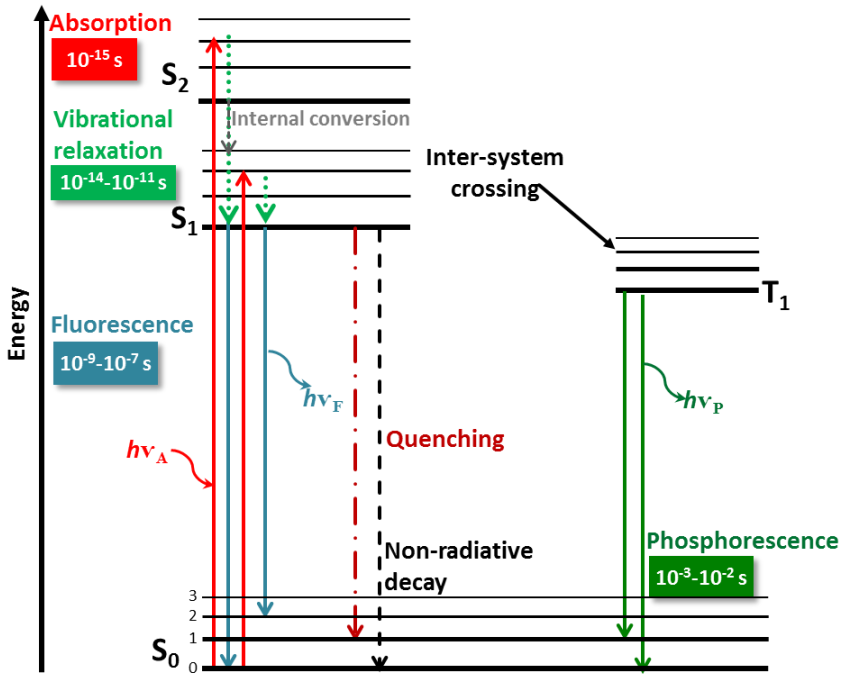

Figure 2.12 Jablonski energy diagram describing the absorption of a photon, $h\upsilon$ of energy by an electron from the singlet ground state, $\mathbf{S_0}$ to an excited state, $\mathbf{S_1}$ or $\mathbf{S_2}$. Some possible processes for energetic decay are illustrated.

(2.5.1) Fluorescence spectroscopy:

(2.5.1.1) Theory of photophysical process

The ground state $\mathbf{S_0}$, first $\mathbf{S_1}$ and second $\mathbf{S_2}$ singlet electronic states are shown with possible vibrational levels 0, 1, 2 and 3 indicated (Fig. 2.12).[296] Excitation can result in an electronic transition to one of the vibrational sub-levels in $\mathbf{S_1}$ or $\mathbf{S_2}$, which rapidly decays ($10^{-11} – 10^{-14}$ s) to the lowest vibrational sub-level in $\mathbf{S_1}$ or $\mathbf{S_2}$through energy loss due to molecular collisions. Any molecules with electrons occupying $\mathbf{S_2}$ then experience an internal conversion ($\leq 10^{-12}$ s) to a vibrational sub-level in $\mathbf{S_1}$ of the same energy. This process is over by the time fluorescence emission (10^{-8} s) occurs from the lowest energy vibrational level within $\mathbf{S_1}$. Fluorescence emission occurs as energy is lost from $\mathbf{S_1}$ to $\mathbf{S_0}$ resulting in typical fluorescence lifetimes of the order of 10^{-9} seconds. The fluorescence lifetime, τ of a molecule is the average time taken for the electronic excitation of a molecule and the return to its electronic ground state. It is defined as the inverse of the combination of the rates of radiative and non-radiative decay of an excited state molecule.[296]

Excitation of a molecules' electron from the HOMO to a LUMO increases the spatial distribution and polarisability as electron density is more diffuse.[295] According to the Franck-Condon principle, the absorption of a photon occurs practically instantaneously for electrons such that the heavier nuclei are not affected within the 10^{-15} s time frames as stipulated by the Born-Oppenheimer approximation and thus nuclei can only readjust afterward as molecular vibrations.[297] During these fast electronic transitions, so-called vertical transitions to vibrational levels that correspond to minimal change in the nuclear coordinates are favoured. Nuclear movements to reorganise to the new electronic configuration manifest as molecular vibration dynamics and characteristically occur with electronic transitions. Some excitation energy is thus converted to vibrational energy. As the molecule undergoes conformational changes, complex formation and interaction with its molecular environment (external conversion), loss of vibrational excitation energy as well as thermal relaxation (non-radiative energy), some energy loss is observed. This is manifested as the Stokes shift of all fluorescent molecules, where the emitted fluorescence photons are of a longer wavelength (lower energy) than the wavelength of the photons absorbed. Hence the emission and absorption spectrum of a fluorescent molecule have maxima at different wavelengths and are thus detected as different colours. [266,296,298]

The entire fluorescence process is cyclical barring the irreversible loss of fluorescence during photobleaching; the same fluorophore gets repeatedly excited and detected. The discrete electronic transitions are detected as a broad emission spectrum where typical fluorescence output is a spectrum plot of fluorescence photon intensity (arbitrary units) versus wavelength (nm). The emission spectrum obtained is usually a mirror image of the $\mathbf{S_0 \rightarrow S_1}$ portion of the absorption spectrum separated by the Stokes shift (Fig. 2.13). The Kasha rule which holds for most fluorescent molecules, observes that the fluorescence emission spectrum is independent of irradiation wavelength because upon excitation, molecules quickly relax to the lowest vibrational excited state following from Vavilov's earlier observation that quantum efficiency is constant despite excitation wavelength. [266] The applicability of the Franck-Condon principle and Kasha's observation account for the mirror symmetry observed. The observed wavelength and shape of the absorption and thus emission spectrum of a fluorophore is then characteristic of the chemical nature of its surroundings providing much information about a potentially unknown system. This feature

makes fluorescent dye molecules good probes of molecular environments in biology and physicochemistry.[295]

As depicted in Fig. 2.12, molecules in $\mathbf{S_1}$ can also undergo a spin conversion from a singlet to a triplet excited state, $\mathbf{T_1}$ and emit energy upon return to the ground state in the form of phosphorescence. Phosphorescence inter-system crossing transitions from $\mathbf{T_1}$ to $\mathbf{S_0}$ are spin forbidden and hence occur at a much slower rate than fluorescence (10^{-3} s). Phosphorescent emissions are also shifted to much longer wavelengths and lower energy relative to fluorescence emissions. Fluorescence is the main consideration of this PhD thesis and is presented here in much detail.

Not all of the molecules initially excited return to the ground state by fluorescence or phosphorescence.[295] Excited molecules can dissipate their energy by decomposition, reaction, heat (external conversion) or re-emission. Other processes like quenching (discussed in detail in Chapter 1 and section 2.5.2) via excited state dynamic interaction or complex formation or fluorescence resonance energy transfer (FRET) can occur to decrease the quantum efficiency, ϕ_E of a molecule, which is defined as the ratio of the number of quanta emitted to the number of quanta absorbed and can be anywhere between 0 (non-fluorescent) and 1.[298] The ϕ_E and fluorescence lifetime, τ of a molecule are characteristic with the former measured relative to a standard and the latter having typical excited state decay times of 0.5 – 20 x 10^{-9} s. [266,298]

(2.5.1.2) Fluorescence spectroscopy: Types and Instrumentation

There are two main types of fluorescence spectroscopy; (1) steady-state fluorescence where the emission spectrum obtained is the wavelength distribution of an emission measured at a single constant excitation wavelength.[299] Steady-state fluorescence spectroscopy provides an equilibrium description of excited state relaxation after the luminescent processes such as internal conversion and vibrational relaxation have been completed. (2) Time-resolved fluorescence emission is monitored as a function of time upon excitation. This technique offers the opportunity to obtain additional information about the molecular environment of the fluorophore. Essentially this is a measurement of the transient decay constant of emitted

fluorescence intensity with time, (*k*). The fluorescence lifetime, τ , can be calculated and used to distinguish between electronic events such as the type of quenching occurring; collisional or static (expanded upon in Chapter 1 and section 2.5.2), the extent of rotational diffusion, resonance energy transfer and neighbour interactions.[300] Resolution of this data can be captured by fast electronics, time correlated single photon counting (TCSPC), time correlated fluorescence imaging or optical gating methods which fall broadly into two categories; (a) time-domain techniques which make use of a pulsed light source such as a laser or flash lamp and (b) techniques where the fluorophore is excited with intensity modulated light which is known as frequency-domain measurements.[301] In the absence of machinery capable of collecting time resolved fluorescence data, the use of steady state fluorescence spectroscopy to monitor fluorescent probes to investigate lipid partitioning, for example, is well established as the instrumentation and analysis provide a simple and robust platform to study these systems in vitro. [294,302–304]

A typical steady state fluorescence spectrophotometer serves to transform continuous illumination of incident light from a lamp (usually xenon) through an excitation monochromator to the sample cuvette via variable slit widths to control background noise. Positioned at 90° to the excitation beam is an emission monochromator also with adjustable slit widths. The emission beam then passes through a scond monochromator before reaching a photomultiplier tube (PMT) where the signal is converted to a voltage and amplified for detection. [299] A simplified version is outlined in Figure 2.14.[305] The right-angle placement of the sample to the excitation beam is crucial for minimisation of interference effects as the elastic light scattering angle is least intense when placed perpendicular to the sample.[306]

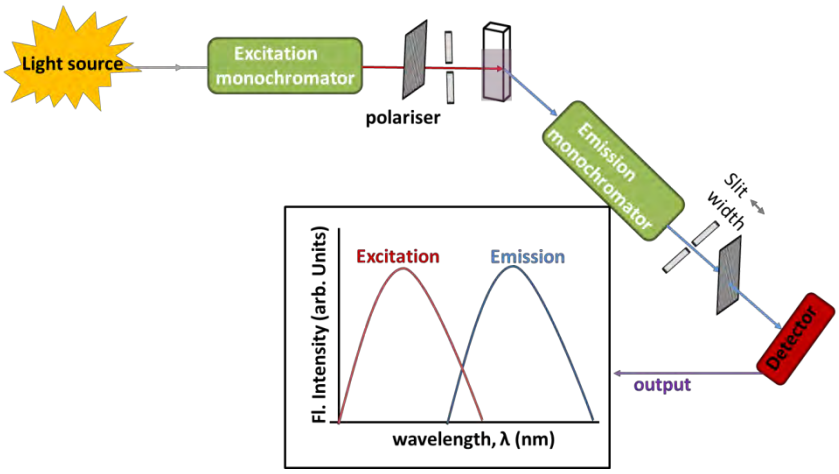

Figure 2.14 Schematic representation of a steady state fluorescence fluorometer to obtain a typical fluorescence spectrum.

(2.5.1.3) Fluorescence spectroscopy: Fluorophores and their environments

The main considerations affecting the emission spectrum and photophysical properties; ϕ_E and τ, include environmental effects or interactions between adjacent fluorophores. The microenvironment of the fluorophore is determined by solvent type including polarity, viscosity, dielectric constant, refractive index, hydrogen bonding capabilities and pH. The concentration of fluorophore, pressure, salt concentration, pH and temperature of the system also play a major role in the processes that dominate the fluorescence profile.[295] The Lippert-Mataga equation (Eqn. 2.5.2) serves as a general description of the effect of these factors on the Stokes shift ($\upsilon_{abs} - \upsilon_{em}$) of a particular fluorophore in a given solvent. This approximates the solvatochromatic effect displayed by several fluorescent probes in their microenvironments, where their emission maximum wavelength is shifted either in a bathochromic (red shift) or hypsochromic (blue shift) manner corresponding to an increase or decrease in solvent polarity for positive solvatochromatic dyes.[297]

$$\upsilon_{abs} - \upsilon_{em} = \frac{2(\mu_e - \mu_g)^2}{c.h.a^3}\left[\frac{2(\epsilon_s - 1)}{(2\epsilon_s + 1)} - \frac{2(n^2 - 1)}{(2n^2 - 1)}\right] \qquad (2.5.2)$$

The solvation shell effects like polarity, quenching interactions and solvent molecule readjustment are accounted for by changes in μ, the dipole moments of the excited (μ_e) and

ground states (μ_g) and ϵ_s, the dielectric constant of the solvent. The refractive index of the solvent, n contributes to vibrational relaxation and internal conversion of the fluorophore. The shift is also inversely dependant on the radius of the fluorophore in the solvent, a and its product with the speed of light, *c* and Planks constant, *h*.[266]

The structure of the fluorophore also plays a major role in the selection of a probe with favourable photophysical properties.[295] Most fluorescent molecules are characterised by conjugated double bonds, particularly aromatic systems. The number of fused rings and degree of substitution affects structural rigidity and subsequent $\pi \rightarrow \pi^*$ singlet state stabilisation which has been shown to increase fluorescence quantum yield.[307]

The main types of fluorophores that exist can be broadly classified into two classes. The first are intrinsic or natural probes, for example, an aromatic amino acid residue in a protein. The more common second class are extrinsic probes of either a covalent or associating nature, where a relationship between an external probe and the system or molecule of interest exists.[308] A well-established technique of monitoring the interactions between a fluorophore excited state and its surroundings is to investigate the quenching of its fluorescence by introduction of a quencher to the system.[308] This specific chemical interaction can be applied to gauge the local environment of the quencher as the quencher must be in close proximity to the probe in order for quenching to occur, as well as provide information on the type of interaction between the quencher and fluorophore.

(2.5.2) Quenching of Fluorescence:

The term quenching refers to the loss of or decrease in fluorescence intensity of the initially excited molecule.[295] Many inter or intramolecular chemical processes may result in such a phenomenon by increasing the amount of non-radiative decay of an excited state to the ground state by reducing the fluorescence lifetime and the quantum yield of a fluorophore. This is achieved either through molecular rearrangement of the fluorophore, energy transfer, excited-state reactions, excited dimer formation (excimer), ground state complex formation or collisions between a fluorophore and quencher via a diffusion process.[308] This work on fluorescence quenching deals primarily with the intermolecular dynamic quenching

that occurs due to the introduction of a heavy metal fluorescence quencher, to a system containing an excited fluorophore, (F*) .

There are two broad mechanisms of quenching relevant to this work; static and collisional quenching. Static quenching is the formation of a non-fluorescent ground state complex between fluorophore, F, and quencher, Q, such that the number of excited state F* molecules present is decreased (Figure 2.15 (a)).[308] Hence the fluorescence lifetime in the presence of Q, τ is characteristically unaffected and the ratio of this to τ_0, the initial lifetime in the absence of Q is unity i.e. τ_0/τ = 1. For this mechanism to hold, concentrations of Q would need to be large enough that the probability of interaction is high. Contrastingly, collisional quenching is a diffusion dependent process of non-radiative energy transfer between F and Q. The interaction between F* molecules and Q is inversely proportional to distance. There should be a vast excess of Q molecules to F* molecules such that intermolecular contact is highly likely, the probability of this occurring is given by k_q , the bimolecular quenching rate constant. For collisional quenching, $\frac{\tau_0}{\tau} = \frac{I_0}{I}$ where I_0 and I are the fluorescence emission intensities of the F in the absence and presence of Q respectively. The lifetime is decreased by depopulation of the excited state and the quantum yield of F* is reduced by decay that is unaccompanied by emission (Figure 2.15 (b)). Since collisional quenching is a diffusion controlled process, its rate constant is also time-dependent.[295]

The lifetimes or the temperature and viscosity dependence of quenching can be used to distinguish static and dynamic quenching as depicted in Figure 2.15. Quenching data presented as a plot of $\frac{I_o}{I}$ versus [Q] conform to a linear relationship between relative fluorescence intensity ($\frac{I_o}{I}$) and the concentration of the quencher, [Q] with an expected y-intercept of unity and a slope equal to $k_q\tau_0 (= K_{SV})$ and K_S for collisional and static quenching respectively. Collisional fluorescence quenching can be described by the Stern-Volmer (SV) equation (2.5.3) [308].

$$\frac{I_o}{I} = 1 + k_q\tau_o[Q] = 1 + K_{SV}[Q] \qquad (2.5.3)$$

k_q is the bimolecular quenching constant or rate at which a F* and Q come into contact; it can be determined experimentally given knowledge of τ_o, practically for collisional quenching it should not be above approximately 2 X 10^{10} $M^{-1}.s^{-1}$ for a fluorophore with a typical τ_o of 1-10 ns .[309]

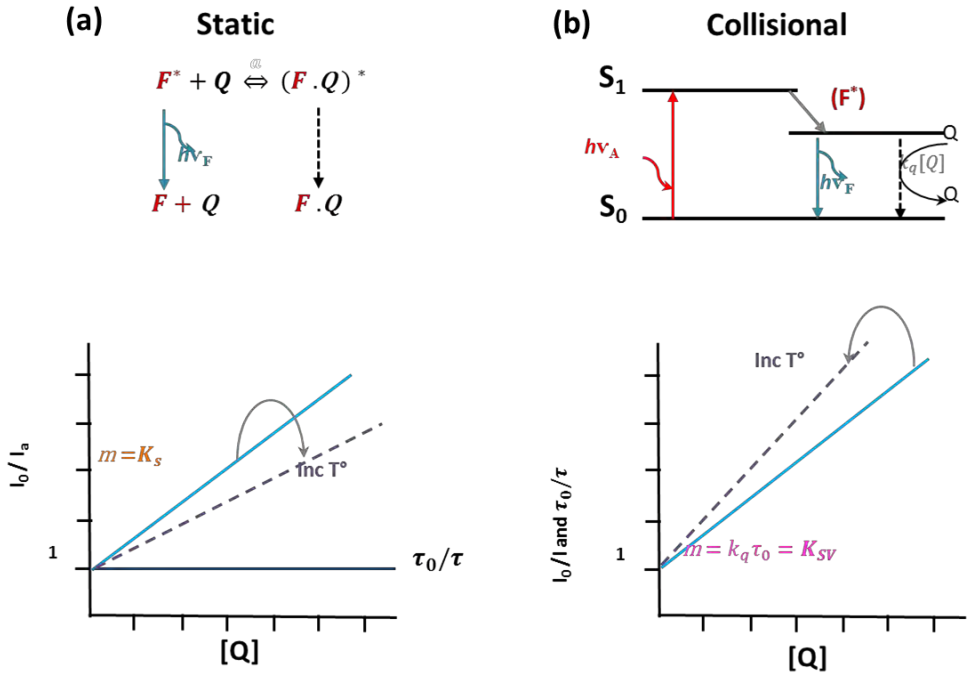

Figure 2.15 Comparison of linear plots generated from **(a)** static and **(b)** collisional quenching scenarios for fluorophore, **F** and Quencher, **Q**. $h\nu_F$ represents normal fluorescence emission, **F*** denotes the excited state. Diagram adapted from Lakowics Principles of Fluorescence spectroscopy.[308]

Upon collision, the fluorophore and quencher form a dynamic complex which can decay to the ground state via quenching with rate constant, k_1, or dissociate with rate constant, k_{-1}. The quenching efficiency of this process can be calculated for effective collisional quenching, $k_1 \gg k_{-1}$. $k_1$is the diffusion controlled bimolecular rate constant and can be calculated from the Smoluchowski equation (2.5.4) which incorporates the collision radii of the molecules, R_f and R_q. $\frac{N_A}{1000}$ is a scaling factor to convert molarity to molecules/ cm^3 where N_A is Avogadro's number, 6.022 x 10^{23} .

$$k_1 = \frac{4\pi N_A}{1000}(R_f + R_q)(\boldsymbol{D}) \qquad (2.5.4)$$

$$\boldsymbol{D} = \frac{kT}{6\pi\eta R} \qquad (2.5.5)$$

The molecular diffusion constant **D**, is the sum of the individual molecules diffusion constants, $\boldsymbol{D}_f$ and $\boldsymbol{D}_q$ and can be estimated from the Stokes-Einstein equation (2.5.5) after considering the effects of solvent viscosity, η and thermal energy (Boltzmann constant multiplied by absolute temperature), kT and molecular radius, R.[309] k_1 is related to k_q through the quenching efficiency, $f_Q = k_q/k_1$. If 50% of encounters between the fluorophore and quencher result in effective quenching, k_q the bimolecular quenching constant is half the diffusion controlled rate constant, k_1.[308]

In the absence of knowledge of τ_o, in steady state measurements, the Stern-Volmer quenching constant, K_{SV} $(= k_q\tau_o)$, is reported as an alternative. ${K_{SV}}^{-1}$ is the concentration of quencher at which $\frac{I_o}{I} = 2$ or 50% of fluorescence is quenched. Without determining if τ_0/τ = 1, differentiation between the two mechanisms of quenching is possible through a variety of methods. Temperature or viscosity variations between experiments can provide information on the mechanism. Collisional quenching at elevated temperatures results in elevated diffusion coefficients, an increase in effective collisions and quenching efficiency, thus k_q is shown to increase with increasing temperature. Conversely, an increase in temperature is likely to result in a decreased stability of the quencher-fluorophore complexes and thus lower values of the static quenching constants, K_s. By observation of elevated temperature or viscosity behaviour or lifetime measurements and presuming static quenching occurs and a ground state complex, FQ is formed, changes in the absorption spectrum of the ground state fluorophore can confirm complexation.

The relationship between $\frac{I_o}{I}$ and [Q] may be found to be non- linear therefore it is important to consider any effects that may decrease fluorescence intensity through mechanisms not considered to be quenching like the inner filter effect. The inner filter effect refers to the absorption of light at the excitation or emission wavelength by any molecules present in solution. This non-linear effect can be accounted for by application of a correction calculation (Eqn 2.5.6).[309] I_{obs} refers to the fluorescence emission intensity recorded and I_{corr} refers to the intensity calculated after accounting for any absorption effects of the species, F and Q present.

$$I_{corr} = I_{obs} \times 10^{\left(-\frac{A_{ex}l_{ex}}{2}+\frac{A_{em}l_{em}}{2}\right)} \quad (2.5.6)$$

A linear Stern-Volmer plot with y-intercept equal to unity is indicative of a single-class of fluorophores, all equally accessible to the quencher as seen in Figure 2.15 (a&b). It is also possible that both static and collisional quenching of F* occur simultaneously, in this case, a modified Stern-Volmer equation (Eqn. 2.5.7) which accounts for both quenching mechanisms is applied. The fluorescence emission measured is a weighted average of the fluorescence produced by the product of the fraction of F molecules not complexed with or not collisionally quenched by Q. The extra term, $\boldsymbol{K_{SV}K_S[Q]^2}$ results in an upward deviation from linearity in a plot of $\frac{I_0}{I}$ versus [Q] toward the y-axis. An example of this is shown in Figure 2.15 (b).

$$\frac{\boldsymbol{I_0}}{\boldsymbol{I}} = (1 + K_S[Q])(1 + K_{SV}[Q]) = \mathbf{1} + (\boldsymbol{K_{SV}} + \boldsymbol{K_S})[\boldsymbol{Q}] + \boldsymbol{K_{SV}K_S[Q]^2} \quad (2.5.7)$$

A downward deviation from linearity toward the x-axis is indicative of systems where fluorophore molecules can be accessible and inaccessible to the quencher, for example, lipid membrane dyes (Fig. 2.16 (a)). [308] The K_{SV} values obtained not only depend on the concentration of Q, but also on molecular contact between F and Q. The latter situation thus can be used to investigate the localisation of fluorophores and by extension, their quenchers, as well as the permeability of two phase systems for example, aqueous bulk solvent and fluorophore stained lipid droplets. Therefore, the K_{SV} values obtained, are also dependent on the relative partitioning, K_p of Q into the local environment of F.[310] In steady-state fluorescence experiments where data is found to conform to a linear SV plot, the quenching efficiency can be related to the total concentration of the partitioned quencher, $[Q]_T$.[310 311]

A common approach to investigating the partitioning of a substance between compartmentalised or aq/lipid systems is by monitoring the deviation of the bimolecular quenching constant, k_q or $K_{SV,}$ with variable total lipid volume, $\boldsymbol{\alpha_L}$.[311–313] Several literature reports discuss the theory behind this approach and so the derivation of the major equations are not presented here. [310,314,315] These methods are predominantly applied to aq/ membrane partitioning measurement, specifically the measurement of vesicle partitioning for ionisable drugs. [303 316] Briefly, for the quencher, Q, partitioning into the neutral lipids to

quench the probe molecule, F, a few different equilibria exist. The distribution of possible species is depicted by the equilibrium equations shown in Fig. 2.16. The green block indicates the acid-base equilibrium that the quencher can undergo in aq solution shown in Eqn. 2.5.8. K_a refers to the dissociation constant for that process and K_p is the lipid membrane partition coefficient for the equilibrium between the concentration of Q in the aqueous phase $[Q]_{aq}$ and the concentration of Q in the lipid phase $\mathbf{[Q]_L}$ shown in blue.

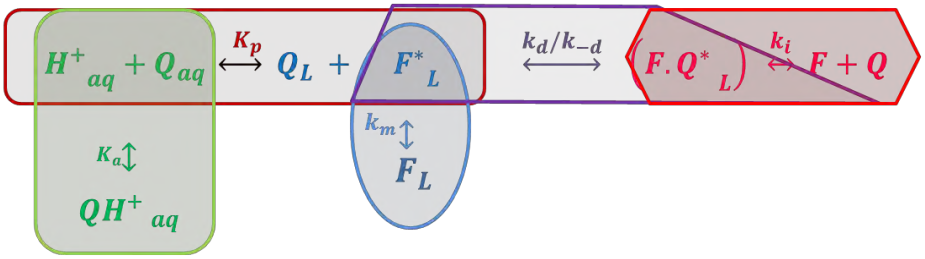

Figure 2.16 A description of the dynamic equilibrium that occurs when the quencher (**Q**), is allowed to partition into the fluorophore, F, stained lipids. $\boldsymbol{k_d}$, $\boldsymbol{k_{-d}}$, $\boldsymbol{k_m}$ and $\boldsymbol{k_i}$ represent the rate constants of complex formation, dissociation and deactivation of F* and the complex, respectively. Subscripts $_{\mathbf{aq}}$ and $_{\mathbf{L}}$ refer to the aqueous and lipid phases.

The interaction between the partitioned quencher and F* (excited state) inside the lipid is determined by the formation of a fluorophore-quencher excited state complex (FQ^*_L) in the lipid phase with rate constants k_d and k_{-d} for the formation and dissociation of the complex. The excited state complex, F-Q* can be deactivated by fluorescence with a rate constant of $\boldsymbol{k_i}$ and likewise the fluorophore excited state can be deactivated with rate constant, k_m. The bimolecular quenching constant, k_q, is defined by the ratio of these rate constants as shown in Eqn 2.5.9 [295] The calculation of k_q from K_{SV} requires the independent measurement of τ_0 of NR in SNLBDs in order for a value of k_q to be obtained. In the absence of the required fluorescence lifetime machinery, K_{SV} is used to approximate k_q. (The use of a fluorescence lifetime value measured under different conditions obtained from literature implies that τ_0 is independent of the change in the conditions, an assumption that must be proven for the value of k_q to be valid.) [317] The partition constant, K_p (Eqn. 2.5.10), is the ratio of the amount of quencher in the lipid phase, $[Q]_L$ relative to the portion of quencher in the aq phase, $[Q]_{aq}$.

For a monoprotic quencher, the fraction of $[Q]_{aq}$ can be calculated from Eqn. 2.5.8 by accounting for the ionisation of the quencher. $[Q]_L$ is given by the SV equation (2.5.3) and summed with $[Q]_{aq}$ yields the total amount of quencher, $[Q]_T$, added to the experiment. Equation 2.5.11 relates both fractions of Q to the ratio of lipid volume to the total volume, which is called the lipid volume fraction and is denoted by $\boldsymbol{\alpha_L}$. The apparent quenching rate, k_q^{app} (K_{SV}/τ_o in Eqn. 2.5.3) is dependent on this ratio such that a plot of $1/k_q^{app}$ versus $\boldsymbol{\alpha_L}$ is a straight line function with y intercept equal to $\frac{1}{k_q K_p}$ and gradient of $\left(\frac{1}{k_q} - \frac{1}{k_q K_p}\right)$.[318]

$$[Q]_{aq} = [\boldsymbol{QH^+}]_{\boldsymbol{aq}} \mathbf{10}^{(\boldsymbol{pK_a - pH})} \tag{2.5.8}$$

$$k_q = {k_d k_i}\Big/{(k_{-d} + k_i)} \tag{2.5.9}$$

$$K_p = {[Q]_L}\Big/{[Q]_{aq}} \tag{2.5.10}$$

$$[\boldsymbol{Q}]_{\boldsymbol{L}} = {[Q]_T}\Big/{\{\alpha_L + (\mathbf{10}^{\boldsymbol{pKa - pH}} + \mathbf{1}).\ \frac{(1-\alpha_L)}{\boldsymbol{K_p}}\}},\ \alpha_L = \frac{V_L}{V_T} \tag{2.5.11}$$

Chapter 3:
Materials, Instrumentation and General Methods

(3.1) Materials

All the materials used in this study were of analytical grade or of the highest grade commercially available and no further purification was performed prior to use unless otherwise stated.

All chemicals were purchased from Sigma Aldrich® (Vorna Valley, South Africa) with any exceptions stated specifically in the relevant sections. All consumables such as Eppendorf and Falcon tubes were obtained from Lasec, Kimix Chemicals or Merck South Africa.

Double distilled deionised Millipore® Direct-Q water was used to prepare all aqueous solutions and is referred to as water.

(3.2) Instrumentation and Accessories

(3.2.1) Weighing Balance

All salts and solid substances used in this study were weighed using a four decimal place Adventurer™ OHAUS weighing balance or a milligram Sartorius 2006 MP balance which were regularly calibrated with mass standards.

(3.2.2) Preparation of solutions

All stock solutions were prepared by weighing each solid on an analytical grade balance and diluting to the required volume in Schott-Duran volumetric flasks. Where further dilution was required Eppendorf pipettes were used to dispense the appropriate volume accurately. Dissolution of all solids was achieved by use of a Snijders vortex or Bandelin Sonorex RK100H sonicator where necessary. For accuracy, all titrations were performed using glass Hamilton syringes.

(3.2.3) pH Measurements

The pH of low volume solutions (µL - 10 mL) was determined using a bench Jenway 3510 pH meter fitted with a 924 007 glass Jenway electrode. The pH of solutions of volumes 10 mL and greater was determined using a Crison MicropH 2000 pH meter and Crison 52 03 glass electrode. Standard solutions at pH 4.00 ± 0.01 (Buffer, reference standard, Sigma B5020) and 7.00 ± 0.01 (Buffer, reference standard, Sigma B4770) were used to calibrate the pH meter at room temperature of ~ 23 °C. Electrodes were stored immersed in a 3 M KCl solution obtained from Sigma Aldrich.

(3.2.4) UV-vis Experiments

All UV-vis spectra were recorded with a Varian Cary 100 spectrophotometer or a Shimadzu UV 1800 Probe at constant temperature by attachment of the cell chamber to an external water bath. Hellma, Suprasil® quartz cuvettes of 1 and 10 mm pathlength in varied volume capacity were used for all measurements.

(3.2.5) Fluorescence Spectrophotometry

A Varian Cary Eclipse fluorometer equipped with a regulated temperature cell holder was used to perform all steady-state fluorescence measurements. Hellma, Suprasil® quartz fluorescence cuvettes of 10 mm pathlength and 1.5 mL volume capacity were used for all measurements.

(3.2.6) Fluorescence Microscopy

Fluorescence microscopy was conducted using a Nikon Diaphot inverted fluorescence microscope with dichroic mirror: DM580. Filters used are mentioned where applicable.

(3.2.7) Infrared Spectroscopy

All IR spectra were recorded using either a Bruker Platinum ATR which was mounted onto a Bruker Tensor 27 FT-IR spectrophotometer or a Perkin Elmer 100 spectrophotomer using an ATR attachment at room temperature (~ 23 °C). The background was run on air and the spectra were collected from 4000 to 400 cm^{-1}.

(3.2.8) Powder X-ray diffraction (PXRD)

PXRD measurements were conducted using a Bruker D8 Advance diffractometer equipped with a Lynxeye detector using CuKα-radiation (λ = 1.5406 Å) at 298 K. Samples were prepared by drying over P_4O_{10} and then crushed to a fine powder which was placed on a zero background sample holder and scanned over the 2θ range 4- 40° with a 0.016° step size. X-rays were generated by a current flow of 40 mA and an accelerating voltage of 30 kV. The receiving slit width was 0.6 mm and 0.25 mm primary and secondary slit widths were used. The output was converted from a text file to an Excel spreadsheet from which PXRD traces were generated.

(3.2.9) NMR experiments

NMR experiments were performed on a Bruker Ultrashield 400 Plus spectrometer at 30 °C in deuterium oxide (D_2O) at 99.9% heavy atom D obtained from Fluka Products supplied by Sigma Aldrich®, South Africa.

(3.2.10) Plates and Plate Reader

Clear 96-well flat form Kartell® plates were used to measure the UV-vis absorbance of multiple samples of increasing concentration on a thermostatted Molecular Devices Spectra-Max 340 PL plate reader at 25 °C at a predetermined λ_{max} (nm) of the absorbing substance for single reads or over the λ range 340-750 nm for the whole spectrum.

(3.2.11) Centrifuge

Centrifugation of suspensions of volumes greater than 2.0 mL were performed with an Eppendorf Centrifuge 5810R in plastic Greiner Falcon tubes (15 mL) or Naglene™ 3115 Oak Ridge polypropylene centrifuge tubes (80 mL) while volumes less than 2.0 mL were centrifuged using an Eppendorf Centrifuge 5410 in plastic Eppendorf tubes.

(3.2.12) Water Baths

All β-haematin formation and kinetics experiments were done at physiological temperature (37 °C). A Fried Electric thermostat was attached to a water bath which was used to heat and maintain the temperature of the water. An external thermometer was also used to measure the temperature of buffer solution in the reaction vessel incubated in the water bath to confirm the required temperature prior to conducting the experiment. All spectrophotometer sample units were attached to an external thermostatted water bath which was maintained at 25 ± 1 °C for the duration of the experiment. The water baths were either a GRANT digital Y6 water bath or a YIH DER BL-710 water bath or a Labcon CPM 100 bath.

(3.2.13) Software

GraphPad Prism version 3 (3.02, April 25, 2000, GraphPad Software Inc.) for windows was used to perform all non-linear least squares analysis, as well as to compute linear representations of data.[319] HypSpec from the HyperQuad 2008 Software package was used to analyse all UV-vis titrations for computation of binding constants.[320] All chemical structures were drawn by the author in ChemBioDraw 11 or ACD/ChemSketch v 12.01 freeware. The Cambridge Structural Database, version 5.36, February 2015, was used to obtain published crystal structures.[231] Images of crystal structures were generated using OLEX^2 version 1.26.[321] Mendeley freeware for windows desktop and web importer was used to generate the bibliography for this work.

(3.3) General Methods

(3.3.1) Washing Procedures

The tendency of Fe(III)PPIX to adsorb onto glass and plastic is well established.[66,72] In order to avoid loss of material resulting in inaccurate concentrations, all Fe(III)PPIX stock solutions were prepared fresh for each experiment and only kept in glass vials for the duration of the experiment. All glassware, Hamilton syringes, Naglene^{TM} centrifuge tubes, stirrer bars, crystallisation dishes, NMR tubes, and quartz cuvettes were extensively washed with 0.1 M NaOH solution, followed by a single rinse with 1 M HNO_3 and a few final rinses with water.

All glassware was dried in a 100 °C oven for 24 hrs prior to each use. Plastic tubes, eppendorfs and pipette tips were discarded after every use to prevent contamination.

(3.3.2) Preparation of Lipid Blend and SNLBDs

A biologically established neutral lipid blend composed of lipids *rac* 1- monostearoylglycerol (MSG): 1-monopalmitoylglycerol (MPG): 1,3-dioleoylglycerol (DOG): 1,3-dilinoleoylglycerol (DLG), 1,3-dipalmitoylglycerol (DPG) in the biological mole ratio 4:2:1:1:1 as previously reported by Sullivan et al., were dissolved in 1:9 (*v*/*v*) acetone : methanol (Ace: MeOH) to afford lipid stock solutions.[124] Individual stock solutions of each lipid were then mixed with each component in the correct volume ratio by sonication and heating to 40 °C to ensure all lipids were dissolved with the total lipid concentration equal to 3.31 mM. Synthetic neutral lipid blend droplets (SNLBDs) were prepared following the method of Hoang et al. on aqueous buffer by depositing the lipid blend stock solution onto the surface of a larger volume of buffer at the desired temperature and pH with a with a syringe of needle gauge 23 (outer diameter 0.64 mm, inner diameter 0.34 mm, wall thickness 0.1524 mm) to prepare a layer of lipid in acetone: methanol solution.[127] The organic layer was rapidly dispersed into the aqueous bulk by vortex to afford SNLBDs.

(3.3.3) The pyridine hemichrome inhibition of β-haematin (Phi-β) assay

The Phi-β assay as developed by Ncokazi and Egan provides a reliable efficient method of quantifying free haem in solution [253]. The authors demonstrated that upon addition of a 5%, v/v, pyridine solution buffered at pH 7.5 to the reaction mixture of Fe(III)PPIX and βH, the pyridine preferentially binds unreacted Fe(III)PPIX to form a low spin bispyridyl complex that has been shown possible to quantify spectrophotometrically at the maximum absorbance wavelength of the Fe(III)PPIX soret band at 405 nm. βH solid does not react with the pyridine solution and therefore the assay was used to calculate % βH formed during the experiment.

(3.3.4) Preparation of stock solutions

(3.3.4.1) 0.1 M NaOH

Sodium hydroxide (NaOH) pellets (1.0 g) were weighed out and dissolved in 250 mL of water, this solution was stored in the dark at room teperature in a tightly sealed glass bottle and used until finished.

(3.3.3.2) 1: 9 Acetone: Methanol solution

Acetone: Methanol (1:9, *v*/*v*) stock solvent referred to as Ace: MeOH was prepared from analytical reagent grade acetone and methanol by premixing 50 mL of acetone with 450 mL of methanol and storing the solvent in an airtight container.

(3.3.3.3) Fe(III)PPIX solutions

All aqueous Fe(III)PPIX solutions were prepared from solid porcine haematin dissolved in 0.1 M NaOH and the required buffer solution to obtain the desired species of Fe(III)PPIX. Non-aqueous Fe(III)PPIX solutions were prepared from solid haematin initially dissolved in DMF and further diluted with the specified solvent to the required concentration.

(3.3.3.4) Antimalarial drug stock solutions

Unless stated, all aqueous experiments involving antimalarial drugs; chloroquine diphosphate (CQ), amodiaquine dihydrochloride dehydrate (AQ), quinidine sulphate dehydrate (QD) and quinine sulphate dehydrate (QN) stock solutions were prepared from their salts. The free base forms of CQ, QD and QN were used to prepare their non-aqueous stock solutions. They were prepared according to the method outlined by Kuter et al. and obtained from the Egan Laboratory.[322]

(3.3.3.5) 30% pyridine stock solution

A 30% pyridine stock solution was prepared fresh for addition to Fe(III)PPIX/ β-haematin solutions in the pyridine hemichrome inhibition (Phi-β) assay. In a 100 mL volumetric flask, 30 mL pyridine was added to a mixture of acetone (40 mL): water (20 mL): HEPES buffer (2 M, pH 7.5, 10 mL). This solution was further diluted to 5% in the Fe(III)PPIX solution of interest.

Chapter 4:
Partitioning of Fe(III)PPIX into Nile Red-labelled synthetic neutral lipid droplets

(4.1) Introduction

Since neutral lipids were first identified and found to be associated with haemozoin (Hz) crystals *in vivo*, synthetic neutral lipid droplets (SNLDs) have been verified as an efficient mediator of β-haematin (βH) formation *in vitro*.[57,118,124,323] Several studies have acknowledged them as the most likely biomolecules responsible for Hz synthesis *in vivo*.[120,127,143] To date, their exact role in this process is unknown. The unique composition of this lipid blend found to be present in the parasite digestive vacuole (DV) is the biologically-established 4:2:1:1:1 mole ratio of acyl glycerols; MSG, MPG, DPG, DOG and DLG, respectively.[124] The presence of this mixture presents as a challenge to elucidate the function of the lipid blend.

As discussed in Chapter 1, it has been postulated that the NLDs provide a lipid-aqueous (aq) interface that effectively nucleates Hz crystals where, upon formation, the hydrophobic crystal migrates to the hydrophobic interior of the lipid.[57,127] Several groups have investigated the interactions of Fe(III)PPIX with model lipid interfaces where the facial orientation and morphology of the resulting crystals imply molecular contact between polar lipid head groups and propionate groups on Fe(III)PPIX.[118,125,128,148,324] It has been shown that synthetic NLDs of the biologically-established blend (SNLBDs) control the number and size of βH crystals formed *in vitro*.[126] The study also demonstrated that these crystals lie on the surface of SNLBDs. The SNLBDs were characterised by TEM and confocal microscopy as non-hollow with continuous hydrophobic lipid interiors occurring in two dominant size populations of 74-146 nm and 366-438 nm.[126] Questions still remain about the nature of the interaction between Fe(III)PPIX and these neutral lipid droplets and their role in the promotion of βH formation is yet unknown. To date no direct measurements of Fe(III)PPIX partitioning into lipid droplets or its lipophilicity have been conducted. The aim of this study was to use fluorescence quenching to determine the partitioning profile of Fe(III)PPIX into SNLBDs found to be associated with Hz *in situ*.[124] Of particular relevance is the behaviour of Fe(III)PPIX and these lipids at DV and cytosolic pH values.[32,325] A main objective was to

determine the partition coefficient as measure of lipophilicity of Fe(III)PPIX under the relevant pH conditions. Furthermore, the effect of four quinoline antimalarial drugs on this partitioning profile as an indication of drug-Fe(III)PPIX complex lipophilicity is presented to determine if their inhibition of Hz crystal formation is related to lipid partitioning.

The intracellular probe Nile Red (NR) is a selective lipid stain used to probe the polarity and location of many lipid structures by fluorescence microscopy and spectroscopy.[120,164,165,326,327] A recent study has shown NR fluorescence in NLBs by confocal microscopy.[127] As mentioned in Chapter 2, heavy metal atoms are known to quench fluorescence emission intensity by a donor-acceptor mechanism that requires molecular contact between the donating species (the fluorophore) and the acceptor (the quencher). [308] Various studies have been conducted to measure the depth of liposome partitioning and micelle or lipid interaction of drugs using fluorescence-quenching techniques.[312,313,328–330] Thus, the relationship between the observed decrease in fluorescence intensity emission of the probe in the specific SNLBD environment and the local concentration of quencher is explored here for the fluorophore and quencher combination of NR and Fe(III)PPIX, respectively.

(4.2) Experimental Methods

(4.2.1) Materials, Instrumentation and General Procedures

All chemicals used were obtained from Sigma-Aldrich® (Vorna Valley, South Africa) and stored at 4°C in the refrigerator prior to use. Lipids were kept at -20°C. Fluorescence spectroscopy studies were performed at 298 K and 318 K by attachment to a thermostatted water bath. Both excitation and emission slit widths were set to 5 nm at an averaging time for data collection set to 0.5 s with scans at a rate of 120 nm/min and a PMT detector voltage of 700 V. The fluorometer was zeroed using the buffer or solvent of interest in the absence of NR. UV-vis spectroscopy experiments were conducted on a Varian Cary 100 spectrophotometer also attached to a thermostatted water bath at 298 K. 1 cm pathlength Hellma® quartz cuvettes were used for all experiments. All titrations were conducted using an appropriately-sized Hamilton syringe. Unless otherwise stated, all experiments were performed at least in triplicate. Solutions prepared in cuvettes (1 mL) were always allowed to equilibrate to the temperature of the thermostatted fluorometer cell-holder for 5 min prior to any measurement. All titration data were corrected for dilution.

Nile red (9-diethylamino-5*H*-benzo[α]phenoxazine-5-one) solutions (10 μM) were prepared in each respective solvent for calibration studies and in acetone for lipid studies. Aqueous buffer stock solutions (50 mM) were prepared from the appropriate salts and adjusted to the required pH with a NaOH slurry: (i) citrate-phosphate buffer pH 2.5-3.5, (ii) citrate buffer pH 3.8-5.55, (iii) MES buffer pH 5.9-6.6 (iv) HEPES buffer pH 7.0-7.9 (v) CHES buffer pH 8.0-10.0 and (vi) disodium phosphate buffer pH 12.00. Fe(III)PPIX stock solutions (10 mM, 1 mM and 0.5 mM) were prepared by dissolving solid porcine haematin in 0.1 M NaOH. Drug stock solutions (10 mM) for chloroquine diphosphate (CQ), amodiaquine dihydrochloride dihydrate (AQ), quinidine sulphate dihydrate (QD) and quinine sulphate dihydrate (QN) were prepared in the appropriate buffer for each pH value investigated, where soluble. For drugs insoluble at certain pH values, a diluted stock concentration was employed to keep the final drug concentration in the cuvette constant.

(4.2.2) Investigation of the relationship between NR fluorescence intensity and concentration

To demonstrate the dependence of NR fluorescence intensity on concentration, NR (10 μM stock) was titrated into acetone. An Ex λ_{max} = 540 nm was set (determined from the absorbance max of the NR spectrum). A plot of the arbitrary fluorescent intensity obtained from a NR concentration range of 0-5 μM in acetone was generated for the emission max wavelengths observed. A straight-line correlation was obtained at Em λ_{max} = 609 nm. The best-fit concentration range of NR was found to be 0-2 μM. A NR concentration of 1 μM, well within the established linear range, was chosen for all further fluorescence studies.

(4.3) Sample Preparation and Analysis Methods

(4.3.1) Preparation of NR stained SNLBDs

Synthetic neutral lipid droplets composed of the established biological blend of mono- and diacylglycerols (SNLBDs) in the mole ratio of 4:2:1:1:1 pre-stained with NR were independently prepared for each experiment. Lipid blend prepared in the manner outlined in Section 3.3.2 was diluted in 1:9 (v/v) acetone:MeOH (1 mM, 100 μL) and premixed with NR stock solution (10 μM, 100 μL) in the probe-to-lipid ratio of 1:100 by sonication. This premix was added drop-wise onto aqueous buffer solution (800 μL) with a syringe to afford NR associated SNLBDs upon mixing. To visualise the aq bulk in contrast to the lipid environment, sodium fluorescein stock solution was diluted in the aq buffer such that the final concentration was 10 μM.

(4.3.2) Analysis of NR-SNLBD

Visualisation of NR-labelled SNLBDs was performed on an 10 μL aliquot placed on a glass slide with cover slip using a fluorescence microscope. Images (100× magnification objective lens) were captured in brightfield and using the green light excitation filter (510-560 nm) for red fluorescence emission with a barrier absorption filter wavelength of 590 nm. Fluorescein images were captured at 20× magnification with green fluorescence excitation and red emission. Exposure time was set to 160-170 ms at 89% power. For fluorescence spectroscopy, the excitation max wavelength (Ex λ_{max}) was determined from the UV-vis

absorbance max of the solution in scanning range of 800-200 nm. Fluorescence emission spectra at Ex λ_{max} were monitored over a time period of 15 min to establish emission max wavelength (Em λ_{max}) and to investigate the reproducibility of fluorescence intensity signal of NR in SNLBDs.

(4.3.3) (a) An investigation of Nile red fluorescence quenching dependence on [Fe(III)PPIX] concentration

Nile red (1 μM) fluorescence was measured in MeOH at Ex λ_{max} = 540 nm and Em range 560-750 nm without Fe(III)PPIX to obtain the fluorescence intensity zero reading, I_{NR} and Em λ_{max} in MeOH. Fe(III)PPIX stock solution (0.5 mM) prepared in MeOH was then titrated into the fluorescence cuvette in aliquots using a 50 μL Hamilton syringe such that the effect of increasing Fe(III)PPIX concentration on fluorescence signal was measured after each Fe(III)PPIX addition. Fe(III)PPIX was added to the cuvette until the final Fe(III)PPIX concentration was 300 μM. A Stern-Volmer (SV) plot of the quenching data was obtained by plotting the ratio of fluorescence intensity at zero concentration of the quencher (Fe(III)PPIX), $\mathbf{I_0}$, and the fluorescence intensity at a specific concentration of Fe(III)PPIX, $\mathbf{I_a}$ versus the concentration of Fe(III)PPIX in question. A linear relationship was obtained up until 70 μM Fe(III)PPIX with slope giving the SV quenching constant, K_{SV}.

(b) Investigation of the nature of quenching mechanisms for Fe(III)PPIX quenching of NR fluorescence

Two methods were employed to infer whether the quenching process occurring in the fluorescence quenching studies described (4.3.3.a) is either (a) static or (b) collisional. (i) The temperature and viscosity dependence of NR fluorescence quenching in the presence of Fe(III)PPIX was used to distinguish static and dynamic quenching. Identical conditions for the quenching experiments described in section (4.3.3.a) at pH 7.51 were used but all fluorescence measurements were conducted at an increased temperature of 318 K as opposed to the standard 298 K. Linear SV plots to obtain K_{SV} were used.

(ii) Absorption spectra were also used to aid in differentiation between the two types of quenching. This was investigated by measuring the UV-vis absorbance spectrum of NR in methanol (5 μM) from 800-200 nm. Solid Fe(III)PPIX was dissolved in MeOH (0.5 mM) and

then titrated in 5 µL aliquots into the cuvette, measuring the corresponding absorbance spectrum at each concentration of Fe(III)PPIX until a concentration of 35 µM was attained. The UV-vis absorbance spectrum of Fe(III)PPIX dissolved in MeOH (35 µM) was also recorded separately. The difference between the absorbance spectrum obtained for Fe(III)PPIX in MeOH alone and the spectrum obtained in the presence of NR is presented to indicate any possible variance between the two. The inner-filter effect (IFE) was also evaluated to determine if a correction was necessary under the conditions applied to quenching experiments.

(4.3.4) Fe(III)PPIX quenching of NR fluorescence in various solvents

Quenching of NR by Fe(III)PPIX was carried out in different solvents to determine whether the quenching process is solvent-independent. The titration procedure described in section 4.3.3.a was followed exactly using solvents of varying polarity as given by their Dimroth-Reichardt hydrophobicity parameter $E_T(30)$ (kcal/mol) values and viscosities (m.Pa.s).[331] The solvents were (from lowest to highest $E_T(30)$): dodecane, toluene, ethyl acetate, chloroform, acetone, dimethylformamide, dimethylsulfoxide, isopropanol, pentanol, butanol, methanol and water. The UV-vis absorbance spectrum of NR in each solvent was recorded and Ex λ_{max} was determined from the max absorbance peak wavelength. A plot of NR Em λ_{max} obtained against solvent $E_T(30)$ was evaluated for polarity dependence.

(4.3.5) Fe(III)PPIX titration into NR labelled SNLBDs

(a) Quenching of NR by Fe(III)PPIX in the presence of the lipid blend was conducted over the pH range 2.50-8.00. A 1:100 premix (200 µL) of NR: NLB was added drop-wise to the appropriate aq buffer (20 mM) for each pH investigated, in a cuvette (800 µL) in such a way as to promote the formation of lipid droplets with minimal disturbance to the lipid-aq interface (method and concentrations as in 4.3.3.a). A zero intensity reading was taken in the absence of Fe(III)PPIX and recorded as I_0. Fe(III)PPIX was then titrated into the cuvette in µL amounts and a reading of the decreased fluorescence intensity was recorded as I_a after each addition for each pH value. A SV plot was generated and K_{SV} constants were obtained for quenching conditions at each pH investigated to obtain a pH profile for NR quenching.

(b) An investigation into Fe(III)PPIX quenching of NR in the absence of SNLBDs was conducted in a solution of similar $E_T(30)$; 50:50 v/v acetone:octanol solution. The quenching procedure in (4.2.5.a) was followed with the following changes. NR stock (acetone) was added to the acetone:octanol solvent system such that the initial concentration was 1 μM, the fluorescence emission at λ_{max} was recorded as I_0. Fe(III)PPIX stock solution was prepared from haematin solid dissolved in DMF and diluted to 0.5 mM in the acetone:octanol solvent system. SV plots were generated from the data and analysed for changes in K_{SV}.

(4.3.6) Measurement of log D_{OW} pH 7.51 of Fe(III)PPIX

The distribution coefficient, D_{OW} of Fe(III)PPIX between octanol and aq buffer (HEPES, pH 7.51, 20 mM) was evaluated by the shake-flask method (OCED Guideline for testing of chemicals 2003) at 37°C.[332] Haematin solid was dissolved in 0.1 M NaOH and premixed into the buffer (3 mL) at a final concentration of Fe(III)PPIX 57.8 μM. This solution was then mixed with an equal volume of pre-saturated (with aq buffer) octanol, shaken vigorously and allowed to equilibrate for 6 h. Each phase was then separated and final Fe(III)PPIX concentrations in each layer were determined by computing absorbance values measured with the extinction coefficients obtained (molar absorptivity coefficient) from linear Beer's Law UV-vis spectroscopy plots in each phase within the concentration range tested.

(4.3.7) (a) Exploring the effect of antimalarials on Fe(III)PPIX partitioning into NR-labelled SNLBDs

To determine whether quinoline drugs CQ, AQ, QD and QN quench NR fluorescence in SNLBDs at the pH values of interest (pH 2.80-12.00) in the absence of Fe(III)PPIX, NR-labelled SNLBDs were prepared according to the method described in Section 4.3.3.a and I_0 fluorescence intensity readings were recorded. Drug stock solutions (10 mM) were prepared in the required aq buffer (20 mM) for the pH investigated and titrated into a cuvette containing NR-SNLBDs. Readings were taken immediately after each drug addition, $I_{[a]}$, and checked for stability after 2 min post-stirring of the solution in separate experiments for

each drug. A plot of the ratio of $\frac{I_0}{I_{[a]}}$ against drug concentration was generated for each antimalarial compound at each pH investigated to determine if any quenching occurred.

(b) The effect of each of the antimalarials chosen on the SV quenching constant, K_{SV}, of Fe(III)PPIX quenching of NR-labelled SNLBDs over the pH range 2.80-12.00 was investigated. The method in section 4.2.5(a) of measuring K_{SV} was followed with the addition of drug stock solution to the cuvette such that the final concentration of each drug was 500 µM prior to any Fe(III)PPIX additions. This fluorescence spectrum was recorded as I_0 followed by the measurement of $I_{[a]}$ for each subsequent Fe(III)PPIX addition. The total amount of Fe(III)PPIX added to the NR+SNLBD+drug system was at least 75 µM for all titrations resulting in an end-point Fe(III)PPIX:drug concentration ratio of 1:6.7 to facilitate drug complexation of all Fe(III)PPIX added. SV plots were generated for each antimalarial at each pH value investigated.

(c) The SNLBD and aq buffer independent experiment conducted in section 4.3.5.c was performed with the inclusion of 500 µM drug stock solution in octanol prior to any Fe(III)PPIX additions to the cuvette. The free base forms of CQ, QD and QN were used to prepare these stock solutions.

(4.4) Results and Discussion

(4.4.1) Nile Red-stained Synthetic Neutral Lipid Blend Droplets

To confirm incorporation of the lipophilic dye Nile Red (NR) into non-hollow synthetic neutral lipid blend droplets (SNLBDs), bright-field and fluorescence microscopy were utilised for visualisation. SNLBDs were prepared following the method first reported by Hoang et al. for MSG by fluorescence microscopy and later demonstrated by confocal microscopy studies on NLBDs. [126,127] The image in Figure 4.1(a) was captured under bright-field illumination which appears to show coalescence of individual SNLBDs of various sizes in the nm to µm range to form larger aggregates. This is consistent with the visualisation of neutral lipid droplets by Ambele et al.[126]

Excitation with green light reveals that the NR red fluorescence emission is localised inside these individual lipid droplets (Fig. 4.1b). Images c-d in Fig. 4.1 contain the aqueous-specific dye fluorescein to show the contrast between the red-stained NR containing SNLBDs and the green stained aq bulk.[333] The nm sized SNLBDs show a red-gold fluorescence (Fig. 4.1c&f) while larger µm sized SNLBDs exhibit a dark red stained interior. This is consistent with the observations of Greenspan et al. who monitored NR localisation in a hydrophobic lipid environment with fluorescence emission maxima (Em λ_{max}) at 515-560 nm (yellow-gold) and at 610 nm (red).[326] The presence of two distinct size populations of SNLBDs has been previously established.[127] The filters available for this experiment were unable to separate these two emissions and significant fluorescence emission overlap was observed in several images. The possibility of photo-bleaching of NR signal from SNLBDs was monitored over several minutes and no observable effect was noted.

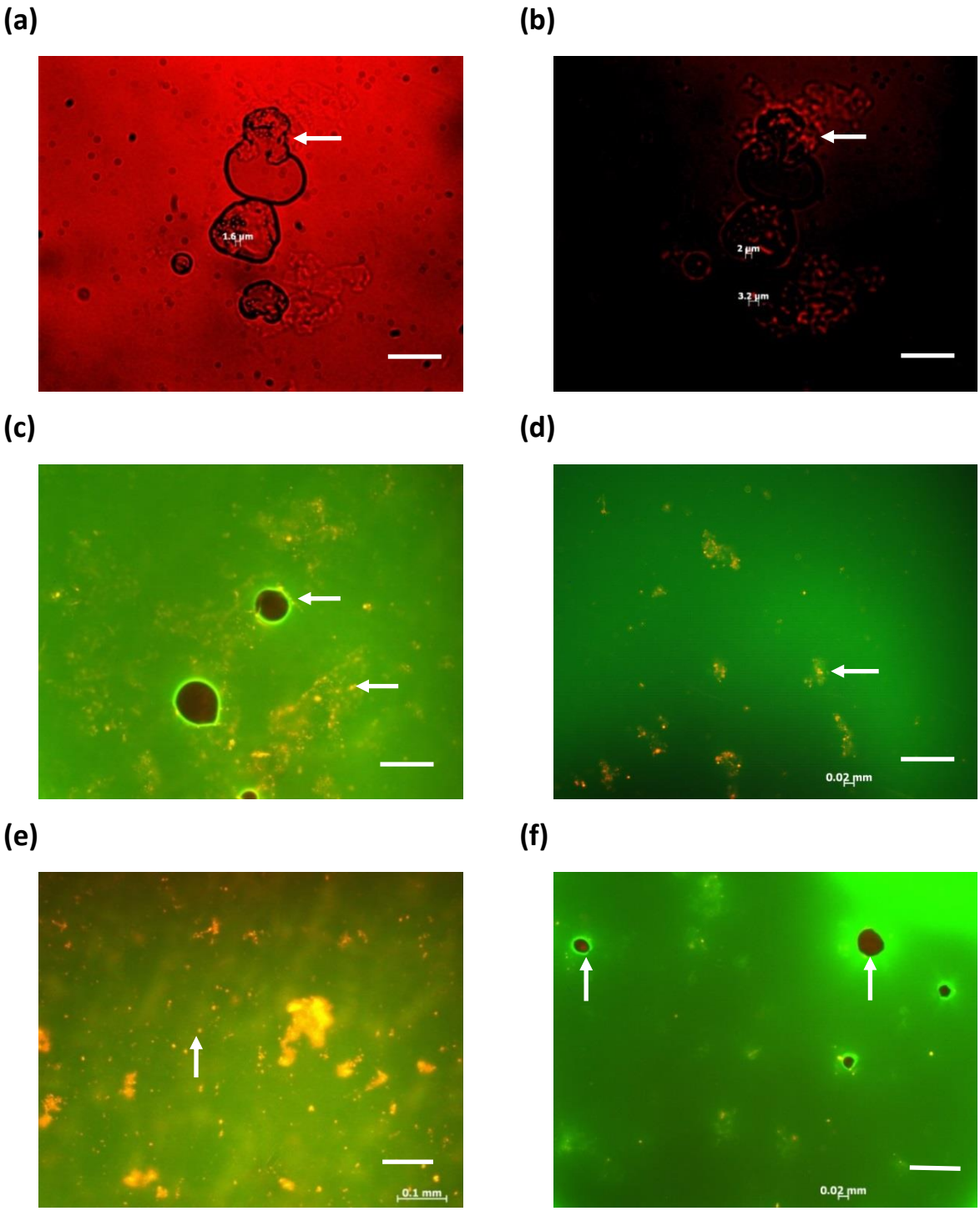

Figure 4.1 Images of SNLBDs stained with NR fluorescent dye captured in **(a)** brightfield (larger aq bubbles around SNLBDs appear as dark lines) and **(b)** under green light excitation (510-560 nm), Aqueous dye fluorescein diluted in aq buffer (HEPES, 50 mM, pH 7.50) **(c-f)** appears green for contrast. A variation in size populations for SNLBDs can be seen with distinctly large (50- 100 µm) droplets and smaller droplets (1-10 µm). White arrows indicate the various sized SNLBDs within a sample. Thick white scale bars represent 100 µm

The fluorescence emission properties of the solvatochromatic dye, NR, are dependent on the physicochemical properties of its microenvironment, particularly its polarity.[164] The fluorescence emission spectrum of NR in SNLBDs dispersed in aq medium displays an Em λ_{max} in the range of 615-618 nm as observed in a typical fluorescence spectrum shown in Fig. 4.2. The NR stock solution was prepared in acetone wherein NR typically displays an Em λ_{max} of 608 - 610 nm.[164] This red shift to slightly longer wavelength is indicative of a change in the local environment of NR molecules upon incorporation into the non-hollow SNLBDs.

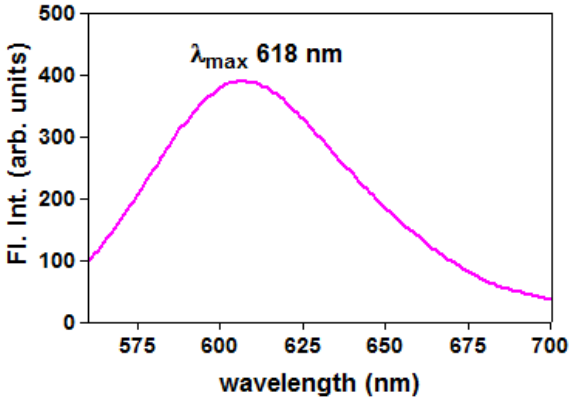

Figure 4.2 A typical fluorescence emission spectrum (Em λ_{max} = 615 - 618 nm) of 1 µM NR-labelled SNLBDs (100 µM) dispersed in aqueous solution, Ex λ_{max} = 540 nm.

The polarity of the unique neutral lipid environment of the SNLBDs was probed by investigating the Em λ_{max} of NR in various solvents with varying polarity. An examination of the relationship between Em λ_{max} and the Dimroth-Reichardt polarity index, $E_T(30)$ (kcal.mol^{-1}), revealed that the NR fluorescence Em λ_{max} observed, increased linearly with increasing $E_T(30)$.[331] For example, the non-polar solvent toluene ($E_T(30)$ = 33.9 kcal.mol^{-1}) induced a NR Em λ_{max} of 589 nm while NR displays an Em λ_{max} of 654 nm in the much more polar solvent water ($E_T(30)$ = 63.1 kcal.mol^{-1}).

A positive linear dependence of Em λ_{max} on $E_T(30)$ can be seen in Figure 4.3 demonstrating the solvatochromism of NR. Theoretical and steady-state fluorescence emission studies attribute this behavior to an increase in the dipole moment of NR during the absorption process upon vertical excitation of the ground state.[334,335] The dipole moment in the return to the ground state (emission process) is decreased and by using the Lippert equation (Eqn.

2.5.2) to model the molecular size and rotation of NR in a solvent of a particular dielectric constant, intramolecular charge transfer via the twisted intramolecular charge transfer (TICT) excited state of NR was proposed as the most likely mechanism. Interpolation using the average Em λ_{max} (617 nm) obtained for NR incorporated into SNLBDs corresponds to an $E_T(30)$ of 45 ± 4 kcal.mol^{-1}. This reveals that the unique interior of SNLBDs possess a polarity that lies between that of the solvent acetone with an $E_T(30)$ = 42.2 kcal.mol^{-1} and octanol, with an $E_T(30)$ = 48.1 kcal.mol^{-1}.

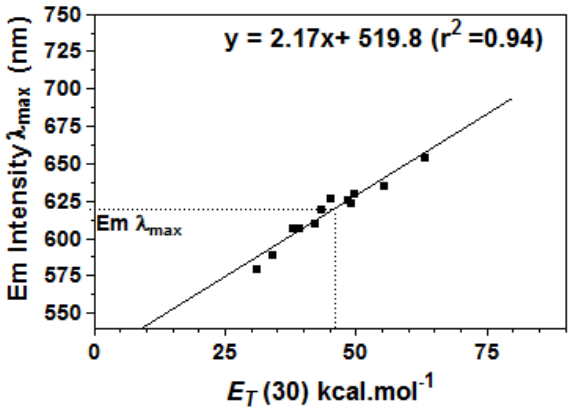

Figure 4.3 Linear correlation (r^2 = 0.94) between the fluorescence Em λ_{max} of NR and the relative polarity indicator, $E_T(30)$ in kcal.mol^{-1}, recorded in various solvents. The dashed interpolation lines indicate the relative polarity of the SNLBDs based on an Em λ_{max} of 618 nm.

In fact, as shown in Fig. 4.4 the fluorescence emission spectrum of NR (Ex λ = 540 nm) in a 50% acetone:octanol mixture (v/v) appears to be virtually the same as that obtained in the SNLBDs (Fig. 4.2) with Em λ_{max} = 618 nm. A wide range of Ex and Em wavelengths of NR have been employed to quantify and selectively stain polar and neutral lipids.[336] Typical intracellular neutral LDs interiors have been classified as non-polar, however; these LDs include esterified cholesterol and triglycerides and they exhibit NR Em λ_{max} in the yellow fluorescence range (535-590 nm). [337] NR has been shown to emit at red emission wavelengths of approximately 616-650 nm when staining phospholipid-cholesterol lipid blends, extracted intracellular lipid contents or when localised in regions of lower polarity within systems of mixed polarity.[338–340] This measurement of the relative polarity of and Stokes shift upon NR incorporation into SNLBDs definitively demonstrates that the

fluorescence signal obtained in these and any further experiments represent NR molecular changes happening in the unique chemical environment of the non-aqueous interior of these lipid droplets.

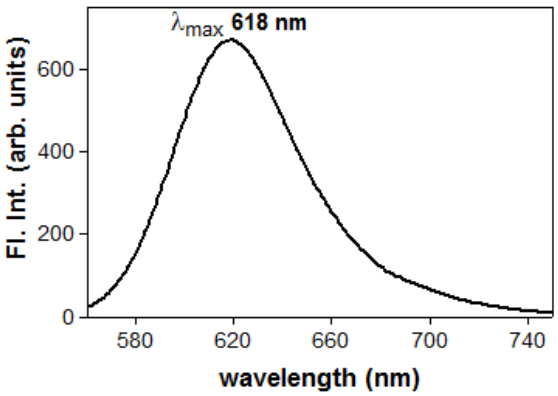

Figure 4.4 NR fluorescence emission spectrum in 50% acetone: octanol (v/v) solution showing the Em λ_{max} = 618 nm.

(4.4.2) Linear dependence of fluorescence intensity of NR on concentration

The concentration dependence of fluorescence emission intensity was determined by titration of NR into acetone prior to performing any quenching experiments. The fluorescence response was found to be linear in the range 0-1 µM NR as depicted in Fig. 4.5 with an inset showing that the response obtained was still proportional to increasing NR concentration up until at least 5 µM NR. However, to avoid any inner-filter absorption effects (IFE), the concentration of NR for all SV experiments was kept low at 1 µM. It is well established that fluorescence measurements performed at sufficiently low concentrations of fluorophore that exhibit a linear proportionality of fluorescence intensity with concentration are generally not subject to the artefacts that result in the inner-filter effect (defined in section 2.5.2).[341]

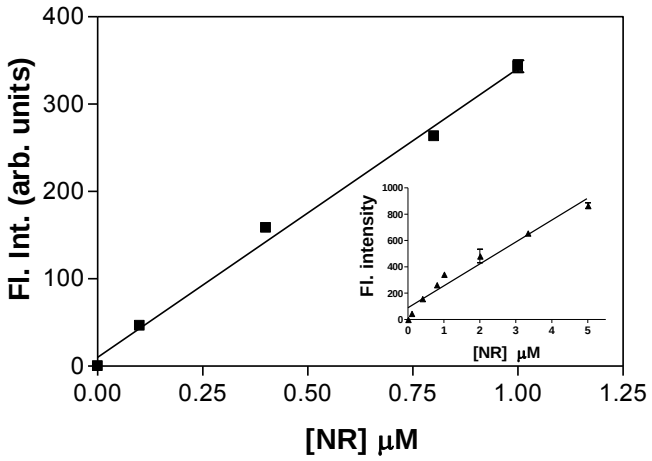

Figure 4.5 Linearity of NR fluorescence emission signal with concentration in acetone excited at 540 nm with Em λ_{max} 609 nm, r^2 = 0.98. Error bars represent the SEM (n=3).

(4.4.3) Fluorescence of NR in the presence of Fe(III)PPIX:

(4.4.3.1) Quenching investigation

The effect of 35 μM Fe(III)PPIX on NR in MeOH is depicted in Figure 4.6. MeOH was chosen as a solvent in which both NR and Fe(III)PPIX are soluble. To confirm that the decrease in fluorescence intensity observed in Fig. 4.6 is a result of quenching and not an artifact of the IFE arising from the inherent optical absorption of NR and Fe(III)PPIX, at the relevant conditions under the which the experiment was conducted, a correction (Eqn. 2.5.6) was applied. There are two components to the IFE correction. Firstly, the primary inner filter effect (PIFE) is a decrease in intensity of the excitation energy due to the optical absorption of the fluorophore and quencher at the excitation wavelength. Secondly, the secondary inner filter effect (SIFE) accounts for a fluorescence intensity decrease that occurs due to fluorophore and quencher absorption of at the emission wavelength.[306]

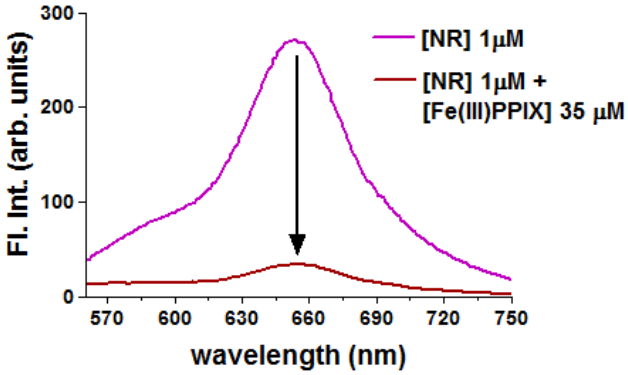

Figure 4.6 The effect of addition of Fe(III)PPIX on NR fluorescence emission. The quenching effect manifests as a decrease in fluorescence intensity.

The PIFE is of greater concern because excitation wavelengths are always shorter than emission wavelengths and thus correspond to greater overlap with the absorption band. [342] A decrease in fluorescence intensity without any change in Em λ_{max} or spectrum shape as observed in Fig. 4.6 is typical of dynamic fluorescence quenching.[308] From this observation it already seemed likely that the quencher, Fe(III)PPIX, was not inducing a stronger absorption or an absorption band shift relative to the absorption of the fluorophore arising from some molecular interaction. For example, the formation of new fluorescent complex between NR and Fe(III)PPIX.[343]

It is generally accepted that the inner-filter correction is not necessary for quencher solution absorbance of <0.2 in excitation and or emission wavelength regions.[341,344] Recent investigations however, have shown that for situations where Stern-Volmer (SV) quenching occurs with high inverse K_{SV} values of 50 M^{-1} even if the quencher absorbance is lower than 0.02 absorbance units, the correction needs to still be applied in order to gain corrected K_{SV} values that serve as an accurate reflection of dynamic quenching.[345] This was revisited upon analysis of K_{SV} values obtained in section 4.4.2.5. The absorbance spectra obtained for all the relevant components are presented in Figure 4.7 for a comparative reference. Both the excitation (540 nm) and the emission (618 nm) maximum wavelength absorbance values of the fluorophore and quencher chromophores, as well as the medium of the experiment, the SNLBDs, are of relevance to the inner filter correction proposed by Lakowics in Eqn. 2.5.6.[299]

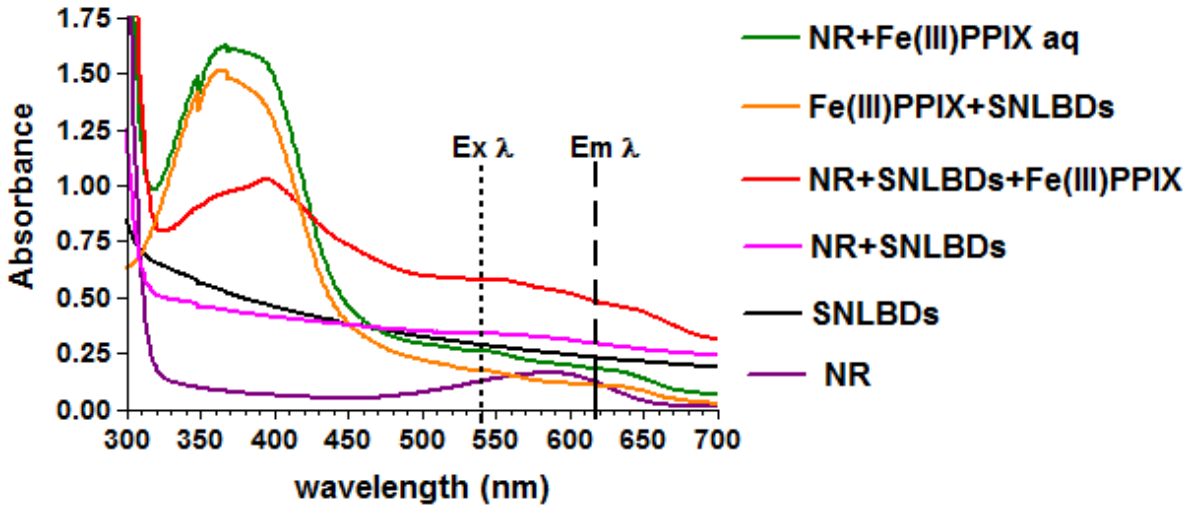

Figure 4.7 UV-vis absorbance spectra of SNLBDs, the fluorophore, NR, and the quencher, Fe(III)PPIX, over the range 300-700 nm. The excitation and emission wavelengths of interest are highlighted for application to the inner filter effect correction. The concentration conditions were as follows: [NR] = 1 μM, [SNLBDs] = 100 μM and [Fe(III)PPIX] = 35 μM dispersed in 20 mM aq citrate buffer, pH 4.80.

Due to their colloidal nature, the turbid SNLBD solution displays a high background absorbance resulting from light scattering by the lipid droplets as seen in Fig. 4.7. To simplify the correction, the absorbance of the SNLBDs was excluded from the calculation, as its concentration was constant across all experiments unless specifically varied and while it was necessary to detect a NR fluorescence signal, the lipid was presumed to affect NR quenching equally for all experiments. The absorbance of 1 μM NR and 35 μM Fe(III)PPIX in MeOH at the Ex and Em λ_{max} was found to be 0.27 and 0.22 absorbance units, respectively. This yields an IFE correction calculated at 3.1 % for fluorophore and quencher chromophore absorbance combined. [346] This value agrees well with reported IFE corrections for this type of fluorescence spectrophotometer (Varian Cary Eclipse) which inherently minimizes the PIFE due to the use of horizontal slits allowing the measurement of fluorescence of solutions of high absorbance.[347] To further confirm that the apparent quenching observed is not merely a result of increasing Fe(III)PPIX concentration and thus increasing optical density of the solution, but due to an interaction between NR or NR* and Fe(III)PPIX, a variety of methods were employed.

(4.4.3.2) Dependence of fluorescence intensity on NR concentration in SNLBDs with and without Fe(III)PPIX

In order to infer the relative partitioning of Fe(III)PPIX into NR-labelled SNLBDs by measurement of NR fluorescence quenching, an initial determination of a constant NR fluorescence intensity in SNLBDs was established. Fig. 4.8 shows the fluorescence emission intensity of NR titrated into SNLBDs. The initial response of fluorescence emission intensity measured at an Em λ_{max} of 618 nm with increasing NR concentration up to 0.25 µM NR was linear, obeying the Beer's Law relationship, which is indicative of non-self-associative fluorophore behaviour.[299] A further increase of NR concentration revealed a levelling-off of fluorescence emission intensity until a consistent signal was obtained at 1 µM NR. This situation was interpreted as one where the fluorescence intensity measured at 618 nm was from SNLBDs saturated with NR such that any increase in NR concentration would not produce a further increase in fluorescence intensity monitored from that concentration of lipid. This has been visualised for NR stained MSG SLBDs by confocal microscopy.[348] Fluorescence kinetic studies were performed on these samples for 15 min, which confirmed that an unchanged equilibrium signal was achieved for 1 µM NR. Finally, the initial fluorescence intensity reading, I_0 , for NR labelled SNLBD preparation at each pH tested was found to be insensitive to the pH of the aqueous medium.

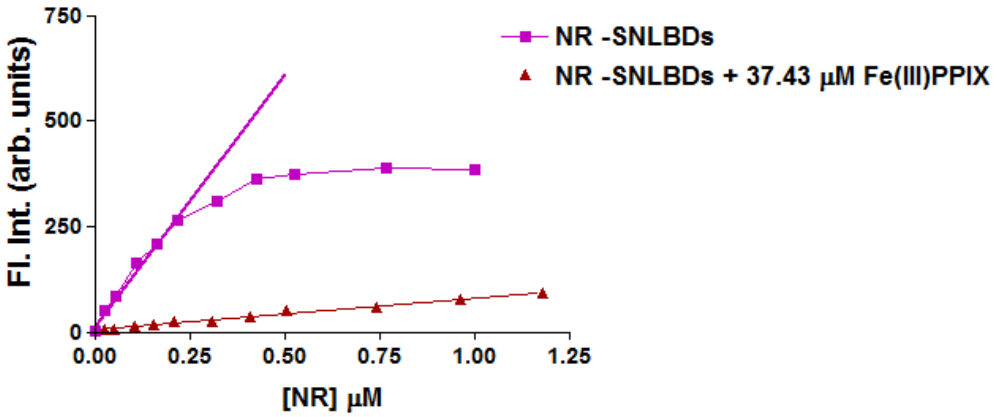

Figure 4.8 The effect of titrating 10 µM NR stock solution alone (purple line) into SNLBDs (100 µM) up to a concentration of 1 µM. The linear response for increasing fluorescence signal with increasing NR concentration (at low concentration) is highlighted with the signal response shown to be steady at 1 µM NR (r^2 = 0.989). NR titration (red line) into Fe(III)PPIX+SNLBDs at 37.43 µM Fe(III)PPIX was found to be linear (r^2 = 0.99) beyond 1 µM NR.

A titration of NR into SNLBDs in the presence of 37.43 µM Fe(III)PPIX solution was performed and the results are presented in Fig. 4.8 for comparison. In the presence of Fe(III)PPIX, the decreased fluorescence emission intensity is due to the dynamic quenching of NR signal and it is important to note that the linear concentration response is maintained beyond a concentration of 1 µM NR. It has been pointed out that, if fluorescence changes observed correspond to low enough concentrations of fluorophore and quencher to produce a linear signal, all inner filter effects can be ignored.[347] This seems to be the case here since the Beer's Law relationship is maintained.[299,349] These conditions were selected as ideal for further quenching experiments and in order to achieve consistency between I_0 readings and these concentrations were maintained throughout.

(4.4.4) Fe(III)PPIX quenching of NR in SNLBDs: Static vs Collisional Quenching

As introduced in Chapter 2, there are two main types of quenching which are relevant to this study; static and collisional. The differences between the two types may be explored in order to gain further information about the mechanism of quenching prevailing in the system of interest.[309] Two methods were employed to infer whether the quenching process occurring for NR stained SNLBDs in the presence of Fe(III)PPIX adhered to a mechanism of either (a) static quenching through the formation of a non-fluorescent ground-state complex between NR (fluorophore) and Fe(III)PPIX (quencher). Or (b) collisional quenching, a diffusion- and, hence time-, temperature- and viscosity-dependent process.[308] The temperature and viscosity dependence of NR fluorescence quenching in the presence of Fe(III)PPIX was used to distinguish between static and dynamic quenching (see Chapter 2, section 2.6 for theoretical background). Linear SV plots (Eqn. 2.5.3) with slopes equal to K_{SV} were obtained under these quenching conditions at temperatures of 25°C and 45°C and are shown in Figure 4.9.(a).

(a)

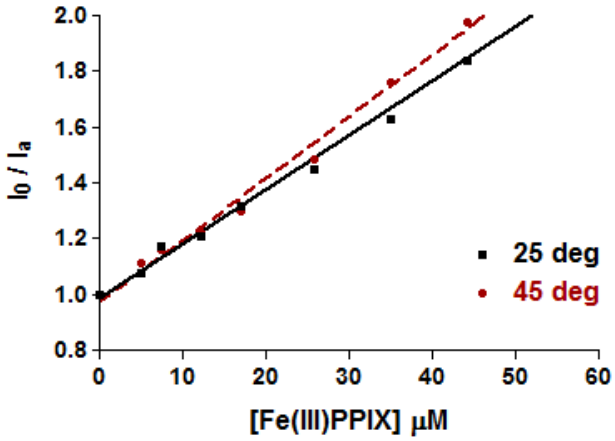

(b)

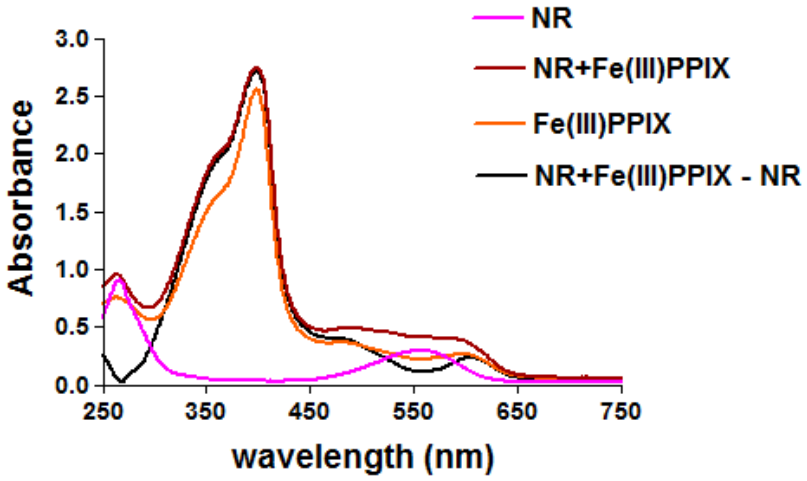

Figure 4.9 (a) Linear SV plots of Fe(III)PPIX quenching of NR-labelled SNLBDs at pH 7.51, at 25°C (r^2 = 0.98) and elevated temperature of 45°C (r^2 = 0.99) to demonstrate the diffusion response. In **(b)** UV-vis absorbance spectra of 5 µM NR + 100 µM Fe(III)PPIX in MeOH and a mixture of the two solutions, as well as the calculated difference between the mixture and NR, are shown.

Collisional quenching at elevated temperatures results in elevated diffusion coefficients and bimolecular quenching constants (k_q) which are expected to increase with increasing temperature.[350] Therefore the slope and hence K_{SV} of a SV plot conducted at 45°C is expected to be larger than the corresponding K_{SV} value at 25°C. This situation is observed for Fe(III)PPIX quenching of NR fluorescence in SNLBDs, with K_{SV} at 25°C = 0.0196 ± 0.0005 and for K_{SV} = 0.0222 ± 0.0004 at 45 °C. This can be interpreted in terms of concentration of the

quencher, [Fe(III)PPIX], at which 50% of fluorescence is quenched , K_{SV}^{-1} (i.e. $\frac{I_o}{I} = 2$), corresponding to 51.2 µM and 45.0 µM respectively.

For static quenching, an increase in temperature is likely to result in a decreased stability of the ground state fluorophore-quencher (NRQ) complex formed and a lower value of the static quenching constant (*K*s) is expected. This is not observed for the system under investigation. In the absence of time-resolved fluorescence experiments to determine if the fluorescence lifetime, τ_0 , without the quencher is affected, the possibility of formation of a ground state FQ complex was explored instead. For this purpose, UV-vis absorption spectra were used to differentiate between the two types of quenching.

Static quenching requires the formation of a ground-state complex between NR and Fe(III)PPIX and would therefore result in a change in the native absorbance spectrum of both the NR and the Fe(III)PPIX.[351] This was investigated by measuring the UV-vis absorbance spectrum of NR, Fe(III)PPIX and a mixture of the two solutions in MeOH from 250-750 nm , see Figure 4.9(b). The difference between the absorbance spectrum obtained for Fe(III)PPIX+NR and the spectrum obtained is presented to indicate any possible variance between the two. Collisional quenching affects only the excited state of the fluorophore and is thus not expected to alter the absorbance spectrum observed for NR. The absorbance maxima of both NR and Fe(III)PPIX remain unchanged indicating that the ground state of both species were unaffected and no appreciable complex is formed. Indeed, the UV-vis spectra obtained for the NR+Fe(III)PPIX mixture appears to be a simple combination of the two. Clear examination of the mixture spectrum obtained when the UV-vis spectrum of NR was subtracted from it, confirmed that essentially no change occurs and thus strongly indicates that the quenching type is collisional.[352]

(4.4.5) The effect of pH on Fe(III)PPIX quenching of NR in SNLBDs

The lipid-aq interface as well as the hydrophobic lipid droplet interior represent two unique physicochemical environments that are thought to facilitate the nucleation and growth processes of the crystallisation of Fe(III)PPIX to form Hz. The interface, composed of long chain acyl glycerols, which are exposed to the polar acidic aq surroundings of the DV, offer what is postulated to be a template for the epitaxial growth of the crystal. [126,127]

Alternatively, the inner leaf of the diacylglycerol phospholipid membrane of the DV has been proposed as the site of Hz heterogeneous nucleation as revealed by water-window X-ray imaging. [324] Modelling of the molecular contacts between free C=O of propionic acid groups on the 100 face of Hz and the OH moiety of the acylglycerols has supported the proposal of epitaxial growth.[130] These studies also propose that Hz crystal growth occurs within the aq environment of the DV, citing the inhibitory action of water-soluble antimalarials as the evidence for this. Later studies showed β-haematin (βH) crystals, (isostructural with Hz) to be in contact with the surface of the SNLBDs *in vitro* and suggested that in the absence of definitive evidence of the biocrystallisation process in contact with lipid droplets *in vivo,* the process may indeed occur at the inner leaflet of the DV membrane bilayer.[126] Regardless of the exact lipid interface that mediates Hz formation *in vivo*, an investigation of the nature of Fe(III)PPIX interaction with lipids was necessary. To achieve the primary objective of this study, assessment of the partitioning of the Hz precursor, Fe(III)PPIX, into NLBDs over a large pH range was conducted.

The introduction of soluble Fe(III)PPIX to an aq suspension of NR stained SNLBDs resulted in the quenching of the NR fluorescence in a concentration dependent manner. This data was collected up to at least 50 μM Fe(III)PPIX at a constant NR+SNLBD concentration in separate experiments from pH 2.80-12.00 to yield linear SV quenching plots with y-intercepts of 1 and K_{SV} from the slopes. All SV plots obtained for Fe(III)PPIX quenching of NR-labelled SNLBDs demonstrated this behaviour, indicative of a single class of fluorophores detected at the Em λ_{max} of 618 nm, all of which were equally accessible to the quencher (see Chapter 2, Section 6.2.5). Figure 4.10 shows two examples of the SV plots obtained which were collected at two pH values of interest, where (a) pH 4.80 is the approximate pH of the DV aq medium and (b) pH 7.00 represents the pH region where the axial ligand attached to the Fe^{3+} metal centre begins to convert from H_2O to OH^-.[72] It is noted that typical K_{SV} values achieved are significantly lower than the 50 M^{-1} where the IFE can pose additional complications.[345]

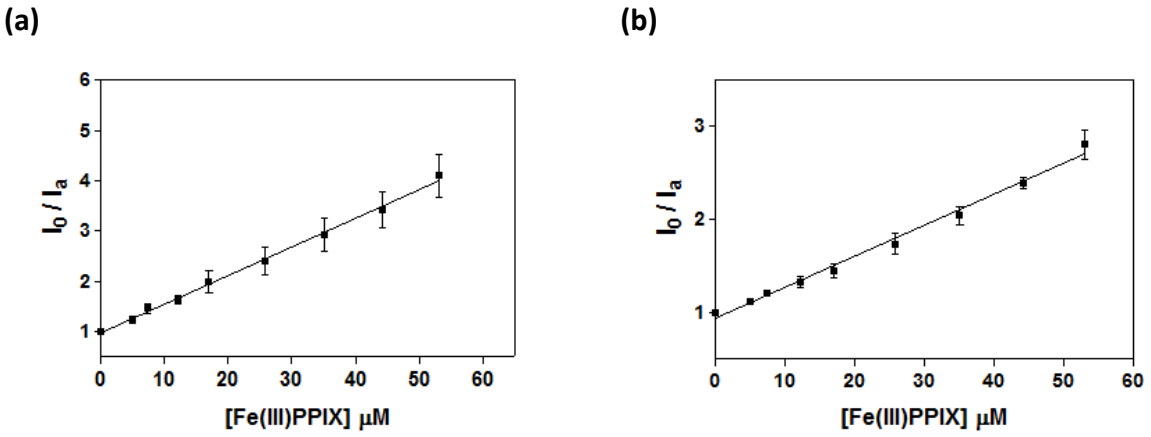

Figure 4.10 Linear SV plots for NR quenching at pH (a) 4.80 (r^2 = 0.89) with K_{SV}^{-1} = 17.6 µM and (b) 7.00 (r^2 = 0.96) and K_{SV}^{-1} = 30.0 µM to illustrate quenching dependence on pH. Error bars represent the SEM (n=5).

In Fig. 4.10, it is shown that for, the pH prevalent in the parasite DV, roughly 1.5 times less Fe(III)PPIX is required to quench 50% of NR fluorescence than under neutral pH conditions. K_{SV} is the product of the fluorescence lifetime of the fluorophore (τ_0) and the bimolecular quenching constant (k_q) (introduced in Chapter 2.5, Eqn. 2.5.3). It is not expected to change as a function of pH because the lipid-interior of the NR-labelled SNLBDs is not likely to be altered by the pH of the aq medium. K_{SV} was found to be dependent on pH of the aq medium. Since the observed NR fluorescence signal arises only from the interior of the SNLBDs, the variation in K_{SV}^{-1} in SNLBDs obtained from pH over the range tested, likely reflects the amount of Fe(III)PPIX that partitions into the SNLBDs.

The relative partitioning of Fe(III)PPIX into the neutral lipid interior of SNLBDs appears to be related to the prevailing axial ligand and thus molecular charge of Fe(III)PPIX in aq solution at a particular pH. This is shown in Table 4.1. For example, under aq acidic pH conditions (< pH 2.5), Fe(III)PPIX has an overall charge of +1 due to summation of the 3+ contribution of the metal ion and the 2- charge on the porphine core of coordinated protoporphyrin IX. Neither propionic acid moeity is deprotonated and the axial ligand is most likely neutral H_2O (Table 4.1). [72]

Table 4.1 Expected partitioning of Fe(III)PPIX over the pH range investigated based on protonation state of the axial ligand attached to Fe(III) central atom.

pH	Axial ligand	Protonation state	Overall charge[a]	Expected [partitioning][b]
< 2.5	H_2O	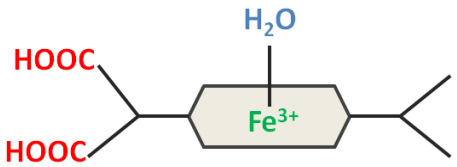	+1	low
2.5 – 5.5	H_2O	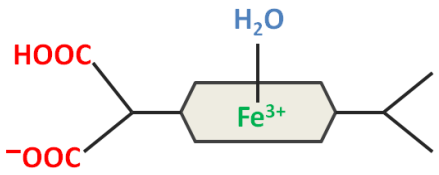	0	high
5.5 – 7.5	H_2O	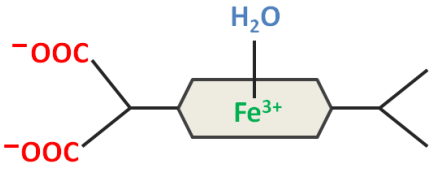	-1	low
≥ 7.6	OH^-	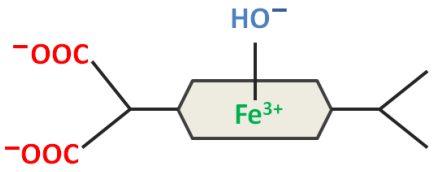	-2	lowest

[a] Addition of the porphyrin ring charge contribution of -2 [353]

[b] [partitioning] refers to the concentration of Fe(III)PPIX in SNLBD estimated from K_{SV}

Thus at very low pH, charged Fe(III)PPIX is not expected to partition well into neutral lipid bodies and more Fe(III)PPIX will be required to quench 50% of NR fluorescence (large K_{sv}^{-1}), since only a small fraction of uncharged Fe(III)PPIX will partition into the hydrophobic interior of the SNLBD where NR resides. As the pH increases to about pH 5.5, deprotonation of one of the propionic acid groups occurs and partitioning of Fe(III)PPIX (μM) is predicted to increase to a maximum for the neutral species, resulting in a maximum K_{sv} value. At alkaline pH as the overall Fe(III)PPIX charge becomes negative, it is expected to decrease again. The results, presented as the log K_{SV} or relative partitioning coefficient of Fe(III)PPIX with

increasing pH in Figure 4.11 confirm the expected trend between pH 2.5 and 8, such that the data is shown to adhere to a sigmoidal curve. Of the most interest is the relative partitioning of Fe(III)PPIX at the pH values corresponding to that of DV and cytosolic pH where Fe(III)PPIX is most likely neutral and anionic respectively (see Table 4.1 and Fig. 4.11). The relatively large data scatter is an inherent result of working with SNLBDs, which scatter light strongly.

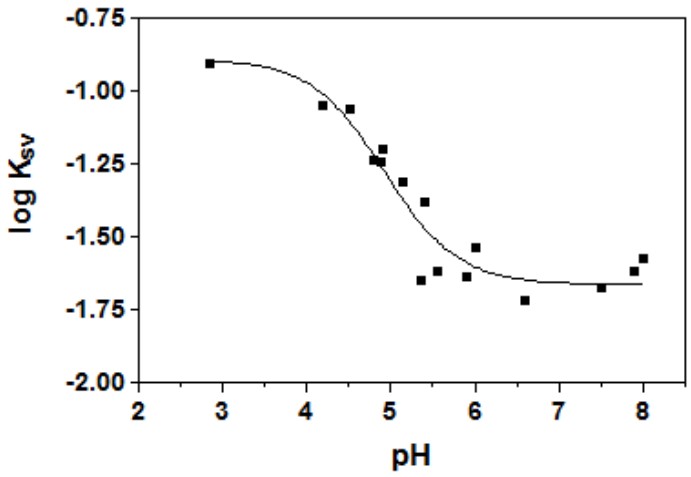

Figure 4.11 Quenching parameter (log K_{sv}) of NR labelled SNLBDs by Fe(III)PPIX vs pH of the aq medium in which lipid droplets were dispersed. Fitting to an equilibrium equation allowed the putative propionate pK_{a1} of Fe(III)PPIX to be obtained. The fitted value was 4.62 ± 0.09.

The data obtained from at least triplicate experiments for each pH value show a decrease in log K_{sv} from low pH to neutral and higher pH values which is attributed to an increase in local concentration of Fe(III)PPIX inside the NLBD as predicted by Table 4.1. The pH profile of Fe(III)PPIX partitioning into SNLBDs could be fitted to a protonation model with a single pK_a value of 4.62 ± 0.09. The value of K_{sv} was 0.021 ± 0.003 μM^{-1} in the deprotonated charged form (pH 7.51) and 0.124 ± 0.007 μM^{-1} (pH 2.85) in the protonated form. Assuming that this difference arises solely as a result of increased Fe(III)PPIX concentration in the SNLBDs, this indicates a 6 ± 1 fold increased accumulation of the protonated relative to the unprotonated form of Fe(III)PPIX in SNLBDs.

It is interesting to note that the pH partitioning profile observed for Fe(III)PPIX resembles the reported pH-dependent profile for the formation of βH.[127] NLDs have been shown to

effectively induce βH formation with the greatest conversion of Fe(III)PPIX occurring at acidic pH values between pH 3 and 5. The %βH formed is markedly decreased at pH values lower or greater than the pH conditions where Fe(III)PPIX is neutral. The authors attributed this trend to the ionisation states of βH at low acidic and basic conditions where both propionic acid groups are unionised and ionised, respectively. In the presence of SNLBDs, the observed trend in Fe(III)PPIX lipophilicity with pH may also account for the effective lipid-mediated conversion of Fe(III)PPIX into βH under DV pH conditions through lipid partitioning.[135] Indeed, the observation here supports the hypothesis that lipid interiors are the most likely site of βH formation.

(4.4.6) Attempts to measure Fe(III)PPIX partitioning constant, K_p

As discussed in chapter 2 (section 2.5.2), evaluation of the partition coefficient, K_p, is in principle possible for the quencher, Fe(III)PPIX, that partitions into the interior of SNLBDs dispersed in aq bulk solution. [311–313,318] Unfortunately, the data scatter was simply too large to obtain meaningful values for K_p. Other attempts to obtain K_p of Fe(III)PPIX from the ratio of the amount of NR quenching that occurred in SNLBDs (K_{SV} SNLBD/aq) and the degree of quenching that was measured in a system independent of lipid droplets were made. However, due to inherent viscosity differences between the micro-environment of the interior of SNLBDs and that of different solvents, this method proved inconclusive.

(4.4.7) Measurement of log D_{OW} for Fe(III)PPIX partitioning between octanol and water

Since *log* D_{lipid} could not be determined directly from K_{SV} data the best alternative was to measure the octanol-water partitioning of Fe(III)PPIX at pH 7.51 where it is soluble in both media. This was done by the shake flask method illustrated in Fig. 4.12. Equation 4.4.1 was used to arrive at a distribution constant, log D_{OW}, of 1.8. Monomeric Fe(III)PPIX was ensured by performing the distribution experiment using pH 7.5 aq HEPES buffer as well as the addition of a 5% pyridine solution to the aq portion following separation of the layers, prior to measurement.[253] The pK_a used to calculate log *P* was 4.62 determined from the protonation model in Fig. 4.12. This value led to a log *P* for Fe(III)PPIX in its neutral form of 2.8 (calculated using Eqn. 4.4.4). A log *P* > 0 implies the majority of the Fe(III)PPIX can be

found in the hydrophobic octanol phase consistent with the lipophilic nature of the unionised form.

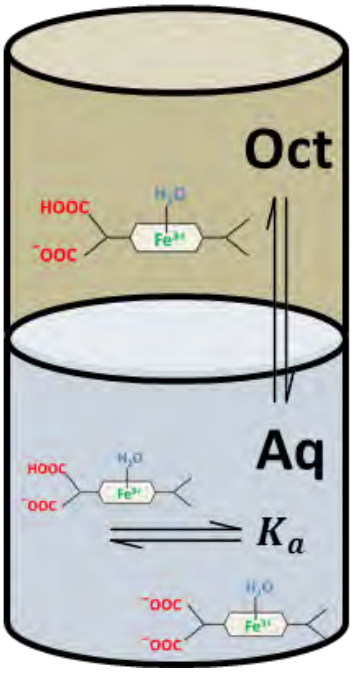

$$\log D_{OW} = \log \frac{[\mathrm{Fe(III)PPIX}]octanol}{[\mathrm{Fe(III)PPIX}]\ aq\ buffer} \qquad (4.4.1)$$

$$pKa_1 = \log \frac{[\mathrm{Fe(III)PPIX.}\ (\mathbf{COO^-/H})\ ]}{[\mathrm{H^+}][\mathrm{Fe(III)PPIX.}\ (\mathbf{COO^-})_{\mathbf{2}}]} \qquad (4.4.2)$$

$$\log D_{OW} = \log P + \log \frac{1}{\left[1 + 10^{(\mathrm{p}K_{a1} - pH)}\right]} \qquad (4.4.3)$$

$$\log P = \log D_{OW} + \log\left[1 + 10^{(\mathrm{p}K_{a1} - \mathrm{pH})}\right] \qquad (4.4.4)$$

Figure 4.12 The system and equations used to determine the octanol-water partition coefficient of Fe(III)PPIX by the shake-flask method. K_a denotes the propionic acid dissociation constant.

This study reaffirms the lipophilic behaviour of Fe(III)PPIX agreeing with several literature reports on the ability of Fe(III)PPIX to traverse membranes and cause haemolysis.[354,355] One study found CO-haem to be readily taken up by phospholipid vesicles in a manner that was dependent on membrane thickness and haem or Fe(III)PPIX speciation.[356] To date no measurements of log *D* or log *P* are available in the literature for Fe(III)PPIX. However, lipid vesicle partitioning studies on mesoporphyrin IX and deuteroporphyrin IX (pictured in Fig. 4.13) have reported that deuteroporphyrins transfer more rapidly through bilayers upon decreasing the pH from 7.5 to 6.5, inferring that the passive transport of porphyrins is controlled by pH and ionisation state.[357] Further studies found zinc protoporphyrins partition into membranes with their charged propionates near the lipid-aq interface.[358]

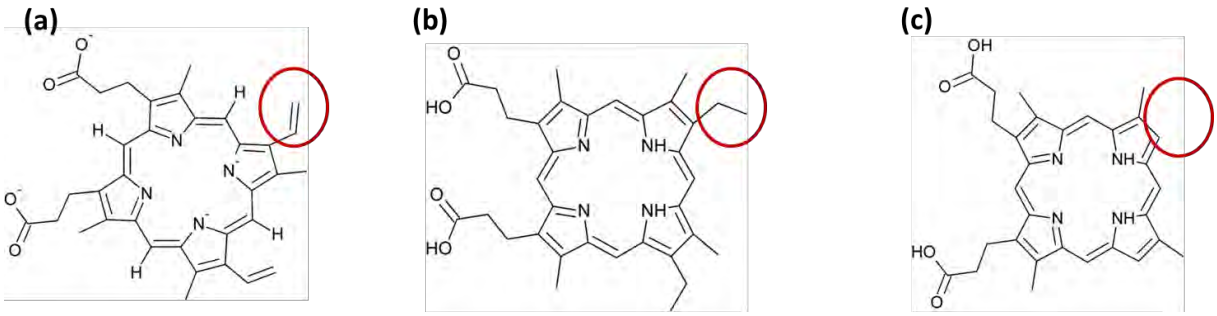

Figure 4.13 A schematic structural representation of the porphyrins; (a) protoporphyrin IX (vinyl group), (b) mesoporphyrin (ethyl group) and (c) deuteroporphyrin (H atoms) The red circle represents the structural differences in R group on pyrrole subunits.

Actual log D_{ow} measurements have been attempted for some porphyrin derivatives to compare with the predicted log *P* and log $D_{pH\ 7.3}$ coefficients against lipid vesicle partitioning.[359] Protoporphyrin IX (no metal group) was predicted to have a distribution coefficient at pH 7.3 of 2.01 and log *P* of 7.27 and ionisation constants of the propionate groups of 4.47 and 4.79 with experimental measurement of log $D_{pH\ 7.3}$ of 2.12 ± 0.21 and a calculated log *P* > 5. Although, inclusion of a metal in the porphyrin core is expected to affect the lipophilicity of the compound, the hydrophobic nature is not expected to be radically changed. In a biological context, Hz has been found to be associated with and inside hydrophobic lipid structures within the *Schistosoma mansoni* parasite or blood- feeding organism, *R. prolixus.*[58] The observed lipophilicity of Fe(III)PPIX supports the proposal that *in vivo* free Fe(III)PPIX concentrates in the millimolar range inside these lipid bodies to facilitate its conversion to Hz crystals. This data confirms the lipophilicity of the protoporphyrins and highlights the plausibility of the hydrophobicity parameters obtained for Fe(III)PPIX in this work, which is the first report of an experimentally-measured distribution coefficient and calculated partition coefficient of Fe(III)PPIX between aq and lipophilic environments.

(4.5) NR fluorescence quenching by Fe(III)PPIX in the presence of antimalarial drugs

Drugs belonging to the quinoline class of antimalarials have been shown to be potent inhibitors of the conversion of Fe(III)PPIX to βH *in vitro* and Hz *in vivo*.[195,202,258,354] Leading theories on the mechanism of action of these types of antimalarials involve the formation of

a drug-Fe(III)PPIX complex in solution.[215,230,360] The strength and resulting potential toxicity of such a complex is postulated as a measure of efficacy of antimalarial action.[246,360] The removal of free Fe(III)PPIX from solution also leads to the formation of less Hz, causing a toxic build-up of Fe(III)PPIX in the DV.[195] Understanding the effect of these antimalarials on the lipid partitioning behaviour of Fe(III)PPIX is a key objective. Monitoring the addition of these antimalarials to Fe(III)PPIX, resulting in a drug-Fe(III)PPIX complex, which is preferentially partitioned into or out of the lipid droplets and is either more strongly lipophilic or allowed to accumulate in the aq media is of great mechanistic interest. Indeed, the drug, CQ has been shown to cause a build-up of Fe(III)PPIX out of the DV, in the parasite cytoplasm at the trophozoite stage of its life-cycle, in a manner that has been linked to its *in vivo* efficacy.[195] This work aims to gain further insight into the lipophilicity of drug-Fe(III)PPIX complexes and the possible role they play in drug activity.

(4.5.1) The effect of known antimalarials on fluorescence of NR labelled SNLBDs

As in section 4.4.1, NR labelled SNLBDs were prepared and the fluorescence spectrum was recorded to ensure that there was a consistent fluorescence emission signal matching that obtained in Fig. 4.2. Fluorescence quenching by halogen-containing compounds has been reported to occur via a similar mechanism to the heavy-metal atom quenching of NR fluorescence investigated for Fe(III)PPIX.[296] Given that the 4-aminoquinoline class of antimalarials chloroquine (CQ) and amodiaquine (AQ) contain a Cl atom, their potential to quench NR fluorescence was first investigated. For the quinoline methanol class of antimalarials – quinine (QN) and its diastereomer, quinidine (QD) – the non-interference of their inherent fluorescent properties was also investigated, although they were considered unlikely to cause any apparent quenching, as they do not contain a heavy atom. The possibility of increasing the absorbance of incident light magnifying the IFE by inclusion of coloured antimalarials also required consideration. The ratio of fluorescence intensity change ($\frac{I_0}{I_a}$), upon addition of aq solutions of antimalarial drugs CQ, AQ, QD and QN to NR-labelled SNLBDs over the pH range 2.80-12.00 was investigated. Figure 4.14 shows the linear

SV plot from Fig. 4.10(a) in section 4.4.5 for Fe(III)PPIX quenching of NR fluorescence alongside the results obtained for the titration of each antimalarial tested at pH 4.80.

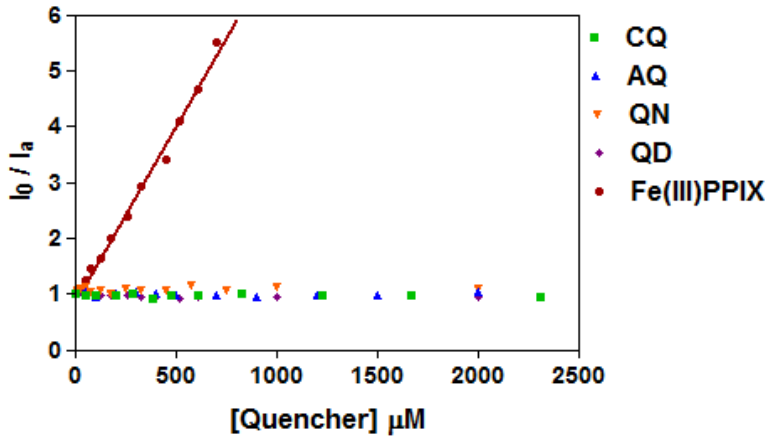

Figure 4.14 SV plot to investigate the possible quenching effect of antimalarial drugs, chloroquine (CQ), amodiaquine (AQ), quinine (QN) and quinidine (QD) on NR fluorescence in SNLBDs in aqueous solution at pH 4.80. The linear SV plot obtained for Fe(III)PPIX quenching of NR fluorescence in SNLBDs is included for comparison.

As depicted in Fig. 4.14, negligible changes in the initial fluorescence intensity, I_0, were observed as each drug was titrated into the NR+SNLBD suspension up to a total drug concentration of 2.5 mM. This final concentration was considerably larger than the 1 µM NR, so that any additional inner filter effects ought to be evident as a considerable change in I at the maximum drug concentration. When compared to the quenching of NR fluorescence observed for Fe(III)PPIX in Fig. 4.14, the drugs display only minor fluctuations about the I_0 value recorded. This small change relative to I_0 was also observed for all other pH solutions examined for the antimalarial drugs tested. This invariance with concentration can be ascribed to two possibilities, the first being simply that the antimalarial drugs tested do not enter the lipid environment of NR-labelled SNLBDs at the pH values under investigation. Warhurst et al. have measured the log P_{OW} and calculated log D at physiologically relevant pH values of 5.2 and 7.4 for the quinoline antimalarials investigated here. [238,257] Table 4.2 lists the applicable physicochemical data reported for these drugs.

Table 4.2: Lipophilicity parameters of quinoline based antimalarials obtained from Warhurst et al. (Reproduced data from Table 1 with BioMed Central open access Charter permission)[257]

DRUG	pK_a 1	pK_a 2	log *P*	Log $D_{5.2}$	Log $D_{7.4}$
CQ	10.18	8.38	4.72	-3.44	0.96
AQ	8.66	7.05	4.26	-1.00	2.83
QD	8.58	4.12	3.17	0.30	1.97
QN	8.58	4.42	2.84	0.40	1.66

The log *P* values reported indicate that all the unionised forms of each quinoline antimalarial are strongly lipophilic and thus are expected to partition into the SNLBD. Under acidic DV pH conditions, the log *D* values show that the 4-aminoquinoline drugs (CQ and AQ) are in fact hydrophilic and not expected to partition into a lipid environment. While this could provide an explanation for the observed lack of halogen quenching of NR fluorescence at low pH, it cannot account for the lack of effect at neutral and higher pH. The quinoline-methanols (QD and QN) are reported to be lipophilic under all relevant pH conditions and thus some lipid accumulation is expected. This indicates that the reason for the observed lack of effect of quinoline antimalarials on NR fluorescence is likely simply an absence of interaction between excited state NR and the drugs. This is fortuitous, since it means that any differences obtained in the quenching behaviour of Fe(III)PPIX in the presence of these antimalarials will be due to changes in the distribution of Fe(III)PPIX between aq solution and lipid. This change must arise from the formation of a drug-Fe(III)PPIX complex and is independent of any spurious drug-NR effects.

(4.5.2) The effect of antimalarials on Fe(III)PPIX fluorescence quenching of NR labelled SNLBDs : A pH study

To investigate the effect of these drugs on the pH-dependent partitioning profile established for Fe(III)PPIX into NR-labelled SNLBDs (section 4.4.5), a concentration of 500 µM drug, where no drug quenching of NR fluorescence was evident (Fig. 4.14) was incorporated into the NR+SNLBD system prior to any Fe(III)PPIX addition. The Fe(III)PPIX-induced quenching of NR fluorescence was measured in SNLBDs dispersed in diluted aq drug medium over the pH

range 2.8-12.0 to generate linear SV plots for each drug. Any change observed from the pH partitioning profile of Fe(III)PPIX (Fig. 4.11) is as a result of the formation of a drug-Fe(III)PPIX complex that displays unique lipophilicity behaviour based on the physicochemical properties of each drug. The plots produced for a representative antimalarial drug, CQ, are presented in Figure 4.15(a). The log of the slopes (K_{SV} values) obtained from those plots were used to generate Fig. 4.15(b) to show the pH partitioning behaviour of Fe(III)PPIX+CQ.

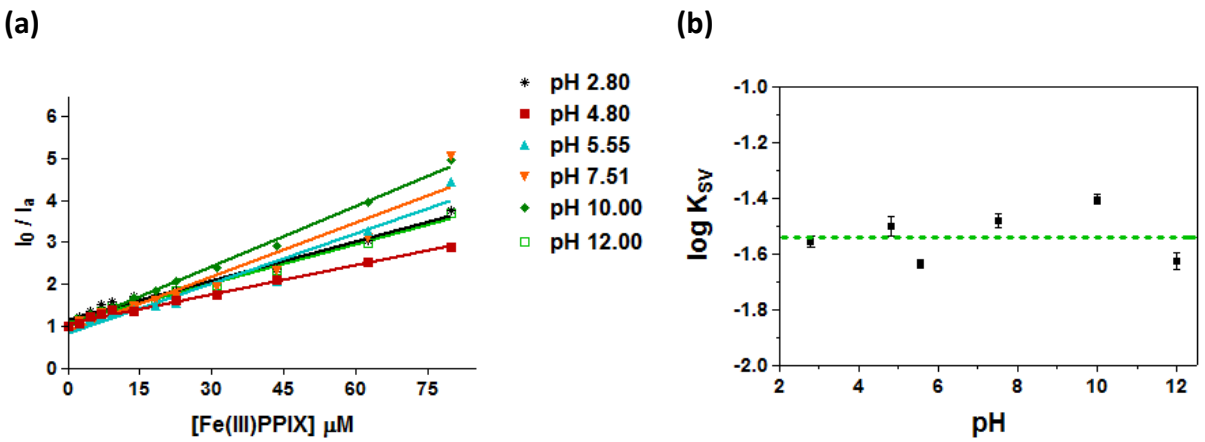

Figure 4.15(a) SV plots of Fe(III)PPIX quenching of NR fluorescence in SNLBDs over the pH range 2.80-12.00 with slopes equal to K_{SV} and y int = 1. **(b)** A partitioning profile (log K_{SV}) showing almost no pH dependence of Fe(III)PPIX induced quenching of NR fluorescence in SNLBDs in the presence of 500 µM CQ. Error bars in **(b)** represent the SEM (n= 4).

The data presented in Fig. 4.15(a) show the distribution of K_{SV} values obtained with all quenching constants occurring in a narrow range about a mean value of K_{SV} = 0.02978 ± 0.0062 μM^{-1} corresponding log K_{SV} = -1.54 ± 0.09 (Fig. 4.15(b)). The quenching behaviour of Fe(III)PPIX in the presence of the 4-aminoquinoline antimalarial CQ (Fig. 4.15(b)) appears to be essentially pH-independent in contrast to the sigmoidal pH-dependent quenching obtained for Fe(III)PPIX alone (Fig. 4.11). This pH partitioning profile was investigated for the other 4-aminoquinoline drug, AQ, and the quinoline methanol drugs, QD and QN. Table 4.3 summarises the quenching results obtained for each drug for comparison with those of Fe(III)PPIX alone at the relevant pH values.

Table 4.3: Quenching data, K_{SV} obtained at pH 4.80 and 7.51 for Fe(III)PPIX alone and comparison with Fe(III)PPIX in the presence of antimalarial drugs.

DRUG	pH 4.80 K_{SV} [μM]$^{-1}$	K_{SV}^{-1} [μM]	pH 7.51 K_{SV} [μM]$^{-1}$	K_{SV}^{-1} [μM]
Fe(III)PPIX	0.058 ± 0.004	17.14	0.023 ± 0.001	43.51
Fe(III)PPIX + CQ	0.028 ± 0.002	35.95	0.033 ± 0.002	30.24
Fe(III)PPIX + AQ	0.027 ± 0.002	35.19	0.017 ± 0.001	58.72
Fe(III)PPIX + QD	0.197 ± 0.002	5.08	0.403 ± 0.070	2.48
Fe(III)PPIX + QN	0.162 ± 0.016	6.18	0.120 ± 0.023	8.36

At each pH, K_{sv} values and the amount of Fe(III)PPIX required to quench 50% of NR fluorescence, K_{SV}^{-1}, in the presence of the antimalarials differ markedly from that obtained for Fe(III)PPIX alone in a way that reflects the differences in each drug's subclass. Indeed, this partitioning behaviour of drug-Fe(III)PPIX complexes can be seen in a plot of log K_{SV} obtained for Fe(III)PPIX in the presence of each antimalarial over the pH range, displayed in Figure 4.16. The data were found to fit to a two-step protonation model as opposed to the single step model used for Fe(III)PPIX alone (Fig. 4.11) to account for the two protonation sites on each of the antimalarials used. [257,361]

The results show that in the presence of 4-aminoquinoline antimalarials (CQ and AQ) there is little change in the partitioning of Fe(III)PPIX over the whole pH range. Both drugs appear to decrease the observed capacity of Fe(III)PPIX to enter SNLBDs under acidic pH conditions where Fe(III)PPIX alone displays maximum lipophilicity. This behaviour is attributed to the formation of a charged complex between the 4-aminoquinolines and Fe(III)PPIX which favours the aq environment over that of the neutral lipid interior of SNLBDs. The differences in partitioning of the drug-Fe(III)PPIX complexes at both pH values, is proposed to be as a result of the varied speciation and charge of the complexes, which are known to control permeability.[362] Although some drugs have been reported to passively cross membranes in their ionised forms, the partitioning of antimalarials into neutral lipid droplets is expected to be greater for the neutral drug than the charged forms.[363] The finding that the neutral form of Fe(III)PPIX preferentially partitions into SNLBDs (section 4.4.6) with a log *P* of 2.8 supports

this and the rationale that a drug-Fe(III)PPIX complex would adhere to the same principle is expected.

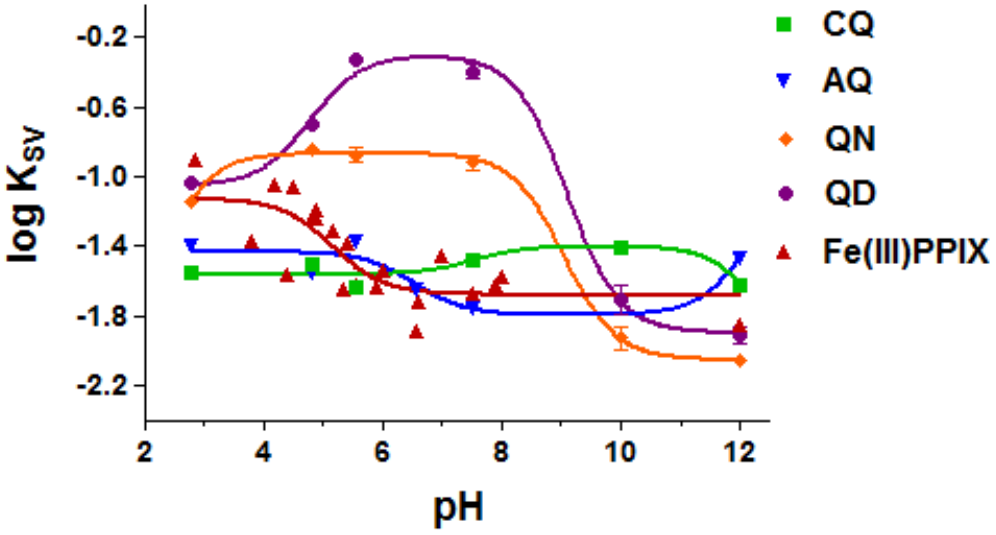

Figure 4.16 Dependence of the log K_{SV} on pH for Fe(III)PPIX quenching of NR in SNLBDs dispersed in diluted aq antimalarial solution. The data were fitted to a two-step pK_a model for each curve. (Error bars calculated as standard deviations of log mean K_{SV} and are smaller than the symbol where not seen.

To investigate this, the percentage ionisation and estimated speciation (based on protonation state i.e. fully protonated, mono-protonated or neutral) of each drug was calculated from the Henderson-Hasselbalch equation based on reported pK_a values.[364] From these calculations, the suggested charges of each drug and its Fe(III)PPIX complex at the relevant pH are displayed in Table 4.4. It must be emphasised that this is a crude approximation, since it assumes no changes in the component pK_a values in the complex. The 4-aminoquinoline, CQ, induces the μ-oxo dimer (Fig. 4.17) form of Fe(III)PPIX in solution at pH 7.4 as shown by magnetic susceptibility experiments and Mössbauer spectroscopy (pH 5.00).[70,224] Its structural analogue, AQ, is thought to interact with Fe(III)PPIX in a similar, 1:2 fashion. Effectively, at certain pH values, the ionisation states of each drug-μ-oxo dimer complex can be approximated by the charge of the drugs and of the protonation states of the four propionate groups in the μ-oxo dimer (Fig. 4.17).

Table 4.4 Speciation and charge of Fe(III)PPIX-drug complexes based on reported drug pK_a values and protonation states at pH 4.80 and 7.50.[364]

DRUG	species pH 4.8 [b]	charge pH 4.8	species pH 7.5[b]	charge pH 7.5	Complex charge pH 4.8[c]	Complex charge pH 7.5[c]
Fe(III)PPIX[a]	–	0	–	-1	–	–
CQ	0% deprotonated	+2	~13% mono deprotonated	+2/+1	**-1**	**-2/-3**
AQ	0% deprotonated	+2	~73% mono deprotonated 6.5% fully deprotonated	+1/0	**-1**	**-3/-4**
QD	~99% mono deprotonated	+1	~92% mono deprotonated, ~7% fully deprotonated	+1/0	**0**	**0/-1**
QN	~100% mono deprotonated	+1	~92% mono deprotonated, ~7% fully deprotonated	+1/0	**0**	**0/-1**

[a] speciation data from Table 4.1 for Fe(III)PPIX alone

[b] Drug pK_a values from Table 4.2 used to calculate speciation at that pH, first deprotonation at quinolinic N, second deprotonation in amino side chain or quinuclidine N.

[c] Addition of Fe(III)PPIX (μ-oxo dimer Fe(III)PPIX charge for 4-aminoquinolines) and predominant drug charges For quinoline methanols, charge distribution based on a 1:1 complex with alkoxide bond (-1) and salt bridge formed

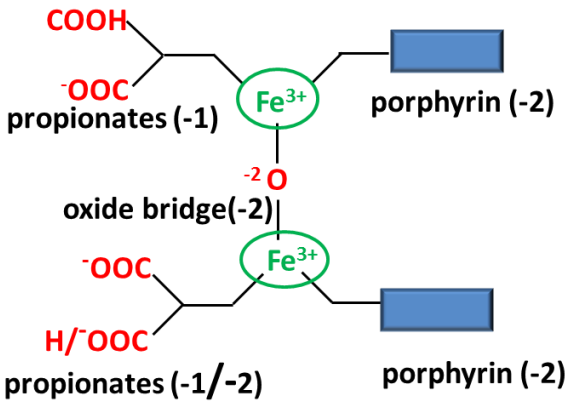

Figure 4.17 A schematic of the charge distribution of the μ-oxo dimer at approximately the pH of the DV (pH 4.80), the four propionic acid groups are shown in red to illustrate their likely charges at this pH. The overall charge of the dominant species at this pH (one propionate protonated) is -3.

At the DV pH, the likelihood that at least one propionate group is charged, is high, however, the presence of the drugs may depress any further protonation of the other propionates to lower pH values. Thus the charge of the μ-oxo dimer of (-3) added to that of the drugs (+2) results in the formation of a charged drug-Fe(III)PPIX complex (-1) at pH 4.80 (Table 4.4). An increase in pH will lead to deprotonation of the propionate group, until at the cytosolic pH, with no propionate groups protonated (-4), CQ forms predominantly a -2 complex with the Fe(III)PPIX μ-oxo dimer and AQ, which is significantly monoprotonated at that pH, forms a -3 complex with Fe(III)PPIX. Therefore as the 4-aminoquinolines are expected to form charged complexes with the Fe(III)PPIX μ-oxo dimer at both the cytosolic and DV pH, their partitioning profiles are not expected to be pH dependent. As is evident in Fig. 4.16, this is the case and in fact the partitioning of the charged 4-aminoquinoline drug-Fe(III)PPIX complexes was found to be decreased compared to Fe(III)PPIX alone which is neutral between pH 2.85 - 5.5. This observation was proposed in an early study on the effects of quinoline antimalarials on the intercalation of Fe(III)PPIX into a phospholipid monolayer where the authors found that the proposed large amphipathic CQ-Fe(III)PPIX dimer complex was unable to intercalate into the lipid monolayer.[133]

The quinoline methanols (QD and QN) on the other hand do show a strongly pH-dependent change in log K_{sv} or partitioning. In Fig. 4.16, it can be seen that both drugs induce an apparent overall increase in the partitioning of Fe(III)PPIX into SNLBDs over the pH range tested. QD appears to produce the most lipophilic complex with the greatest amount of Fe(III)PPIX quenching occurring in the presence of this drug under the relevant pH conditions. This can be rationalised in the following way, the quinoline methanol drugs, QD and QN have been proven by crystal structure to form monomeric complexes with Fe(III)PPIX through an alkoxide linkage from the drug to the Fe(III) centre, in the solid state.[230] The crystals were obtained in non-aqueous solution and it was found that the protonated drug quinuclidine nitrogen (N) was involved in a hydrogen bond association with the anionic propionate oxygen of Fe(III)PPIX to form the neutral complex seen in Fig. 4.18.[365] The presence of at least one propionic acid group was confirmed by the presence of a IR peak at 1702 cm^{-1}.[230] The porphyrin charge is -2, the metal is +3 and the alkoxide bond contributes -1 in addition to the -1 and +1 from the salt bridge to form an overall neutral complex.

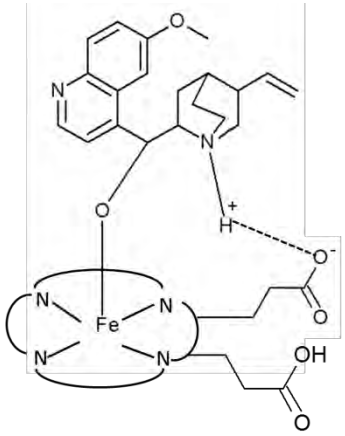

Figure 4.18 Representation of the structure of the neutral quinoline methanol-Fe(III)PPIX complex as shown from solid state X-ray crystallography.[230] The porphyrin ring of Fe(III)PPIX is shown schematically to just show the alkoxide bond to the Fe(III) and one propionate group involved information of a salt bridge with the NH^+ of the drug quinuclidine ring.

In an aqueous medium this complex would be expected to exhibit a charge distribution dependent on the protonation state of the Fe(III)PPIX propionate groups and the nitrogen atoms of the drug as determined by the pH of the solution. Fig 4.19 shows the protonation state of each component and the likely quinoline methanol drug-Fe(III)PPIX complex formed at a particular pH over the range investigated. The charge of the resultant complex formed is dependent on the alkoxide bond (-1 charge) between the drug benzylic alcohol (deprotonated) and Fe(III) metal and the prevalence of the intramolecular hydrogen bond over a certain pH range. At low pH (less than pH 4.4) where all propionates and drug N atoms would be protonated, the salt bridge formation would be unlikely and the overall charge of a drug-Fe(III)PPIX complex would be +2 resulting in low to moderate partitioning as observed in Fig. 4.16. Above pH 4.4, when the quinoline N and presumably at least one propionate group would be deprotonated, the formation of the intramolecular hydrogen bond is likely and thus the partitioning of the drug-Fe(III)PPIX complex would be expected to increase to a maximum for this neutral complex. This is also observed in Fig. 4.16. In fact the extent of partitioning for the quinoline methanol drug-Fe(III)PPIX complexes in this pH range is larger than observed for neutral Fe(III)PPIX alone indicating that the neutral drug-Fe(III)PPIX complex is more lipophilic than neutral Fe(III)PPIX. This is probably due to the inherent lipophilicity of the individual quinoline methanol drugs with both drugs having a log *P* of greater than the 2.8 calculated for Fe(III)PPIX in section 4.4.7 (Table 4.2). This increase in

drug-Fe(III)PPIX complex lipophilicity is maintained even beyond the pH at which the other propionate group of Fe(III)PPIX would be deprotonated (pK_a reported as approximately 5-6 in free Fe(III)PPIX)[74,366] and the overall complex charge would be -1 (Fig. 4.19). This increased lipophilicity may also be due to the prevalence of the intramolecular hydrogen bond.

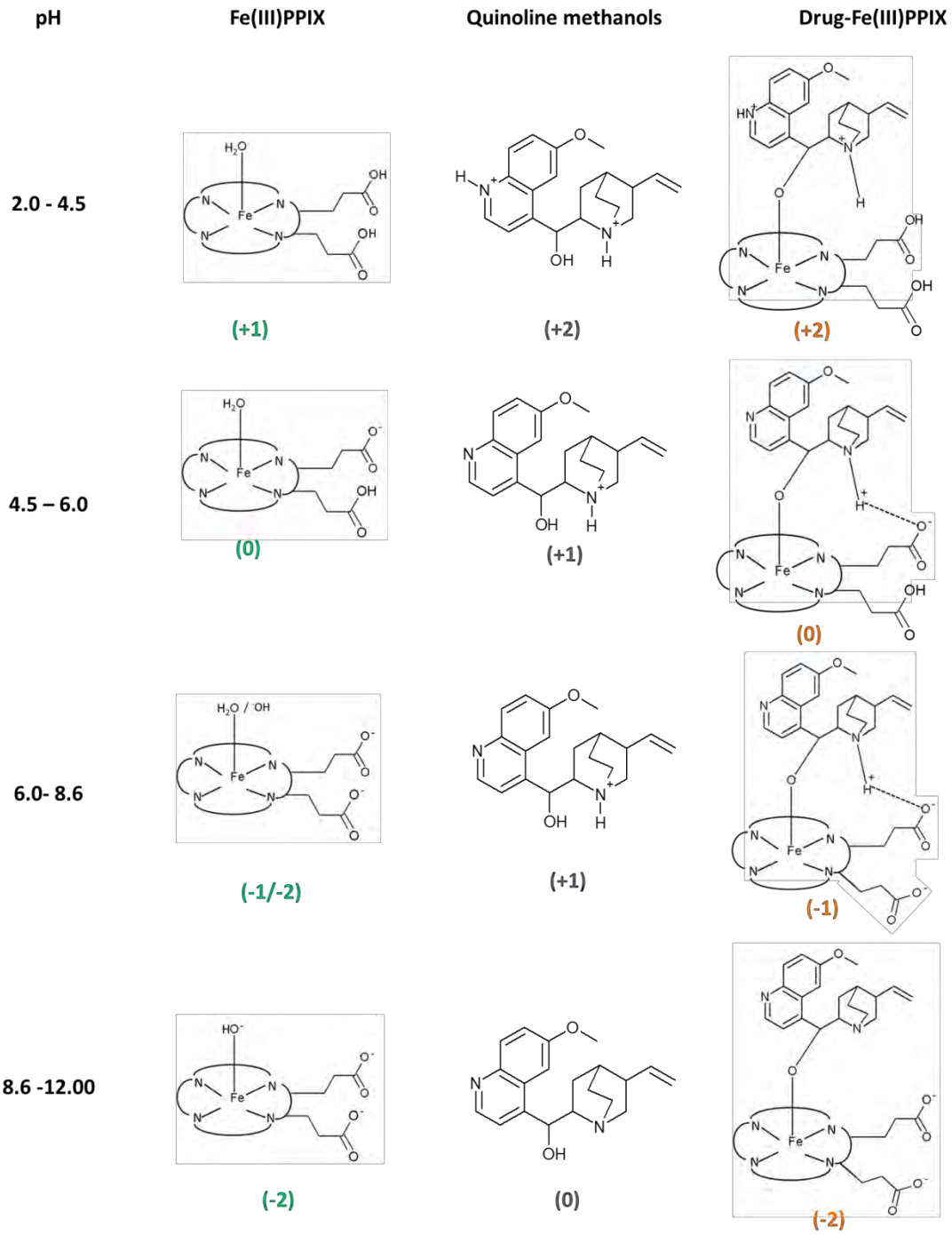

Figure 4.19 Schematic representations to show the charge distribution across the pH range investigated for Fe(III)PPIX and the quinoline methanol drugs and the drug-Fe(III)PPIX complex formed.

Possible reasons for this have previously been explored using molecular mechanics simulations on Fe(III)PPIX with QD and QN under conditions where their quinuclidine N is protonated and propionate groups of Fe(III)PPIX are unprotonated, approximating speciation at pH 7.5 *in vacuo*.[228] The formation of an intramolecular salt bridge between the protonated quinuclidine N on the drug and the charged propionate group of Fe(III)PPIX were shown to be favourable in a non-aq environment with a lower strain energy penality (with respect to lowest energy conformation) identified for QD than QN.[228] In an aq environment, QD-Fe(III)PPIX was found to be more likely to form this intramolecular hydrogen bond, independent of medium, owing to preorganisation arising from its fairly rigid structure which is not the case for QN-Fe(III)PPIX. The recent publication of the crystal structures of QD-Fe(III)PPIX highlighted the ease with which QD forms this bond despite the prevalence of other hydrogen bond donors in the crystallisation solvent.[230]

The propensity to form an intramolecular hydrogen bond in media of low dielectric constant was also observed for Fe(III)PPIX complexes with ferroquine and its ruthenium analogue.[367] This was correlated to their increased lipophilicity over other analogues and CQ in open conformations and thus enhanced antimalarial activity against sensitive and resistant strains *in vitro*.[368] The presence of an intramolecular hydrogen bond would be expected to increase the lipophilicity of a complex, given the smaller degree of surface area that is exposed upon adopting a folded conformation. Indeed the observed increase in the relative amount of partitioning across the pH range for the QD-Fe(III)PPIX complex over QN-Fe(III)PPIX is interesting and perhaps can be rationalised in terms of the stereochemical difference between QD and QN, which is known to be a source of different chemical and pharmacokinetic properties.[257,368] QD is also reported to form a stronger complex with Fe(III)PPIX in solution, relative to QN and has been shown to be a better inhibitor of βH formation *in vitro*.[218,257] In light of these findings, it is proposed that QD forms a more lipophilic complex with Fe(III)PPIX due to structural preorganisation that may account for its observed increased antimalarial efficacy over its diastereomer, QN.

The increased partitioning for the QD-Fe(III)PPIX complex and to some extent also the QN-Fe(III)PPIX complex relative to Fe(III)PPIX alone appears to persist to pH values above pH 8.5, after which the quinuclidine N is deprotonated and the overall charge of the quinoline methanol drug-Fe(III)PPIX complex would be -2 (Fig. 4.19). As shown in Fig. 4.16, above this

pH, the partitioning of these complexes was observed to decrease to a minimum, even lower than that measured for Fe(III)PPIX alone.

It must be noted that confirmation of the formation of this type of coordination complex between Fe(III)PPIX and the quinoline methanol drugs has so far only been confirmed in the solid state where the crystals were formed from evaporation of each solution in organic solvents.[230] An alternative hypothesis that the same complexes do not form in aqueous solution has been suggested even in these crystal structure publications, where the authors state that no evidence of this complexation was observed in aqueous solution where unchanged UV-vis spectra in the charge-transfer region of Fe(III)PPIX were observed when mixed with QD.HSO_4 in aqueous solution.[220,230] While it is known that QN associates with monomeric Fe(III)PPIX in aqueous solution, whether this association is as a result of direct coordination of the benzylic alcohol or π-stacking interactions or both, remains undetermined.[369] If the drug-Fe(III)PPIX complexes partitioning into SNLBDs are not alkoxide coordination compounds, the charge distribution of the complex would simply be a combination of the protonation states of the individual components (see Fig. 4.19) over the pH range tested. This means that the only pH range at which a neutral complex would be formed would be between pH 6-8.6, which may account for the increase in partitioning observed for these drugs over this range (Fig. 4.16). The overall increase in lipophilicity observed for these drug complexes compared to neutral Fe(III)PPIX alone would then probably simply be a result of the contribution of the lipophilic drug to the complex.

A third hypothesis also exists, in which the coordinating ligand is not an alkoxide but the drug benzylic alcohol. Such a model has previously been proposed, since the typical pK_a of an uncoordinated benzyl alcohol is about 14.3 suggesting that under acidic pH conditions, if metal coordination did not depress the pK_a drastically, this group would be protonated.[370] This was addressed for the solid state complexes in the report of the crystal structures by analysis of the Fe-O bond length and an IR peak at 1702 cm^{-1} which was found to be consistent with an alkoxide rather than OH coordination, but the possibility that the alcohol complex prevails in solution state cannot be discounted.[230] This would affect the charge distribution of the complexes in the same way as the non-coordination complex discussed in the previous paragraph. However, the increased lipophilicity of these complexes over

Fe(III)PPIX can still be explained by the formation of the folded hydrogen bonded structure seen in Fig 4.18, with OH as the coordinating ligand instead of the alkoxide.

Thus, while the exact nature of the quinoline methanol drug-Fe(III)PPIX complex in solution remains unclear, the result that these drugs markedly increase the observed neutral lipid partitioning of Fe(III)PPIX is clearly shown by the experiments reported in Fig. 4.16. There is support for this increased lipophilicity in the literature as QN has been shown to increase Fe(III)PPIX phospholipid monolayer intercalation.[133] It was suggested that the quinoline-methanol drug interacts with Fe(III)PPIX differently to CQ in solution and proposed that monomeric Fe(III)PPIX, which is the most likely form of Fe(III)PPIX in the QD/QN-Fe(III)PPIX complex, exerted a greater effect on the surface pressure of the monolayer than dimeric Fe(III)PPIX, implying greater intercalation.

(4.5.3) Evaluating the distribution and partition coefficients, log D_{OW} and log P of Fe(III)PPIX in the presence of known antimalarials

Attempts to directly measure the partitioning of Fe(III)PPIX-drug complexes between octanol and water proved unsuccessful owing to changes in the extent of complex formation in each layer as a function of concentration. Estimation of the distribution coefficients of Fe(III)PPIX-drug complexes was attempted by using the sum of the literature log *P* values for each drug and that calculated using Eqn. 4.4.3 for Fe(III)PPIX, based on the principle of a fragment approach utilised in *clogP* predictions.[257,371] This calculation however, assumes that formation of the complex does not alter the lipophilicity and acid dissociation constants of each of the individual components which experimentally has been proven invalid.[372] Although the effect of these antimalarials on Fe(III)PPIX partitioning into SNLBDs has been found to display a pH dependence for the quinoline methanol drugs and not the 4-aminoquinolines which can be rationalised by the charge of the drug-Fe(III)PPIX complex under the relevant pH conditions, the log *P* of these complexes could not be evaluated.

(4.6) Summary

Neutral lipid blend droplets (NLBDs) with non-hollow hydrophobic interiors, were confirmed to form from the unique blend of neutral acylglycerols found in the parasite DV *in vitro*.[124] Nile Red (NR) was found to localise and fluoresce inside these lipid droplets in a concentration dependent manner with Em λ_{max} = 618 nm, establishing the relative polarity of these NLBD interiors to be between that of acetone and octanol with an $E_T(30)$ of 45 ± 4 kcal.mol^{-1}. Soluble Fe(III)PPIX was shown to quench NR fluorescence in a concentration-dependent manner by a collisional quenching mechanism that conforms to a linear Stern-Volmer model. The current study has shown, by measuring the extent of this quenching, that Fe(III)PPIX spontaneously and rapidly accumulates in SNLBDs. The extent of this localisation was found to occur in a pH-dependent manner such that a pH partitioning profile of Fe(III)PPIX in SNLBDs was obtained. This pH partitioning profile was found to fit to a single protonation model with pK_{a1} for Fe(III)PPIX of 4.62 ± 0.09. The greatest amount of Fe(III)PPIX partitioning into SNLBDs was observed under acidic pH conditions correlating with the prevalence of the neutral species of Fe(III)PPIX. Interestingly, this pH dependence was found to mirror that of βH formation in the presence of NLBDs.[127] Measurement of the octanol-water partitioning of Fe(III)PPIX revealed a log D_{OW} of 1.8. This allowed the first report of the partition coefficient of the unionised form of Fe(III)PPIX (log *P*), calculated to be 2.8. Effectively, this indicates that Fe(III)PPIX is strongly lipophilic suggesting approximately a 400-fold partitioning of the neutral form of Fe(III)PPIX into SNLBDs relative to the aqueous medium.

Quinoline-based antimalarials were found not to quench NR fluorescence in SNLBDs at any pH despite their reported lipophilicity. The 4-aminoquinoline antimalarials form Fe(III)PPIX-drug complexes that, although they quench NR fluorescence, do so in a manner that displays almost no pH dependence. These charged complexes were found to be less lipophilic than the individual drug and neutral Fe(III)PPIX at the DV pH. In the presence of Fe(III)PPIX, drugs in the quinoline methanol class of antimalarials exhibited a pH-dependent partitioning profile with respect to NR quenching with the greatest amount of partitioning occurring under acidic pH conditions that approximate those in the parasitic DV. This observation was rationalised by their ability to form a neutral complex with Fe(III)PPIX in solution. Quinidine (QD) was found to form the most lipophilic complex with Fe(III)PPIX probably due to a

previously-established “preorganisation” effect for formation of the intramolecular hydrogen bond which results in a relatively closed structure of the complex, increasing its lipophilicity.[228,230] This relative measure of the effect of known antimalarials on the lipophilicity of Fe(III)PPIX is the first report of its kind and the relevance of this trend for biological activity requires further investigation. This work also highlighted the difficulty in studying lipid systems due to their colloidal nature. Studies on detergents as lipid mimics to enable more robust investigation into the nature of Fe(III)PPIX-“lipid” interactions were thus proposed and are described in the following chapter.

Chapter 5:
An investigation of the speciation of Fe(III)PPIX in amphiphilic solution

(5.1) Introduction

Fe(III)PPIX exhibits a complicated speciation profile in solution.[72] In aq solution at the optimal pH for βH formation (pH 4.80), the dominant Fe(III)PPIX species is the π-π dimer, characterised by two five-coordinate Fe(III)PPIX molecules that interact via π-π stacking interactions of their non-coordinated faces, with their axial ligands facing outward. [66,72] It was recently proposed that the conversion to βH from Fe(III)PPIX π-π dimers is facilitated by the spontaneous formation of a carboxylate linkage between one of the propionate groups of each Fe(III)PPIX to the Fe(III) centre of the opposite Fe(III)PPIX, assisted by loss of the axial ligand in a lipophilic environment.[132] The π-π dimer is thought to serve as the nucleation precursor of βH.[55] After probing the Fe(III)PPIX monomer - μ-oxo dimer equilibrium, Casabianca et al. proposed that the strong interaction between the μ-oxo dimer species and certain antimalarials, inhibits the conversion to βH in solution.[223] The hypothesis that the prevailing Fe(III)PPIX species in solution can effectively hinder βH formation in detergent solution is explored here.

Unavailability of the means for direct study of the conversion of Fe(III)PPIX to Hz inside the parasite DV remains a barrier to elucidating the mechanism of its formation. While several studies on the behaviour of Fe(III)PPIX in aqueous and organic solvent systems have provided insight into its nature, only an indirect comparison between these systems and the lipid environment found to be associated with Hz, in the DV, is possible. [66,68,72,373,374] To aid in understanding the role of this lipid environment in promoting βH formation, it has been proposed that detergents can act as suitable 'lipid mimics' for the study of the Fe(III)PPIX speciation and the formation of βH.[118,375] Several reports have exploited the ability of certain detergents to effectively mediate the formation of βH in acidic solution as initiators for evaluating the potential βH inhibition activity of lead compounds.[154,155] Though these assays provide an effective means to determine whether a compound can inhibit βH formation, the role of the detergent is not well understood. This chapter aims to investigate the interaction between several detergents and Fe(III)PPIX in solution.

Detergents comprise of an extensive category of amphiphilic molecules that exhibit unique interfacial and surface tension properties that can be classified according to the charge of the polar head group.[376] The three broad categories are ionic, non-ionic and zwitterionic detergents. This study was aimed at investigating the species of Fe(III)PPIX in amphiphilic solution and ability to form βH, so that a detergent belonging to each class was initially chosen for study. The charged detergents that bear anionic and cationic head groups chosen were, sodium dodecyl sulfate (SDS) and hexadecyl-trimethyl-ammonium bromide (CTAB), respectively. Neutral detergents, octylphenoxypolyethoxyethanol (NP-40) and polyoxyethylene (20) sorbitan monolaurate (TWEEN-20) were selected for further study as they have previously been shown to effectively produce βH (Fig. 5.1). [154,155] Finally, for the zwitterionic detergent, 3-[(3-cholamidopropyl)dimethylammonio]-1-propanesulfonate (CHAPS) was also chosen. It has been long believed that detergents induce monomeric Fe(III)PPIX in solution since Simplicio first showed that haemin monomers exist in SDS micelle solution.[377,378] Hence, it is often assumed in the literature that all detergents monomerise Fe(III)PPIX, however, subsequent spectroscopic investigations have revealed a diverse speciation profile in different detergent systems in a manner that may be related to the nature of the detergent head group. [223,379] Therefore the main objective of this work was to study the effect of detergent monomers and micelles on Fe(III)PPIX speciation in solution to gain insights into the prevailing Fe(III)PPIX species in amphiphilic solution that promotes βH formation.

Charged detergents

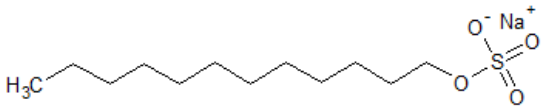

Sodium dodecyl sulfate **(SDS)**

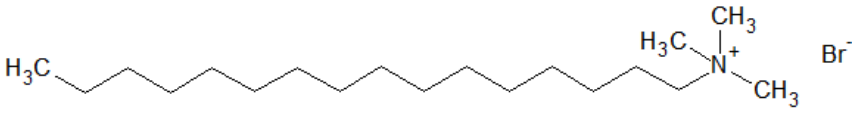

hexadecyl-trimethyl-ammonium bromide **(CTAB)**

Non-ionic detergents

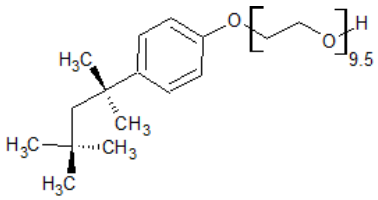

octylphenoxypolyethoxyethanol, Nonident P40 **(NP-40)**

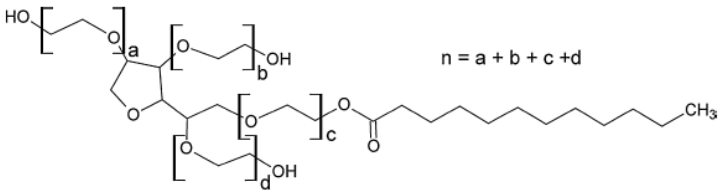

Polyoxyethylene (20) sorbitan monolaurate , (n=20) **(TWEEN-20)**

Zwitterionic detergent

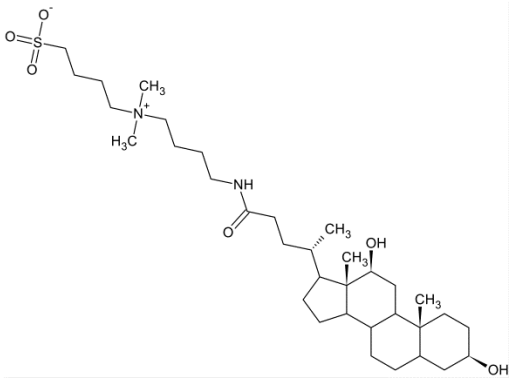

3-[(3-Cholamidopropyl)dimethylammonio]-1-propanesulfonate **(CHAPS)**

Figure 5.1 Structures of the different detergents used in this study.

(5.2) Experimental Procedures

(5.2.1) Materials, Instrumentation and General Procedures

All chemicals used were obtained from Sigma-Aldrich® (Vorna Valley, South Africa) except Nonident P-40 (NP-40, Shell Chemical Co.) detergent was obtained from Pierce Biotechnology, Rockford, Illinois and was used without further purification. It was stored as a 167 mM stock solution at 4 °C in the fridge. Detergent stock solutions were prepared from standard solutions of each detergent in water in volumetric flasks. All Fe(III)PPIX stock solutions were prepared fresh for each experiment by dissolving haematin porcine solid in 0.1 M NaOH solution. Aqueous drug stock solutions were prepared from the appropriate salts.

(5.2.2) Spectrophotometric titrations

(5.2.2.1) Determination of the critical micellar concentration (CMC) of detergents

The detergent CMC was determined in aq buffer solution by monitoring the fluorescence intensity response of the lipophilic fluorescent probe, NR, upon increasing detergent concentration in the fluorescence cuvette. The technique used was adapted from published methodology.[161,380] Detergent stock solutions (30 mM) were prepared in acetate buffer (50 mM, pH 4.80) and diluted step-wise in the buffer in separate volumetric flasks to produce a series of detergent solutions of increasing concentration. NR stock solution (10 mM) was prepared in methanol and diluted to 1 µM in each aq buffer-detergent solution so that the total NR concentration was constant for each reading. Final solutions were mixed well in the dark for 1 hr and allowed to equilibrate in a covered cuvette at 310 K for 20 mins prior to fluorescence measurement. The excitation wavelength, Ex λ_{max} (550 nm) was determined from the peak maximum of NR in the UV-vis absorbance spectrum recorded in an aq-detergent solution. An aliquot from each solution containing NR+detergent was excited at 550 nm and the fluorescence intensity response was recorded at 310 K. The change in Em λ_{max} was plotted against the concentration of detergent in the cuvette. The CMC value was taken as the mid-point of the discontinuity in the plot determined using linear extrapolations in GraphPad Prism. The point of intersection of two linear least-squares functions were calculated by evaluating the change in the y-intercept divided by the change in the slope for

all three replicates. The CMC is reported as the mean with the error estimated as the standard error in the mean.

(5.2.2.2) Investigation of speciation of Fe(III)PPIX in amphiphilic solution over the pH range 4.0-8.2

The changes in intensity of the absorbance profile of Fe(III)PPIX with decreasing pH were monitored using UV-vis spectroscopy from 200-800 nm. All experiments were conducted in a 2 mL 1 cm pathlength quartz cuvette at 298 K. Fe(III)PPIX stock solutions (0.01 M) were prepared fresh for each experiment from 0.1 M NaOH. A working solution of Fe(III)PPIX in the appropriate detergent was prepared by diluting the Fe(III)PPIX in an aq detergent solution, the final Fe(III)PPIX concentration was 100 µM and the detergent concentration was either (i) below or (ii) above the CMC determined in 5.2.2.1. The final concentrations used for each detergent are listed in Table 5.1.

Table 5.1 Tabulated concentrations (M) of each detergent used for study either below or above the CMC values determined in 5.2.2.1.

Detergent	Below CMC (M)	Above CMC (M)
SDS	4.0×10^{-3}	16.0×10^{-3}
CTAB	0.5×10^{-3}	6.00×10^{-3}
NP-40	1.0×10^{-4}	6.50×10^{-4}
TWEEN-20	4.0×10^{-5}	2.5×10^{-4}
CHAPS	3.0×10^{-3}	12.0×10^{-3}

This working solution was diluted in aq CHES buffer (0.02 M) solution so that the initial volume and concentration of the Fe(III)PPIX solution was 1 mL and 7.45 µM at pH 8.15. All titrations were performed by lowering the initial pH with µL additions of perchloric acid of variable concentrations using a Hamilton syringe, the pH was measured after each addition and the spectrum recorded after 2 min to allow for equilibration. A continuous blank absorbance of the background was automatically subtracted from the spectrum by titrating acid into a solution containing all the experimental constituents except Fe(III)PPIX. Each absorbance spectrum was individually corrected for dilution.

(5.2.2.3) Association constants of Fe(III)PPIX and antimalarial drugs in NP-40 solution

NP-40 solution (0.2 mM) and HEPES buffer (20 mM) were premixed to prepare aq buffer+detergent titration solutions at pH 7.5. Aqueous drug stock solutions (0.1 mM) were made and added to the NP-40 and HEPES buffer solution so that the working solution concentration of drug was 0.02 mM. Fe(III)PPIX stock solution (1 mM) was prepared from haematin solid dissolved in 0.1 M NaOH and the aq buffer-detergent solution. Fe(III)PPIX solution was titrated in µL amounts using a Hamilton syringe into the aq drug-detergent solution in the sample cuvette. The UV-vis spectrum from 200-800 nm of this solution was recorded after each addition. A reference cuvette served as a blank solution where the same volume of the Fe(III)PPIX solvent system was added and its background absorbance was automatically subtracted from the sample absorbance. Each absorbance reading was corrected for dilution. Titration data were analysed using the HypSpec® software package over the wavelength range tested.

(5.2.2.4) Fluorescence emission response of NR in TWEEN-20 solution

The fluorescence emission response of the dye NR in TWEEN-20 solution was investigated. Several solutions of increasing TWEEN-20 concentration from 0 - 0.25 mM were prepared in aqueous buffer solution (HEPES, 20 mM) at pH 7.00 and 298 K and premixed with NR (1 µM) prior to fluorescence measurement. The excitation wavelength used in section 5.2.2.1 was employed to obtain fluorescence spectra. The shift in maximum fluorescence intensity and wavelength of the NR emission peak was monitored as a function of increasing detergent concentration. A stock solution of Fe(III)PPIX (0.5 mM) was titrated into the maximum NR+ detergent concentration solution (0.25 mM) to monitor the fluorescence quenching behavior of Fe(III)PPIX in detergent micelles.

(5.2.3) Job Plots

To determine the stoichiometric ratio of the Fe(III)PPIX-drug interaction, a Job plot for each drug with Fe(III)PPIX was constructed by monitoring the UV-vis changes at the most intense absorbance band as the drug and Fe(III)PPIX mole fraction was varied from 0-1.[381] All solutions were prepared in the solvent system used for determination of drug-Fe(III)PPIX association constants in 5.2.2.2. The total combined molar concentration of drug and Fe(III)PPIX solutions was kept constant at 20 μM. Drug stock solutions (0.5 mM) were prepared in 0.02 M HEPES (pH 7.5) and NP 40 (0.2 mM). Fe(III)PPIX stock solution (0.4 mM) was prepared afresh for each experiment by dissolving haematin solid in 0.1 M NaOH and NP 40 (0.2 mM). Fifteen working solutions were prepared containing Fe(III)PPIX present in a mole fraction (x[Fe(III)PPIX]) of 0, 0.1, 0.2, 0.3, 0.4, 0.45, 0.5, 0.55, 0.6, 0.65, 0.70, 0.75, 0.80, 0.9 and 1.00 by varying the volume of Fe(III)PPIX added. The drug stock solution was added to this so that each solution contained a mole fraction of drug equal to 1.0 – x[Fe(III)PPIX]. Each solution was diluted to the final volume and concentration with the addition of a solution of NP-40 (0.2 mM)/ HEPES (20 mM)/ water to maintain the pH and detergent concentration. The UV-vis spectrum of each solution was measured at 298 K and analysed at the maximum absorbance wavelength.

(5.2.4) Evaluation of detergent ability to mediate β-haematin formation

Detergent stock solutions were diluted to the appropriate concentrations listed in Table 5.1 above and below their determined CMC (section 5.2.2.1) in sodium acetate buffer (0.02 M, pH 4.80). 50 mL of this solution was allowed to reach 37°C by pre-equilibration for 30 min in five Schott-Duran crystallisation dishes in a thermostatted water bath. A haemin stock solution (0.01 M) was prepared in 0.1 M NaOH and added dropwise to the detergent solution so that the final Fe(III)PPIX concentration was 100 μM. The solution was left to incubate for 5 h at 37°C. A control experiment was set up and incubated in the absence of any detergent. The resultant brown precipitate or solution was collected by centrifugation in 80 mL transparent polycarbonate Nalgene® centrifuge tubes at 10 000 rpm for 20 min using an Eppendorf 5810R centrifuge. The clear supernatant was discarded for reactions where a precipitate was observed and the pellet was washed with a 30% v/v pyridine stock solution (1 mL, 30% pyridine; 40% acetone, 25% H_2O, and 10% HEPES buffer (2 M, pH 7.5) to complex

unreacted Fe(III)PPIX. After a second centrifugation, the pellet was washed with H_2O and collected by vacuum filtration. The amount of βH formed (% yield) for each detergent was evaluated by quantifying the amount of bis-pyridyl-Fe(III)PPIX complex in a 200 µL extract of supernatant, measured by UV-vis absorbance at 405 nm in a clear 96-well plate, in the manner of the pyridine hemichrome inhibition (Phi-β) assay previously described by Ncokazi and Egan.[253] The absorbance value obtained for each sample was subtracted from that of the control and converted to a percentage by taking the ratio of that difference and the absorbance of the control multiplied by 100. The solid was was dried and stored in a desiccator over P_4O_{10} until characterised by IR spectroscopy.

(5.2.5) Surface tension of detergent solutions

Solutions of each detergent at the concentrations specified in Table 5.1 were prepared from acetate buffer (50 mM, pH 4.80) to measure the dynamic surface tension, γ, using a Du Nouy ring tensiometer (Kruss K12 with standard platinum ring) and a glass vessel of diameter 50 mm and height 43 mm. All components were cleaned using absolute ethanol. The detergent solution was allowed to equilibrate to 25 ± 1°C in the tensiometer chamber for 5 min prior to measurement. All measurements were corrected using a Harkins and Jordan correction.[382]

(5.2.6) Magnetic susceptibility

Magnetic susceptibility measurements of Fe(III)PPIX in detergent solution was performed using the Evan's NMR method (introduced in section 2.3). Fe(III)PPIX solution was prepared from haemin solid (0.010 g) dissolved in 0.1 M NaOD (1 mL). The appropriate detergent was diluted to a concentration above its CMC in D_2O and added to the Fe(III)PPIX solution. The required pD was achieved by addition of 1 M deuterated hydrochloric acid (DCl) in µL amounts before diluting the solution in a volumetric flask with D_2O. The final Fe(III)PPIX concentration was either 3.15 or 0.790 mM. This solution (300 µL) was then transferred to the inner tube of a co-axial NMR tube. The reference sample in the outer tube was prepared from the same components with the exclusion of the Fe(III)PPIX. A diamagnetic correction of

-5.09 x 10^{-7} cm^3 g^{-1} was used (in the manner outlined in section 2.3) to calculate the magnetic susceptibility, μ, of Fe(III)PPIX in each detergent solution.

(5.2.7) ^{1}H Nuclear magnetic resonance (NMR) spectroscopy

Haemin solid (0.010 g) was dissolved in 0.1 M NaOD (1 mL) to afford a 15.34 mM stock solution. An aq TWEEN-20 detergent stock solution (1 mM) was prepared in D_2O, the pD was adjusted to 7.00 with 0.1 M DCl. The ^{1}H NMR spectrum of the detergent solution was recorded at 310 K. The Fe(III)PPIX stock solution was then diluted to 0.5 mM in a deuterated aq-detergent solution and the ^{1}H NMR spectrum was recorded at 310 K for comparison.

(5.3) Results and Discussion

(5.3.1) Use of a fluorescent probe to determine the CMC of detergents

Above a certain concentration in solution, detergent molecules form self-assembled aggregates that change the surface properties of the solution.[383,384] Below this threshold concentration detergents exist as monomers or premicellar aggregates that, upon reaching the critical micellar concentration (CMC), form detergent micelles, where the solution is characterised by a new set of defined physicochemical properties.[159,171] The presence of aqueous buffers in addition to a variation in pH and temperature are known to affect the CMC of a particular detergent solution.[385,386] Thus, any studies performed in the presence of a detergent require precise knowledge of the aggregation state of the detergent in the solution under the experimental conditions. The use of detergents to determine the behaviour of Fe(III)PPIX in amphiphilic solution was investigated under the prevailing pH and temperature conditions of the parasitic DV namely, pH 4.80 and 37 °C. The lipophilic probe, NR was employed to measure the CMC of each detergent used by monitoring the increase in fluorescence emission intensity upon increasing the detergent concentration using a reported assay.[161] Figure 5.2 depicts the increase in NR fluorescence emission as the concentration of the detergent SDS is increased.

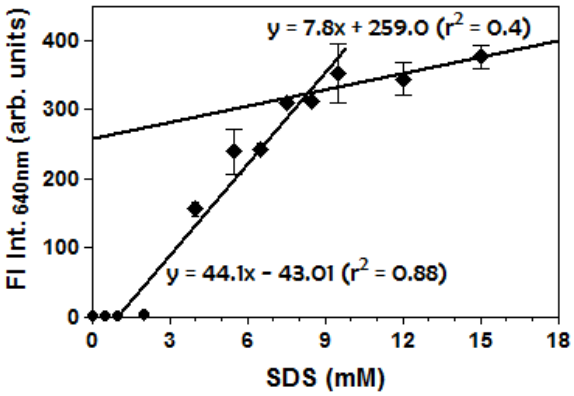

Figure 5.2 An example of the graph obtained when monitoring NR fluorescence intensity at Em λ_{max} upon increasing detergent concentration. The detergent studied was SDS and the CMC obtained from the discontinuity in the linear regression lines was 8.52 ± 0.35 mM.

NR is known to exhibit very low fluorescence in aq solution, as the CMC of SDS was approached, a rapid increase in the non-polar environments in the solution was observed, corresponding to a marked increase in NR fluorescence intensity from those regions.[161] The CMC value is approximated by calculating the detergent concentration at the point of intersection of linear regression lines generated upon fitting the linear response regions of the graph separately.[161] This procedure was performed for all the detergents utilised and the CMC values obtained under the specified conditions are shown in Table 5.2. A direct comparison to literature values is not possible as most reported CMC values are obtained for aq solutions with high NaCl concentrations.[385] However the ranges of CMC values obtained are within the expected range given the reported CMC values of each detergent.[387]

Table 5.2 CMC values obtained for each detergent determined by fluorescence spectroscopy at pH 4.80, 50 mM buffer and 310 K.

Detergent	**observed CMC (mM), (*n*=3)**
SDS	8.5 ± 0.4
CTAB	1.6 ± 0.6
NP-40	0.4 ± 0.2
TWEEN-20	0.10 ± 0.01
CHAPS	6.1 ± 0.2

It must be noted that the CMC is an equilibrium property of the bulk solution and the values reported here are only expected under the described conditions.[388] Hence, the detergent concentrations for each experiment were chosen to be either well above or below this range.

(5.3.2) Evaluation of the ability of detergents to promote β-haematin formation

To mimic the neutral lipids that have been reported to mediate Hz formation *in vivo*, detergents have been employed to catalyse the formation of βH *in vitro* for assaying potential drug candidates.[154,155,173] The ability of each detergent to mediate βH formation at pH 4.80 and 37 °C was evaluated by incubation with Fe(III)PPIX at concentrations above and

below their CMC values (concentrations listed in Table 5.1). βH formation was confirmed by the presence of characteristic stretching frequencies at 1657 and 1208 cm^{-1} in the ATR-FTIR spectrum of the dried product.[44] The IR spectrum of the product is shown in Fig. 5.3 for the detergent, TWEEN-20, at a concentration below its CMC and exhibits the strong absorbance bands that correspond to the C-O and C=O stretching frequencies of the coordinated carboxylate moiety of βH as discussed in Chapter 2.[44]

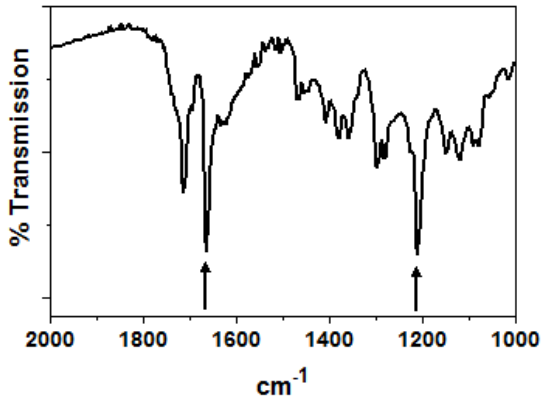

Figure 5.3 ATR-IR spectrum of βH produced from TWEEN-20 detergent incubated at pH 4.80, 37°C overnight with Fe(III)PPIX at a concentration below its CMC. The diagnostic stretching frequencies of the coordinated carboxylate group in βH occurring at 1660 and 1208 cm^{-1}, are indicated by arrows.

The total percentage yield of βH formed as mediated by a particular detergent at a concentration either above or below its CMC value are listed in Table 5.3. Both neutral detergents were found to mediate βH formation above and below their CMC values. The charged detergents failed to initiate βH formation at either concentration. Interestingly, the zwitterionic detergent, CHAPS proved capable of mediating βH formation, but only when micelles were present in solution was enough βH formed for analysis. CHAPS detergent monomers have previously been reported to mediate βH formation, however, that study reported an equally low yield of 7% βH.[155] Previous studies have reported that neutral detergents are capable of promoting βH formation below their CMC values in a pH dependent manner such that NP-40 and TWEEN-20 have been used to prepare βH for assaying drug inhibition activity .[9,11,12] SDS micelles have been reported to mediate βH formation but in very low yields.[9,30] Here, however, if any βH did form, it was present at a concentration below the limits of detection. These observations indicate that the charge of

the detergent affected their ability to facilitate the conversion of Fe(III)PPIX to βH, consequently, the properties and effects of the detergent warranted further investigation.

Table 5.3 Detergent ability to mediate βH at pH 4.80, 37°C as confirmed by ATR-IR spectroscopy. The presence of βH is indicated by **+**, while its absence is denoted by **-** .

Detergent	above/ below CMC	βH	% βH (*n*=3)
SDS	above	-	0
	below	-	
CTAB	above	-	0
	below	-	
NP-40	above	+	91 ± 1
	below	+	95 ± 0.2
TWEEN-20	above	+	94 ± 0.3
	below	+	64 ± 2
CHAPS	above	+	62 ± 3
	below	- [a]	11 ± 3.5

[a] % yield too low to detect by FTIR

(5.3.3) The surface tension of detergent solutions

It was recently found by Huy et al. that a series of small normal alcohols were capable of inducing βH formation at 37 °C and pH 4.80.[148] It was reported that the ability of these alcohols to induce increasing yields of βH was correlated with their degree of hydrophobicity (hydrocarbon chain length) and their ability to solubilise Fe(III)PPIX in aq acidic buffer solution. An overall reduction in the surface tension of aqueous solution was suggested to facilitate favourable interactions with nuclei on specific faces of the growing crystal.[148] It had been previously suggested that a limiting step in the crystallisation of βH was low levels of Fe(III)PPIX solubility in acidic solution.[67] A later study on the ability of DMSO and a series of variable chain length polyethylene glycols (PEGS) confirmed that an increase in Fe(III)PPIX solubility at acidic pH was correlated to βH formation.[150] Furthermore, the authors suggest that the solubilised Fe(III)PPIX acts as a source for nucleating βH and not precipitated

Fe(III)PPIX deposits. The conclusion that a microenvironment of reduced polarity favours this solubilisation of Fe(III)PPIX and is correlated to βH formation echoed Huy's findings.

It was noted in this study that all the detergents increased the solubility of Fe(III)PPIX in acidic solution to pH values below that of the DV environment. Consequently, the ability of the neutral and zwitterionic detergents to promote βH formation to varying degrees can probably not be attributed to increased solubilisation alone. In light of that observation, the equilibrium surface tension of each detergent at a concentration above and below its CMC value was measured and compared with the value obtained for aq acetate buffer at pH 4.80. The results are displayed for comparison in Table 5.4.

Table 5.4 Surface tension ($mN.m^{-1}$) of the detergents solutions in acetate buffer (50 mM, pH 4.80) under investigation.

Detergent	below CMC	above CMC
SDS	32.61 ± 0.01	32.54 ± 0.01
CTAB	37.06 ± 0.02	39.53 ± 0.01
NP-40	29.80 ± 0.03	30.14 ± 0.02
TWEEN-20	35.84 ± 0.86	34.88 ± 0.18
CHAPS	44.87 ± 0.61	44.21 ± 0.33
Acetate buffer	71.90 ± 0.04	

Interestingly, there appeared to be minimal difference between the surface tension measured for each detergent under both concentration conditions. In the literature, it has been reported that the CMC can often be determined using surface tension measurements, where the region of micellisation corresponds to either an initial discontinuity in the surface tension value with increasing detergent concentration or a marked decrease in surface tension upon micellisation.[389,390] A report on the CMC determination of TWEEN-20 using surface tension measurements found that the surface tension decreases linearly with the log of the detergent concentration until just below the reported CMC value and then stays constant at higher concentrations.[391] The results found here suggest that under the conditions used and at concentrations below each detergent CMC, these detergents exist in a metastable aggregated state that displays most of the physicochemical properties of detergent micelle solution. What can be concluded from the surface tension measurements

is that all the detergents tested decreased the surface tension of aq acetate buffer solution considerably, regardless of their ability to mediate βH formation.

(5.3.4) The effect of pH on Fe(III)PPIX speciation in detergent solution

In solution, Fe(III)PPIX has been shown to exist as a monomer, π-π dimer or μ-oxo dimer depending on the pH, salt concentration or nature of the solvent environment.[72] In aqueous solution, Fe(III)PPIX is predominantly a π-π dimer with hydroxide ($^{-}$OH) or water (H_2O) as the axial ligand at high and low pH, respectively.[66] The acid dissociation constant (pK_a) for this conversion has been determined at 7.1 ± 0.2.[66] However, in aqueous solution at very high pH values in the range 11-12 and increased salt concentrations, Blauer et al. reported bands in a Fe(III)PPIX UV-vis spectrum characteristic of the μ-oxo dimer species with a split Soret band at 340 and 380 nm and the charge transfer (CT) band at 565 nm with a distinct shoulder at 600 nm.[79] The characteristic features of the UV-vis spectrum of each species has been discussed in detail in Chapter 2. To determine if different detergents stabilise a particular Fe(III)PPIX species in solution, the effect of pH on Fe(III)PPIX speciation in the detergent solution, was explored quantitatively. It has been shown that UV-vis is a viable tool to distinguish between Fe(III)PPIX speciation in solution based on identification of characteristic bands in the spectrum.[66,72,282] Since the spectra give qualitative information only, it was necessary to support this with other evidence. In this regard, magnetic measurements are a useful tool. As discussed in Chapter 2, a theoretical magnetic moment, μ, of the monomeric species of Fe(III)PPIX can be determined using the Evans NMR method (see section 2.3, Eqn. 2.3.2), of which, there are several possibilities corresponding to the number of unpaired electrons in each Fe(III)PPIX species of interest.

The Fe(III)PPIX species in each detergent was interpreted based on comparison with reported literature magnetic moment values for each Fe(III)PPIX species in conjunction with the findings from UV-vis spectroscopy. The results for selected detergent solutions above their CMC values are shown in figures 5.4-5.6. The magnetic susceptibility of Fe(III)PPIX could only be measured in detergent solutions above their CMC values as a consistent frequency shift was not obtained at concentrations below the CMC. A meaningful reading could also not be obtained for NP-40 as the stock solution was already diluted in non-deuterated aqueous solution. Of particular interest, were the differences in the Fe(III)PPIX spectrum

obtained with detergents that do not mediate βH formation compared with those that do at pH 4.80.

(5.3.4.1) Charged Detergents

Neither the anionic SDS detergent nor the cationic CTAB detergent were capable of promoting βH formation at concentrations above or below their CMC.

(5.3.4.1.1) SDS

The UV-vis spectra of Fe(III)PPIX in anionic SDS micelles under basic pH (10.0) and acidic pH (4.8) conditions are presented in figure 5.4. The Q bands (450-550 nm) and CT regions (550-650 nm) in each spectrum are expanded to provide information about the Fe(III)PPIX species present under those conditions. A comparison of the spectra obtained to a Fe(III)PPIX spectrum acquired in solvent systems known to promote a particular species, are presented.[72]

(a) SDS above CMC **(b)**

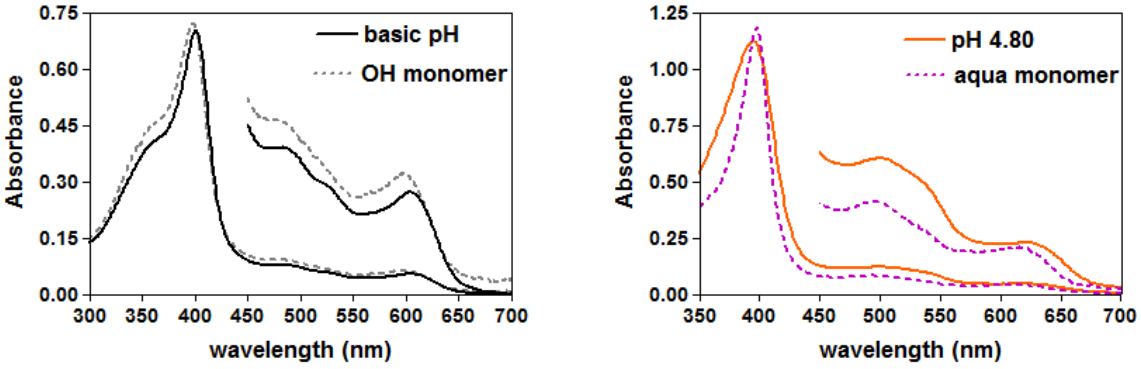

Figure 5.4 UV-vis spectra of Fe(III)PPIX in SDS detergent micelle solutions (solid lines) under basic **(a)** and acidic pH conditions **(b)** corresponding to pH 10.0 and 4.8, respectively. Traces obtained were compared with a Fe(III)PPIX spectrum (dashed lines) obtained from a solvent system that was known to favour monomeric Fe(III)PPIX with $^{-}$OH axial ligand (aq 80% MeOH, 20 mM CHES buffer, pH 10, grey) or with axial H_2O ligand (aq 80% MeOH, 20 mM acetate buffer, pH 4.8, purple).[72]

At pH 7 - 12.5, Fe(III)PPIX has been reported to be encapsulated into SDS micelles in its monomeric form, although earlier studies assumed this Fe(III)PPIX to be six-coordinate.[377,379] Later studies provided UV-vis evidence of this when Blauer et al. dissolved haemin (Fe(III)PPIX where X=Cl) in SDS solution and reported a spectrum that was characterised by

the diagnostic Q bands (450 -550 nm) and prominent CT band at 605 nm of the hydroxyl ($^{-}$OH) monomer form of Fe(III)PPIX.[392] Indeed, at pH 10.0, the Fe(III)PPIX spectrum in SDS micelles, appears to be that of a Fe(III)PPIX monomer with an $^{-}$OH axial ligand (Fig. 5.4(a)). As the pH is decreased to pH 4.8, the equilibrium in SDS micelles, appears to favour the monomeric Fe(III)PPIX species with H_2O axial ligand since the spectrum is similar to this species. The same changes in Fe(III)PPIX speciation were noted for Fe(III)PPIX in SDS below its CMC, however, at pH 4.8, some degree of $^{-}$OH monomer was still present. Acid dissociation constant measurements have been conducted for Fe(III)PPIX in SDS detergent micelles, with a reported pK_a value of 5.5, indicating that the presence of this detergent may depress the observed protonation equilibrium to lower pH values than in pure aq solution.[393] These assignments were confirmed for Fe(III)PPIX in SDS micelles as the magnetic moment, $\mu_{eff,}$ obtained was 4.03 μ_B under basic pH conditions (pH 8.35) corresponding to a Fe(III) spin state of S = $^3/_2$. The intermediate spin monomeric Fe(III)PPIX species with $^{-}$OH as the axial ligand and a resultant spin state of S = $^3/_2$, yields a theoretical magnetic moment of 3.9 μ_B. This has been reported for intermediate spin five co-ordinate Fe(III) octaethytetraazaporphyrins with magnetic moments between 3.9-3.94 μ_B.[394] Studies on a heme peptide model, have demonstrated that the presence of the weaker field axial $^{-}$OH ligand at high pH causes a decrease in the magnetic moment observed, arising from a mixture of the admixed, S= 3/2 spin state and high spin, S= 5/2 state.[395] At pH 4.8, the μ_{eff} was measured to be 4.95 μ_B, a value that is indicative of the presence of a significant fractions of high-spin (S = $^5/_2$), pentacoordinate Fe(III) with H_2O as the axial ligand as recently reported by Stanek and Dziedzic-Kocurek for solid monomeric Fe(III) complexes using SQUID and Mössbauer spectroscopy.[396] They showed that monomeric Fe(III)PPIX corresponds to a magnetic moment of 5.92 μ_B.[282,396] These data indicate that a prevalence of monomeric Fe(III)PPIX at acidic pH appears not to favour βH formation.

(5.3.4.1.2) CTAB

By contrast, the cationic detergent, CTAB, induced the μ-oxo dimer species of Fe(III)PPIX at high pH in aq detergent solution. This was shown by a clear match of the spectra obtained in this detergent to that of Fe(III)PPIX in 40% dimethyl sulfoxide (DMSO) in aq buffer at pH 10.0, a solution reported to induce the μ-oxo dimer species as seen in figure 5.5(a).[72] The Fe(III)PPIX spectrum at both pH values was characterised by the split Soret band at 400 nm

and the double-humped CT/Q bands at 550-650 nm (Fig. 5.4(b)).[282] This behaviour has been noted before in cationic detergent solutions of ferrimyoglobin, where the authors reported a stabilisation of the Fe(III)PPIX spectrum corresponding to the μ-oxo dimer species at pH 8.35.[397,398] As the pH was decreased, CTAB micelles seemed to stabilise the μ-oxo dimer species to some extent, such that the Fe(III)PPIX spectrum obtained at the pH of the DV (pH 4.80) appeared to still be predominantly the μ-oxo dimer with possibly some of the H_2O monomer species (Fig. 5.4(b)).

(a) CTAB above CMC **(b)**

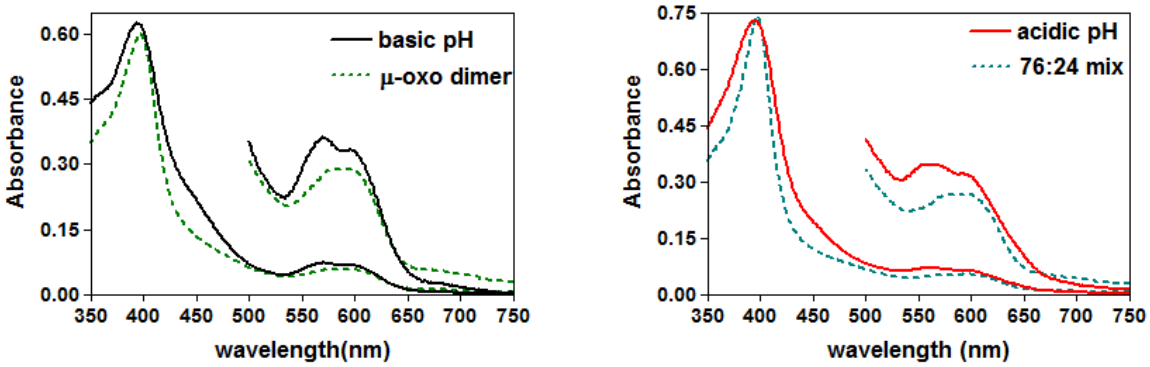

Figure 5.5 UV-vis spectra of Fe(III)PPIX in CTAB detergent micelle solutions (solid lines) under basic **(a)** and acidic pH conditions **(b)** corresponding to pH 10.0 and 4.8, respectively. Traces obtained were compared with a Fe(III)PPIX spectrum (dashed lines) obtained from a solvent system that was known to produce either the μ-oxo dimer (40% aq DMSO, 20 mM CHES buffer, pH 10, green), or the monomer with axial H_2O ligand (aq 80% MeOH, 20 mM acetate buffer, pH 4.8) or a mixture of two species 76% μ-oxo dimer and 24 % aqua monomer (red) , as was the case for CTAB at acidic pH.[72]

The magnetic moment of Fe(III)PPIX in CTAB solutions at high pH was measured as 2.26 μ_B. Although the μ-oxo dimer species of Fe(III)PPIX has been shown to have a lower magnetic moment, it does not correspond to a spin state of S = $^1/_2$, as sometimes stated. Rather it exhibits strong antiferromagnetic coupling between the Fe(III) centres that has a temperature dependent J-coupling constant of −110 ± 15 cm^{-1}.[224,396] Kuter et al. reported a measured magnetic moment of the μ-oxo dimer at 303 K, as 2.13 μ_B which compared well with a computed value using this J-coupling constant of 2.0 μ_B.[282] Low spin species, like a reported $(imidazole)_2$-Fe(III)PPIX complex, with S = $^1/_2$ have a theoretical magnetic moment of 1.78 μ_B.[224,399,400] Under acidic pH conditions, a magnetic moment of 3.75 μ_B was determined, the presence of a significant fraction of the μ-oxo dimer species likely decreases

the magnetic contribution from the high-spin H_2O monomeric Fe(III)PPIX species, effectively decreasing the μ_{eff} to 3.75 μ_B. This value of μ_{eff} could also be ascribed to the ad-mixed π-π dimer, but the UV-vis spectrum (Fig. 5.5b) is not consistent with this interpretation. This observation clearly dispels earlier misconceptions that all detergents induce monomeric Fe(III)PPPIX regardless of pH, owing to the idea that the hydrophobic interactions between the porphyrin and micelle interior were proposed to be stronger than the porphyrin-porphyrin interactions that drive aggregation.[378,379,401]

(5.3.4.2) Neutral and Zwitterionic Detergents

The neutral and zwitterionic detergents that do promote βH formation, at concentrations both above and below their CMC values, also exhibit an effect on the aq speciation of Fe(III)PPIX. The spectra of Fe(III)PPIX in these detergent solutions are shown in Fig. 5.6. Like the detergent, CTAB, the neutral detergents (NP-40 and TWEEN-20) and CHAPS, at concentrations both above and below their CMC values, promote the μ-oxo dimer species of Fe(III)PPIX in basic pH solution (Fig. 5.6 (a,c&e)). Confirming this, the magnetic moments obtained for Fe(III)PPIX in both TWEEN-20 and CHAPS under basic pH conditions were found to correspond to a μ-oxo dimer at μ_{eff} of 1.72 and 2.1 μ_B, respectively.

However, unlike CTAB, at low pH, these detergents, promote the formation of the π-π dimer species of Fe(III)PPIX characterised by the broad Soret band between 350-400 nm and a single CT band at 650 nm (Fig. 5.6(b,d&f)). The neutral detergents were found to do so at concentrations above and below their CMC values. The zwitterionic detergent, CHAPS, below its CMC appears to induce a species at low pH that is a mixture made up of predominantly monomeric Fe(III)PPIX. Interestingly, under these conditions only very low yields of βH were formed by this detergent. At acidic pH, assignment of the dominant Fe(III)PPIX species in TWEEN-20 solution was possible using magnetic susceptibility measurements. TWEEN-20 which mediates βH formation at low pH, was confirmed to do so from an ad-mixed spin-state, S= $^3/_2$, $^5/_2$, with a μ_{eff} of 4.62 μ_B, which has been shown in literature to correspond to the π-π dimer species of Fe(III)PPIX. [66,72,224]

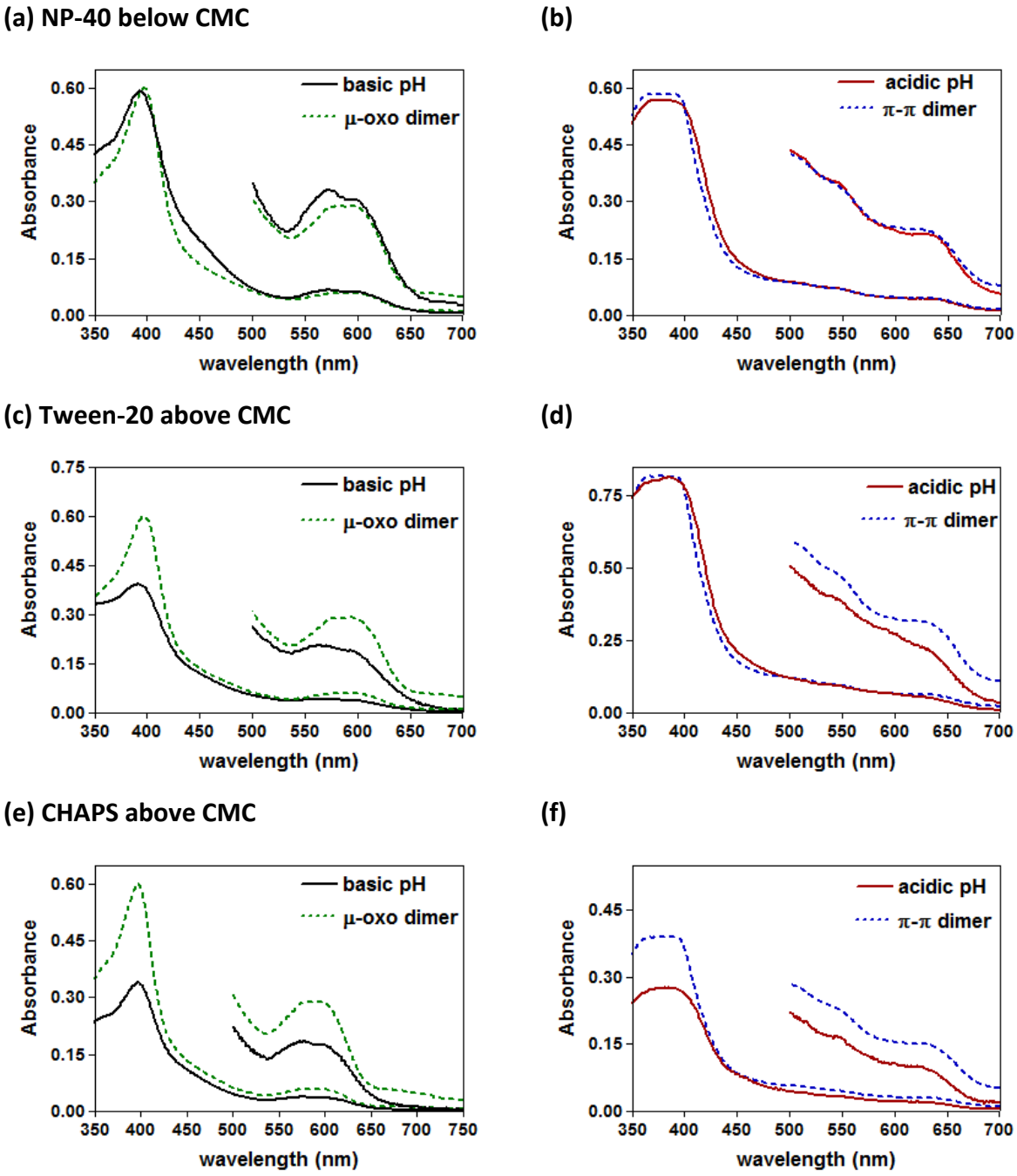

Figure 5.6 UV-vis spectra of Fe(III)PPIX in neutral and zwitterionic detergent solutions under basic **(a,c&e)** and acidic conditions **(b,d&f)** corresponding to pH 10.0 (solid black lines) and 4.8 (solid red lines), respectively where at the latter pH, βH formation is induced. Dashed lines correspond to the characteristic spectrum of either the μ-oxo dimer (40% aq DMSO, 20 mM CHES buffer, pH 10, green) or π-π dimer (aq 20 mM MES buffer, pH 6.0, blue) species of Fe(III)PPIX the in solvent systems where those species are known to be prevalent.

The presence of five-coordinate Fe(III) porphyrins in quantum mechanically ad-mixed spin states of S = $^3/_{2,}$ $^5/_2$, has been confirmed, for example in the tetraphenyl porphyrin derivative, Fe(TTP)($B_{11}CH_{12}$).C_7H_8, which was found by crystal structure analysis to possess a face to face (π-π) dimer structure of two non-covalently associated Fe(III) porphyrins.[402] The temperature dependence of the magnetic susceptibility of this compound was measured and the magnetic moment was found to vary from 2 μ_B at 6 K to 4.2 μ_B at 300 K, with the proposed predominant S = $^3/_2$ state making a larger contribution to the quantum mechanical mixing of each spin state to account for the lower value.[402] The zwitterionic detergent, CHAPS, was found to stabilise the μ-oxo dimer species to some degree at acidic pH as the magnetic moment obtained (μ_{eff} of 3.53 μ_B) is lower than expected for the spin ad-mixed π-π dimer species alone.

It was reported by Casabianca et al. that TWEEN-20 and DTAB, at concentrations above their CMC values, induce the μ-oxo dimer form of Fe(III)PPIX at higher pH, and the monomeric form at lower pH values.[223] This assignment was based on the incorrect assumption that Fe(III)PPIX in aqueous solution is a μ-oxo dimer at pH 7.00 and thus these detergents were judged not to affect the aqueous speciation of Fe(III)PPIX.[220] In fact, this result led the authors to suggest that the presence of the μ-oxo dimer species may serve as a precursor to βH formation, citing the observed strong interaction of the antimalarial drug, CQ, with the μ-oxo dimer form of Fe(III)PPIX in these solutions, as the proposed mechanism of βH inhibition.[223] However, as mentioned, it has been shown that in aqueous solution at neutral pH, Fe(III)PPIX is predominantly a π-π dimer.[66,68,72] Subsequently, it has also been shown that CQ is responsible for inducing μ-oxo dimer formation in aqueous solution, the presence of which has been correlated to absence of βH formation.[224]

These spectra appear to indicate that for the detergents tested, those that stabilise the π-π dimer species of Fe(III)PPIX at the pH of the DV, are the only ones that form βH. The other detergents, that fail to promote βH, all seem to induce a different Fe(III)PPIX species or the presence of mixed speciation at low pH. However, these techniques could not be used to determine the extent of μ-oxo dimer or monomer formation.

(5.3.5) Evaluation of the speciation changes of Fe(III)PPIX in detergent solution

To measure the extent of μ-oxo dimer formation spectrophotometric titrations to determine the effect of pH on Fe(III)PPIX in detergent solution at concentrations both above and below the detergent CMC values was conducted. The data were analysed according to the equilibrium speciation changes observed from the UV-vis spectra and magnetic susceptibility data such as those in Fig 5.5 and 5.6. The changes observed in the UV-vis spectrum of Fe(III)PPIX in selected detergent solutions that exhibited a dimer equilibrium between the μ-oxo dimer, $[(Fe(III)PPIX)_2O]$, and the π-π dimer, $[H_2O/HO-Fe(III)PPIX]_2$, species over the pH range investigated (described in Eqn. 5.1.1), were fitted to a sigmoidal curve to first establish the log of the ratio of π-π dimer (M_2H_n) to μ-oxo dimer, (abbreviated as M_2). This simplified model makes the assumption that, at no point in the titration do these detergents result in significant concentrations of monomeric Fe(III)PPIX. This was considered valid as the characteristic UV-vis spectrum features and high spin magnetic moment of the monomeric Fe(III)PPIX species were absent in these detergents at all pH values investigated. A plot of the log ratio of these dimer absorbance values versus the pH at which the absorbance was collected was linear. In this analysis the y-intercept corresponds to log *K* and the slope, *n*, the number of protons released in converting the π-π dimer species either with hydroxide, water, or both as the axial ligands on the Fe(III) ions to the μ-oxo dimer (Eqn. 5.2). This analysis was adapted from Brown's original dimerisation equilibrium outlined in Chapter 1.[374]

$$[H_2O/HO-Fe(III)PPIX]_2 \underset{\leftarrow}{\overset{K}{\rightleftharpoons}} [(Fe(III)PPIX)_2O](aq) + \boldsymbol{n}\, H^+\,(aq) + H_2O\,(l) \quad (5.1.1)$$

$$K = \frac{[M_2][H^+]^n}{[M_2H_n]} \quad (5.1.2)$$

$$\log K = \log \frac{[M_2]}{[M_2H_n]} - n.pH$$

$$\log \frac{[M_2]}{[M_2H_n]} = n.pH + \log K \quad (5.2)$$

The dimer equilibrium constant, *K,* (Eqn. 5.1.2) was then used to calculate the distribution of each species as a function of the total Fe(III)PPIX concentration added to the detergent solution, M_T, using Eqn. 5.3.1 From this, the total % μ-oxo dimer species at the pH and Fe(III)PPIX concentration at which the detergent produced βH was determined. The value obtained in Eqn. 5.3.2 was converted to a percentage of total Fe(III)PPIX in solution.

$$[M_T] = 2[M_2H_n] + 2[M_2] \tag{5.3.1}$$

$$[M_2] = \frac{K\,[M_T]}{2([H^+]^n + K)} \tag{5.3.2}$$

An example of a detergent that promoted this equilibrium, TWEEN-20 (above its CMC concentration) is shown in Fig. 5.7. The titration data and resultant sigmoidal fit of the change in absorbance at the Soret region are depicted in (a-b). The straight line fit of the log ratio of each species versus pH is shown in Fig. 5.7(c) to obtain the dimer equilibrium constant as a log K of -6.6 for the conversion of the π-π dimer to the μ-oxo dimer. The observed slope of unity indicates that the π-π dimer consists of one Fe(III)PPIX molecule with a $^-$OH axial ligand and another with a H_2O axial ligand (Fig. 5.7(c)).

Unlike the neutral detergents, the charged detergents did not at any point in the titration induce the π-π dimer species of Fe(III)PPIX. Therefore an alternative equilibrium was set-up to describe the absorbance changes observed in those solutions. As the concentration of H^+ ions was decreased in solution, the monomeric Fe(III)PPIX species, MH_n, bearing either the $^-$OH or H_2O axial ligand was converted into the μ-oxo dimer species, $\boldsymbol{M_2}$, which is described by the equilibrium in Eqn. 5.4.1. The dimerisation equilibrium constant, log *K,* could then be calculated in the same manner as above using Eqn. 5.5.

$$2\,[H_nO - Fe(III)PPIX] \underset{\leftarrow}{\overset{K}{\rightleftharpoons}} [(Fe(III)PPIX)_2O]\,(aq) + \boldsymbol{n}\,H^+\,(aq) + H_2O\,(l) \tag{5.4.1}$$

$$K = \frac{[M_2][H^+]^n}{[MH_n]^2} \tag{5.4.2}$$

$$\log \frac{[M_2]}{[MH_n]^2} = n.pH + \log K \tag{5.5}$$

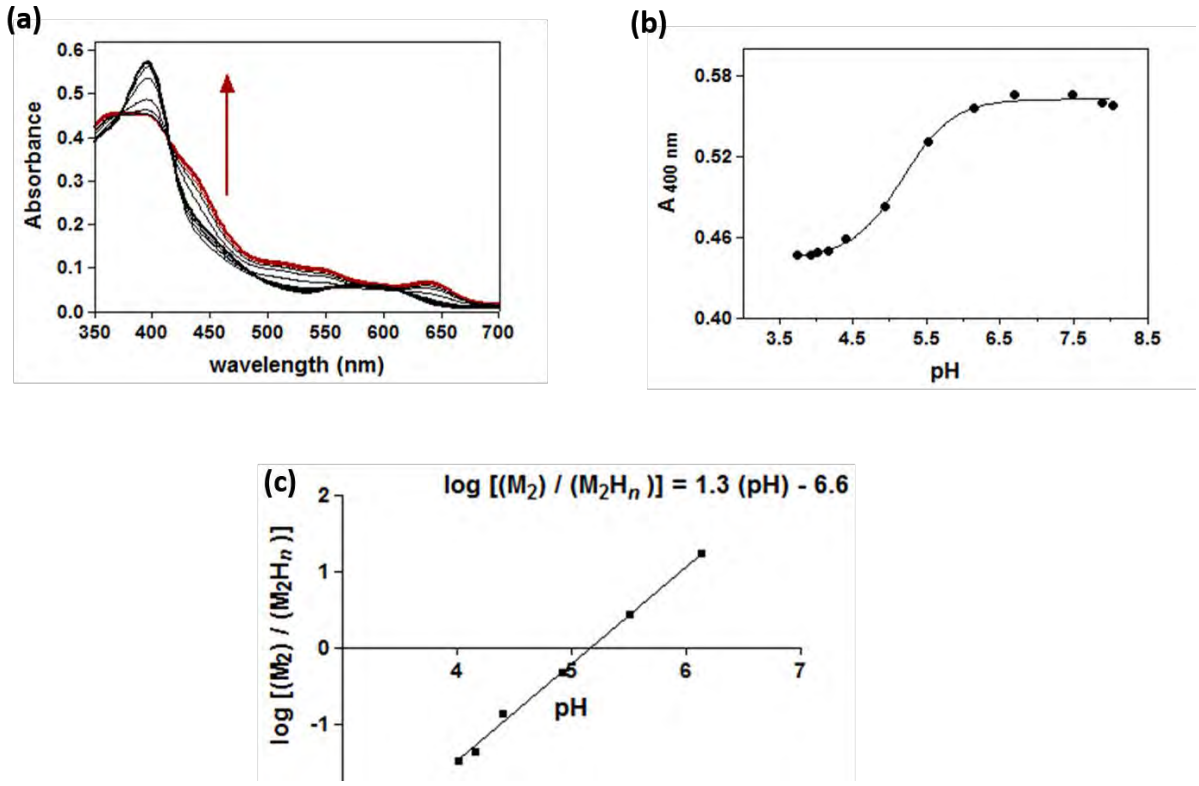

Figure 5.7(a) An example of the spectroscopic changes observed for Fe(III)PPIX in TWEEN-20 solution, above its CMC, over the pH range 3.75 - 8.2. The arrow indicates the direction of the π-π dimer to μ-oxo dimer equilibrium corresponding to the spectrum at low to high pH at 400 nm. The sigmoidal pH dependence of the maximum absorbance at the Soret band, λ=400 nm is shown in **(b)**. A plot of the log ratio of μ-oxo dimer (M_2) to π-π dimer, (M_2H_n) versus pH **(c)** was linear with slope of 1.3 ± 0.04 and y-intercept = -6.6 ± 0.2, r^2 = 0.99.

The value of log *K,* allowed for the calculation of the percentage (%) μ-oxo dimer species in each detergent, this speciation can be predicted at any pH or Fe(III)PPIX concentration in the manner illustrated by Asher et al. for the 40% aq DMSO solutions, using the total Fe(III)PPIX concentration, M_T, in Eqn. 5.6, which can be substituted in to 5.4.2 to yield the proportion of M_2 at a particular pH and Fe(III)PPIX concentration.[72]

$$[M_T] = 2[M_2] + [MH_n] \qquad (5.6)$$

A three-dimensional surface plot could be rendered from the pH, total [Fe(III)PPIX] and the corresponding % μ-oxo dimer prevailing in detergent solution under a specific combination of conditions. The plots showing the distribution of the μ-oxo dimer species for the detergent, TWEEN-20, below its CMC value and for CTAB, above its CMC value are shown in Fig. 5.8(a) and (b). The neutral detergent, TWEEN-20, induces the μ-oxo dimer at high pH regardless of Fe(III)PPIX concentration. It can be seen from the shape of the speciation curve (Fig. 5.8(a)) that the % μ-oxo dimer does not show any dependence on Fe(III)PPIX concentration and this species was found to be stable only at pH values above pH 6.5. By contrast, it can be seen that the cationic detergent, CTAB, stabilises the μ-oxo dimer species to much lower pH values, especially at higher Fe(III)PPIX concentrations. At the Fe(III)PPIX concentration (100 μM corresponding to log [Fe(III)PPIX] = -4) and pH at which the test for βH formation was conducted, over 90 % of the total Fe(III) in the solution was present as the μ-oxo dimer. However, at very low Fe(III)PPIX concentration values, the μ-oxo dimer species is not prevalent below pH 5, an observation which was consistent with the mixed UV-vis spectrum and magnetic moment obtained in this solution at acidic pH in Fig. 5.5 (5.4.3.1).

(a)

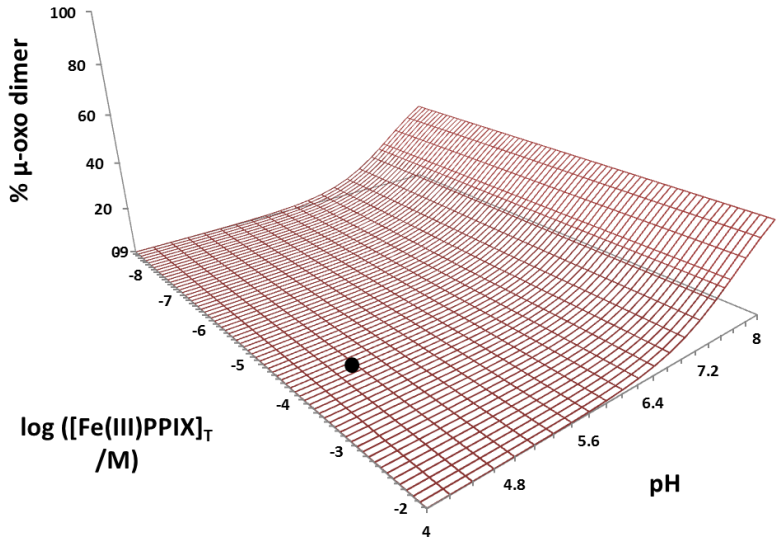

(b)

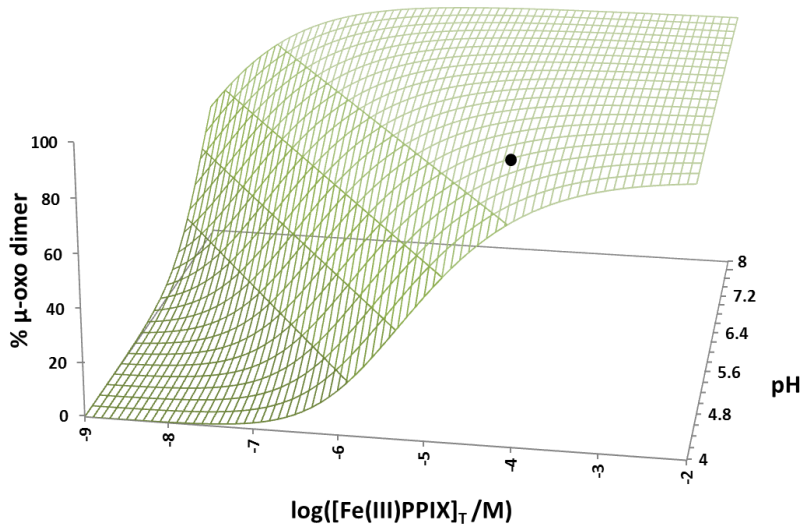

Figure 5.8 The dependence of the % µ-oxo dimer species on pH and Fe(III)PPIX concentration prevalent in detergent solution that **(a)** forms βH, TWEEN-20 (above CMC) and **(b)** fails to promote βH **,** CTAB (above CMC). The black dot indicates the % µ-oxo dimer under the pH and total Fe(III)PPIX concentration conditions employed for the βH formation experiment. This is 0.7% in TWEEN-20 and 92% in CTAB solution.

These calculations were performed for all the detergents at concentrations both above and below the CMC except SDS which produced the monomeric species regardless of pH. The results are presented in Table 5.5 to offer a comparison of the total % μ-oxo dimer present in a particular detergent solution at the Fe(III)PPIX concentration and pH conditions of the βH formation experiment.

Table 5.5 Equilibrium constants, *log* K, for the formation of the μ-oxo dimer species from π-π dimeric and monomeric Fe(III)PPIX, obtained from spectrophotometric pH titration data. The corresponding % μ-oxo dimer prevalent under the experimental pH and Fe(III)PPIX concentration conditions for the formation of βH experiment is listed for each detergent.

Detergent	CMC	*slope*[b]	*n*	*log K*[c]	% μ-oxo dimer
CHAPS	below	1.2 ±0.06	1	-1.3 ± 0.3	32
$M_2H_n \rightleftharpoons M_2 + nH^+$	above	0.85 ± 0.1	1	-5.06 ± 0.6	26
CTAB	below	0.99 ± 0.04	1	0.59 ± 0.03	87
$2MH_n \rightleftharpoons M_2 + 2nH^+$	above	0.86 ± 0.001	1	1.07 ± 0.25	92
NP-40	below	1.8 ± 0.13	2	-10.1 ± 1.5	0
$M_2H_n \rightleftharpoons M_2 + nH^+$	above	1.5 ± 0.25	1/2	-11.1 ± 1	0
TWEEN-20	below	1.3 ± 0.04	1	-7.5 ± 0.5	0.2
$M_2H_n \rightleftharpoons M_2 + nH^+$	above	1.4 ± 0.09	1	-6.6 ± 0.2	0.7
SDS [a]	below	-	-	-	0
MH_n	above	-	-	-	0

[a] SDS induces monomeric Fe(III)PPIX over the pH range used in equilibrium fitting.
[b] slope of linear plot of the log ratio of each species vs pH. The integer, *n* corresponds to the total number of H^+ released by the formation of μ-oxo dimer, described by Eqn. 5.2 and 5.5.
[c] Equilibrium constants calculated from the y-intercepts of straight line fits described using Eqns. 5.2 and 5.5

A negative log K indicates the equilibrium disfavours the μ-oxo dimer at pH 0. Thus the smaller (ie. more negative) the value, the lower the proportion of μ-oxo dimer at pH 4.8, the value at which βH is prepared. While the dimerisation equilibrium constant, has been reported for conversion of monomeric Fe(III)PPIX species to dimers, and the conversion between the μ-oxo dimer and the π-π dimer in mixed aq solvents has been observed, this is apparently the first report of an equilibrium constant (log K) for the conversion of the π-π dimer to the μ-oxo dimer.[72] A pH-dependent conditional dimer equilibrium constant can be

calculated for the transformation of the π-π dimer species to the μ-oxo dimer using Eqn. 5.7.1 and 5.7.2.

$$K_{obs} = \frac{K}{[H^+]^n} \tag{5.7.1}$$

$$\log K_{obs} = \log K + n.pH \tag{5.7.2}$$

For NP-40 above and below its CMC value, the conditional dimer equilibrium constant, log K_{obs} was calculated at a basic pH of 8.0 and the acidic pH of the DV, pH 4.8. These values are shown in Table 5.6. At pH 8, where the μ-oxo dimer is prevalent, log K_{obs} is large and positive, however, at pH 4.80, where the π-π dimer species is prevalent, negative log K_{obs} values were obtained. It is interesting to note that this detergent was the only one found to favour the π-π dimer Fe(III)PPIX species with both axial ligands being H_2O. This was evident from the number of protons released upon formation of the μ-oxo dimer which was found to correspond to two ($n \approx 2$). This is in accord with the following equilibrium:

$$[H_2O - Fe(III)PPIX]_2 \underset{\leftarrow}{\overset{K}{\rightleftharpoons}} [(Fe(III)PPIX)_2O](aq) + 2H^+(aq) + H_2O\ (l)$$

By contrast, TWEEN-20 and CHAPS promote formation of a mixed π-π dimer with one axial H_2O and one ^-OH ligand, resulting in the release of only one proton (n=1) with an equilibrium corresponding to:

$$[HO - Fe(III)PPIX][H_2O - Fe(III)PPIX] \underset{\leftarrow}{\overset{K}{\rightleftharpoons}} [(Fe(III)PPIX)_2O](aq) + H^+(aq) + H_2O\ (l)$$

The dimerisation equilibrium constant, $\log K_{obs}$, for the monomer to μ-oxo dimer equilibrium in CTAB detergent was also calculated and the values at pH 8.0 and 4.8 are presented in Table 5.6. The corresponding pH-dependent dimerisation constant for the μ-oxo dimer- monomer equilibrium has been previously investigated in 40% aq DMSO at pH 10.0 and 7.4 and log K_{obs} was reported as 7.69 and 2.5, respectively.[72] The log K_{obs} values obtained here indicate that in the cationic detergent, CTAB, the μ-oxo dimer species is stabilised to much lower pH values. A further observation is that CTAB appears to stabilise the monomer with ^-OH as the axial ligand, even at low pH. The equilibrium (with n= 1), thus corresponds to:

$$[HO-Fe(III)PPIX]+[H_2O-Fe(III)PPIX] \underset{}{\overset{K}{\rightleftharpoons}} [(Fe(III)PPIX)_2O]\,(aq)+H^+(aq)+H_2O\,(l)$$

This is probably as a result of the positively charged detergent favouring the negatively charged Fe(III)PPIX species.

Table 5.6 Conditional dimerisation constants, logK_{obs} , of Fe(III)PPIX for the conversion of the π-π dimer or monomer species to the μ-oxo dimer at basic and acidic pH in selected detergent solutions.

detergent	CMC (above/below)	log K	log $K_{obs_{pH\ 8}}$	log $K_{obs_{pH\ 4.8}}$
NP-40	below	-10.1 ± 1.5	5.9 ± 0.6	-0.50 ± 0.05
	above	-11.1 ± 1.0	4.9 ± 0.5	-1.50 ± 0.15
CTAB	below	0.59 ± 0.03	8.59 ± 0.4	5.39 ± 0.3
	above	1.07 ± 0.25	9.66 ± 2.2	5.87 ± 1.3

The data presented here show that the prevalence of the π-π dimer form of Fe(III)PPIX at acidic pH in selected detergent solutions is correlated with their ability to mediate βH formation. This in itself does not provide evidence of a definitive nucleation species of βH since the π-π dimer is already established as the dominant form of Fe(III)PPIX in aqueous solution at the pH of the DV, but it does show that promotion of either the monomer or μ-oxo dimer by detergents disfavours βH formation. It has been previously suggested that the π-π dimer Fe(III)PPIX species prevalent in aqueous solution is converted to the μ-propionato form of Fe(III)PPIX upon association with a lipid environment.[55,132] These findings are consistent with this hypothesis. Owing to their lipophilic nature, it is proposed that the ability of selected detergents to mimic a lipid environment allows for facilitation of formation of this μ-propionato form of Fe(III)PPIX. In a non-polar hydrophobic environment this dimer can then associate via hydrogen bonding to form the growing βH crystal. On the other hand, the hypothesis that detergent micelles mimic lipid droplets at first sight fails to explain the observed ability of the neutral detergents to promote significant amounts of βH formation at concentrations well below their observed CMC values.

As mentioned above and in Chapter 1, detergent monomers have been reported to aggregate into pre-micellar aggregates at concentrations below their CMC values which are capable of exhibiting unusual bulk solution properties. [167,170,171,403,404] Early computational

studies on the structure of detergents at various concentrations in solution have demonstrated the existence of dimers and higher aggregates that adopt conformations which align their outer fatty acid-like chains with more than half their hydrophobic surface removed from contact with water.[167] Later works by Hadgiivanova and Diamant, showed both experimentally, by demonstrating the polydispersity of detergent solutions below their CMC values and theoretically, by using proposed thermodynamic models and Kramers' reaction rate theory to compute the lifetimes of these aggregates, that once the required activation energy barrier to achieve a degree of monodispersity has been realised, metastable premicellar aggregates exist at sizes that do not significantly differ from the micelle size.[169,170,388] This phenomenon probably explains the observed ability of these neutral detergents to mediate βH formation at concentrations both above and below their CMC values. It is suggested that the Fe(III)PPIX can interact with the detergent premicellar aggregates in the same way that it interacts with the micelles to form βH. Having found that this interaction is between the π-π dimer species and the neutral detergents plays an important role in βH formation, an experiment was next performed to establish which part of the detergent molecule is involved in this interaction with Fe(III)PPIX. For this purpose ^{1}H NMR spectroscopy was performed using TWEEN-20, which was available as a solid.

(5.3.6) Probing the interaction between neutral detergent micelles and Fe(III)PPIX by NMR spectroscopy

The ability of neutral detergents to induce a particular Fe(III)PPIX species at the pH of the digestive vacuole may be the sole determinant of their ability to mediate βH formation, however, the mechanism by which they do so is unknown. To investigate the interaction of Fe(III)PPIX with TWEEN-20 micelles, a comparison of the ^{1}H NMR spectrum obtained for the detergent in the absence and presence of Fe(III)PPIX was made and is shown in Fig. 5.9. TWEEN-20 is an ethoxylated sorbitan monolaurate compound (Fig. 5.9(a)) that has been well characterised in aqueous solution by ^{1}H NMR in the literature.[405,406] The characteristic structural components such as the sorbitan ring protons, the methylene protons of the polyethoxylate chains and the monolaurate fatty acid chain methyl protons are the most diagnostic signals in the spectrum, appearing at specific chemical shifts as seen in Fig. 5.9(b). The most deshielded protons are those that comprise the fatty acid chain. The terminal

methyl protons appear at 0.9 ppm, followed by the aliphatic methylene groups at 1.3 ppm, with the satellite peaks corresponding to the α and β CH_2 protons adjacent to the ester of the fatty acid group, at 2.4 and 1.6 ppm, respectively. The largest proton signal arises from the methylene protons of the polyethyleneoxide chains at 3.7 ppm. A small shoulder signal is seen which corresponds to the methylene protons on the sorbitan ring whose chemical shift coincides with the polyethyleneoxide signal. A separate downfield signal appearing at 4.2 ppm corresponds to the methyl protons of the polyethylene glycol adjacent to the fatty acid ester (Fig. 5.9(c)).

The presence of unpaired electrons in a compound have been shown to be useful for characterising its distance and orientation-dependant effects on a bulk sample by measuring the changes in the NMR spectrum of that sample.[407] This method of exploiting the paramagnetism of the compound of interest has been applied widely in the field of membrane bound peptide or protein structure determination.[408,409] Fe(III)PPIX is paramagnetic in its π-π dimer state and any effect it has on the reported ^{1}H NMR chemical shifts of specific protons from the functional groups in TWEEN-20 micelles would signify a proximity interaction. The ^{1}H NMR spectrum of the Fe(III)PPIX π-π dimer in D_2O has been reported in the literature with assignments of proton signals that appear well above 4.5 ppm, therefore it was judged that any shifted or new signals observed in the TWEEN-20 ^{1}H NMR spectrum from 0-4.5 ppm arose from an interaction with the paramagnetic centre of Fe(III)PPIX and not from the porphyrin protons.[66]

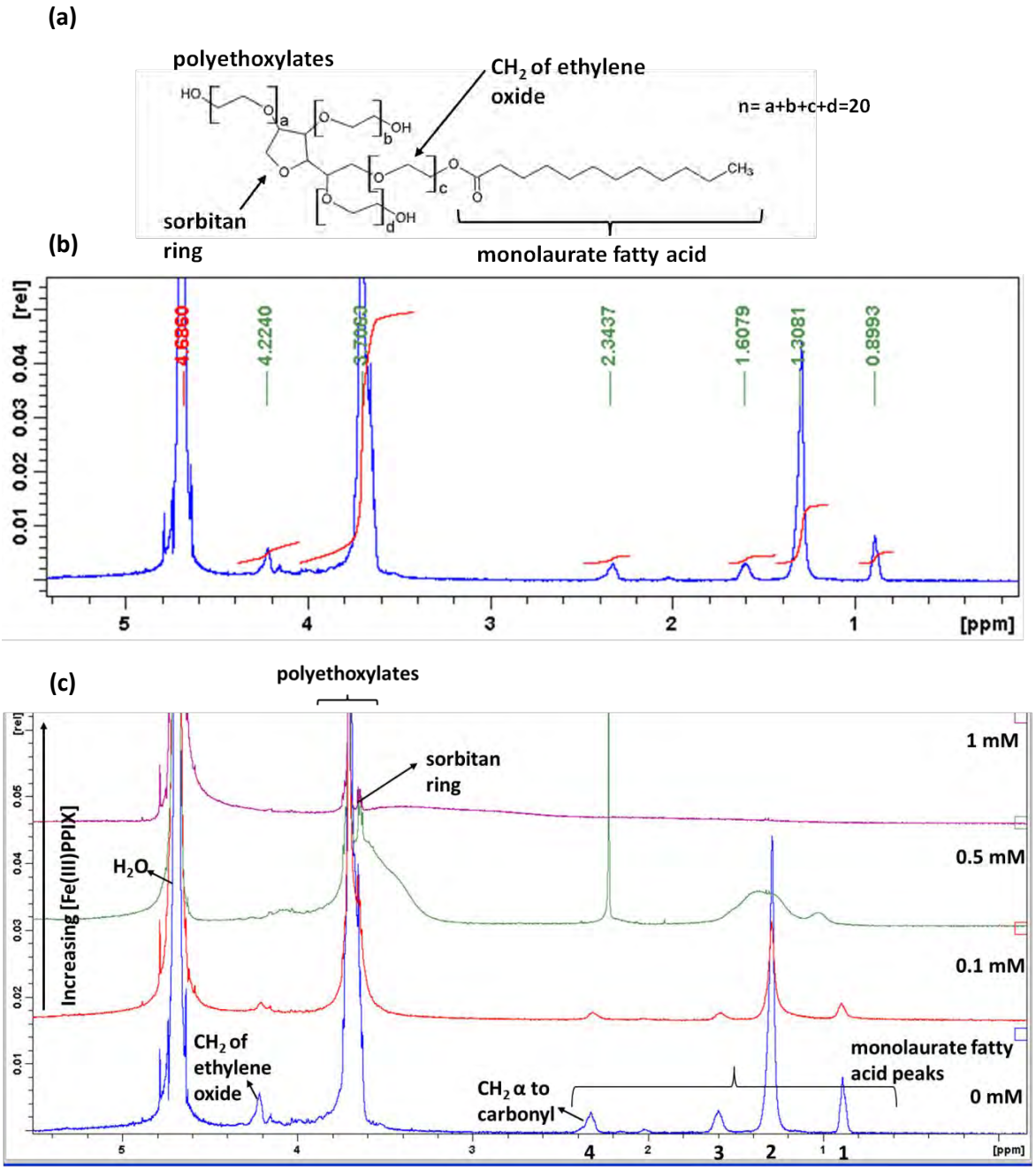

Figure 5.9 (a) The molecular structure of TWEEN-20 with each functional group moiety highlighted and labelled corresponding to the peaks observed in **(b)**, the ^{1}H NMR spectrum of TWEEN-20 detergent micelles in D_2O with peak chemical shifts indicated. A comparison of this native TWEEN-20 spectrum and that obtained with increasing concentrations of paramagnetic Fe(III)PPIX is presented in **(c)**, with the diagnostic proton peaks assigned to the functional groups illustrated on the structure. The deshielding effects of Fe(III)PPIX on the fatty acid proton signals (1 and 2) and upfield shift of signal 3 of TWEEN-20, (1mM at pH 7, blue) for increasing concentration from 0.1 mM (red) to 0.5 mM (green) were observed until finally at 1mM Fe(III)PPIX (purple), all the fatty acid signals are broadened and shifted downfield.

It can clearly be seen in Fig. 5.8(c) that increasing Fe(III)PPIX concentration in micellar TWEEN-20 solution results in a marked effect on the fatty acid chains of the molecule with significant peak broadening observed from 0.1-0.5 mM Fe(III)PPIX. Furthermore, the ^{1}H NMR signals from the terminal methyl group and methylene protons of the hydrocarbon chain appear to have disappeared from their native peak frequencies in the aliphatic proton region (1.3-2.4 ppm) entirely at the maximum concentration of Fe(III)PPIX used (1 mM). All the other functional group proton signals appear to be unaffected apart from the general line broadening reported for sample NMR signals in the presence of paramagnetic compounds.

In the previous chapter, it was shown that Fe(III)PPIX is lipophilic and partitions into neutral lipid droplets. As pictured in Chapter 1 (Fig. 1.18), TWEEN-20 detergent micelles can be considered as spherical structures with their polar headgroups exposed to the aqueous bulk and their fatty acid chains comprising the hydrophobic interior of the structure.[162] The hydrophobic nature of the interior of TWEEN-20 micelles was confirmed by monitoring the maximum emission intensity wavelength shifts of the solvatochromatic dye, NR, with increasing detergent concentration. The effect of micellisation on NR fluorescence emission intensity and wavelength is shown in Fig. 5.10. A hypsochromic (ie. to shorter λ) shift upon incorporation of NR into the hydrophobic interior is noted in the inset of Fig. 5.10.

Indeed, addition of an aq Fe(III)PPIX stock solution to the NR stained micelle solution investigated in Fig. 5.11, resulted in linear Stern-Volmer quenching plot up to 25 μM Fe(III)PPIX with 10.2 ± 0.3 μM required for 50% quenching of NR fluorescence inside the micelle. Interestingly, the λ_{max} of this NR signal (629 nm) indicates that the interior of the TWEEN-20 micelle has an $E_T(30)$ of 50.2 ± 4 kcal.mol^{-1} (interpolation from Fig. 4.3, Chapter 4), this is more polar than the interior of the SNLBD and closer to the polarity of soluble alcohols like 1-propanol (50.7 kcal.mol^{-1}) which incidentally have also been found to be capable of promoting βH formation.[148,331] The $E_T(30)$ of TWEEN-20 micelles has not been determined under these conditions, however, $E_T(30)$ values for other neutral detergents such as Triton-X-100 and a polyethoxylene laurel ether, Brij 35, are reported as 53 and 52.8 kcal.mol^{-1} respectively.[410]

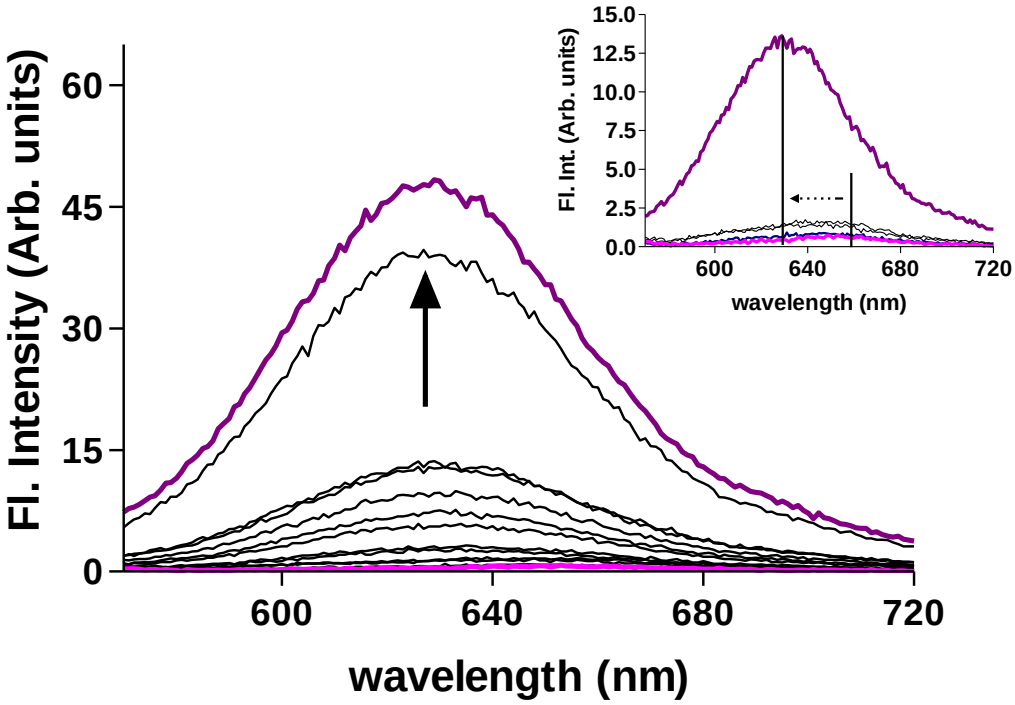

Figure 5.10 Fluorescence emission response of solvatochromatic dye, NR (1 μM), in increasing concentrations of TWEEN-20 solution, the direction of intensity increase upon detergent micellisation is highlighted with the solid black arrow. The inset shows the wavelength shift of the maximum emission intensity (670 nm to 629 nm) upon NR incorporation into the hydrophobic micelle interior.

From the effect of Fe(III)PPIX on the ^{1}H NMR signals of TWEEN-20 micelles observed in Fig. 5.9(c), and the quenching of NR localised in the hydrophobic detergent micelle interior (Fig. 5.11), it can be concluded that under these concentration conditions, Fe(III)PPIX partitions into the neutral detergent micelles and interacts with the hydrophobic fatty acid interior. Whether this interaction is responsible for the detergents ability to promote the π-π dimer and βH formation from Fe(III)PPIX in solution seems likely but remains unproven.

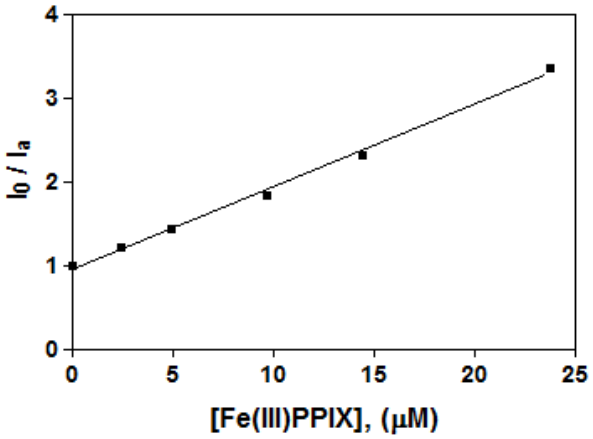

Figure 5.11 Linear SV plot for Fe(III)PPIX quenching of NR fluorescence inside neutral detergent, TWEEN-20, micelles at pH 7.0, (r^2 = 0.99).

(5.3.7) The effect of neutral detergent on drug-Fe(III)PPIX association

It was recently shown by UV-vis and IR spectroscopy, diffusion and magnetic susceptibility measurements and magnetic circular dichroism (MCD) techniques that the antimalarial drug, CQ, induces the μ-oxo dimer form of Fe(III)PPIX in solution.[224] Kuter et al. reported a log association constant for CQ and Fe(III)PPIX, log K' of 6.5 ± 0.2, which when added to the established dimerisation constant for Fe(III)PPIX at the pH investigated (log $K_{\text{pH 7.4}}$ = 6.82 ± 0.06) amounts to a log K_{obs} of 13.3 ± 0.2 for the interaction of two Fe(III)PPIX molecules to one drug molecule.[66,224] In the present study, NP-40 was found to produce the largest yield of βH at a concentration below its CMC value, which was shown to correspond to a Fe(III)PPIX dimer equilibrium that favoured the π-π dimer species at the acidic pH of the experiment. In fact, this detergent was found to favour the π-π dimer species of Fe(III)PPIX beyond neutral pH.

Therefore, in an effort to determine if the manner in which this neutral detergent stabilises the π-π dimer Fe(III)PPIX species in solution affects the established interaction of Fe(III)PPIX with antimalarials in aq solution, the association constant of Fe(III)PPIX with CQ in the presence of NP-40 below its CMC was determined by spectrophotometric titration of Fe(III)PPIX solution into a drug and detergent solution at pH 7.50. The changes in the UV-vis spectrum shown in Fig. 5.12(a), noted upon increasing Fe(III)PPIX concentration in solution, were analysed over the entire spectrum in the Hypspec® program using the simplified model

proposed by Kuter et al. for the conversion of predominantly dimeric Fe(III)PPIX to the CQ-μ-oxo-Fe(III)PPIX complex.[224] The equilibrium is shown in Eqn. 5.8.1, from which the association constant for CQ and the Fe(III)PPIX dimer, K', could be determined using Eqn. 5.8.2. This association was added to the pre-established dimerisation constant, *K*, determined for conversion of monomeric Fe(III)PPIX to the μ-oxo dimer form in aqueous solution under the pH conditions of the experiment as shown by Eqn 5.8.3.

$$M_2 + CQ \overset{K'}{\Leftrightarrow} CQ.M_2 \tag{5.8.1}$$

$$K' = \frac{[CQ.M_2]}{[M_2][CQ]} \tag{5.8.2}$$

$$K' \times K = K_{obs} \tag{5.8.3}$$

The theoretical absorbances generated for the drug-Fe(III)PPIX complex by the fitting the model described in Eqn. 5.8.1 were compared to the experimental absorbance values measured at the wavelength that corresponded to the region of greatest change (λ =390 nm) upon increasing Fe(III)PPIX concentration, this is shown in Fig. 5.12(b). Analysis of the UV-vis spectrum changes upon addition of Fe(III)PPIX with the development of the characteristic split Soret band at 400 nm and the appearance of the double humped Q/CT peak between 550 and 650 nm in the experimental and calculated data for the complex confirmed that the μ-oxo dimer species of Fe(III)PPIX was present in the complex that formed in detergent solution.

The stoichiometry of binding between Fe(III)PPIX and CQ in the presence of NP-40 was confirmed using Job's method of continuous variation.[381] The Job plot determined for the Fe(III)PPIX.CQ complex in NP-40 detergent solution at 25 °C, displayed in Fig. 5.12(c), indicated that the binding occurred in a 2:1 stoichiometry of two Fe(III)PPIX molecules to every CQ molecule.

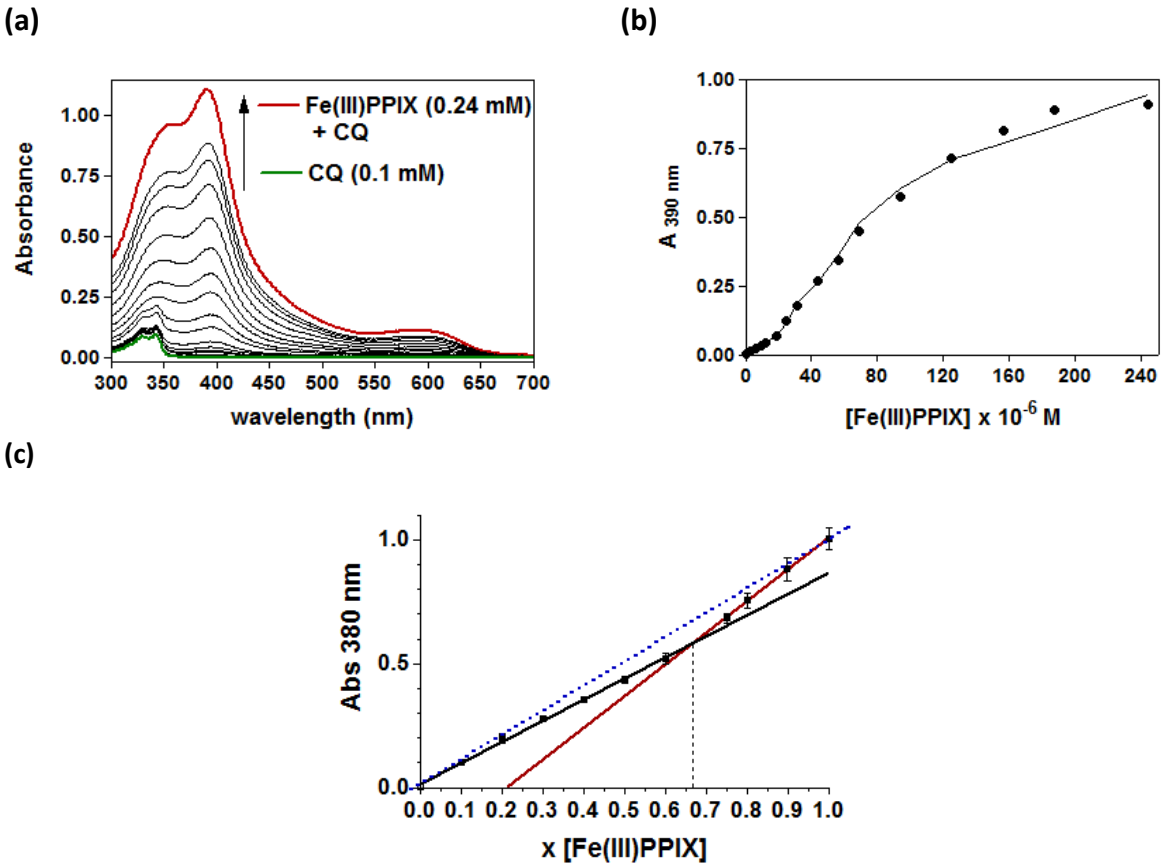

Figure 5.12(a) The UV-vis spectrum changes upon titration of Fe(III)PPIX and NP-40 detergent stock solution (1 mM) into a solution of CQ (0.02 mM, pH 7.5) and NP-40 (0.2 mM). The arrow indicates the direction of increasing Fe(III)PPIX concentration. **(b)** The most pronounced changes in the UV-vis spectrum were found at 390 nm and were plotted against the predicted absorbance values for the complex from the fit of the data to the equilibrium in Eqn.5.8.1. **(c)** The stoichiometry of Fe(III)PPIX binding to CQ to form the Fe(III)PPIX.CQ complex was determined from a Job plot by the intersection of the solid black and red lines, the black dashed line shows the mole fraction of Fe(III)PPIX present in the complex, as 0.66 ± 0.02. The dashed blue line represents the theoretical Beers law relationship for increasing Fe(III)PPIX concentration.

This indicates that the detergent had no effect on the binding stoichiometry for this complex compared to pure aq solution.[224] Similarly the value obtained for log K' for the association of Fe(III)PPIX and CQ in NP-40 solution was 6.7 ± 0.01, which when added to the dimerisation constant, log *K* (6.82 ± 0.02) yielded a log K_{obs} of 13.5 ± 0.02, that matched the association obtained in pure aq solution.[224] Similarly, measurements of the association constants of the quinoline methanol antimalarials, QD and QN, in pure aqueous solution and in NP-40 solution below its CMC value, yielded approximately the same log K' values for each drug

with and without detergent , these are listed for comparison in Table 5.7. Likewise, the stoichiometry of interaction determined at pH 7.50 revealed a 1:1 interaction of these drugs with monomeric Fe(III)PPIX, under both conditions.

Table 5.7 Association constants, log K' for quinoline methanol drugs with Fe(III)PPIX at pH 7.5 (20 mM HEPES) with a 1:1 stoichiometry in pure aq and NP-40 (0.2 mM) solution.

Drug	log K' aq	log K' NP-40
QD	5.23 ± 0.06	5.10 ± 0.05
QN	5.03 ± 0.02	4.80 ± 0.03

These results indicate that although certain detergents stabilise a particular species of Fe(III)PPIX in solution, the drug-Fe(III)PPIX interaction that has been established to favour a different Fe(III)PPIX species dominates this equilibrium. This suggests that the observed association between these antimalarials and Fe(III)PPIX is stronger than the detergent effect, at least below their CMC values. Ideally, measurement of the effect of detergent micelles on this association would provide more insight into the nature of the Fe(III)PPIX-detergent interaction, however, these solutions proved too turbid to allow measurement of the small changes that occur in the UV-vis absorbance spectrum upon drug-Fe(III)PPIX complexation. In spite of this, given that this neutral detergent appears not to be strongly associated with Fe(III)PPIX in solution, further investigation of its interaction with Fe(III)PPIX to effectively form βH was undertaken via kinetic investigation. This is described in the next chapter.

(5.4) Summary

The ability of various detergents to mediate βH formation at the pH and temperature of the parasite DV was explored. The anionic and cationic detergents, SDS and CTAB, respectively, failed to promote βH formation at concentrations both above and below their measured CMC values. The uncharged neutral and zwitterionic detergents, TWEEN-20, NP-40 and CHAPS were found capable of initiating βH formation at both concentrations. However, the efficiency at which they did so varied. To explain this, a comprehensive study of the effect of each detergent (above and below their CMCs) on Fe(III)PPIX speciation in solution using UV-vis spectroscopy and magnetic susceptibility measurements was conducted. The pH response of this speciation profile was measured and a pH independent dimerisation constant was calculated for each detergent above and below the CMC. These data showed that the detergents that significantly stabilised the π-π dimer form of Fe(III)PPIX in acidic pH solution, were able to promote βH formation. Those that induced a significant percentage of either the monomeric or μ-oxo dimer form of Fe(III)PPIX at low pH, resulted in no βH formed. To illustrate this for the most efficient βH initiator, NP-40, below its CMC value, a pH dependent π-π to μ-oxo dimer equilibrium constant, log K_{obs}, was determined at basic pH 8.0 and found to be 5.9, favouring the μ-oxo dimer and -0.5 at pH 4.8, favouring the π-π dimer species. However, this π-π dimer species stabilisation was not found to prevent CQ-Fe(III)PPIX association to form the μ-oxo dimer with a stoichiometry and association constant essentially unchanged from aqueous solution.

It was also shown by fluorescence quenching and ^{1}H NMR spectroscopy that Fe(III)PPIX partitions into the hydrophobic interior of the detergent micelle to interact with the fatty acid part of the detergent. While, there can be no doubt that all detergent solutions increase the solubility of Fe(III)PPIX and decrease the surface tension in acidic aq solution in a manner that provides a favourable environment for its crystallisation, the point of differentiation between the detergents tested that do not promote βH formation and those that do, appears to be related to their ability to induce the π-π dimer form of Fe(III)PPIX, coupled to the favourable hydrophobic microenvironment that the detergent micelles and premicellar aggregates provide. The correlation of uncharged detergents with this ability to favour the π-π dimer form of Fe(III)PPIX in solution at low pH is interesting in the biological context of this

process given the probable role of neutral mono and diacylglycerols and/or zwitterionic membrane phospholipids, in mediating Hz formation.

Chapter 6:
Kinetics of NP-40 mediated β-haematin formation and effect of known quinoline antimalarials

(6.1) Introduction

The biocrystallisation of Hz remains an essential target in the development of novel antimalarials. Quinoline antimalarials are known inhibitors of βH formation although their precise mechanism of inhibition is still unclear.[239] In the absence of definitive knowledge of the mechanism of formation of βH, the rate determining step is not entirely certain. Nonetheless, as discussed in Chapter 1, the processes of crystal nucleation and growth are thought to be rate-determining and their inhibition can occur through several proposed mechanisms, namely; the precipitation of Fe(III)PPIX [57,411], the formation of a drug-Fe(III)PPIX complex,[208,234] or interference in crystal growth when a drug binds to the fastest growing face of the crystal.[28,236] Recently, Gildenhuys et al. proposed a crystal growth kinetic model that can account for the exponential kinetics observed at a lipid-aqueous interface.[63] The kinetics of βH formation and its inhibition by antimalarials was shown to conform to an apparent first order process that can be fitted to the Avrami equation (6.1) when the Avrami constant, *n*, is 1 corresponding to random (non-spontaneous) nucleation and crystal growth in one dimension.[63]

$$\frac{m_R}{m_0} = e^{-(zt^n)} \qquad (6.1)$$

The model proposed that the observed decrease in the rate and hence in percentage of βH formed, at a given t, in the presence of drugs is due to the existence of two processes which compete with the formation of βH from Fe(III)PPIX. One reaction involves the irreversible formation of a precipitated drug-Fe(III)PPIX complex that removes a portion of the Fe(III)PPIX available for conversion to βH at higher drug concentrations. Another process where the drug was proposed to adsorb onto the growing crystal surface was suggested to account for the observed decreases in rate of βH formed and dominates at lower drug concentrations.[63] It has been proposed that by assaying the strength of adsorption of lead drug compounds onto βH at a lipid-aq interface, it may be possible to predict their potential as βH inhibitors by this process.

Although lipids are likely responsible for mediating βH formation *in vivo,* the lipids comprising the droplets that are found to be associated with Hz, are expensive and often difficult to study because of large data scatter in the presence of lipid emulsions, an effect also noted in Chapter 4.[124,126] On the other hand, in Chapter 5, under physiological pH and temperature conditions, NP-40 was shown to effectively mediate the formation of βH and has been used as a cheaper 'lipid-mimic' in assays for potential βH inhibitors.[155,174,175] Measurement of the kinetics of NP-40 mediated βH formation is a useful way of comparing the mechanism of inhibition in these two systems. The key objective of this chapter was thus to compare the kinetic profiles obtained in this detergent solution with those reported for neutral lipid droplets. A further objective was to directly investigate the proposed process of drug adsorption onto the βH crystal surface in a detergent environment. These observations were aimed at establishing to what extent this neutral amphiphilic detergent is a genuine lipid 'mimic' for investigation of the inhibition of Hz formation.

(6.2) Experimental Methods

(6.2.1) Materials, Instrumentation and General Procedures

Nonident P-40 (NP-40, Shell Chemical Co.) detergent was obtained from Pierce Biotechnology, Rockford, Illinois and was used without further purification. It was stored as a 167 mM stock solution at 4°C in the fridge. All other chemicals were purchased from Sigma Aldrich® (Vorna Valley, South Africa). A Fe(III)PPIX stock solution (0.0023 g, 10 mL) was prepared by dissolving solid haematin (porcine) in 0.1 M NaOH (4 mL) and acetone:MeOH (1:9, *v*/*v*, 6 mL). Plastic sterile Greiner bio-one CELLSTAR® 15 mL tubes were employed as vessels for each experiment. Spectrophotometric assay experiments were analysed using a plate-reader and Graph Pad Prism v3 software was employed to calculate all models and to plot curves. Characterisation of βH was done by ATR-FTIR spectroscopy [44] and PXRD analysis by comparing characteristic stretching frequencies and diffraction peaks respectively with those reported in the literature (discussed in Chapter 2, section 2.4). [45] Unless otherwise stated, all experiments were performed at least in triplicate. Acetate buffer stock solutions (1 M) were prepared fresh for each experiment by dissolving sodium acetate solid in an appropriate amount of acetic acid solution in a volumetric flask so that the final pH of the buffer was 4.80 ± 0.01. 30% pyridine stock and 2 M HEPES buffer (pH 7.5) solutions were prepared daily according to the method outlined in Chapter 3. Aqueous stock solutions of chloroquine (CQ) and quinidine (QD) were prepared fresh for each sample set by dissolving the solids from the free base drugs at 10 mM and 5 mM respectively in acetate buffer (1 M).

(6.2.2) Sample Preparation and Analysis Procedures

(6.2.2.1) Evaluating the kinetics of β-haematin formation in the presence NP-40 (below the CMC)

In a 15 mL Falcon tube, acetate buffer (4.9 mL, 1M, pH 4.8) was premixed with aqueous NP-40 detergent stock (100 µL, 2.5 mM) so that the final concentration of detergent was 50 µM. The mixture was equilibrated at 37 °C for 30 min in a thermostatted water bath prior to the start of the experiment. Fe(III)PPIX stock solution (363 µM, 50 µL) was added to the buffer-detergent solution in the reaction tubes with a Hamilton syringe. The final Fe(III)PPIX

concentration in the Falcon tube was 3.58 µM. The solution was briefly vortexed and allowed to incubate at 37 °C in the water-bath for variable time periods. To test if any βH formed during the experiment that was not as a result of the presence of NP-40, a control experiment with the 1M acetate buffer, not containing NP-40 was tested for %βH formation for each time point in every experiment. The absorbance recorded at 405 nm for this control was used as the zero reading and any signal detected was subtracted from each sample.

(6.2.2.2) Measurement of percentage β-haematin formed

Modification of the pyridine hemichrome inhibition (Phi-β) assay

The amount of βH (% yield) formed was calculated using the pyridine hemichrome inhibition (Phi-β) assay method previously described by Ncokazi and Egan.[253] After the designated incubation time (0 - 420 min), the reaction in the Falcon tube was stopped for individual tubes by immediate quenching, facilitated by addition of 30% v/v pyridine stock solution (1 mL, 30% pyridine; 40% acetone, 25% H_2O, and 10% HEPES buffer (2 M, pH 7.5), to each tube. Tubes were then vortexed and centrifuged at 4000 rpm for 15 min. 200 µL aliquots from the supernatant of each tube were measured at the Soret band absorbance of Fe(III)PPIX at 405 nm using a clear 96 well plate. The control Fe(III)PPIX reading was set up for each experiment with the same constituents with the exception of NP-40. Upon addition of the 5% pyridine solution, the absorbance detected at 405 nm in this sample corresponds to the initial concentration of Fe(III)PPIX in the reaction mixture. Any βH formed corresponding to the recorded decrease in the amount of Fe(III)PPIX available for reaction with pyridine that resulted from incubation of Fe(III)PPIX in aqueous acidic buffer at 37 °C in plastic tubes was thus accounted for in all experiments. This absorbance was converted into a % βH formed by normalisation relative to the control described in equation 6.1. Data for each time point was collected with several replicates in separate experiments and analysed using the in-built exponential decay equation by nonlinear least squares fitting in GraphPad Prism v3 to determine the rate constant, z (min^{-1}) and the time taken to form 50% of the final βH yield, $t_{1/2}$ (min) .

$$\%\ \beta H = \left(\frac{A_{405nm}\ \ Control\ Fe(III)PPIX_{\,t=0} - A_{405nm} Fe(III)PPIX\ sample}{A_{405nm}\ \ Control\ Fe(III)PPIX_{\,t=0}}\right) \times 100 \qquad (6.1)$$

(6.2.2.3) Evaluating the kinetics of β-haematin formation in the presence NP-40 detergent and antimalarials

The potential of known antimalarials to affect the observed kinetic profile of βH formation in NP-40 was investigated by the following experiment. The protocol described in section 6.2.2.1 was set up with the addition of the desired antimalarial drug (CQ or QD) stock solution to each tube of acetate buffer at the pre-incubation stage. The final drug concentrations investigated ranged from 0 to 0.2 mM for each time point from 0 - 420 min. Each drug concentration, at each time point served as a separate experiment which was investigated at least in triplicate for both antimalarial drugs. The kinetic parameters of each drug concentration were measured and analysed as described in 6.2.2.2.

To prove that the dark pigmented solid isolated from the reaction mixture left over after the addition of 30% pyridine was in fact βH, the ATR-FTIR spectrum of the dried product was obtained and is shown in Fig. 6.1. The characteristic stretching frequencies of the coordinated propionate moiety were observed at 1660 and 1208 cm^{-1} as expected (see Chapter 1 and 2) for βH.

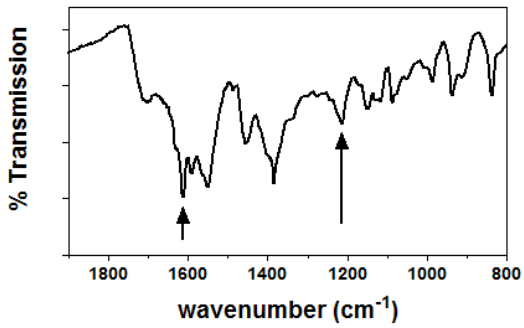

Figure 6(a) ATR-FTIR spectrum of the reaction product of NP-40 mediated βH formation in the presence of 0.05 mM CQ after 6 h incubation. The diagnostic stretching frequencies at 1660 and 1208 cm^{-1} are indicated with arrows.

(6.2.3) Adsorption of CQ and QD onto preformed β-haematin

(6.2.3.1) β-haematin preparation and analysis

βH was prepared from a pentanol-aqueous interface according a recently reported method adapted from earlier publications by the Egan group. [57,126,412] Citrate buffer solutions (20 mM, 50 mL × 6, pH 4.80) prepared from solid sodium citrate salt and a NaOH slurry was transferred to several Schott-Duran crystallisation dishes of 9 cm internal diameter. Pentanol (15 ml × 6) was added to each dish forming a distinct interface which was allowed to incubate at 37 °C in a thermostatted water-bath for 60 min. Haemin solid was dissolved in 0.1 M NaOH with sonication and then mixed with acetone:MeOH (1:9 v/v) in a 6:4 v/v ratio to make a 2mg/ mL Fe(III)PPIX stock solution. The Fe(III)PPIX stock solution (1.5 mL) was then gently added to the top of the pentanol layer in each dish with a 23 gauge needle syringe. Migration of the Fe(III)PPIX solution to the aq-pentanol interface was observed to be immediate and the crystallisation reaction was allowed to proceed under a watch-glass at 37°C for 6 h. The reactions were quenched by agitation of the interface and addition of water to each dish. The contents of the crystallisation dish were filtered by vacuum filtration using Whatman® filter disks (0.22 µm). The resulting crystals were washed with 1 ml of a solution of the 30% pyridine solution to bind unreacted Fe(III)PPIX in the manner of the Phi-β assay in section 6.2.2.2. The contents of each dish were then transferred to 80 mL transparent polycarbonate Nalgene® centrifuge tubes and centrifuged at 10 000 rpm for 20 min using an Eppendorf 5810 R centrifuge. The crystals were washed extensively with water and centrifuged again, the supernantent was discarded and the resultant dark brown solid was dried and stored in a desiccator over P_4O_{10}.

(6.2.3.2) Adsorption experiments

The adsorption of antimalarial drugs, CQ and QD to preformed βH crystals was tested in the presence and absence of detergent NP-40. Aqueous drug solutions (2 mL) in acetate buffer (1 M, pH 4.80) at drug concentrations of 0.1 mM were pre-equilibrated at 37°C in a thermostatted water-bath in glass vials. Separate experiments were set up for each drug, in the absence and presence of NP-40. NP-40 stock solution was added to the mixture so that the final NP-40 concentration was 0.05 mM in 2 mL of drug and acetate buffer solution. The UV-vis absorbance spectrum of the contents of each vial was recorded from 200 - 800 nm at

37°C. βH crystals (1 mg) were added to a vial containing each drug in the presence and absence of NP-40 and the mixture was allowed to incubate at 37 °C for 55 h. Control experiments containing each drug or βH crystals only in the presence and absence of NP-40 were also incubated. 1 mL aliquots were extracted from the supernatant of each vial and the UV-Vis absorbance spectrum was recorded of the supernatant above settled βH. A Beers law plot of each drug absorbance in the presence and absence of NP-40 was generated and used to calculate the molar absorptivity coefficient (Ɛ) at their λ_{max} (343 nm for CQ and 332 nm for QD). The final concentration of each drug post-incubation was calculated from the absorbance obtained and Ɛ calculated using Beer's Law to measure of the amount of crystal adsorption for each drug.

(6.3) Results and Discussion

(6.3.1) Kinetic profile of β-haematin formation mediated by NP-40

The ability of amphiphilic solutions to mediate βH formation has been well established.[67,141,148,154,155] To ensure the process had proceeded successfully in the presence of NP-40 and the correct product was obtained, the dark brown product was isolated from the reaction solution and dried for 48 h prior to performing solid state characterisation. ATR-FTIR spectroscopy and PXRD were employed to characterise the reaction product. These methods have previously been used to definitively prove the formation of βH initiated by lipophilic systems.[63,127,155]

(6.3.1.1) Characterisation of NP-40 product

Figure 6.1 depicts an ATR-FTIR spectrum that is characteristic of βH with the diagnostic carboxylate peaks at 1660 and 1208 cm^{-1} corresponding to the C=O and C-O stretches of the coordinated propionate moiety (Discussed in Chapter 1 and 2). The spectrum of the unreacted Fe(III)PPIX starting material is presented to highlight the differences. The positions of the stretching frequencies of both uncoordinated carboxyl groups were present at 1714 and 1620 cm^{-1} justifying the conclusion in Chapter 5 that NP-40 induces π-π dimers and not μ-propionato dimers that would exhibit the characteristic stretching frequencies at 1660 and 1208 cm^{-1}.

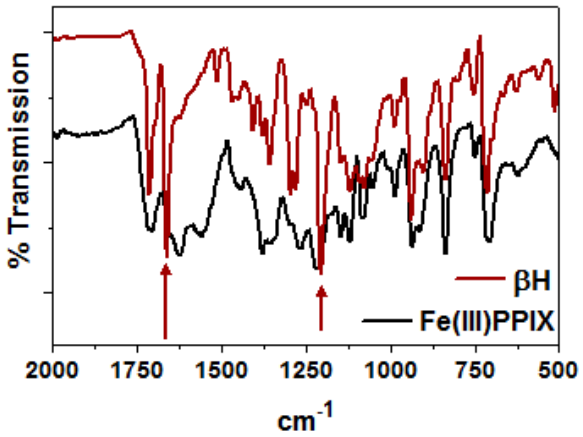

Figure. 6.1 Infrared spectra of Fe(III)PPIX starting material (black) and the product obtained when Fe(III)PPIX was incubated in the presence of NP-40 (red). Characteristic stretching frequencies of βH are indicated by arrows at 1660 and 1208 cm^{-1}.

The PXRD pattern obtained with the same sample shown in Fig. 6.2 confirms the identity of the product as βH with the dominant 100 and 131 reflections labelled. The pattern obtained matches well with those previously reported for βH formed from an NP-40 solution.[155] The results from these techniques agree well with the literature standards of βH characterisation and confirm that NP-40 efficiently facilitated βH formation. [27,44]

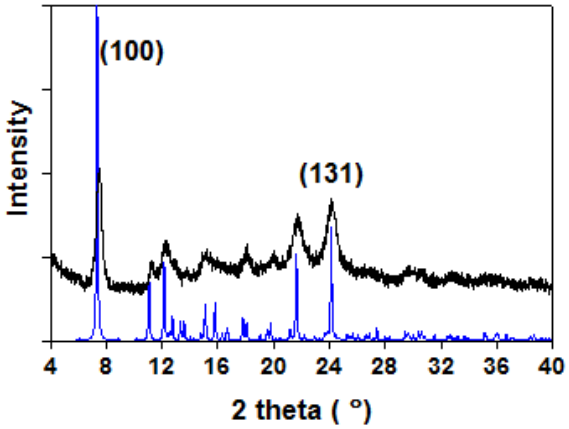

Figure 6.2 PXRD pattern of βH obtained from NP-40 solution (black), with the characteristic (100) and (131) reflections labelled. The calculated PXRD pattern obtained from the structure reported by Pagola et al is shown for comparison (blue).[27]

(6.3.1.2) NP-40 kinetics

NP-40 is known to promote βH formation, although the kinetics of this process have not been reported.[155] To address this, the % βH formed from Fe(III)PPIX in an acidic aq solution of NP-40 over the course of 7 h was measured and the rate constant, *z*, was determined. Data were fitted to a non-linear least squares exponential function to generate the kinetic profile shown in Fig. 6.3. Incubation of Fe(III)PPIX in acetate buffer (4.5 M) under acidic pH conditions has been reported to initiate βH formation with a half-life of approximately 30 min.[67] However, under these much lower temperature and acetate concentration conditions, the % conversion to βH in the absence of NP-40, was found to be insignificant.

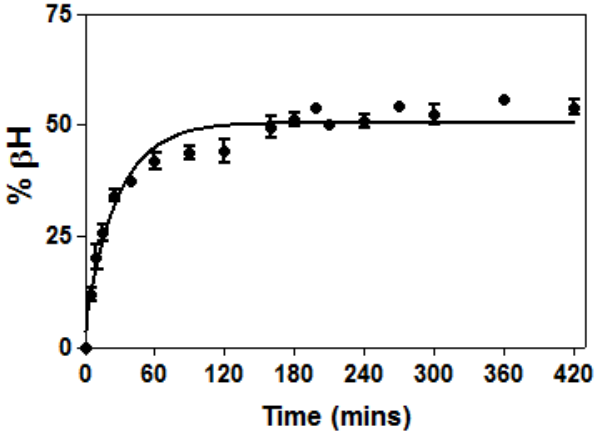

Figure 6.3 The kinetic profile of NP-40 mediated βH formation over the time period of 0-420 min. Data as fitted with a non-linear least squares exponential function in GraphPad Prism , r^2 =0.93. The error bars represent standard error of the mean (SEM) values, n= 5.

The observed kinetic profile is exponential in shape (Fig. 6.3), corresponding to the Avrami equation with, *n*=1 (Eqn. 6.1). Mathematically, this is indistinguishable from first-order kinetics and can be fitted with a simple exponential function. This can be interpreted as instantaneous nucleation of βH crystals with growth in one-dimension.[138,139] The growth rate resembles that observed for the formation of βH at a lipid-aq interface, where the mode of nucleation has been proposed to occur from a fixed number of preformed nuclei templated by the lipid OH head groups at the air-aq interface. [63,127,143] This proposal is supported by evidence that when layered on an aq surface, a model lipid, MMG forms clusters with its OH groups exposed. Preferential Fe(III)PPIX interaction with that surface, effectively induces oriented βH crystals via their 100 faces.[125] Indeed, the kinetic profile observed for NP-40, indicates that no induction period of slow nucleation occurs at the early time-points and the time-dependent data was found not to be sigmoidal as previously reported for acetate buffer-mediated βH formation at 60°C.[67] In that case, an Avrami constant of n= 4 correlating to sporadic nucleation and three-dimensional crystal growth was observed.[67]

A total yield of 56 ± 2% βH was calculated according to Eqn. 6.1 with a rate constant, *z* of 0.037 ± 0.003 min^{-1}, corresponding to a half-life ($t_{1/2}$) of 19 ± 1 min. This yield is somewhat lower than the earliest report of NP-40 mediated βH formation (74%) and the yield obtained in Chapter 5.[155] It should be noted however, that direct comparison between experiments can only be done if both the concentrations of initial starting material and NP-40 are

consistent. When testing the effects of inducer and Fe(III)PPIX concentration on inhibition of crystallisation assay results, Nhien and co-workers found that both components as well as the incubation time affected the outcome of the tests.[173] This needs to be considered when comparing results from assays performed under varied concentration conditions.

Previous studies have reported *z* values for the biologically-established neutral lipid blend (NLB) on the order of 1.6 ± 0.02 min^{-1} with $t_{1/2}$ of approximately 26 seconds to form 80-90 % βH.[143] The lipid blend components were found to mediate the formation of βH with rate constants of DOG > DLG > MPG > MSG in an order found to be inversely correlated to their activation energy established in an earlier study.[135] The monoacylglycerol component, MPG was found to facilitate conversion of almost 80% Fe(III)PPIX to βH on a favourable time scale with $t_{1/2}$ equal to 8.15 min, such that the kinetics of inhibition of βH formation could be measured.[63] NP-40 mediated βH formation occurs much more slowly than the MPG lipid mediated process.

The observed ability of NP-40 to promote Fe(III)PPIX π-π dimers in solution (Chapter 5) cannot be assumed for the neutral lipid. And so if indeed, NP-40 detergent polar head groups can serve as a nucleation template for βH crystal formation in the manner reported for lipid OH groups, this process must be much less efficient in detergent solution than at the lipid-aq interface. While the rate is lower, it is still sufficient to form βH on a reasonable time scale. Thus given that the detergent is more stable and cheaper, it remains a viable alternative to lipids for the production of βH, especially for its application in high-throughput screening.

(6.3.2) Kinetics of β-haematin formation mediated by NP-40 in the presence of antimalarial drugs

Chloroquine (CQ) and quinidine (QD) are known to target the process of βH formation and are believed to act against the malaria parasite by inhibiting Hz formation. [67,208,246] The exact mechanism by which this is achieved has been a matter of dispute, but recent research has proved that at least for CQ, Hz formation in *P. falciparum* is inhibited in a dose-dependent manner which correlates with an observed increase in free Fe(III)PPIX that correlates with

parasite death.[195] Use of the NP-40 system as a mediator of βH formation to assay the inhibitory activity of antimalarial compounds is well-established and is widely employed to determine the 50% βH inhibitory concentration (IC_{50}) of prospective novel drugs.[155,176] This method has been used to screen large compound libraries for hit compounds as it provides an indication of efficacy at decreasing the amount of βH formed. Furthermore, comparisons can be made relative to known βH inhibitors and antimalarial standards.[174,175]

A detailed investigation of the time dependence of NP-40 mediated βH formation in the presence of known inhibitors, CQ and QD was undertaken. Figure 6.6 is a composite of all the kinetic curves obtained for βH formation in the presence of increasing drug concentration, over the time period of 0 - 360 min. The kinetic profiles obtained and seen in Fig. 6.4(a and b), show a gradual decrease in the observed rate constant, z_{obs}, in the presence of increasing drug concentration. This is evident from the fact that the exponential curves converge to the maximum yield at longer times in the presence of higher drug concentrations. Both graphs (a) and (b) indicate that over 6 h, the two drugs CQ and QD, exhibit similar kinetic profiles despite the fact that the former is a member of the 4-amino quinoline family and the latter, a quinoline methanol.

Figure 6.4(c) shows the dose-dependent decrease in z_{obs} which is in agreement with previously reported inhibition studies with the drug, CQ.[63,142] A comparison of the change in rate constant between the two drugs reveals that the rate constants in the presence of CQ are higher than those observed with QD and the decrease in z_{obs} for QD is sharper than CQ over the same concentration range despite CQ being reported as the more efficient inhibitor.[239] A slice through the kinetic data after 90 min of incubation with CQ and QD was evaluated to determine if an IC_{50} could be obtained from the dose-response behavior, the resultant sigmoidal curves are shown in Fig. 6.5.

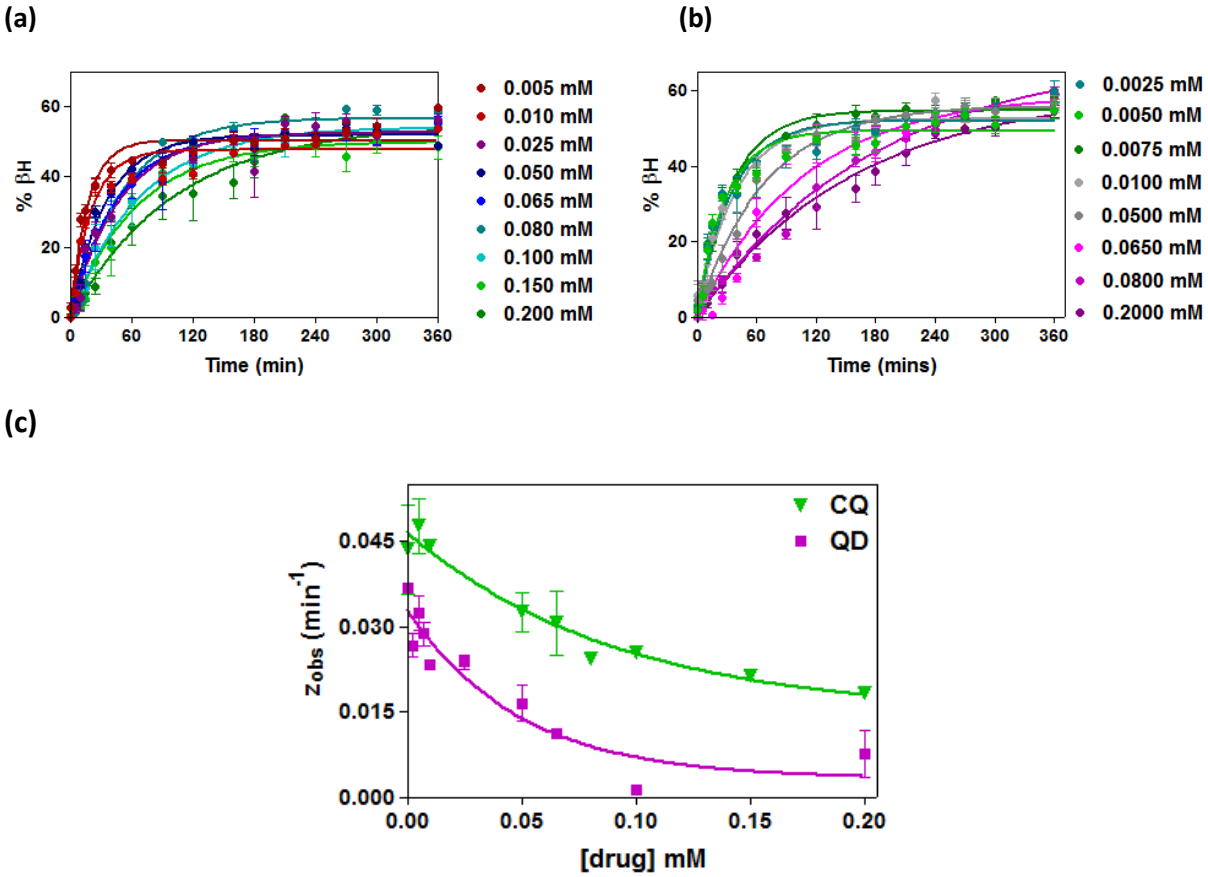

Figure 6.4 Kinetic curves for inhibition of βH formation in the presence of increasing doses of (**a**) CQ and (**b**) QD from 0 - 360 min. Rate constants, z_{obs}, were obtained by fitting the data to an exponential function. (**c**) The effect of increasing drug concentration on z_{obs} is shown for CQ (green) and QD (purple). Error bars represent SEM (n ≥ 3) for each point.

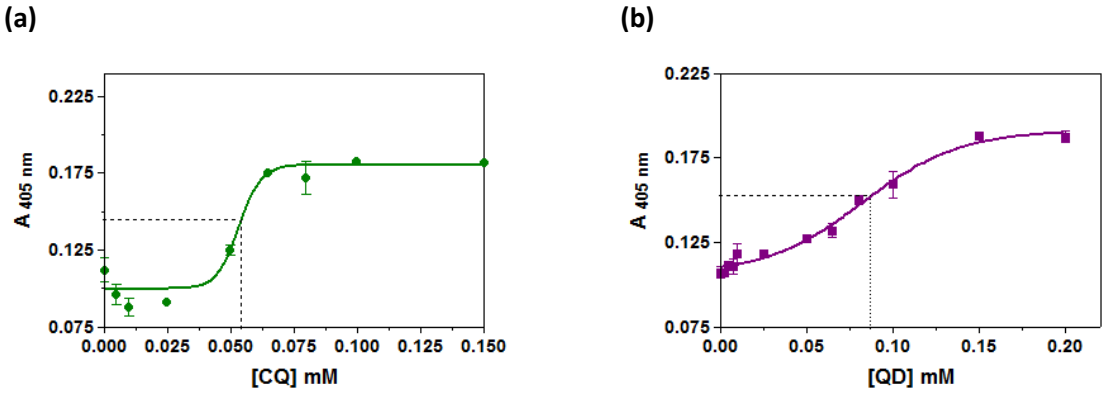

Figure 6.5 Dose response curves of the amount of unreacted Fe(III)PPIX measured at $A_{405\ nm}$ in the presence of NP-40 and drugs at the 90 min time point; **(a)** chloroquine (r^2 = 0.99) and **(b)** quinidine (r^2 = 0.99). The data was analysed with a sigmoidal curve function in GraphPad prism. The IC_{50} points are highlighted by dotted lines on each graph. The error bars represent SEM, (n= 4).

Figure 6.5(a) depicts the efficacy of CQ in inhibiting βH formation at 90 min. An IC_{50} of 54 ± 2.8 μM was determined. The IC_{50} for QD (Fig. 6.5(b)) was found to be 82.26 ± 4.7 μM. The smaller the IC_{50}, the better the drug activity against βH formation, this is a trend observed for CQ and QD not only in lipophilic assays but for *in vitro* anti-parasitic activity against drug-sensitive strains as well.[239,413] The detergent system yields IC_{50} values for CQ and QD that are higher than those reported in the lipid system after 30 min of incubation, where CQ and QD showed an IC_{50} of 16.4 ± 0.5 μM and 51.5 ± 5.8 μM, respectively.[240] While the values obtained here are within the same order of magnitude, this observation highlights that despite the widespread use of detergent systems to assay for potential βH inhibitors, the detergent system does not appear to show the same time and rate dependence of βH inhibition by known antimalarials as the biologically relevant neutral lipid. Furthermore, IC_{50} values are dependent on incubation time.

Although an IC_{50} can be approximated from the kinetic data at 90 min and the initial rates of βH formation from 0 – 180 min are relatively slower for both drugs when compared with NP-40 (Fig. 6.3), the final yield of βH is independent of inhibitor identity and even concentration once the reactions have reached completion. This can be clearly seen in Fig. 6.4 (a&b). For CQ, the drug concentration is seen to affect the rate of βH formation over the early incubation time-period with the initial yield calculated to be markedly lower than the drug-independent value, below 120 min. Beyond the 2 h point, the yields appear to be virtually identical to NP-40 in the absence of drug. By contrast, the decrease in rate constant the presence of QD appears to be about twice as low as for CQ (Fig. 6.4(c)). Interestingly, the observed final yield appears to plateau at an average of 52 and 55 % βH for incubation with CQ and QD, respectively, with no apparent decrease in yield at very high drug concentrations. The fact that both known antimalarial drugs fail to fully inhibit the formation of βH has been previously observed with different βH initiator systems, where the inhibition mechanism was proposed to be as a result of a reversible reaction between Fe(III)PPIX and the drug to form a solution complex of drug-Fe(III)PPIX.[142,246,414] Pre-formed βH seed crystals incubated for 48 h with quinoline antimalarials were shown to exhibit an inhibitory effect on the lag and crystal growth phases of βH crystallization that is reversible after 40 h.[246] This observation contrasts with the reported kinetic profile for CQ inhibition of βH formation in the presence of lipid droplets, where it was shown that at sufficiently high concentrations of

the drug, the final yield of βH decreased.[63] The authors proposed that the inhibition that occurred at very high drug concentrations, was irreversible resulting in a precipitated drug-Fe(III)PPIX complex.[63]

(6.3.3) A mechanism to account for the kinetic behaviour of βH formation in the presence of CQ and QD.

Gildenhuys et al. investigated the kinetics of βH formation in the presence of a model neutral lipid mediator, MPG, and antimalarials CQ and QD. They proposed a theoretical crystal growth kinetic model that endeavours to explain why these known antimalarial drugs fail to fully inhibit βH formation at low concentrations.[63] In the absence of any inhibitor, the process describing the growth of **βH** crystals from free dissolved Fe(III)PPIX designated **H(aq)** in scheme 6.1, proceeds with rate constant, ***z*** (described section 6.3.1.2). Introduction of a drug, **D**, to this system, scheme 6.1(**A**), causes this growth to proceed with a decreased rate constant, z_{obs}. The model was based on the proposal that quinoline antimalarials bind to the fastest-growing face of βH crystals , **Xs**, in process **C** of scheme 6.1 which reduces the available sites for βH growth, but is reversible.[28]

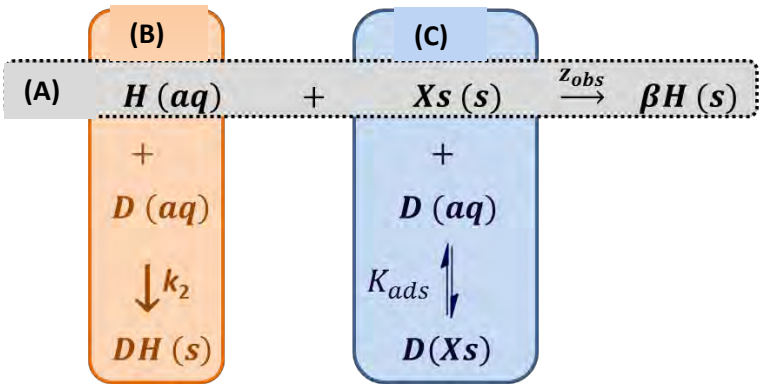

Scheme 6.1: Kinetic model to describe the inhibition of βH formation in the presence of drug, ***D***. Competing processes are depicted with rate constants $z_{obs,}$ for (**A**) growth of βH crystals at growth sites (***Xs***) from Fe(III)PPIX (***H***) in aqueous solution. k_2 and K_{ads} are respectively, the rate and adsorption equilibrium constants for (**B**) the formation of an irreversible precipitated drug+Fe(III)PPIX complex (***DH***) and (**C**) reversible drug adsorption to crystal surface growth sites to form an adsorbed drug complex, (***D*(*Xs*)**).

In the presence of a drug, **D**, which can occupy sites on the growing crystal surface, the continued growth of the βH crystal is dependent on the concentration of drug bound via the number of unoccupied sites onto which further Fe(III)PPIX molecules attach. Since, the adsorption of drug onto the βH crystal face in process **C** can be equated to the formation of a drug monolayer, the process could be modelled using the Langmuir isotherm to describe the equilibrium adsorption process. The rate constant for formation of βH in the presence of an adsorbing drug, $\boldsymbol{z_{obs}}$, is then given by Eqn. 6.2. Where, **z** is the rate constant of βH formation in the absence of drug and $(\mathbf{1}-\boldsymbol{\theta})$ refers to the number of unoccupied sites on the βH crystal.

$$\boldsymbol{z_{obs}} = \boldsymbol{z}(\mathbf{1}-\boldsymbol{\theta}) = \frac{\boldsymbol{z}}{\mathbf{1}+\boldsymbol{K_{ads}}[\boldsymbol{D}]} \qquad (6.2)$$

The adsorption equilibrium constant, $\boldsymbol{K_{ads}}$, was obtained from the slope of a plot of $\frac{\mathbf{1}}{\boldsymbol{z_{obs}}}$ versus drug concentration, **[D]** to yield a y-intercept of $\frac{\mathbf{1}}{\boldsymbol{z}}$, and slope, $\frac{\boldsymbol{K_{ads}}}{\boldsymbol{z}}$ (Eqn. 6.3.)[63]

$$\frac{\mathbf{1}}{\boldsymbol{z_{obs}}} = \frac{\boldsymbol{K_{ads}}}{\boldsymbol{z}}[\boldsymbol{D}] + \frac{\mathbf{1}}{\boldsymbol{z}} \qquad (6.3)$$

To explain the decrease in yield observed at higher drug concentrations, the complexation of free Fe(III)PPIX, **H(aq)** with drug in solution to form an insoluble drug-Fe(III)PPIX complex, **DH** (**B**), which precipitates irreversibly, thus, removing a portion of Fe(III)PPIX, **(H)** from the reaction was postulated. The theoretical kinetic curves predicted by Scheme 6.1 are presented in Fig. 6.6(a) and the effect of this additional process on the plot of $\frac{\mathbf{1}}{\boldsymbol{z_{obs}}}$ vs [D] is shown in Fig. 6.6(b). As seen in Fig. 6.4, in contrast to the lipid catalysed process, NP-40 mediated βH formation in the presence of antimalarials, CQ and QD, does not display a decrease in % yield of βH even at the highest drug concentrations. This suggests that the irreversible precipitation step (**B** in scheme 6.1) does not occur and an alternative scheme for the NP-40 mediated process holds.

(a) **(b)**

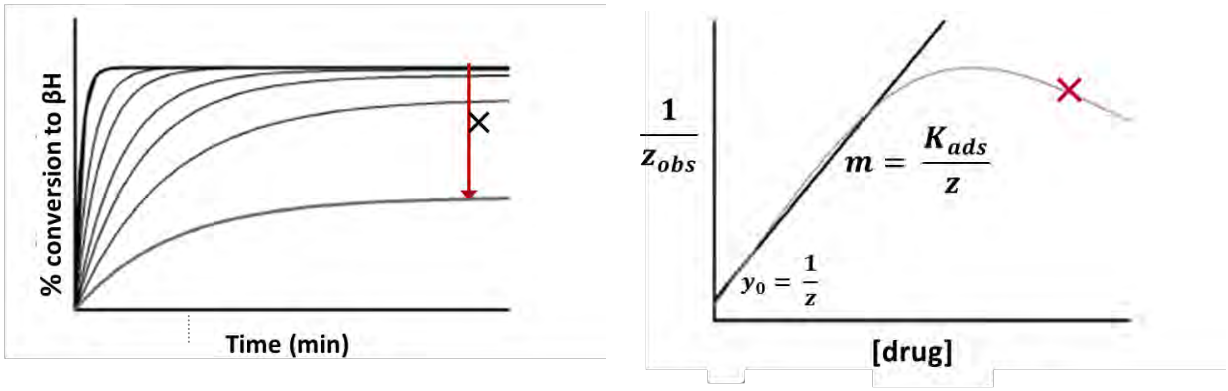

Figure 6.6(a) The theoretical prediction of the kinetics describing the conversion of Fe(III)PPIX to βH as a function of drug concentration with a decreased yield at higher drug concentrations according to scheme 6.1 as previously reported in a lipid-mediated system.[63] **(b)** Linear dependence of the inverse rate constant on drug concentration at low drug concentration. At high drug concentrations, a deviation from linearity is predicted according to scheme 6.1. The crosses indicate behaviour not observed for NP-40 mediated βH formation in the presence of drugs.

In the absence of this predicted decrease in yield, a plot of the inverse of the rate constants, $z_{obs,}$ against drug concentration was predicted to be linear. This was indeed found to be the case (Fig. 6.7).

(a) **(b)**

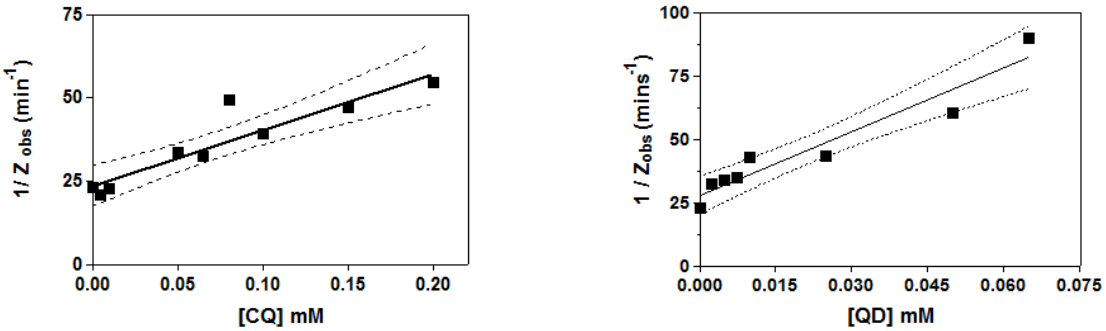

Figure 6.7: Plots of $\frac{1}{z_{obs}}$ versus **[D]** for **(a)** CQ (r^2 =0.85 , P = 1.00). P-values > 0.5 from a runs test indicate a linear plot. **(b)** QD (r^2 = 0.92, P= 0.51) log K_{ads} and z were determined from the slope and y-intercept, respectively.

It is observed in Fig. 6.7 that the dependence of $1/ z_{obs}$ on drug concentration was linear up to the highest drug concentration tested, unlike the lipid system, where at higher drug concentrations, a deviation from linearity was observed.[63] The values obtained for both drugs are listed in Table 6.2. The *z* values determined from the reciprocal y-intercepts of each graph in Fig. 6.7 are the same (within one standard deviation), having an average value of 0.039 ± 0.005 min^{-1} for βH formation in NP-40 solution. This corresponds to a half-life of 17.5 ± 0.3 min for the reaction and is comparable with the independently measured half-life of 19 ± 1 min in section 6.3.1.2 for NP-40 in the absence of drug.

Table 6.2: Adsorption and rate constants evaluated for antimalarial drugs from kinetic data obtained for NP-40 mediated βH formation.

Drug	slope x 10^3 ($min.M^{-1}$)	y-intercept (min)	K_{ads} x 10^3 (M^{-1})	log K_{ads}	*z* (min^{-1})
CQ	168 ± 27	24 ± 3	7 ± 1	3.85 ± 0.07	0.043 ± 0.005
QD	837 ± 101	28 ± 3	30 ± 4	4.48 ± 0.05	0.036 ± 0.004

Adsorption equilibrium constants, $K_{ads,}$ were calculated from the slope of the plots in Fig. 6.7 multiplied by *z*, for each drug tested, indicating that QD was more strongly adsorbed than CQ, with a higher log $K_{ads.}$ While the strength of drug adsorption of QD is similar to that reported for the lipid system, CQ was found to adsorb more strongly than QD in that system.[63]

In a possible alternative model (scheme 6.2), $K_{1,}$ is a measure of the affinity that each drug has for Fe(III)PPIX in solution. Indeed, some studies have claimed that the ability to bind Fe(III)PPIX to form a drug-Fe(III)PPIX complex is correlated to βH inhibition and even antimalarial strength.[208,230] Quinoline drugs have also been claimed to block incorporation of Fe(III)PPIX into the growing crystal by forming a drug-Fe(III)PPIX complex that exhibits superior solubility over Fe(III)PPIX in aq solution.[415] While the observed kinetics here are consistent with the proposed adsorption process in scheme 6.2(**B**), kinetic experiments are

insufficient to demonstrate this, since model (**C**) in which equilibrium association of drug with Fe(III)PPIX is mathematically indistinguishable from model (**B**).

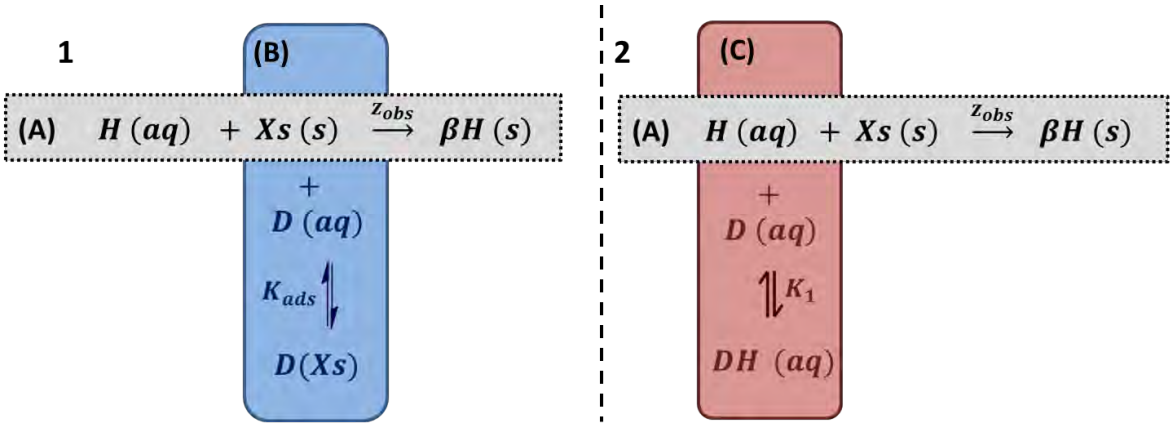

Scheme 6.2: Proposed processes to describe the kinetics of the inhibition of NP-40 mediated βH formation in the presence of drug, ***D.*** The growth of βH crystals from Fe(III)PPIX **(*H*)** in aqueous solution **(A)** is depicted with rate constants $z_{obs,}$. **(1)** The adsorption process (**B**) for the drug binding to crystal surface, ***Xs*** to form a drug+ βH crystal complex, ***D(Xs***), is described by rate constant, $K_{ads.}$ **(2)** Process **C** describes the association of drug and Fe(III)PPIX in solution to form a drug+Fe(III)PPIX complex (***DH***), the association is given by, K_1.

(6.3.4) Adsorption of antimalarial drugs to βH crystal surface

Since kinetics experiments cannot distinguish between the two models in scheme 6.2, an effort was made to directly determine whether these drugs adsorb onto pre-formed βH. βH crystals for adsorption were collected from the interface between pentanol and aq buffer according to a published procedure. [57,126] The identity of βH was confirmed using ATR-FTIR and PXRD techniques, the characteristic reflections and stretching frequencies are shown in Fig. 6.8(a) and (b), respectively.[27,44]

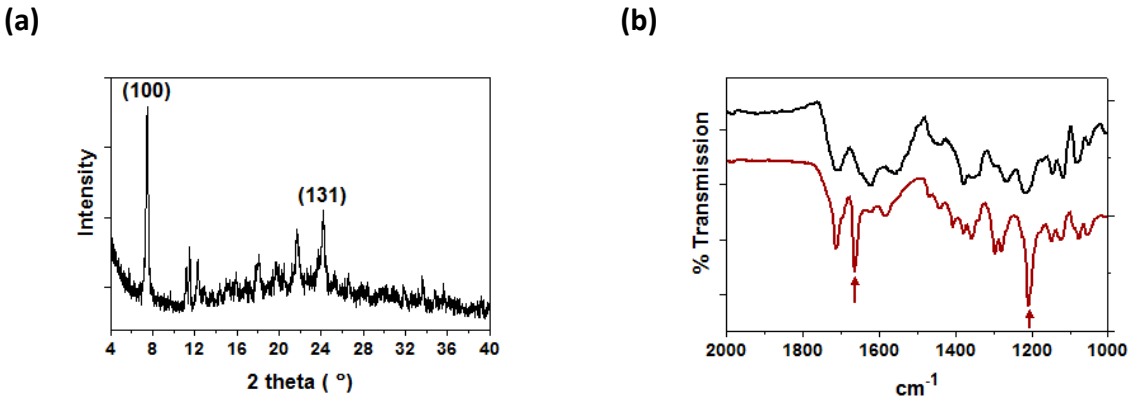

Figure 6.8 (a) PXRD pattern with the labelled characteristic (100) and (131) reflections **(b)** ATR-FTIR spectra of the starting material, Fe(III)PPIX, (black) and βH prepared at the pentanol-aq interface (red) with diagnostic stretching frequencies at 1660 and 1211 cm^{-1} indicated by red arrows.

The concentration of drug in solution pre and post-incubation with βH crystals at 37 °C was recorded using UV-vis spectroscopy (Fig. 6.9). A reduction in drug concentration was observed for both drugs which was attributed to drug adsorption to the βH crystals. No such decrease was evident in the absence of βH. Standard drug concentration curves and Beer's Law were used to generate the molar absorptivity constant, Ɛ of CQ at λ_{max} 343 nm (17 ± 1 $M^{-1}.cm^{-1}$) and QD at λ_{max} 332 nm (11.9 ± 0.9 $M^{-1}.cm^{-1}$) under the conditions employed which were used to calculate the concentration of drug adsorbed. In aq solution at 0.2 µmol drug/ mg βH added, QD has been reported to adsorb almost three times as much as CQ.[230,240] The effect of NP-40 detergent on this adsorption profile for CQ and QD was investigated.

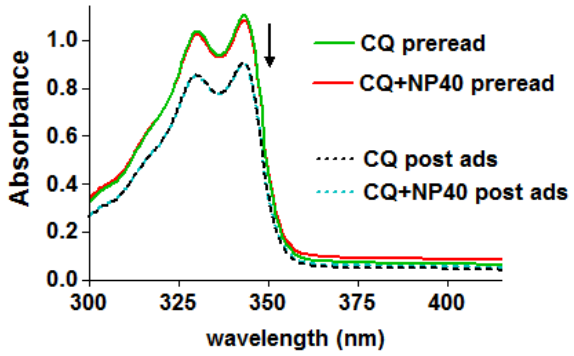

Figure 6.9 UV-vis absorbance spectra of CQ (0.05 mM) before and after a period of incubation with βH at 37 °C in the absence and presence of NP-40. The post adsorption decrease in absorbance of the CQ peak is highlighted by the black arrow.

A comparison of the concentration of drug adsorbed in the absence and presence of NP-40 at 0.2 µmol drug/ mg βH added is shown in Fig. 6.10. The presence of the NP-40 detergent at the concentration used for the kinetics experiments was determined to have no effect on the adsorption of the drugs. This indicates that the ability of this detergent to promote βH formation, centres around the initial step of the crystallisation reaction as well as any detergent-Fe(III)PPIX interactions that are relevant to its mechanism and not any association between the βH product and NP-40.

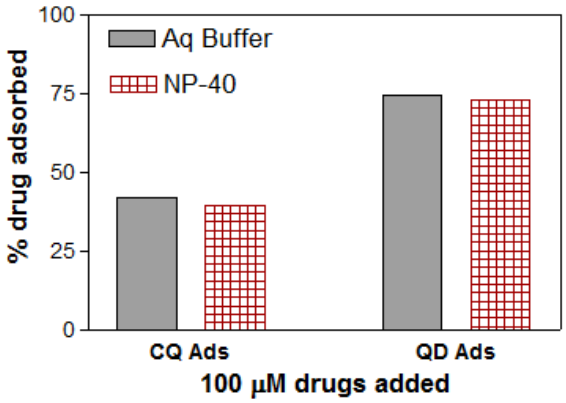

Figure 6.10 Average adsorption of antimalarials CQ (42 %) and QD (75 %) to βH crystals in the absence and presence of NP-40.

The adsorption profiles of the two drugs differ where QD displayed almost twice the adsorption of CQ. This is consistent with the measured adsorption constant from kinetics, which gave a larger value for QD.[230,240] This independent experiment confirms the stronger adsorption of QD to crystals, in both aq and detergent solution, further highlighting the differences between this system and the lipid environment.

(6.4) Summary

The neutral detergent, NP-40 was observed to initiate βH formation, doing so at rates that are at least forty times slower than that reported for the biologically prevalent neutral lipid blend.[143] Despite this, the exponential-shaped kinetic profile found closely resembles that obtained at a neutral lipid-aq interface and similarly, the data was also found to fit the Avrami equation, with n = 1, correlating to a random nucleation mechanism and one-dimensional crystal growth that results in linear βH crystals.[63] The yields of βH formed with NP-40 were approximately 56% compared to 80% conversion for the neutral lipid blend. While the kinetics are slower and less efficient in NP-40 solution than at a lipid-aq interface, βH is still formed, fortuitously at half-life times that are sufficiently slow to study the efficacy of inhibitory drugs tested *in vitro*.

The inhibitory activity of the 4-aminoquinoline drug, CQ and quinoline-methanol, QD was determined from the dose-dependent kinetic data at 90 min incubation time and the trend in activity observed correlates with that found for previously reported biological-activities against a CQ-sensitive parasite strain.[239] Detailed kinetics of each drug over the concentration range 0-0.2 mM were also investigated to afford z_{obs}, the rate constant of βH formation in the presence of drug. z_{obs} was found to decrease in a dose-dependent manner for both drugs, but the same final % yield of βH after 6 h was consistently achieved. The inhibition reaction in NP-40 solution was thus concluded to be reversible at extended incubation times under the drug concentrations tested, with no precipitation of a drug-Fe(III)PPIX complex detected.

To explain the observed decrease in the rate βH formation in the presence of drug, a model utilised for the lipid-aq system was simplified, incorporating only the possibility of a competing reaction involving the adsorption of drugs to βH for the NP-40 system. In the NP-40 system, the decrease in rate constant of βH formation found to be caused by antimalarials, CQ and QD, could be used to measure the adsorption of these drugs to a βH crystal face. The strength of this adsorption, determined from both the kinetics data and an independent experiment, was larger for QD than CQ. This time dependence is important to be aware of when using detergents as βH initiators for assaying potential βH inhibition

activity at different incubation times can affect the IC_{50} obtained. Indeed, this has been observed for other βH inhibition assays.[253]

Kinetic experiments do not provide a conclusive means to distinguish between mechanisms. Thus the possibility that an association between Fe(III)PPIX and these drugs in solution, which may be responsible for their reported antimalarial activity, could not be discounted. The adsorption was, however, directly detected by depletion of the drugs from solution by βH. This work serves to illustrate the differences in behaviour of the detergent system versus the lipid droplet system when mediating βH formation and need be considered when assaying for potential βH inhibitors, using detergents. While the two systems are similar, they are clearly not identical.

Chapter 7: Conclusions and Future Work

(7.1) Overall conclusion

Achieving the sustainable development goal of complete malaria eradication is a priority for improved healthcare in the ninety-seven affected countries, the majority of which are on the African continent. With the emergence of widespread resistance to frontline drug treatments and the complications of co-infections, the need to develop novel and targeted drug therapies is still relevant.[416] During the intraerythrocytic stage of its life-cycle, the malaria parasite is thought to convert at least 80% of the host's red blood cell ferriprotoporphyrin IX (Fe(III)PPIX) into the crystal, haemozoin (Hz) inside an acidic organelle called the digestive vacuole (DV).[16] Hz is composed of hydrogen bonded cyclic dimers of Fe(III)PPIX coordinated through the propionic acid of one porphyrin ring to the Fe(III) of the other porphyrin in a reciprocal fashion (μ-propionato dimers).[27] The precise steps involved in the biomineralisation of the potentially toxic, Fe(III)PPIX, to the relatively benign, Hz crystal, are yet to be elucidated, however, this parasite specific pathway represents a unique drug target with a significant success rate.[417] To understand the mechanism of Hz formation, *in vivo*, pertinent questions about the state of Fe(III)PPIX under the acidic pH conditions that prevail in the parasite DV, need be addressed. Furthermore, as a growing amount of recent evidence suggests that lipids are involved in the biomineralisation process, further insight into their possible roles was necessary. Despite mixed proposals on the specific type and location of lipid involved in this process, recent works have identified a unique blend of neutral acylglycerol lipid droplets (NLBDs) present in the DV to efficiently mediate biologically relevant concentrations of Hz formation.[113,124] This thesis aimed to provide some understanding of the interaction between Fe(III)PPIX and the proposed NLBDs that have been reported to be associated with Hz, *in vivo.*

To achieve this, Chapter 4 measured the extent of Fe(III)PPIX quenching of nile red (NR) labelled NLBDs. The results presented there have shown that soluble Fe(III)PPIX is lipophilic and capable of partitioning into synthetic NLBDs in a pH dependent manner. This pH dependence was found to reflect the ionisation state of Fe(III)PPIX in solution as the largest proportion of Fe(III)PPIX partitioning and NR quenching was observed for the neutral species at approximately the pH of the parasite DV (pH 4.80) which coincidently correlated with the

reported pH dependence of neutral lipid mediated β-haematin (βH) formation.[127] A plot of the inverse of the Stern-Volmer quenching constant, K_{SV}^{-1}, against pH was found to fit a single-step protonation model with a pK_{a1} of 4.62 ± 0.09 for Fe(III)PPIX. Validation of the lipophilicity of Fe(III)PPIX was provided by measurement of the octanol-water partition coefficient at pH 7.5. The charged form of Fe(III)PPIX at pH 7.5 was found to be lipophilic with a log D_{ow} of 1.8 corresponding to a log P of 2.8 for the still more lipophilic unionised form. This represented a 400-fold accumulation of neutral Fe(III)PPIX in SNLBDs compared to the aqueous bulk medium. This study confirmed that Fe(III)PPIX prefers a non-aqueous environment, which is capable of facilitating its conversion to βH.

The 4-amino quinoline drugs, chloroquine (CQ) and amodiaquine (AQ) were shown to form charged complexes with Fe(III)PPIX that decreased the proportion of Fe(III)PPIX partitioned into SNLBDs with no pH dependence observed over the range investigated. Conversely, the quinoline-methanol drugs, quinidine (QD) and quinine (QN) were found to form neutral drug-Fe(III)PPIX complexes at low pH that readily partition into SNLBDs. This increased partitioning was found to persist up to pH 8.5 after which, both the quinuclidine and quinoline ring nitrogens are deprotonated, resulting in a charged drug-Fe(III)PPIX complex that exhibited less partitioning. QD was found to effect the greatest increase in lipid partitioning of Fe(III)PPIX which was thought to arise from the lower strain energy associated with the formation of a pre-established intramolecular hydrogen bond between the $^{+}$NH of the drug quinuclidine ring and the COO^{-} of a Fe(III)PPIX propionate group.[228] This suggests that QD possesses a degree of preorganisation to adopt the folded conformation which has been shown to increase lipophilicity that is absent for its diastereomer, QN.[367] These data suggest that these two different families of quinoline antimalarials affect the lipophilicity of Fe(III)PPIX according to the types of complexes they form with Fe(III)PPIX in a lipid environment. While it appears that the biological activity of the more effective 4-aminoquinolines over the quinoline methanol drugs can be rationalised by their effect of decreasing Fe(III)PPIX partitioning, a systematic study on antimalarials of variable potency and their lipophilicity effects would need to be made to confirm this.

The use of an established lipophilic fluorophore, NR, to monitor Fe(III)PPIX partitioning into NLBDs represents a unique model system to study Fe(III)PPIX metabolism in other systems. This methodology provides a biologically relevant indication of how Fe(III)PPIX interacts with

lipids over a pH range that can be useful when applied to the different blood-feeding organisms or other Fe(III)PPIX associated diseases.

For many years, a poor understanding of the complicated speciation of Fe(III)PPIX in solution has hampered the understanding of its self-association to form the μ-propionato dimer that comprises the unit cell of a βH crystal. Furthermore, the colloidal nature of the biological lipid blend was found to incur a large amount of light-scatter and thus rendered spectroscopic characterisation of Fe(III)PPIX in this environment difficult. Several assays for screening potential βH inhibitors employ neutral detergents as lipid 'mimics' to induce crystallisation of Fe(III)PPIX though no studies into the way in which they do this have been reported.[154,155,175] Fe(III)PPIX in amphiphilic detergent solution represents an environment where common spectroscopic techniques can be used to investigate the structural implications of this environment on the potentially complicated state of Fe(III)PPIX. Chapter 5 focussed on illuminating the nature of Fe(III)PPIX in several detergent solutions both above and below their critical micellar concentration (CMC). The prevailing Fe(III)PPIX species at approximately the pH of the DV and cytosol in detergent solutions were characterised by analysis of the characteristic UV-visible absorbance spectra with qualitative comparison to that of known Fe(III)PPIX species. Magnetic susceptibility measurements were used to confirm the spin-state and anti-ferromagnetic coupling of the central Fe(III) atom in each solution. Contrary to previous literature reports, detergent solutions were found to induce varied speciation of Fe(III)PPIX in solution and not just the monomeric form as previously thought.[377,379] The neutral and zwitterionic detergents TWEEN-20, NP-40 and CHAPS, at both concentrations were found to stabilise the predominant aqueous species of Fe(III)PPIX, the π-π dimer, at acidic pH. Contrastingly, the anionic and cationic charged detergents, SDS and CTAB, respectively, were observed to induce the monomer form of Fe(III)PPIX in acidic solution. Specifically, SDS induced the monomeric form of Fe(III)PPIX throughout the pH range investigated exhibiting a change in the axial ligand (from H_2O to ^{-}OH) while at the approximate pH of the DV, CTAB was found to stabilise a mixture of the monomer with the ^{-}OH axial ligand and the μ-oxo dimer species. With the exception of SDS, all the other detergent solutions were shown to stabilise the antiferromagnetic μ-oxo dimer species at basic pH.[224]

A correlation was observed between the observed ability of neutral and zwitterionic detergents to promote the π-π dimer Fe(III)PPIX species in solution and the successful mediation of βH formation at 37°C and pH 4.80. Previous studies have proposed that detergents, long-chain alcohols and polyethylene glycols induce βH formation by solubilising Fe(III)PPIX in acidic solution and facilitating loss of the H_2O axial ligand to form the μ-propionato βH precursor in a non-aqueous environment.[148,150] While all the detergents tested were able to solvate Fe(III)PPIX in acetate solution, with a measured decrease in the surface tension of the detergent solutions, not all the detergents were able to promote βH formation under these conditions. The charged detergents that favoured formation of the monomer or a monomer/ μ-oxo dimer mixture at the DV pH were found not to promote βH formation. This correlation of the prevalence of the π-π dimer species as a precursor to βH formation in lipophilic solution has been previously suggested and explored using MD simulations, from which the authors reported that conversion from the π-π dimer to the μ-propionato dimer of βH is easily facilitated in the non-aqueous environment.[57]

Using preliminary ^{1}H NMR and fluorescence quenching of NR fluorescence in neutral detergent, TWEEN-20 micelles, Fe(III)PPIX was shown to partition into these micelles at neutral pH. These data tentatively indicate that the π-π dimer Fe(III)PPIX species is located inside the hydrophobic detergent micelle in solution. Whether this partitioning is essential for βH formation remains unclear as the surface tension measurements, UV-visible spectra and βH formation tests indicate that there is little difference between the detergent solutions at the concentrations above and below their observed CMC. This observation may be correlated to the existence of pre-micellar detergent aggregates in solutions that occur below the detergent's measured CMC.[167]

Nevertheless, while Fe(III)PPIX partitioning into detergent micelles or association with the hydrophobic regions of premicellar aggregates may occur, the detergent's ability to interact with Fe(III)PPIX and affect its speciation appears to be weaker than that of quinoline antimalarial drugs. CQ has been shown to induce and strongly associate with the μ-oxo dimer form of Fe(III)PPIX in aqueous solution at pH 7.4.[224] It was shown here that the neutral detergents ability to stabilise the π-π dimer species at even basic pH solution, failed to affect this association. The value of log $K_{obs_{pH\ 7.5}}$ was measured at 13.50 ± 0.02 in NP-40 (below

CMC) with almost no difference to the reported value of 13.3 ± 0.2 in aqueous solution. The stoichiometry of CQ-Fe(III)PPIX association was found to be 1:2 in both aqueous and detergent solution. Similarly, the association of QD and QN with monomeric Fe(III)PPIX was found to be unaffected by this detergent.[230]

In light of these findings, in Chapter 6, the kinetics of NP-40 mediated βH formation in the absence and presence of drugs, CQ and QD, was investigated. Of particular relevance was the detergent ability to mimic the model lipid suspension in which the kinetics of βH formation have been measured and reported.[63] The neutral detergent was found to induce βH formation with a half-life, $t_{1/2}$ of 19 ± 1 min which was at least forty times slower than that reported for the NLBDs. Despite this decrease in rate constant, the kinetic profile was found to match the reported exponential-shape for the neutral lipid. The data was likewise found to fit the Avrami equation with an Avrami constant of *n*=1 corresponding to instantaneous nucleation and linear growth to form βH crystals. Both drugs were found to decrease the rate of NP-40 mediated βH formation in a concentration dependent manner. However, the observed decrease in rate constants of βH formation with both drugs was not found to lead to an eventual decrease in βH yield in the NP-40 detergent system. This was a deviation from the kinetic model outlined for the lipid system where an increase in drug concentration was accompanied by an eventual decrease in the yield of βH formed.[63]

In the lipid system, Fe(III)PPIX was proposed to associate irreversibly with the drugs to form a drug-Fe(III)PPIX complex at high concentration that precipitated out of solution. Furthermore the quinoline antimalarials were shown to adsorb to the fastest growing surface of the βH crystal with rate constant, log K_{ads}. While no precipitation of a drug-Fe(III)PPIX complex was observed in the detergent system, the observed decrease in equilibrium constant in the presence of antimalarials was shown to arise from the independently measured adsorption of these drugs to the βH crystal surface. QD, with a log K_{ads} of 4.48 ± 0.05 was found to exhibit a stronger adsorption constant than CQ with log K_{ads} of 3.85 ± 0.07. While kinetic experiments cannot distinguish between mechanisms in solution and the interaction of these drugs with Fe(III)PPIX has been established in this detergent solution, the results indicated that the neutral detergent prevented the proposed precipitation of the drug-Fe(III)PPIX complex, favouring the adsorption pathway for inhibition, which was thus observed to be reversible. This finding represents a key difference

between the NLBD system and the neutral detergent 'mimic', which may be sufficient as an initiator of crystallisation for screening inhibition potential but should be cautiously used to infer lipid mechanisms of action.

In the rational design and identification of novel antimalarials, a sound understanding of the mechanisms by which known drugs act is essential. While no definitive mechanism of action for all the quinoline antimalarials has been established, a number of physicochemical factors affecting their interaction with Fe(III)PPIX need be considered. This work highlights the importance of; (1) the ability of drugs to affect Fe(III)PPIX partitioning into neutral lipids, (2) the dominance of drug-Fe(III)PPIX association with regards to Fe(III)PPIX speciation in aqueous and lipophilic environments and (3) the ability of these drugs to decrease the rate of βH formation in detergent solution by adsorbing onto the surface of βH crystals in a manner that may be attributed to their mechanism of action.

Finally, some important questions about the Hz formation pathway have been addressed here. In a review by Pisciotta and Sullivan, the authors question the state of Fe(III)PPIX prior to crystallisation and ponder whether drug-Fe(III)PPIX complexes can still make crystal dimers from solution, among other pertinent questions about the mechanism of Hz crystal formation and drug-Fe(III)PPIX complexation.[132] While, the state of Fe(III)PPIX in neutral detergent solution under acidic pH conditions can only be tentatively compared to the *in vivo* Fe(III)PPIX speciation that prevails as a result of the likely association with a lipid environment in the parasite DV, this work shows that Fe(III)PPIX speciation is affected by a lipophilic association and the neutral detergents that do promote Fe(III)PPIX crystallisation, do so from the π-π dimer species of Fe(III)PPIX. Significant correlation between the π-π dimer species of Fe(III)PPIX in acidic solution from which βH was formed led to the conclusion that this species and not the μ-oxo dimer or monomeric forms of Fe(III)PPIX, serves as a precursor to the βH formation pathway. However, the question of whether this species is the nucleating species of βH still remains unanswered.

While it has been shown that Fe(III)PPIX readily partitions into NLBDs and detergent micelles, one cannot assume that this hydrophobic environment is necessarily the location of Hz formation *in vivo,* since detergent solutions were found equally capable of stabilising the π-π dimer and promoting βH formation below their CMC presumably from proposed

non-aqueous regions comprised of pre-micellar aggregates. The kinetics experiments in this neutral detergent environment, also show that while quinoline antimalarial-Fe(III)PPIX complexes may form in solution, the drugs appear to act chiefly by slowing the rate of crystallisation through drug adsorption to the crystal in a mechanism that is observed to be reversible. This thesis contributes toward a growing understanding of the mechanism of Hz formation in the context of Fe(III)PPIX behaviour in lipophilic solution, several key insights to the role of this non-aqueous environment in the crystallisation process have been identified.

(7.2) Future Work

The observed ability of Fe(III)PPIX to partition into SNLBDs raises an interesting question as to the precise location of Hz formation. Both free acylglycerol lipid droplets[143] and DV membrane phospholipids[131] have been shown to induce βH formation and are proposed to be the site of Fe(III)PPIX crystallisation.[126] To explore the alternative proposal, it is suggested that Fe(III)PPIX quenching studies of NR labelled phospholipids be performed to (a) determine if the zwitterionic DV membrane phospholipids form lipid droplets with a hydrophobic interior which soluble Fe(III)PPIX is capable of partitioning into. And (b), to establish if the potential Fe(III)PPIX partitioning into phospholipids is also pH dependent in a manner that corresponds to βH formation.

On the other hand, while Fe(III)PPIX has been shown to be lipophilic, this does not directly imply that Hz formation occurs inside a lipid but may only require the lipid-aqueous interface for facilitating crystallisation. Hence an investigation into the behaviour of Fe(III)PPIX at lipid-aqueous interfaces is proposed. Several reports of βH formation and inhibition in such solutions have been published however, none offer the comprehensive account of Fe(III)PPIX speciation provided here for detergent solutions. While the qualitative assignment of Fe(III)PPIX speciation in these solutions is not feasible using UV-visible spectroscopy due to the observed light scatter associated with lipid solutions, the magnetic susceptibility of Fe(III)PPIX isolated from deuterated lipid-aqueous interfaces can be measured and used to assign the induced spin-state of Fe(III) to infer the dominant speciation. Similarly, the effect of addition of the quinoline antimalarials to the measured magnetic moment in these solutions under biomimetic conditions may provide definitive conclusions about their ability to shift the Fe(III)PPIX speciation equilibrium upon complexation.

While neutral detergents may not provide an exact mimic of the environment of the NLBD, they still represent a viable lipophilic solution in which studies on drug-Fe(III)PPIX complexation may be conducted. To date very few reports on the association of quinoline drugs and other βH inhibitors with Fe(III)PPIX in aqueous solution exist. It is suggested that neutral detergent solution can be used as a suitable medium for measurements of drug-

Fe(III)PPIX association constants. Furthermore, the proposed ability of these detergents to solubilise Fe(III)PPIX at low pH, may allow for collection of this data at the pH of the DV.

Recent investigations of another biomineralisation process, formation of bone apatite from calcium phosphate solution, provided a large degree of insight into the nucleation mechanism (classical and non-classical) of the crystal using vitrified samples analysed by cryo transmission electron microscopy (cryo-TEM) and dual-axis cryo electron tomography.[418,419] Direct comparison of the morphological changes in calcium phosphate was coupled to measurements of the changes in polydispersity and zeta-potentials over time which enabled study of the aggregation state during crystallisation. While it is acknowledged that the Fe(III)PPIX system is not the same as the calcium phosphate system, it is proposed that the neutral lipid mediated transformation of amorphous Fe(III)PPIX to crystalline βH could possibly be monitored using these techniques. Addition of a quinoline antimalarial would be required to decrease the rate of crystallisation allowing for a suitable time-period of study. Fortuitously, the proposed adsorption of these drugs to the growing crystal surface may be visualised using these techniques.

A large limitation of this work is that all experiments were performed on synthetic neutral lipids, lipid mimics and *in vitro* preparations of Fe(III)PPIX and drug solutions. In support of the conclusions provided, a correlation between the observed *in vitro* behavior with *in vivo* studies on the state of Fe(III)PPIX in the parasite DV is proposed. Advances in the application of existing laser resonance Raman spectroscopy techniques to resolve the signal from monomeric Fe(III)PPIX that would be distinguishable from Hz may potentially provide this validation through evaluation of *in situ* changes in Fe(III)PPIX speciation prior to and after Hz formation.[420] The finding that βH forms from the π-π dimer form of Fe(III)PPIX in neutral detergent solution can be explored in parasite samples potentially providing a definitive species of Fe(III)PPIX to target for inhibition of Hz formation. Furthermore, increased understanding of the process of βH nucleation may lead to elucidation of its mechanism of formation.

References

1. R. Carter and K. N. Mendis, *Clin. Microbiol. Rev.*, 2002, **15**, 564–594.

2. *World Malaria Report 2014* ,World Health Organization, Geneva, Switzerland, 2014. http://www.who.int/malaria/publications/world_malaria_report_2014/en/, (Accessed 10/03/2015)

3. E. W. Johansson, H. Newby, and R. Steketee, *Roll Back Malaria, World Malaria Day 2010: Africa Update*, UNICEF, Geneva, Switzerland, 2010, www.rollbackmalaria.org, (Accessed 10/03/2015)

4. *Strategy for the selection and early development of combination drugs for the treatment of uncomplicated P. falciparum malaria,* Medicines for Malaria, Geneva, Switzerland , 2010. (Accessed 11/03/2015)

5. P. Byakika-Kibwika, E. Ddumba, and M. Kamya, *Afr. Health Sci.*, 2007, **7**, 86–92.

6. D. E. Goldberg, R. F. Siliciano, and W. R. Jacobs, *Cell*, 2012, **148**, 1271–83.

7. J. Cox-Singh, T. M. E. Davis, K.-S. Lee, S. S. G. Shamsul, A. Matusop, S. Ratnam, H. A. Rahman, D. J. Conway, and B. Singh, *Clin. Infect. Dis.*, 2008, **46**, 165–171.

8. M. Delves, D. Plouffe, C. Scheurer, S. Meister, S. Wittlin, E. A. Winzeler, R. E. Sinden, and D. Leroy, *PLoS Med.*, 2012, **9**, e1001169.

9. R. Ménard, J. Tavares, I. Cockburn, M. Markus, F. Zavala, and R. Amino, *Nat. Rev. Microbiol.*, 2013, **11**, 701–12.

10. M. Prudêncio, A. Rodriguez, and M. M. Mota, *Nat. Rev. Microbiol.*, 2006, **4**, 849–856.

11. F. Ehlgen, J. S. Pham, T. de Koning-Ward, A. F. Cowman, and S. A. Ralph, *PLoS One*, 2012, **7**, e38781.

12. P. G. McQueen and F. E. McKenzie, *PLoS Comput. Biol.*, 2008, **4**, e1000149.

13. P. M. Andrysiak, W. E. Collins, and G. H. Campbell, *Infect. Immun.*, 1986, **54**, 609–612.

14. L. D. Sibley, *Science*, 2004, **304**, 248–253.

15. P. Loria, S. Miller, M. Foley, and L. Tilley, *Biochem. J.*, 1999, **339**, 363–370.

16. T. J. Egan, J. M. Combrinck, J. Egan, G. R. Hearne, H. M. Marques, S. Ntenteni, B. T. Sewell, P. J. Smith, D. Taylor, D. A. van Schalkwyk, and J. C. Walden, *J. Biochem.*, 2002, **365**, 343–347.

17. V. L. Lew, T. Tiffert, and H. Ginsburg, *Blood*, 2003, **101**, 4189.

18. P. J. Rosenthal and S. R. Meshnick, *Mol. Biochem. Parasitol.*, 1996, **83**, 131–139.

19. R. Banerjee, J. Liu, W. Beatty, L. Pelosof, M. Klemba, and D. E. Goldberg, *Proc. Natl. Acad. Sci. U. S. A.*, 2002, **99**, 990–995.

20. I. Y. Gluzman, S. E. Francis, A. Oksman, C. E. Smith, K. L. Duffin, and D. E. Goldberg, *J. Clin. Invest.*, 1994, **93**, 1602–1608.

21. G. H. Coombs, D. E. Goldberg, M. Klemba, C. Berry, J. Kay, and J. C. Mottram, *Trends Parasitol.*, 2001, **17**, 532–537.

22. K. K. Eggleson, K. L. Duffin, and D. E. Goldberg, *J. Biol. Chem.*, 1999, **274**, 32411–32417.

23. I. W. Sherman and L. Tanigoshi, *Int. J. Biochem.*, 1970, **1**, 635–637.

24. M. Krugliak, J. Zhang, and H. Ginsburg, *Mol. Biochem. Parasitol.*, 2002, **119**, 249–256.

25. J. M. Rifkind and E. Nagababu, *Antioxid. Redox Signal.*, 2012, 18, 2274–2283.

26. M. Paoli, R. Liddington, J. Tame, A. Wilkinson, and G. Dodson, *J.Mol.Biol.*, 1996, **256**, 775.

27. S. Pagola, P. W. Stephens, D. S. Bohle, A. D. Kosar, and S. K. Madsen, *Lett. to Nat.*, 2000.

28. R. Buller, M. L. Peterson, Ö. Almarsson, and L. Leiserowitz, *Cryst. Growth Des.*, 2002, **2**, 553–562.

29. T. J. Egan, *Mol. Biochem. Parasitol.*, 2008, **157**, 127–36.

30. C. D. Fitch and P. Kanjananggulpan, *J. Biol. Chem.*, 1987, **262**, 15552–15555.

31. S. Ohkuma and B. Poole, *Proc. Natl. Acad. Sci.*, 1978, **75**, 3327–3331.

32. R. Hayward, K. J. Saliba, and K. Kirk, *J. Cell Sci.*, 2006, **119**, 1016–25.

33. A. Radfar, A. Diez, and J. M. Bautista, *Free Radic. Biol. Med.*, 2008, **44**, 2034–2042.

34. K. Becker, L. Tilley, J. L. Vennerstrom, D. Roberts, S. Rogerson, and H. Ginsburg, *Int. J. Parasitol.*, 2004, **34**, 163–189.

35. D. Monti, N. Basilico, S. Parapini, E. Pasini, P. Olliaro, and D. Taramelli, *FEBS Lett.*, 2002, **522**, 3–5.

36. S. Kumar and U. Bandyopadhyay, *Toxicol. Lett.*, 2005, **157**, 175–188.

37. V. Jeney, J. Balla, A. Yachie, Z. Varga, G. M. Vercellotti, J. W. Eaton, and G. Balla, *Blood*, 2002, **100**, 879–887.

38. N. Campanale, C. Nickel, C. . Daubenberger, D. . Wehlan, J. J. Gorman, N. Klonis, K. Becker, and L. Tilley, *J. Biol. Chem.*, 2003, **278**, 27354–27361.

39. M. Sirover, *Biochim. Biophys. Acta*, 1999, **1432**, 159–184.

40. S. E. Francis, D. J. Sullivan, and D. E. Goldberg, *Annu. Rev. Microbiol.*, 1997, **51**, 97–123.

41. M. D. Maines, *FASEB J.*, 1988, **2**, 2557–2568.

42. A. Hamsik, *Zeitschrift für Physiol. Chemie*, 1936, **190**, 199–215.

43. T. J. Egan, in *On Biomimetics*, ed. L. Pramatarova, InTech Europe, Rijeka, 1st edn., 2011, pp. 373–394.

44. A. F. G. Slater, W. J. Swiggard, B. R. Ortonf, W. D. Flitter, D. E. Goldberg, A. Cerami, and G. B. Henderson, *Proc. Natl. Acad. Sci.*, 1991, **88**, 325–329.

45. D. S. Bohle, R. E. Dinnebier, S. K. Madsen, and P. W. Stephens, *J. Biol. Chem.*, 1997, **272**, 713–716.

46. S. Kapishnikov, a. Weiner, E. Shimoni, P. Guttmann, G. Schneider, N. Dahan-Pasternak, R. Dzikowski, L. Leiserowitz, and M. Elbaum, *Proc. Natl. Acad. Sci.*, 2012, **109**, 11188–11193.

47. D. S. Bohle, P. Debrunner, P. A. Jordan, S. K. Madsen, and C. E. Schulz, *J. Am. Chem. Soc.*, 1998, **120**, 8255–8256.

48. D. S. Bohle, A. D. Kosar, and P. W. Stephens, *Acta Crystallogr. Sect. D Biol. Crystallogr.*, 2002, **58**, 1752–1756.

49. D. Taramelli, D. Monti, F. Omodeo-Salè, N. Basilico, S. Parapini, E. Pasini, L. Lombardi, and P. Olliaro, *Parassitologia*, 2001, **43**, 45–50.

50. D. S. Bohle, A. D. Kosar, and S. K. Madsen, *Biochem. Biophys. Res. Commun.*, 2002, **294**, 132–135.

51. P. Hartman and W. G. Perdok, *Acta Crystallogr.*, 1955, **8**, 525–529.

52. T. Straasø, A. Tkatchenko, S. Kapishnikov, L. Kronik, and L. Leiserowitz, *Cryst. Growth Des.*, 2011, **11**, 3332–3341.

53. T. Straasø, N. Marom, I. Solomonov, L. K. Barfod, M. Burghammer, R. Feidenhans'l, J. Als-Nielsen, and L. Leiserowitz, *Cryst. Growth Des.*, 2014, **14**, 1543–1554.

54. D. S. Bohle, E. L. Dodd, and P. W. Stephens, *Chem. Biodivers.*, 2012, **9**, 1891–1902.

55. N. Klonis, R. Dilanian, E. Hanssen, C. Darmanin, V. Streltsov, S. Deed, H. Quiney, and L. Tilley, *Biochemistry*, 2010, **49**, 6804–11.

56. M. Walczak, K. Lawniczak-Jablonska, A. Sienkiewicz, I. N. Demchenko, E. Piskorska, G. Chatain, and D. S. Bohle, *Nucl. Instruments Methods Phys. Res. Sect. B Beam Interact. with Mater. Atoms*, 2005, **238**, 32–38.

57. T. J. Egan, J. Y.-J. J. Chen, K. A. de Villiers, T. E. Mabotha, K. J. Naidoo, K. K. Ncokazi, S. J. Langford, D. McNaughton, S. Pandiancherri, and B. R. Wood, *FEBS Lett.*, 2006, **580**, 5105–10.

58. M. F. Oliveira, S. W. Kycia, A. Gomez, A. J. Kosar, D. S. Bohle, E. Hempelmann, D. Menezes, M. A. Vannier-Santos, P. L. Oliveira, and S. T. Ferreira, *FEBS Lett.*, 2005, **579**, 6010–6.

59. M. S. Walczak, K. Lawniczak-Jablonska, a. Sienkiewicz, M. T. Klepka, L. Suarez, a. J. Kosar, M. J. Bellemare, and D. S. Bohle, *J. Non. Cryst. Solids*, 2010, **356**, 1908–1913.

60. M. S. Walczak, K. Lawniczak-jablonska, A. Wolska, M. Sikora, A. Sienkiewicz, L. Su, A. J. Kosar, M. Bellemare, and D. S. Bohle, *J. Phys. Chem. B*, 2011.

61. K. Begum, H.-S. Kim, V. Kumar, I. Stojiljkovic, and Y. Wataya, *Parasitol. Res.*, 2003, **90**, 221–224.

62. D. S. Bohle and E. L. Dodd, *Inorg. Chem.*, 2012, **51**, 4411–4413.

63. J. Gildenhuys, T. Le Roex, T. J. Egan, and K. A. De Villiers, *J. Am. Chem. Soc.*, 2013, **135**, 1037–1047.

64. D. S. Bohle, E. L. Dodd, A. J. Kosar, L. Sharma, P. W. Stephens, L. Suárez, and D. Tazoo, *Angew. Chemie - Int. Ed.*, 2011, **50**, 6151–6154.

65. B. R. Wood, S. J. Langford, B. M. Cooke, J. Lim, F. K. Glenister, M. Duriska, J. K. Unthank, and D. Mcnaughton, 2004, **3**, 9233–9239.

66. K. A. de Villiers, C. H. Kaschula, T. J. Egan, and H. M. Marques, *J. Biol. Inorg. Chem.*, 2007, **12**, 101–17.

67. T. J. Egan, W. W. Mavuso, and K. K. Ncokazi, *Biochemistry*, 2001, **40**, 204–213.

68. M. P. Crespo, L. Tilley, and N. Klonis, *J. Biol. Inorg. Chem.*, 2010, **15**, 1009–22.

69. D. Kuter, V. Streltsov, N. Davydova, G. A. Venter, K. J. Naidoo, and T. J. Egan, *Inorg. Chem.*, 2014, **53**, 10811–10824.

70. P. A. Adams, P. M. Berman, T. J. Egan, P. J. Marsh, and J. Silver, *J. Inorg. Biochem.*, 1996, **63**, 69–77.

71. T. J. Egan and H. M. Marques, *Coord. Chem. Rev.*, 1999, **190-192**, 493–517.

72. C. Asher, K. A. de Villiers, and T. J. Egan, *Inorg. Chem.*, 2009, **48**, 7994–8003.

73. J. Shack and W. M. Clarke, *J. Biol. Chem.*, 1947, **171**, 143–187.

74. J. E. Falk, *PORPHYRINS A N D METALLOPORPHYRINS*, Elsevier Scientific Publishing Company, Amsterdam, The Netherlands, Amsterdam, 1975.

75. G. Blauer and H. Rottenberg, *Acta Chem. Scand.*, 1963, **17**, S216–221.

76. B. S. B. Brown, T. C. Dean, and P. Jones, *Biochem. J.*, 1970, **117**, 733–739.

77. E. B. Fleischer and T. S. Srivastava, *Jacs*, 1968, **1725**, 2403–2405.

78. G. Blauer and B. Zvilichovsky, *Arch. Biochem. Biophys.*, 1968, **127**, 749–755.

79. G. Blauer and B. Zvilichovsky, *Biochim. Biophys. Acta - Protein Struct.*, 1970, **221**, 442–449.

80. R. F. Pasternack, P. R. Huber, P. Boyd, G. Engasser, L. Francesconi, E. Gibbs, P. Fasella, G. Cerio Venturo, and L. C. de Hinds, *Jacs*, 1972, **94**, 4511–4517.

81. K. Shibata and Y. Inada, *Biochem. Biophys. Res. Commun.*, 1962, **9**, 323–327.

82. H. Goff and L. O. Morgan, *Inorg. Chem.*, 1976, **15**, 3180–3181.

83. S. B. Brown, P. Jones, and I. R. Lantzke, *Nature*, 1969, **223**, 960–961.

84. E. B. Fleischer, J. M. Palmer, T. S. Srivastava, and A. Chatterjee, *J. Am. Chem. Soc.*, 1971, **93**, 3162–3167.

85. M. O. Senge, in *The Porphyrin Handbook*, eds. K. M. Kadish, R. Guilard, and K. M. Smith, Academic Press, New York, Volume 10., 2000, p. 254.

86. K. S. Murray, *Coord. Chem. Rev.*, 1974, **12**, 1–35.

87. L. Cheng, J. Lee, D. R. Powell, and G. B. Richter-Addo, *Acta Crystallogr. Sect. E Struct. Reports Online*, 2004, **60**, 1340–1342.

88. D. H. O'Keeffe, C. H. Barlow, G. A. Smythe, W. H. Fuchsman, T. H. Moss, H. R. Lilienthal, and W. S. Caughey, *Bioinorg. Chem.*, 1975, **5**, 125–47.

89. L. B. Dugad, V. R. Marathe, and S. Mitra, *Indian Acad. Sci. (Chem. Sci.)*, 1985, **95**, 189–205.

90. D. H. Dolphin, J. R. Sams, and B. T. Tsang, *Inorg. Chem.*, 1977, **16**, 711–713.

91. H. Masuda, T. Taga, K. Osaki, H. Sugimoto, Z. Yoshida, and H. Ogoshi, *Inorg. Chem.*, 1980, **19**, 950–955.

92. A. Osuka and K. Maruyama, *J.Am.Chem.Soc*, 1988, **1**, 4454–4456.

93. J.-C. Chambron, V. Heitz, and J.-C. Sauvage, in *The Porphyrin Handbook*, eds. K. M. Kadish, R. Guilard, and K. M. Smith, Academic Press, New York, Volume 6., 1999, p. 7946.

94. A. P. Gorka, A. de Dios, and P. D. Roepe, *J. Med. Chem.*, 2013, **56**, 5231–46.

95. M. T. Reetz, *J. Am. Chem. Soc.*, 2013, **135**, 12480–96.

96. A. F. Slater and A. Cerami, *Nature*, 1992, **355**, 167–9.

97. A. C. Chou and C. D. Fitch, *Life Sci.*, 1992, **51**, 2073–2078.

98. A. C. Chou and C. D. Fitch, *Biochem. Biophys. Res. Commun.*, 1993, **195**, 422–7.

99. A. Dorn, R. Stoffel, H. Matile, A. Bubendorf, and R. G. Ridley, *Lett. to Nat.*, 1995, **374**, 269–271.

100. D. J. Sullivan, I. Y. Gluzman, and D. E. Goldberg, *Science*, 1996, **271**, 219–222.

101. R. E. Hayward, D. J. Sullivan, and K. P. Day, *Exp. Parasitol.*, 2000, **96**, 139–146.

102. H. Noedl, W. H. Wernsdorfer, R. S. Miller, and C. Wongsrichanalai, *Antimicrob. Agents Chemother.*, 2002, **46**, 1658–1664.

103. V. Papalexis, M. A. Siomos, N. Campanale, X. G. Guo, G. Kocak, M. Foley, and L. Tilley, *Mol. Biochem. Parasitol.*, 2001, **115**, 77–86.

104. A. V. Pandey, V. K. Babbarwal, J. N. Okoyeh, R. M. Joshi, S. K. Puri, R. L. Singh, and V. S. Chauhan, *Biochem. Biophys. Res. Commun.*, 2003, **308**, 736–743.

105. V. Desakorn, A. M. Dondorp, K. Silamut, W. Pongtavornpinyo, D. Sahassananda, K. Chotivanich, P. Pitisuttithum, A. M. Smithyman, N. P. J. Day, and N. J. White, *Trans. R. Soc. Trop. Med. Hyg.*, 2005, **99**, 517–524.

106. T. Akompong, M. Kadekoppala, T. Harrison, A. Oksman, D. E. Goldberg, H. Fujioka, B. U. Samuel, D. Sullivan, and K. Haldar, *J. Biol. Chem.*, 2002, **277**, 28923–28933.

107. D. J. Sullivan, *Int. J. Parasitol.*, 2002, **32**, 1645–1653.

108. G. S. Noland, N. Briones, and D. J. Sullivan, *Mol. Biochem. Parasitol.*, 2003, **130**, 91–99.

109. D. Jani, R. Nagarkatti, W. Beatty, R. Angel, C. Slebodnick, J. Andersen, S. Kumar, and D. Rathore, *PLoS Pathog.*, 2008, **4**, e1000053.

110. M. Marti, J. Baum, M. Rug, L. Tilley, and A. F. Cowman, *J. Cell Biol.*, 2005, **171**, 587–592.

111. N. L. Hiller, S. Bhattacharjee, C. van Ooij, K. Liolios, T. Harrison, C. Lopez-Estraño, and K. Haldar, *Science*, 2004, **306**, 1934–1937.

112. M. Chugh, V. Sundararaman, S. Kumar, V. S. Reddy, W. A. Siddiqui, K. D. Stuart, and P. Malhotra, *Proc Natl Acad Sci U S A*, 2013, **110**, 5392–5397.

113. M. A. Ambele, PhD Thesis, University of Cape Town, 2013.

114. G. G. Holz, *Bull. World Health Organ.*, 1977, **55**, 237–248.

115. B. J. Visser, R. W. Wieten, I. M. Nagel, and M. P. Grobusch, *Malar. J.*, 2013, **12**, 442.

116. A. Cerami, K. Bendrat, and B. J. Berger, *Anal. Biochem.*, 1995, **231**, 151–156.

117. K. Bendrat and B. J. Berger, *Nature*, 1995, **378**, 138–139.

118. C. D. Fitch, G. Cai, Y.-F. Chen, and J. D. Shoemaker, *Biochim. Biophys. Acta - Mol. Basis Dis.*, 1999, **1454**, 31–37.

119. A. Dorn, S. R. Vippagunta, H. Matile, A. Bubendorf, J. L. Vennerstrom, and R. G. Ridley, *Biochem. Pharmacol.*, 1998, **55**, 737–747.

120. K. E. Jackson, N. Klonis, D. J. P. Ferguson, A. Adisa, C. Dogovski, and L. Tilley, *Mol. Microbiol.*, 2004, **54**, 109–22.

121. I. Coppens and O. Vielemeyer, *Int. J. Parasitol.*, 2005, **35**, 597–615.

122. A. K. Tripathi, S. K. Garg, and B. L. Tekwani, *Biochem. Biophys. Res. Commun.*, 2002, **290**, 595–601.

123. A. K. Tripathi, S. I. Khan, L. A. Walker, and B. L. Tekwani, *Anal. Biochem.*, 2004, **325**, 85–91.

124. J. M. Pisciotta, I. Coppens, A. K. Tripathi, P. F. Scholl, J. Shuman, S. Bajad, V. Shulaev, and D. J. Sullivan, *Biochem. J.*, 2007, **402**, 197–204.

125. K. A. de Villiers, M. Osipova, T. E. Mabotha, I. Solomonov, Y. Feldman, K. Kjaer, I. Weissbuch, T. J. Egan, and L. Leiserowitz, *Cryst. Growth Des.*, 2009, **9**, 626–632.

126. M. A. Ambele, B. T. Sewell, F. R. Cummings, P. J. Smith, and T. J. Egan, *Cryst. Growth Des.*, 2013, **13**, 4442–4452.

127. A. N. Hoang, K. K. Ncokazi, K. A. de Villiers, D. W. Wright, and T. J. Egan, *Dalton Trans.*, 2010, **39**, 1235–44.

128. S. Kapishnikov, T. Berthing, L. Hviid, M. Dierolf, A. Menzel, F. Pfeiffer, J. Als-Nielsen, and L. Leiserowitz, *Pnas*, 2012, **109**, 11184–11187.

129. E. Hempelmann, C. Motta, R. Hughes, S. A. Ward, and P. G. Bray, *Trends Parasitol.*, 2003, **19**, 23–26.

130. S. Kapishnikov, A. Weiner, E. Shimoni, G. Schneider, M. Elbaum, and L. Leiserowitz, *Langmuir*, 2013, **29**, 14595–14602.

131. N. T. Huy, Y. Shima, A. Maeda, T. T. Men, K. Hirayama, A. Hirase, A. Miyazawa, and K. Kamei, *PLoS One*, 2013, **8**, e70025.

132. J. M. Pisciotta and D. Sullivan, *Parasitol. Int.*, 2009, **57**, 89–96.

133. H. Ginsburg and R. A. Demel, *Chem. Phys. Lipids*, 1984, **35**, 331–347.

134. R. Stiebler, D. Majerowicz, J. Knudsen, K. C. Gondim, D. W. Wright, T. J. Egan, and M. F. Oliveira, *PLoS One*, 2014, **9**, e88976.

135. A. N. Hoang, R. D. Sandlin, A. Omar, T. J. Egan, and D. W. Wright, *Biochemistry*, 2010, **49**, 10107–16.

136. I. Weissbuch, M. Lahav, and L. Leiserowitz, *Cryst. Growth Des.*, 2003, **3**, 125–150.

137. L. N. Poloni and M. D. Ward, *Chem. Mater.*, 2014, **26**, 477–495.

138. A. Sharples, in *Introduction to polymer crystallization*, Edward Arnold, London, 1st edn., 1966, pp. 45–59.

139. M. Avrami, *J. Chem. Phys.*, 1939, **7**, 1103.

140. M. Avrami, *J. Chem. Phys.*, 1940, **8**, 212.

141. T. J. Egan and M. G. Tshivhase, *Dalton Trans.*, 2006, **42**, 5024–32.

142. R. F. Pasternack, B. Munda, A. Bickford, E. J. Gibbs, and L. M. Scolaro, *J. Inorg. Biochem.*, 2010, **104**, 1119–24.

143. M. A. Ambele and T. J. Egan, *Malar. J.*, 2012, **11**, 337–350.

144. I. Solomonov, M. Osipova, Y. Feldman, C. Baehtz, K. Kjaer, I. K. Robinson, G. T. Webster, D. Mcnaughton, B. R. Wood, I. Weissbuch, and L. Leiserowitz, *J.Am.Chem.Soc*, 2007, **129**, 2615–2627.

145. P. Overath and H. Träuble, *Biochemistry*, 1970, **12**, 2625–2634.

146. J. C. Eriksson and S. Ljunggren, *Langmuir*, 1996, **11**, 1145–1153.

147. M. Digel, R. Ehehalt, and J. Füllekrug, *FEBS Lett.*, 2010, **584**, 2168–75.

148. N. T. Huy, A. Maeda, D. T. Uyen, D. T. X. Trang, M. Sasai, T. Shiono, T. Oida, S. Harada, and K. Kamei, *Acta Trop.*, 2007, **101**, 130–8.

149. A. S. Myerson, *Handbook of Industrial Crystallization*, Butterworth-Heinemann, Boston, 2nd edn., 1993.

150. R. Stiebler, A. N. Hoang, T. J. Egan, D. W. Wright, and M. F. Oliveira, *PLoS One*, 2010, **5**, e12694.

151. M. A. Ketchum, K. N. Olafson, E. V Petrova, J. D. Rimer, and P. G. Vekilov, *J. Chem. Phys.*, 2013, **139**, 121911.

152. K. N. Olafson, J. D. Rimer, and P. G. Vekilov, *Cryst. Growth Des.*, 2014, **14**, 2123–2127.

153. K. N. Olafson, M. A. Ketchum, J. D. Rimer, and P. G. Vekilov, *Pnas*, 2015, **early edit**.

154. N. T. Huy, D. T. Uyen, A. Maeda, D. T. X. Trang, T. Oida, S. Harada, and K. Kamei, *Antimicrob. Agents Chemother.*, 2007, **51**, 350–3.

155. M. D. Carter, V. V Phelan, R. D. Sandlin, B. O. Bachmann, and D. W. Wright, *Comb. Chem. High Throughput Screen.*, 2010, **13**, 285–292.

156. R. M. Garavito and S. Ferguson-Miller, *J. Biol. Chem.*, 2001, **276**, 32403–32406.

157. J. J. Morelli and G. Szajer, *J. Surfactants Deterg.*, 2000, **3**, 539–552.

158. P. Banerjee, J. B. Joo, J. T. Buse, and G. Dawson, *Chem. Phys. Lipids*, 1995, **77**, 65–78.

159. M. J. Rosen, in *Surfactants and Interfacial Phenomena*, John Wiley & Sons, Inc., Hoboken, NJ, USA, 3rd edn., 2004, pp. 105–167.

160. N. Anoune, M. Nouiri, Y. Berrah, J.-Y. Gauvrit, and P. Lanteri, *J. Surfactants Deterg.*, 2002, **5**, 45–53.

161. K. Goodling, K. Johnson, L. Lefkowitz, and B. Wesley, *J. Chem. Educ.*, 1991, **71**, 8–12.

162. E. Takai, S. Ikawa, K. Kitano, J. Kuwabara, and K. Shiraki, *J. Phys. D. Appl. Phys.*, 2013, **46**, 295402–12.

163. J. L. Smith, *J. Pathol. Bacteriol.*, 1911, **15**, 53–55.

164. P. Greenspan and S. D. Fowler, *J.lipid Res.*, 1985, **26**, 781–789.

165. M. M. G. Krishna, *J. Phys. Chem. A*, 1999, **103**, 3589–3595.

166. N. Sarkar, K. Das, D. Nath, and K. Bhattacharyya, *Langmuir*, 1994, **10**, 326–329.

167. M. J. Vold, *Langmuir*, 1992, **8**, 1082–1085.

168. M. J. Vold, *J. Colloid Interface Sci.*, 1987, **116**, 129–133.

169. R. Hadgiivanova and H. Diamant, *J. Phys. Chem. B*, 2007, **111**, 8854–8859.

170. R. Hadgiivanova and H. Diamant, *J. Chem. Phys.*, 2009, **130**, 114901–1149015.

171. D. N. LeBard, B. G. Levine, R. DeVane, W. Shinoda, and M. L. Klein, *Chem. Phys. Lett.*, 2012, **522**, 38–42.

172. L. D. Song and M. J. Rosen, *Langmuir*, 1996, **12**, 1149–1153.

173. N. T. T. Nhien, N. T. Huy, D. T. Uyen, E. Deharo, P. T. Le Hoa, K. Hirayama, S. Harada, and K. Kamei, *Trop. Med. Health*, 2011, **39**, 119–26.

174. R. D. Sandlin, M. D. Carter, P. J. Lee, J. M. Auschwitz, S. E. Leed, J. D. Johnson, and D. W. Wright, *Antimicrob. Agents Chemother.*, 2011, **55**, 3363–9.

175. R. D. Sandlin, K. Y. Fong, K. J. Wicht, H. M. Carrell, T. J. Egan, and D. W. Wright, *Int. J. Parasitol. Drugs Drug Resist.*, 2014, **4**, 316–325.

176. R. Raj, V. Mehra, J. Gut, P. J. Rosenthal, K. J. Wicht, T. J. Egan, M. Hopper, L. a. Wrischnik, K. M. Land, and V. Kumar, *Eur. J. Med. Chem.*, 2014, **84**, 425–432.

177. K. Krafts, E. Hempelmann, and A. Skórska-Stania, *Parasitol. Res.*, 2012, **111**, 1–6.

178. Y. Tu, *Nat. Med.*, 2011, **17**, 1217–1220.

179. C. Faurant, *Parasite*, 2011, **18**, 215–218.

180. J. Achan, A. O. Talisuna, A. Erhart, A. Yeka, J. K. Tibenderana, F. N. Baliraine, P. J. Rosenthal, and U. D'Alessandro, *Malar. J.*, 2011, **10**, 144.

181. S. R. Meshnick and M. J. Dobson, in *Antimalarial Chemotherapy: Mechanisms of Action, Resistance, and New Directions in Drug Discovery*, ed. P. J. Rosenthal, Humana Press, XI., 2001, pp. 15–25.

182. World Health Organization, *Guidelines for the treatment of malaria, 2nd edition*, Geneva, Switzerland, 2010.

183. A. Brossi, B. Venugopalan, L. Dominguez Gerpe, H. J. Yeh, J. L. Flippen-Anderson, P. Buchs, X. D. Luo, W. Milhous, and W. Peters, *J. Med. Chem.*, 1988, **31**, 645–50.

184. S. R. Meshnick, *Int. J. Parasitol.*, 2002, **32**, 1655–1660.

185. S. Kamchonwongpaisan, N. Vanitchareon, and Y. Yuthavong, in *Lipid-Soluble Antioxidants: Biochemistry and Clinical Applications*, eds. A. S. H. Ong and L. Packer, Birkhäuser Basel, Basel, Molecular., 1992, pp. 363–372.

186. R. K. Haynes and S. Krishna, *Microbes Infect.*, 2004, **6**, 1339–1346.

187. R. K. Haynes, D. Monti, D. Taramelli, N. Basilico, S. Parapini, and P. Olliaro, *Antimicrob. Agents Chemother.*, 2003, **47**, 1175.

188. W. Peters, *Postgrad. Med. J.*, 1973, **49**, 573–583.

189. A. Yayon, Z. I. Cabantchik, and H. Ginsburg, *EMBO J.*, 1984, **3**, 2695–2700.

190. D. C. Warhurst and D. J. Hockley, *Nature*, 1967, **214**, 935–6.

191. O. Famin and H. Ginsburg, *Biochem. Pharmacol.*, 2002, **63**, 393–398.

192. H. C. Hoppe, D. A. Van Schalkwyk, U. I. M. Wiehart, S. A. Meredith, J. Egan, and B. W. Weber, *Antimicrob. Agents Chemother.*, 2004, **48**, 2370–2378.

193. C. A. Homewood, D. C. Warhurst, W. Peters, and V. C. Baggaley, *Nature*, 1972, **235**, 50–52.

194. P. B. Macomer, H. Sprinz, and A. J. Tousimis, *Nature*, 1967, **214**, 937–939.

195. J. M. Combrinck, T. E. Mabotha, K. K. Ncokazi, M. A. Ambele, D. Taylor, P. J. Smith, H. C. Hoppe, and T. J. Egan, *ACS Chem. Biol.*, 2013, **8**, 133–7.

196. M. Mungthin, P. G. Bray, R. G. Ridley, and S. A. Ward, *Antiinfect. Agents Med. Chem.*, 1998, **42**, 2973–2977.

197. F. Kwakye-Berko and S. R. Meshnick, *Mol. Biochem. Parasitol.*, 1989, **35**, 51–55.

198. S. R. Meshnick, *Parasitol. Today*, 1990, **6**, 77–79.

199. R. Zidovetzki, I. W. Sherman, J. Prudhomme, and J. Crawford, *Parasitology*, 1994, **108**, 249–255.

200. A. M. Silva, A. Y. Lee, S. V Gulnik, P. Maier, J. Collins, T. N. Bhat, P. J. Collins, R. E. Cachau, K. E. Luker, I. Y. Gluzman, S. E. Francis, A. Oksman, D. E. Goldberg, and J. W. Erickson, *Proc. Natl. Acad. Sci. U. S. A.*, 1996, **93**, 10034–10039.

201. E. Deharo, D. Barkan, M. Krugliak, J. Golenser, and H. Ginsburg, *Biochem. Pharmacol.*, 2003, **66**, 809–817.

202. T. J. Egan, D. C. Ross, and P. A. Adams, *FEBS Lett.*, 1994, **352**, 54–57.

203. C. H. Kaschula, T. J. Egan, R. Hunter, N. Basilico, S. Parapini, D. Taramelli, E. Pasini, and D. Monti, *J. Med. Chem.*, 2002, **45**, 3531–3539.

204. E. Milner, W. McCalmont, J. Bhonsle, D. Caridha, D. Carroll, S. Gardner, L. Gerena, M. Gettayacamin, C. Lanteri, T. Luong, V. Melendez, J. Moon, N. Roncal, J. Sousa, A. Tungtaeng, P. Wipf, and G. Dow, *Bioorganic Med. Chem. Lett.*, 2010, **20**, 1347–1351.

205. F. Dubar, J. Khalife, J. Brocard, D. Dive, and C. Biot, *Molecules*, 2008, **13**, 2900–2907.

206. H. Ginsburg, E. Nissani, and M. Krugliak, *Biochem. Pharmacol.*, 1989, **38**, 2645–54.

207. S. N. Cohen, K. O. Phifer, and K. L. Yielding, *Nature*, 1964, **202**, 805–806.

208. A. C. Chou, R. Chevli, and C. D. Fitch, *Biochemistry*, 1980, **19**, 1543–9.

209. C. D. Fitch, P. Kanjananggulpan, and J. S. Mruk, in *International Symposium on Malaria*, Rio de Janeiro, 1986, pp. 235–240.

210. P. R. Vashi and H. M. Marques, *J. Inorg. Biochem.*, 2004, **98**, 1471–82.

211. A. Dorn, S. R. Vippagunta, H. Matile, C. Jaquet, J. L. Vennerstrom, and R. G. Ridley, *Biochem. Pharmacol.*, 1998, **55**, 727–736.

212. S. Moreau, B. Perly, and J. Biguet, *Biochimie*, 1982, **64**, 1015–1025.

213. S. R. Vippagunta, A. Dorn, H. Matile, A. K. Bhattacharjee, J. M. Karle, W. Y. Ellis, R. G. Ridley, and J. L. Vennerstrom, *J. Med. Chem.*, 1999, **42**, 4630–4639.

214. S. R. Vippagunta, A. Dorn, R. G. Ridley, and J. L. Vennerstrom, *Biochim. Biophys. Acta*, 2000, **1475**, 133–140.

215. K. Bachhawat, C. J. Thomas, N. Surolia, and A. Surolia, *Biochem. Biophys. Res. Commun.*, 2000, **276**, 1075–1079.

216. I. R. Lantzke and D. W. Watts, *Jacs*, 1966, **453**, 815–821.

217. G. S. Collier, J. M. Pratt, C. R. de Wet, and C. F. Tshabalala, *Biochem. J.*, 1979, **179**, 281–289.

218. T. J. Egan, W. W. Mavuso, D. C. Ross, and H. M. Marques, *J. Inorg. Biochem.*, 1997, **68**, 137–145.

219. T. J. Egan, E. Hempelmann, and W. W. Mavuso, *J. Inorg. Biochem.*, 1999, **73**, 101–107.

220. A. Leed, K. Dubay, L. M. B. Ursos, D. Sears, A. C. De Dios, and P. D. Roepe, *Biochemistry*, 2002, **41**, 10245–10255.

221. A. C. de Dios, L. B. Casabianca, A. Kosar, and P. D. Roepe, *Inorg. Chem.*, 2004, **43**, 8078–84.

222. L. B. Casabianca, A. David, J. K. Natarajan, J. N. Alumasa, P. D. Roepe, C. Wolf, and A. C. de Dios, *Inorg. Chem.*, 2008, **47**, 6077–81.

223. L. B. Casabianca, J. B. Kallgren, J. K. Natarajan, J. N. Alumasa, P. D. Roepe, C. Wolf, and A. C. de Dios, *J. Inorg. Biochem.*, 2009, **103**, 745–8.

224. D. Kuter, S. J. Benjamin, and T. J. Egan, *J. Inorg. Biochem.*, 2014, **133**, 40–9.

225. D. C. Warhurst, *Biochem. Pharmacol.*, 1981, **30**, 3323–3327.

226. D. V Behere and H. M. Goff, *J.Am.Chem.Soc*, 1984, **106**, 4945–4950.

227. J. N. Alumasa, A. P. Gorka, L. B. Casabianca, E. Comstock, and C. Angel, *J. Inorg. Biochem.*, 2011, **105**, 467–475.

228. K. A. de Villiers, H. M. Marques, and T. J. Egan, *J. Inorg. Biochem.*, 2008, **102**, 1660–7.

229. J. M. Karle and I. L. Karle, *Antimicrob. Agents Chemother.*, 1991, **35**, 2238–2245.

230. K. A. de Villiers, J. Gildenhuys, and T. Roex, *ACS Chem. Biol.*, 2012, **7**, 666–671.

231. F. H. Allen, *Acta Crystallogr. Sect. B Struct. Sci.*, 2002, **58**, 380–388.

232. A. C. De Dios, R. Tycko, L. M. B. Ursos, and P. D. Roepe, *J. Phys. Chem. B*, 2003, **30**, 5821–5825.

233. M. J. Dascombe, M. G. B. Drew, H. Morris, P. Wilairat, S. Auparakkitanon, W. a. Moule, S. Alizadeh-Shekalgourabi, P. G. Evans, M. Lloyd, A. M. Dyas, P. Carr, and F. M. D. Ismail, *J. Med. Chem.*, 2005, **48**, 5423–5436.

234. T. J. Egan, R. Hunter, C. H. Kaschula, H. M. Marques, A. Misplon, and J. Walden, *J. Med. Chem.*, 2000, **43**, 283–291.

235. S. Nsumiwa, D. Kuter, S. Wittlin, K. Chibale, and T. J. Egan, *Bioorg. Med. Chem.*, 2013, **21**, 3738–48.

236. D. J. Sullivan, I. Y. Gluzman, D. G. Russell, and D. E. Goldberg, *Proc. Natl. Acad. Sci.*, 1996, **93**, 11865–11870.

237. D. J. Sullivan, H. Matile, R. G. Ridley, and D. E. Goldberg, *J. Biol. Chem.*, 1998, **273**, 31103–31107.

238. D. C. Warhurst, J. C. P. Steele, I. S. Adagu, J. C. Craig, and C. Cullander, *J. Antimicrob. Chemother.*, 2003, **52**, 188–93.

239. S. R. Hawley, P. G. Bray, M. Mungthin, J. D. Atkinson, P. M. O'Neill, and S. A. Ward, *Antimicrob. Agents Chemother.*, 1998, **42**, 682–686.

240. J. Gildenhuys, PhD thesis, University of Stellenbosch, 2013.

241. K. J. Wicht, J. M. Combrinck, P. J. Smith, and T. J. Egan, *Bioorg. Med. Chem.*, 2014, **In Press**.

242. B. L. Tekwani and L. A. Walker, *Comb. Chem. High Throughput Screen.*, 2005, **8**, 63–79.

243. H. R. Bhat, U. P. Singh, P. Gahtori, S. K. Ghosh, K. Gogoi, A. Prakash, and R. K. Singh, *New J. Chem.*, 2013, **37**, 2654.

244. W. Satimai, P. Sudathip, S. Vijaykadga, A. Khamsiriwatchara, S. Sawang, T. Potithavoranan, A. Sangvichean, C. Delacollette, P. Singhasivanon, J. Kaewkungwal, and S. Lawpoolsri, *Malar. J.*, 2012, **11**, 300.

245. Y. Kurosawa, A. Dorn, M. Kitsuji-Shirane, H. Shimada, T. Satoh, H. Matile, W. Hofheinz, R. Masciadri, M. Kansy, and R. G. Ridley, *Antimicrob. Agents Chemother.*, 2000, **44**, 2638–2644.

246. C. R. Chong and D. J. Sullivan, *Biochem. Pharmacol.*, 2003, **66**, 2201–2212.

247. M. A. Rush, M. L. Baniecki, R. Mazitschek, J. F. Cortese, R. Wiegand, J. Clardy, and D. F. Wirth, *Antimicrob. Agents Chemother.*, 2009, **53**, 2564–2568.

248. G. Garavito, M. C. Monje, S. Maurel, A. Valentin, F. Nepveu, and E. Deharo, *Exp. Parasitol.*, 2007, **116**, 311–313.

249. K. M. Durango, A. R. Maciuk, A. Harfouche, S. T. Guttierez, C. Jullian, J. Quintin, K. Spelman, E. Mouray, P. Grellier, B. Figadere, K. Muñoz-durango, A. Maciuk, and S. Torijano-gutiérrez, *Anal. Chem.*, 2012.

250. N. T. Huy, D. T. Uyen, M. Sasai, D. T. X. Trang, T. Shiono, S. Harada, and K. Kamei, *Anal. Biochem.*, 2006, **354**, 305–307.

251. A. V Pandey, N. Singh, B. L. Tekwani, S. K. Puri, and V. S. Chauhan, *J. Pharm. Biomed. Anal.*, 1999, **20**, 203–207.

252. N. Basilico, E. Pagani, D. Monti, P. Olliaro, and D. Taramelli, *J. Antimicrob. Chemother.*, 1998, **42**, 55–60.

253. K. K. Ncokazi and T. J. Egan, *Anal. Biochem.*, 2005, **338**, 306–19.

254. D. T. Xuan Trang, N. T. Huy, D. T. Uyen, M. Sasai, T. Shiono, S. Harada, and K. Kamei, *Anal. Biochem.*, 2006, **349**, 292–296.

255. S. Parapini, N. Basilico, E. Pasini, T. J. Egan, P. Olliaro, D. Taramelli, and D. Monti, *Exp. Parasitol.*, 2000, **96**, 249–56.

256. M. C. Joshi, K. J. Wicht, D. Taylor, R. Hunter, P. J. Smith, and T. J. Egan, *Eur. J. Med. Chem.*, 2013, **69**, 338–347.

257. D. C. Warhurst, J. C. Craig, I. S. Adagu, D. J. Meyer, and S. Y. Lee, *Malar. J.*, 2003, **2**, 1–14.

258. C. D. Fitch, *Life Sci.*, 2004, **74**, 1957–72.

259. S. R. Hawley, P. G. Bray, P. M. O'Neill, B. K. Park, and S. A. Ward, *Biochem. Pharmacol.*, 1996, **52**, 723–733.

260. B. M. Tissue, in *Characterization of Materials*, ed. E. N. Kaufmann, John Wiley & Sons, Inc., Hoboken, NJ, USA, 2nd edn., 2012, pp. 1–13.

261. C. B. Faust, *Modern Chemistry Techniques*, Royal Society of Chemistry, London, 1997.

262. D. Skoog, D. West, F. Holler, and S. Crouch, *Fundamentals of Analytical Chemistry*, Brooks/Cole, Belmont, California, 8th edn., 2013.

263. P. A. Cox, *Introduction To Quantum Theory And Atomic Structure*, Oxford University Press, Oxford, 1st edn., 1996.

264. J. W. Verhoeven, *Pure&Appl. Chem.,* 1996, **68**, 2223–2286.

265. V. Majidi, in *Encyclopedia of Physical Science and Technology*, ed. R. A. Meyers, Academic Press, London, 3rd edn., 2002, pp. 765–786.

266. M. Sauer, J. Hofkens, and J. Enderlein, *Handbook of Fluorescence Spectroscopy and Imaging*, Wiley-VCH, Weinheim, Germany, 2011.

267. R. Giovannetti, in *Macro to Nano Spectroscopy*, ed. J. Uddin, InTech, 2012, pp. 87–108.

268. M. Gouterman, in *The porphyrins*, ed. D. Dolphin, Academic Press, New York, volume 3., 1968, pp. 35–45.

269. A. G. Sykes, Ed., in *ADVANCES IN INORGANIC CHEMISTRY*, Academic Press, London, volume 36., 1991, pp. 201–255.

270. M. Gouterman, C. Weiss, and H. Kobayashi, *J. Mol. Spectrosc.*, 1965, **16**, 415–450.

271. T. Hashimoto, Y.-K. Choe, H. Nakano, and K. Hirao, *J. Phys. Chem. A*, 1999, **103**, 1894–1904.

272. I. Dragomir, A. Hagarman, C. Wallace, and R. Schweitzer-Stenner, *Biophys. J.*, 2007, **92**, 989–98.

273. M. Nappa and J. S. Valentine, *J. Am. Chem. Soc.*, 1978, **100**, 5075–5080.

274. M. W. Makinen and A. K. Churg, in *Iron Porphyrins*, eds. A. B. P. Lever and H. B. Gray, Addison-Wesley, Reading, M.A, 1st edn., 1983, pp. 141–235.

275. T. P. Wijesekera and D. Dolphin, in *Methods in Porphyrin Photosensitization*, Springer US, 1985, pp. 229–266.

276. M. Kasha, *Radiat. Res. Soc.*, 1963, **20**, 55–70.

277. M. Kasha, H. R. Rawls, and M. A. El-Bayoumi, *Pure Appl. Chem.*, 1965, **11**, 371–392.

278. O. Q. Munro and H. M. Marques, *Inorg. Chem.*, 1996, **35**, 3752–3767.

279. T. Miyahara, H. Nakatsuji, J. Hasegawa, A. Osuka, N. Aratani, and A. Tsuda, *J. Chem. Phys.*, 2002, **117**, 11196.

280. W. Rhodes and M. Chase, *Rev. Mod. Phys.*, 1967, **39**, 348–361.

281. T. B. J. Pinter, E. L. Dodd, D. S. Bohle, and M. J. Stillman, *Inorg. Chem.*, 2012, **51**, 3743–53.

282. D. Kuter, G. A. Venter, K. J. Naidoo, and T. J. Egan, *Inorg. Ch*, 2012, **51**, 10233–10250.

283. M. D. Cohen and E. Fischer, *J. Chem. Soc.*, 1962, 3044–3052.

284. M. Greger, M. Kollar, and D. Vollhardt, *Phys. Rev. B*, 2013, **87**, 195140.

285. J. S. Miller and M. Drillon, Eds., *Magnetism: Molecules to Materials IV*, Wiley-VCH Verlag, Weinheim, Germany, 4th edn., 2002, vol. 4.

286. A. Earnshaw, *Introduction to magnetochemistry*, Academic Press, London, 1968.

287. G. A. Bain and J. F. Berry, *J. Chem. Educ.*, 2008, **85**, 532.

288. A. Wold and K. Dwight, in *Solid state Chemistry: Synthesis, structure and properties of selected oxides and sulfides*, Springer-US, 1st edn., 1993, pp. 47–51.

289. K. Dziedzic-kocurek and D. Okła, *Nukleonika*, 2013, **58**, 83–86.

290. D. F. Evans, *J. Chem. Soc.*, 1959, 2003–2005.

291. B. H. Stuart, *Infrared Spectroscopy:Fundamentals and Applications*, John Wiley&Sons, Ltd, West Sussex, England, 1st edn., 2004.

292. P. W. Atkins, *Physical Chemistry*, Oxford University Press, Oxford, 4th edn., 1991.

293. Z. Monsef Khoshhesab, *Infrared Spectroscopy-Materials Science, Engineering and Technology*, InTech, Rijeka, 1st edn., 2012.

294. N. Ramanujam, in *Encyclopedia of Analytical Chemistry: Applications , Theory and Instrumentation*, ed. R. . Meyers, John Wiley & Sons, Ltd, Chichester, 1st edn., 2000, pp. 20–56.

295. B. Valeur, *Molecular Fluorescence Principles and Applications*, Wiley-VCH, Weinheim, 1st edn., 2001, vol. 8.

296. J. R. Lakowicz, in *Principles of Fluorescence Spectroscopy*, Springer-US, New York, Third., 2006, pp. 1–26.

297. J. R. Albani, *Principles and Applications of Fluorescence Spectroscopy*, Blackwell Publishing, Oxford, First., 2007.

298. A. Nathir and F. Al-Rawashdeh, in *Macro to nano Spectroscopy*, ed. J. Uddin, InTech, Rijeka, 2012.

299. J. R. Lakowicz, in *Principles of Fluorescence Spectroscopy*, Springer-US, New York, Third., 2006, pp. 27–61.

300. D. P. Millar, *Curr. Opin. Struct. Biol.*, 1996, **6**, 637–642.

301. J. R. Lakowicz, in *Principles of Fluorescence Spectroscopy*, Springer-US, New York, 3rd edn., 2006, pp. 97–155.

302. G. A. Caputo and E. London, *Biochemistry*, 2003, **42**, 3265–3274.

303. M. A. R. B. Castanho and M. J. E. Prieto, *Biochim. Biophys. Acta*, 1998, **1373**, 1–16.

304. E. W. Mosmuller, E. H. Pap, A. J. Visser, and J. F. Engbersen, *Biochim. Biophys. Acta*, 1994, **1189**, 45–51.

305. W. E. Moerner and D. P. Fromm, *Rev. Sci. Instrum.*, 2003, **74**, 3597.

306. K. Pawlak, G. E. Bialek-Bylka, and A. Skrzypczak, in *Applications of Ionic Liquids in Science and Technology*, ed. S. Handy, InTech Europe, Rijeka, Croatia, 1st edn., 2011, pp. 401–420.

307. J. R. Lakowicz, in *Principles of Fluorescence Spectroscopy*, Springer US, New York, Third., 2006, pp. 205–235.

308. J. R. Lakowicz, in *Principles of Fluorescence Spectroscopy*, Springer-US, New York, Third., 2006, pp. 278–330.

309. M. van de Weert and L. Stella, *J. Mol. Struct.*, 2011, **998**, 144–150.

310. E. Blatt, R. C. Chatelier, and W. H. Sawyer, *J. Biophys.*, 1986, **50**, 349–356.

311. N. Santos, *Biochim. Biophys. Acta - Biomembr.*, 2003, **1612**, 123–135.

312. E. Blatt, R. C. Chatelier, and W. H. Sawyer, *Chem. Phys. Lett.*, 1964, **108**, 397–400.

313. M. Vermeir and N. Boens, *Eur. Biophys. J.*, 1992, **56**, 47–56.

314. J. R. Lakowicz, D. Hogen, and G. Omann, *Biochim. Biophys. Acta*, 1977, **471**, 401–11.

315. G. M. Omann and M. Glaser, *Biophys. J.*, 1985, **47**, 623–7.

316. M. V. Encinas and E. A. Lissi, *Chem. Phys. Lett.*, 1982, **91**, 55–57.

317. M. . Hoffman, L. Moggi, F. Bolletta, and G. . Hug, *J.Phys.Chem.*, 1989, **18**, 219–543.

318. G. Omann and J. R. Lakowicz, *Science*, 1977, **197**, 465–7.

319. H. Motulsky, *Prism*, 1999, 7–14.

320. P. Gans, A. Sabatini, and A. Vacca, *Talanta*, 1996, **43**, 1739–1753.

321. O. V Dolomanov, A. J. Blake, N. R. Champness, and M. Schröder, *J. Appl. Crystallogr.*, 2003, **36**, 1283–1284.

322. D. Kuter, PhD Thesis, University of Cape Town, 2014.

323. N. M. Q. Palacpac, Y. Hiramine, F. Mi-ichi, M. Torii, K. Kita, R. Hiramatsu, T. Horii, and T. Mitamura, *J. Cell Sci.*, 2004, **117**, 1469–80.

324. S. Kapishnikov, A. Weiner, E. Shimoni, P. Guttmann, G. Schneider, and N. Dahan-pasternak, *PNAS*, 2012, **109**, 11188–11193.

325. Y. Kuhn, P. Rohrbach, and M. Lanzer, *Cell. Microbiol.*, 2007, **9**, 1004–13.

326. P. Greenspan, E. P. Mayer, and S. D. Fowler, *J. Cell Biol.*, 1985, **100**, 965–973.

327. M. V Ranall, B. G. Gabrielli, and T. J. Gonda, *Biotechniques*, 2011, **51**, 35–6, 38–42.

328. J. F. Aranda, Coutinho.A, M. N. Berberan-Santos, M. J. E. Prieto, and J. C. Gomez-Fernandez, *Biochim. Biophys. Acta*, 1989, **985**, 26–32.

329. A. Jenei, L. Ma´tyus, and J. Szo¨llosi, *J. Photochem. Photobiol. B Biol.*, 2006, **83**, 223–236.

330. B. De Castro, P. Gameiro, L. F. C. Lima, and C. Matos, *Colloids Surfaces A Physicochem. Eng. Asp.*, 2001, **190**, 205–212.

331. C. Reichardt, *Chem. Rev.*, 1994, **94**, 2319–2358.

332. The Organisation for Economic Co-operation and Development, *OCED GUIDELINES FOR THE TESTING OF CHEMICALS*, 2003.

333. G. Weber and F. W. J. Teale, *Trans. Faraday Soc.*, 1958, **54**, 640.

334. W.-G. Han, T. Liu, F. Himo, A. Toutchkine, D. Bashford, K. M. Hahn, and L. Noodleman, *Chemphyschem*, 2003, **4**, 1084–94.

335. C. M. Golini, B. W. Williams, and J. B. Foresman, *J. Fluoresc.*, 1998, **8**, 395–404.

336. F. Alonzo and P. Mayzaud, *Mar. Chem.*, 1999, **67**, 289–301.

337. G. Diaz, M. Melis, B. Batetta, F. Angius, and A. M. Falchi, *Micron*, 2008, **39**, 819–24.

338. S. Mukherjee, H. Raghuraman, and A. Chattopadhyay, *Biochim. Biophys. Acta*, 2007, **1768**, 59–66.

339. G. Hungerford, A. Rei, and M. I. C. Ferreira, *FEBS J.*, 2005, **272**, 6161–9.

340. J. Romel Malapascua, *African J. Biotechnol.*, 2012, **11**, 13518–13527.

341. C. A. Parker and W. T. Rees, *Analyst*, 1962, **87**, 83.

342. Q. Gu, *Improvement of Corrections for Fluorescence Inner Filter Effects Under Non-ideal Beam Conditions Based on Effective Geometric Parameters*, ProQuest, 2007.

343. P. K. Behera, T. Mukhurjee, and A. K. Mishra, *J. Lumin.*, 1995, **65**, 131–136.

344. J. Moan, K. Berg, H. B. Steen, T. Warloe, and K. Madslein, in *Photodynamic Therapy: Basic Principles and Clinical Applications*, eds. B. W. Henderson and T. J. Dougherty, Marcel Dekker Inc, New York, 1st edn., 1992, pp. 19–37.

345. I. E. Borissevitch, *J. Lumin.*, 1999, **81**, 219–224.

346. M. M. Puchalski, M. J. Morra, and R. von Wandruszka, *Fresenius. J. Anal. Chem.*, 1991, **340**, 341–344.

347. A. V Fonin, A. I. Sulatskaya, I. M. Kuznetsova, and K. K. Turoverov, *PLoS One*, 2014, **9**, e103878.

348. A. N. Hoang, PhD Thesis, Vanderbilt University, 2010.

349. K. Pawlak, A. Skrzypczak, and G. E. Bialek-bylka, in *Applications of Ionic Liquids in Science and Technology*, ed. S. Handy, InTech Europe, Rijeka, Croatia, 1st edn., 2011, vol. 1, pp. 401–420.

350. W. R. Ware and J. S. Novros, *J. Phys. Chem.*, 1966, **129**, 3246–3253.

351. L. Stella, M. van de Weert, H. D. Burrows, and R. Fausto, *J. Mol. Struct.*, 2014, **1077**, 1–3.

352. G. Behera, B. Mishra, P. Behera, and M. Panda, *Adv. Colloid Interface Sci.*, 1999, **82**, 1–42.

353. K. M. Kadish, K. M. Smith, and R. Guilard, Eds., *The Porphyrin Handbook: Phthalocyanines: Spectroscopic and Electrochemical Characterization, Volume 16*, Academic Press, San Diego, 16th edn., 2006.

354. A. C. Chou and C. D. Fitch, *J. Clin. Invest.*, 1981, **68**, 672–7.

355. M. Warren and A. Smith, *Tetrapyrroles: Birth, Life and Death*, Springer Science & Business Media, 2009.

356. J. S. Olson and W. R. Light, *J. Biol. Chem*, 1990, **265**, 15632–15637.

357. S. Bonneau, N. Maman, and D. Brault, *Biochim. Biophys. Acta*, 2004, **1661**, 87–96.

358. M. Kępczyński, B. Ehrenberg, and M. Ke, *Photochem. Photobiol.*, 2002, **76**, 486–492.

359. M. Kępczyński, R. P. Pandian, K. M. Smith, and B. Ehrenberg, *Photochem. Photobiol.*, 2002, **76**, 127–134.

360. T. J. Egan, *J. Inorg. Biochem.*, 2006, **100**, 916–26.

361. S. A. Bourne, K. De Villiers, and T. J. Egan, *Acta Crystallogr. C.*, 2006, **62**, 53–7.

362. R. Mannhold, Ed., *Molecular Drug Properties Measurement and Prediction*, Wiley-VCH Verlag GmbH & Co. KGaA, Weinheim, Germany, 1st edn., 2008.

363. J. Swarbrick, G. Lee, J. Brom, and N. P. Gensmantel, *J. Pharm. Sci.*, 1984, **73**, 1352–5.

364. D. C. Warhurst, J. C. Craig, I. S. Adagu, R. K. Guy, P. B. Madrid, and Q. L. Fivelman, *Biochem. Pharmacol.*, 2007, **73**, 1910–26.

365. A. M. D. S. D. Acharige and M. C. Durrant, *Transit. Met. Chem.*, 2014, **39**, 721–726.

366. H. M. Marques, *Inorg. Chem.*, 1990, **29**, 1597–1599.

367. F. Dubar, T. J. Egan, B. Pradines, D. Kuter, K. K. Ncokazi, D. Forge, C. Pierrot, H. Kalamou, J. Khalife, E. Buisine, C. Rogier, I. Forfar, C. Slomianny, O. X. Trivelli, S. Kapishnikov, L. Leiserowitz, D. Dive, and C. Biot, *ACS Chem. Biol.*, 2011, **6**, 275–287.

368. J. M. Karle, I. L. Karle, L. Gerena, and W. K. Milhous, *Antimicrob. Agents Chemother.*, 1992, **36**, 1538–1544.

369. L. B. Casabianca, D. An, J. K. Natarajan, J. N. Alumasa, P. D. Roepe, C. Wolf, and A. C. De Dios, 2008, **47**, 6077–6081.

370. H. M. Marques, T. J. Egan, and K. A. de Villiers, in *Structure and Function*, ed. P. Comba, Springer Science & Business Media, Heidelberg, 1st edn., 2009, pp. 87–105.

371. A. Avdeef, *Absorption and Drug Development: Solubility, Permeability, and Charge State*, John Wiley & Sons, 2003.

372. N. Bodor, Z. Gabanyi, and C.-K. Wong, *J. Am. Chem. Soc.*, 1989, **111**, 3783–3786.

373. M. Zhu, B. W. Puls, C. Frandsen, J. D. Kubicki, H. Zhang, and G. A. Waychunas, *Inorg. Chem.*, 2013, **52**, 6788–97.

374. B. S. B. Brown, M. Shillcock, and P. Jones, *J. Biochem.*, 1976, **153**, 279–285.

375. A. V Pandey, S. K. Joshi, B. L. Tekwani, and V. S. Chauhan, *Anal. Biochem.*, 1999, **268**, 159–161.

376. D. Linke, *Methods Enzymol.*, 2009, **463**, 603–17.

377. J. Simplicio, *Biochemistry*, 1972, **11**, 2525–2528.

378. J. Simplicio and K. Schwenzer, *Biochemistry*, 1973, **12**, 1923–9.

379. S. Mazumdar, O. K. Medhi, and S. Mitra, *Inorg. Chem.*, 1988, **27**, 2541–2543.

380. M. C. A. Stuart, J. C. van de Pas, and J. B. F. N. Engberts, *J. Phys. Org. Chem.*, 2005, **18**, 929–934.

381. W. R. Carmody, *J. Chem. Educ.*, 1964, **41**, 615–616.

382. W. Harkins and H. Jordan, *Jacs*, 1930, **52**, 1751–1772.

383. D. Myers, in *Surfaces, Interfaces, and Colloids: Principles and Applications*, John Wiley & Sons, Inc., New York, USA, 2nd edn., 1999, pp. 363–387.

384. A. Chattopadhyay and E. London, *Anal. Biochem.*, 1984, **139**, 408–412.

385. A. Chattopadhyay and K. G. Harikumar, *FEBS Lett.*, 1996, **391**, 199–202.

386. A. Jakubowska, *J. Colloid Interface Sci.*, 2010, **346**, 398–404.

387. P. H. Roos, in *Protein Liquid Chromatography*, ed. M. Kastner, Elsevier, Amsterdam, 1st edn., 2000, pp. 61–68.

388. I. a. Nyrkova and A. N. Semenov, *Macromol. Theory Simulations*, 2005, **14**, 569–585.

389. A. Patist, S. S. Bhagwat, K. W. Penfield, P. Aikens, and D. O. Shah, *J. Surfactants Deterg.*, 2000, **3**, 53–58.

390. P. H. Elworthy and K. J. Mysels, *J. Colloid Interface Sci.*, 1966, **7**, 331–347.

391. K. L. Mittal, *J. Pharm. Sci.*, 1972, **61**, 1334–1335.

392. A. Boffi, T. K. Das, S. della Longa, C. Spagnuolo, and D. L. Rousseau, *Biophys. J.*, 1999, **77**, 1143–9.

393. D. K. Das, C. Bhattaray, and O. K. Medhi, *J. Chem. Soc., Dalt. Trans. (Cambridge, Engl. 2003)*, 1997, **24**, 4713–4717.

394. J. P. Fitzgerald, B. S. Haggerty, A. L. Rheingold, L. May, and G. A. Brewer, *Inorg. Chem.*, 1992, **31**, 2006–2013.

395. O. Q. Munro, M. De Wet, H. Pollak, J. van Wyk, and H. M. Marques, *Faraday Trans.*, 1998, **94**, 1743–1752.

396. J. Stanek and K. Dziedzic-Kocurek, *J. Magn. Magn. Mater.*, 2010, **322**, 999–1003.

397. K. Gersonde, A. Seidel, and H. Netter, *J. Mol. Biol.*, 1965, **14**, 37–47.

398. G. Blauer, D. Harmatz, and B. Zvilichovsky, *FEBS Lett.*, 1973, **34**, 344–346.

399. L. A. Yatsunyk, A. Dawson, M. D. Carducci, G. S. Nichol, and F. Ann Walker, *Inorg. Chem.*, 2006, **45**, 5417–5428.

400. D. Kuter, K. Chibale, and T. J. Egan, *J. Inorg. Biochem.*, 2011, **105**, 684–92.

401. O. K. Medhi, S. Mazumdar, and S. Mitra, *Inorg. Chem.*, 1989, **7**, 3243–3248.

402. G. P. Gupta, G. Lang, Y. J. Lee, W. R. Scheidt, K. Shelly, and C. A. Reed, *Inorg. Chem.*, 1987, **18**, 3022–3030.

403. R. G. Alargova, I. I. Kochijashky, M. L. Sierra, and R. Zana, 1998, **7463**, 5412–5418.

404. S. Gokturk and M. Tuncay, *J. Surfactants Deterg.*, 2003, **6**, 325–330.

405. M. Verbrugghe, E. Cocquyt, P. Saveyn, P. Sabatino, D. Sinnaeve, J. C. Martins, and P. Van der Meeren, *J. Pharm. Biomed. Anal.*, 2010, **51**, 583–9.

406. M. Verbrugghe, P. Sabatino, E. Cocquyt, P. Saveyn, D. Sinnaeve, P. Van der Meeren, and J. C. Martins, *Colloids Surfaces A Physicochem. Eng. Asp.*, 2010, **372**, 28–34.

407. J. Koehler and J. Meiler, *Prog. Nucl. Magn. Reson. Spectrosc.*, 2011, **59**, 360–89.

408. E. Schrank, G. E. Wagner, and K. Zangger, *Molecules*, 2013, **18**, 7407–7435.

409. G. Wider and K. Wüthrich, *Curr. Opin. Struct. Biol.*, 1999, **9**, 594–601.

410. K. A. Zacharlasse, N. Van Phuc, and B. Kozanklewicz, *J. Phys. Chem.*, 1981, **1613**, 2676–2683.

411. T. J. Egan, *J. Inorg. Biochem.*, 2002, **91**, 19–26.

412. Y. Corbett, S. Parapini, S. D'Alessandro, D. Scaccabarozzi, B. C. Rocha, T. J. Egan, A. Omar, L. Galastri, K. a Fitzgerald, D. T. Golenbock, D. Taramelli, and N. Basilico, *Microbes Infect.*, 2015, **17**, 184–194.

413. M. O. Pjeill, P. G. Bray, S. R. Hawley, S. A. Ward, and B. K. Park, *Pharmacol. Ther.*, 1998, **77**, 29–58.

414. T. J. Egan and K. K. Ncokazi, *J. Inorg. Biochem.*, 2005, **99**, 1532–1539.

415. L. M. B. Ursos, K. F. DuBay, and P. D. Roepe, *Mol. Biochem. Parasitol.*, 2001, **112**, 11–17.

416. B. Witkowski, J. Lelièvre, M.-L. Nicolau-Travers, X. Iriart, P. Njomnang Soh, F. Bousejra-Elgarah, B. Meunier, A. Berry, and F. Benoit-Vical, *PLoS One*, 2012, **7**, e32620.

417. T. J. Egan, *Targets*, 2003, **2**, 115–124.

418. W. J. E. M. Habraken, J. Tao, L. J. Brylka, H. Friedrich, L. Bertinetti, A. S. Schenk, A. Verch, V. Dmitrovic, P. H. H. Bomans, P. M. Frederik, J. Laven, P. van der Schoot, B. Aichmayer, G. de With, J. J. DeYoreo, and N. a J. M. Sommerdijk, *Nat. Commun.*, 2013, **4**, 1507.

419. F. Nudelman, A. J. Lausch, N. a J. M. Sommerdijk, and E. D. Sone, *J. Struct. Biol.*, 2013, **183**, 258–269.

420. B. R. Wood, S. J. Langford, B. M. Cooke, F. K. Glenister, J. Lim, and D. McNaughton, *FEBS Lett.*, 2003, **554**, 247–252.